ResearchOnline@JCU

This file is part of the following work:

Chapman, Lucy H. (1999) ***Geology and genesis of the George Fisher Zn-Pb-Ag deposit Mount Isa, Australia.*** **PhD Thesis, James Cook University.**

Access to this file is available from:

https://doi.org/10.25903/5c20326edef84

Copyright © 1999 Lucy H. Chapman

The author has certified to JCU that they have made a reasonable effort to gain permission and acknowledge the owners of any third party copyright material included in this document. If you believe that this is not the case, please email researchonline@jcu.edu.au

Geology and Genesis of the George Fisher Zn-Pb-Ag deposit, Mount Isa, Australia.

Volume 2

Thesis submitted by

Lucy H. Chapman B.Sc.(Hons.)

in August, 1999,

for the degree of Doctor of Philosophy

in the School of Earth Sciences,

James Cook University.

LIST OF TABLES AND FIGURES

PART A
GEOLOGY, SETTING AND MINERALIZATION STYLES OF THE GEORGE FISHER ZN-PB-AG DEPOSIT, MOUNT ISA, AUSTRALIA.

LIST OF TABLES

1. Summary of the major structural elements developed in the Mount Isa area.
2. Summary of major deformation events and mineralization styles at George Fisher and comparison with previous structural studies.
3. Summary of mineralization style classification scheme at George Fisher.
4. Metal budgets for the Mount Isa, Hilton and George Fisher deposits.

LIST OF FIGURES

1. Map of the Mount Isa-McArthur minerals province.
2. Stratigraphic framework of the Western Fold Belt, Mount Isa Inlier.
3. Geological map illustrating major structural and stratigraphic elements of the Mount Isa area.
4. Geology map of George Fisher and surrounds.
5. Interpreted plan geology map of the main economic zone at 12 level at George Fisher.
6. Interpreted geological cross-section at 7200mN illustrating major structural and stratigraphic elements at George Fisher.
7. Simplified stratigraphic column with metal distribution patterns and dominant gangue at the George Fisher deposit.
8.
   (a) Stratigraphic sections for the H stratigraphic interval from 7020mN to 7820mN.
   (b) Stratigraphic sections for the E and F stratigraphic intervals from 7020mN to 7820mN.
   (c) Stratigraphic sections for the D, C and B stratigraphic intervals from 7020mN to 7820mN.
9.
   (a) Planar laminated to massive stylolitic, medium-bedded mudstone.
   (b) Banded mudstones display distinctive light grey calcitic and dark grey dolomitic banding and forms gradational contact with overlying pyritic siltstone.

(c) Graded bedding intervals within a banded mudstone.

(d) Thin shaly banded mudstone characterized by pyritic black shale and cross-bedded shaly siltstone bedding intervals.

(e) Rhythmically laminated carbonaceous siltstone.

(f) Photomicrograph of a rhythmically laminated pyritic siltstone interval.

(g) Intercalated banded mudstone and rhythmically laminated pyritic siltstone with abundant white planar calcite bands.

(h) Nodular carbonate occurs as bedding parallel and displacive, wavy layers in thin pyritic siltstone beds.

(i) Photomicrograph illustrating textural similarity between white calcite band and nodular calcite.

(j) Banded, calcitic and dolomitic banded mudstone contains solitary and stacked white band couplets.

10. Interpretative cross-sections at 7020mN, 7180mN, 7300mN and 7820mN illustrating major stratigraphic subdivisions and late-stage faults.

11. Mapped sections illustrating mesoscale structural features in the C ore zone, 7200mN underground cross-cut.

12.

(a) Photomicrograph illustrating pervasive development of a D_1 bedding-parallel foliation in variably carbonaceous mudstone.

(b) Photomicrograph of a bedding-parallel and symmetrically infilled quartz-K-feldspar-sphalerite-hydrophlogopite vein.

(c) Photomicrograph illustrating crenulate sphalerite vein margins.

(d) Vertically oriented thin section photomicrograph illustrating microstructural effects of D_2.

13. Photomicrograph and line diagram illustrating microstructural effects of D_3 and D_4.

14.

(a) Rhythmically laminated pyritic siltstone folded around a D2 fold that has been variably rotated into inclined and subhorizontal fold orientations.

(b) Flat-lying fold developed in intercalated rhythmically laminated pyritic siltstones and banded mudstones.

(c) Complex refold patterns produced by the superposition of D_4 folds on D_2 folds rotated by D3.

(d) Inclined D_2 fold in a pyritic siltstone bounded by fine-grained sphalerite breccias.

15.
(a) Rhythmically laminated carbonaceous siltstone-hosted sphalerite style.

(b) Rhythmically laminated pyritic siltstone-hosted honey-coloured sphalerite.

(c) Nodular calcite-hosted sphalerite.

(d) Photomicrograph illustrating preferential development of sphalerite in coarser-grained nodular calcite layers.

(e) Spheroidal pyrite and sphalerite distributed along layers in black shale.

(f) Thin section photomicrograph of shale-hosted sphalerite.

(g) Fine-grained honey-coloured sphalerite irregularly distributed along planar beds in a medium-bedded mudstone.

(h) Steel grey, fine-grained galena hosted by feldspathic mudstone.

16.
(a) Example of a range of mineralization styles developed in a single drill core specimen.

(b) Thin section photomicrograph of a sphalerite breccia-vein.

(c) Fine-grained sphalerite breccia and nodular-carbonate-hosted sphalerite in a rhythmically laminated pyritic siltstone.

(d) Stratabound fine-grained sphalerite breccias in a banded mudstone.

(e) Coarse-grained galena occurs as breccia matrix.

(f) Fine-grained galena breccia characterized by rounded clasts of variable composition.

(g) Mixed sulphide breccia containing flame-like pyrite-, sphalerite-, and galena-rich domains.

(h) Feldspathic rock with relict fine-grained pyritic laminations cross-cut by discordant chalcopyrite-bearing veins.

(i) Very coarse-grained sphalerite-galena-pyrite-pyrrhotite-calcite-dolomite vein.

(j) Coarse-grained honey-coloured sphalerite-galena-calcite typical of L70-type fault-fill.

17.
(a) Distribution of sphalerite and galena-dominant mineralization styles compared with Zn and Pb assay data for the E and F stratigraphic intervals.

(b) Distribution of sphalerite and galena-dominant mineralization styles compared with Zn and Pb assay data for the D, C and B stratigraphic intervals.

18. Simplified stratigraphic columns for Mount Isa, Hilton and George Fisher.

Part B
Evolution of Zn-Pb-Ag and Cu Mineralization at the George Fisher deposit, Mount Isa, Australia.

List of Tables

1. Alteration and mineralization paragenesis at the George Fisher deposit.

2. Summary of major features of each paragenetic stage and key timing criteria.

3. Common metal transport and precipitation models proposed for sediment-hosted Zn-Pb deposits.

4. Metal precipitation mechanisms derived to account for common textural associations at George Fisher.

List of Figures

1. Carbonate distribution logs superimposed on a stratigraphic plan map of the H stratigraphic interval.

2. Carbonate distribution logs superimposed on a stratigraphic plan map of the E and F stratigraphic intervals.

3.
   (a) Carbonate distribution logs superimposed on a stratigraphic plan map of the D, C and B stratigraphic intervals.

   (b) Silicate-sulphide distribution logs superimposed on a stratigraphic plan map of the D, C and B stratigraphic intervals.

4.
   (a) Light grey calcite alteration irregularly developed in a dark grey, ferroan dolomite-bearing medium-bedded mudstone.

   (b) Stage I calcite alteration selectively developed in a ferroan dolomite-bearing banded mudstone.

   (c) Photomicrograph illustrating extensive Stage I calcite alteration in a medium-bedded mudstone interval.

   (d) Bedding-parallel to discordant nodular calcite developed in a rhythmically laminated pyritic siltstone.

   (e) Microcrystalline subhedral to rhombohedral calcite crystals in a nodular calcite layer line microscopic vughs which are infilled by sphalerite.

5.
   (a) BSE image illustrating abundant Stage I rhombohedral calcite and Stage IV sphalerite infill in a microscopic nodular layer.

   (b) Two nodular calcite layers separated by a fine ferroan dolomite-quartz lamination with spheroidal pyrite (BSE image).

   (c) BSE image illustrating diffuse nature of layer-parallel white band contacts.

(d) Quartz concentrated around a carbonaceous stylolite (BSE image).

6.
(a) Plot of whole rock abundances of quartz versus ferroan dolomite and Stage I calcite.

(b) Plot illustrating whole rock abundances of quartz versus Stage I calcite.

7.
(a) Celsian-hyalophane-K-feldspar alteration preferentially developed along mudstone layers.

(b) Buff-coloured celsian-hyalophane-K-feldspar alteration in a medium-bedded mudstone.

8.
(a) Discordant vein sequentially infilled by Stage III celsian, hyalophane, K-feldspar and calcite (BSE image).

(b) BSE image illustrating paragenetic associations within a sphalerite breccia-vein.

(c) Hyalophane-K-feldspar alteration concentrated in a dolomitic banded mudstone rather than rhythmically laminated pyritic siltstone (BSE image).

(d) Ultrafine-grained celsian-hyalophane-K-feldspar developed along spheroidal pyrite and ferroan dolomite grain contacts (BSE image).

9.
(a) Photomicrograph of ultrafine-grained celsian-hyalophane-K-feldspar developed in a Stage I calcite-altered banded mudstone.

(b) Photomicrograph of a calcite-celsian-hyalophane-K-feldspar vein that cross-cuts a stylolite bearing abundant spheroidal pyrite.

10.
(a) Intergrowths of bitumen and sphalerite occur interstitial to quartz-carbonate in a banded mudstone (photomicrograph).

(b) Stringers of brown bitumen contain sphalerite, pyrite and galena inclusions (photomicrograph).

(c) Photomicrograph illustrating the edge of a migrabitumen-sphalerite-brassy pyrite alteration zone in a Stage I calcite-altered mudstone bed.

(d) Calcite-quartz-brassy pyrite infill after fragmented migrabitumen (photomicrograph).

(e) Photomicrograph of textural zonation exhibited by meso-impsonite.

11. Plot of maximum versus minimum bitumen reflectance (in oil) for migrabitumen populations 1 and 2.

12.
(a) Brassy pyrite alteration band irregularly bounded by hydrophlogopite and contained within a sphalerite-rich band (photomicrograph).

(b) Semi-massive sphalerite breccia with coarse grained celsian-hyalophane-K-feldspar-calcite clasts (photomicrograph).

(c) Photomicrograph illustrating paragenetic associations from an economic intersection containing breccia-vein-hosted sphalerite.

(d) Sphalerite alteration of fine- to coarse-grained carbonate and Ba-K-feldspar in breccia-veins and wall rock (photomicrograph).

(e) Photomicrograph of a sphalerite breccia-vein.

13. Model proposed for the paragenetic and structural evolution of breccia-vein-hosted sphalerite at George Fisher.

14.

(a) Warped Stage V sugary ferroan dolomite vein set cross-cuts Stage IV stratiform sphalerite (photomicrograph).

(b) Preferential development of folds, and irregular brecciation of a sugary dolomite vein in sphalerite bands.

15.

(a) Coarse-grained galena breccia containing large clasts of banded and stratiform sphalerite (photomicrograph).

(b) Medium-grained galena breccia selectively developed in banded sphalerite (photomicrograph).

(c) Photomicrograph illustrating abundance of sphalerite clasts in a medium-grained galena breccia.

(d) Galena breccia containing fragments of sphalerite with ragged contacts (photomicrograph).

(e) Medium- to coarse-grained galena microbrecciates banded sphalerite (photomicrograph).

(f) Photomicrograph illustrating interconnectivity of galena textural varieties.

(g) Fine-grained galena breccia with elongate clasts of fine-grained sphalerite breccia.

(h) Photomicrograph of fine-grained galena breccia with abundant ultrafine sphalerite clasts.

(i) Galena-yellow pyrite-pyrrhotite vein preferentially developed in a sphalerite band.

16.

(a) Chalcopyrite veinlets superimposed on a deformed sugary dolomite vein and host rock.

(b) Stage VII magnetite, chlorite, biotite and ankerite-siderite alteration.

(c) Pyrrhotite microbreccias developed along clast margins and bedding planes.

(d) Biotite and zoned celsian-hyalophane-K-feldspar infill developed along alternate vein walls with pyrrhotite infill in the vein core.

(e) Lenticular pyrrhotite alteration pod in a mudstone (photomicrograph).

(f) Stage VII galena as selective replacement of Stage VIII biotite (photomicrograph).

(g) Ultrafine-grained carbonate-dominant and phengite+muscovite-dominant alteration zones developed in a banded mudstone (photomicrograph).

(h) Pyrrhotite and rare chalcopyrite lenses preferentially developed in Stage I calcite-rich mudstones and layer-parallel white bands.

(i) Dark-coloured sphalerite enveloped and microbrecciated by irregular orange-brown sphalerite (photomicrograph).

(j) Inclusion-free Stage VIII sphalerite rimmed by inclusion-free calcite occurs as overgrowths on Stage IV sphalerite (photomicrograph).

17.

(a) Plots illustrating metal grade association for Zn versus Pb, Cu versus Zn and Cu versus Pb for diamond drill holes graphically logged as part of this study.

(b) Plots illustrating metal grade association for Zn versus Pb for the H through to A stratigraphic intervals.

(c) Plots illustrating metal grade association for Cu versus Zn for the H through to A stratigraphic intervals.

(d) Plots illustrating metal grade association for Cu versus Pb for the H through to A stratigraphic intervals.

18.

(a) Simplified long sections for A through to H stratigraphic ore-bearing intervals illustrating Zn/Zn+Pb.

(b) Simplified long sections for A through to H stratigraphic ore-bearing intervals illustrating Cu/Cu+Pb.

19.

(a) Plot of $^{208}Pb/^{204}Pb$ versus $^{206}Pb/^{204}Pb$ for Stage VII and IXa galena from a range of textural settings.

(b) Plot of $^{207}Pb/^{204}Pb$ versus $^{206}Pb/^{204}Pb$ for Stage VII and IXa galena from a range of textural settings.

(c) Plot illustrated in (b) superimposed on Pb-age model curve derived by Sun et al., (1994).

20.

(a) Plot of $\delta^{34}S$ for adjacent samples.

(b) Plot of $\delta^{34}S$ and sample location with respect to northing.

21. Schematic stratigraphic column and mineral distribution logs illustrating spatial-temperature-temporal zonation patterns at George Fisher.

22. Cartoon log fO_2-pH diagram illustrating approximate stability fields for aqueous sulphur species and iron mineral stability fields relative to metal solubility contours.

PART C
MULTIPLE EPISODES OF HYDROTHERMAL CARBONATE FORMATION IN THE PROTEROZOIC URQUHART SHALE AND SIGNIFICANCE FOR THE ORIGIN OF MOUNT ISA-STYLE ZN-PB-AG AND CU MINERALIZATION.

LIST OF TABLES

1. Summary of previous interpretations on the origin of Urquhart Shale host rock carbonate constituents.

2. Modified paragenesis of the George Fisher deposit with emphasis on carbonate evolution.

3. Summary table listing carbonate chemistry.

4. Summary of carbonate constituents of the Urquhart Shale in the Mount Isa area.

LIST OF FIGURES

1. Carbonate distribution patterns projected onto 12L plan map illustrating the distribution of Zn-Pb and Cu mineralization.

2. Schematic cross-sections at 7180mN.
   (a) Distribution of pervasive Stage VIII alteration zones.
   (b) Distribution of Cu mineralization compared with Zn-Pb mineralization.

3. Stylized cross-section of Hilton Mine illustrating large-scale distribution of Cu and Zn-Pb mineralization, and ankerite- and siderite-rich portions of stratigraphy.

4. Simplified northern cross-section of Mount Isa Mine illustrating large-scale distribution of Cu and Zn-Pb mineralization, and nodular dolomite-rich portions of stratigraphy.

5. Ternary diagrams illustrating carbonate compositions from George Fisher and distal Urquhart Shale.
   (a) George Fisher - Stage OI ferroan dolomite and I calcite.
   (b) George Fisher - Stage VIII ferroan carbonates.
   (c) Distal Urquhart Shale.

6.
   (a) Stage OI early dolomite alteration developed in a banded mudstone (BSE image).

   (b) Abundant zoned Stage OI early dolomite grains with variable grain outlines and core composition (BSE image).

   (c) High magnification BSE image illustrating systematic zonation of ankerite and ferroan dolomite around an inclusion-rich dolomite core.

(d) BSE image illustrating abundance of Stage OI early ferroan dolomite in a rhythmically laminated pyritic siltstone.

7.

(a) Stage I calcite alteration in a layer-parallel white calcite band (BSE image).

(b) BSE image illustrating Stage I calcite alteration in a medium-bedded mudstone and preservation of irregular clots of Stage OI early ferroan dolomite.

(c) BSE image illustrating contact relationships between a nodular calcite layer and rhythmically laminated pyritic siltstone.

(d) BSE image illustrating ultrafine network of Stage I calcite developed along quartz-Stage OI ferroan dolomite grain boundaries.

8.

(a) Dominant carbonate constituents in a mudstone sampled from the B stratigraphic interval (BSE image).

(b) High magnification BSE image illustrate Stage VIII zoned ferroan ankerite-ankerite-ferroan dolomite rhombs.

(c) BSE image of a nodular carbonate band with pervasive Stage VIII ferroan carbonates.

(d) Stage VIII zoned ferroan dolomite-ankerite rhombs pre-date abundant quartz alteration.

9. Geological map of the Mount Isa area illustrating major structural and stratigraphic elements and general area from which samples of distal Urquhart Shale were collected.

10.

(a) Dominant carbonate constituents in a mudstone distal to mineralization (BSE image).

(b) Zoned, subhedral and euhedral dolomite-ferroan dolomite grains enveloped by ferroan dolomite matrix and replaced by calcite (BSE image).

11. Plots illustrating variation in carbonate compositions of Stage OI early dolomites from a number of settings at George Fisher and examples of carbonate constituents of Urquhart Shale distal to Mount Isa Mine.

(a) $(Fe,Mn)CO_3$ (mol. %) versus $MgCO_3$ (mol. %)
(b) $FeCO_3/MnCO_3$ versus $MgCO_3$ (mol. %)
(c) $MnCO_3$ (mol.%) versus $FeCO_3$ (mol.%)

12. Plots illustrating variety in carbonate compositions of Stage I calcites at George Fisher and Urquhart Shale distal to Mount Isa.

(a) $(Fe,Mn)CO_3$ (mol. %) versus $MgCO_3$ (mol. %)
(b) $FeCO_3/MnCO_3$ versus $MgCO_3$ (mol. %)
(c) $MnCO_3$ (mol.%) versus $FeCO_3$ (mol.%)

13. Plots illustrating variation in composition of Stage VIII carbonates at George Fisher.

(a) $(Fe,Mn)CO_3$ (mol. %) versus $MgCO_3$ (mol. %)
(b) $FeCO_3/MnCO_3$ versus $MgCO_3$ (mol. %)
(c) $MnCO_3$ (mol.%) versus $FeCO_3$ (mol.%)

14. Plots illustrating variation in carbonate compositions of carbonates at George Fisher.

(a) $FeCO_3/MnCO_3$ versus $MgCO_3$ (mol. %)
(b) $MnCO_3$ (mol.%) versus $FeCO_3$ (mol.%)

15. Ternary diagrams illustrating range of carbonate compositions.
(a) George Fisher
(b) Mount Isa and Hilton

16. Plots illustrating variation in carbonate compositions at George Fisher, Hilton and Mount Isa.
(a) $FeCO_3/MnCO_3$ versus $MgCO_3$ (mol. %)
(b) $MnCO_3$ (mol.%) versus $FeCO_3$ (mol.%)

17. $\delta^{18}O$ and $\delta^{13}C$ variation relative to stratigraphic position.

18. Plots of depth versus $\delta^{13}C$ and $\delta^{18}O$ superimposed against simplified stratigraphic column for the I interval.

19. Plots of depth versus $\delta^{13}C$ and $\delta^{18}O$ superimposed against simplified stratigraphic column for the C interval.

20. Plot illustrating $\delta^{13}C$ versus $\delta^{18}O$ for carbonates from George Fisher.

21. Plots illustrating $\delta^{13}C$ and $\delta^{18}O$ compositions for carbonates from George Fisher compared with Mount Isa, Hilton and Lake Moondarra.
(a) Point data for George Fisher, Hilton and Lake Moondarra and fields defined by Mount Isa carbonates based on location.
(b) Proposed fields for different carbonate populations and fluid/rock exchange lines.

22.
(a) Simplified stratigraphic column illustrating the distribution of major rock types, nodular carbonate banding, economic sulphides and alteration assemblages at George Fisher.

(b) Simplified stratigraphic column illustrating the distribution of major rock types, nodular carbonate banding, economic sulphides and alteration assemblages at Hilton including generalized comparison with George Fisher.

(c) Simplified metal and alteration distribution patterns at Mount Isa including comparison with George Fisher.

PART A

Regional Deformation Event	Mount Isa Mine	Lake Moondarra area	Hilton and George Fisher area
pre-D_1			Foliation - parallel S_0
D_1	Wide-spaced carbonaceous seams subperpendicular to S_0. Development of the Mount Isa and Paroo fault zone.	E-W trending folds and foliation subperpendicular S_0. Variably striking, steep dipping faults.	
D_2	Folds not recognized. Pervasive foliation subparallel S_0.	N-S trending folds with vertical penetrative cleavage. Dyke intrusion post- folding, faulting.	NNW-SSE trending, upright folds, shallow plunge, well-developed foliation. Major faulting including Paroo and Hanging wall fault. Dyke intrusion.
$D_{2.5}$	Mesoscopic folds with subhorizontal axial planes. No foliation recorded.	?	Mesoscopic folds with subhorizontal axial planes. No foliation recorded.
D_3	Upright NNW-SSE trending, steeply south-plunging folds and penetrative cleavage. Reactivation and rotation of S_2.	NNW-SSE trending folds, variable plunge, with penetrative cleavage.	Intensification of S_2. Spatially restricted NNW-SSE trending folds.
post-D_3	Local folds and crenulation. Brittle faults.	NNW-SSE trending, steep dipping faults including the Spring Creek and Transmitter Faults.	Local NW-SE trending folds. Brittle faulting including Transmitter and Gidyea Creek Faults. Reactivation along Mt Isa and Paroo Fault Zone.

Table 1. Summary of the major structural elements developed in the Mount Isa area. Compiled from Perkins (1984), Swager (1985), Winsor (1986), Bell et al. (1988), Valenta (1994) and Bell and Hickey (1998).

Deformation event George Fisher	Mesoscopic and microscopic characteristics	Correlation with macroscopic structural effects	Correlation with regional deformation events (Table 1)
D_1	1. Bedding parallel foliation. 2. **Bedding parallel Sp-Qtz-Cal-Hphl-Kfs veins common.** Syn- to post-foliation development?	Not evident.	Equivalent to pre-D_1 bedding parallel foliation at Hilton Mine recorded by Valenta (1994).
D_2	1. Upright N-S trending folds, axial planar and bedding subparallel composite S_{1-2} foliations.	Upright folds developed throughout deposit of D_2 age?	Fold and fabric orientation equivalent to regional D_2 event (e.g. Wilkins, 1986).
D_3	1. Subhorizontal folds locally developed. No foliation recorded. 2. Fibrous Qtz-Carb veins.	Open folds developed in upper stratigraphy on Section J702mN?	Fold orientations equivalent to $D_{2.5}$ event (cf. Bell and Hickey, 1998).
D_4	1. Small-scale NW-SE to NNW-SSE trending small-scale folds and axial planar foliation locally developed. 2. Fibrous qtz-carbonate veins. 3. NW-SE and NE-SW conjugate **Gn±Sp±Carb** vein set (i.e. discordant vein-hosted galena) spatially associated with **fine grained Sp- or Gn- rich breccia/shear zones** (i.e. fine grained Sp- or Gn- or mixed sulphide breccias). 4. Planar Qtz-Chl-Carb±Py±Sp pre- to post-fold development.	Upright folds developed at macroscale? Possible that increase in number of small-scale folds to north of the main economic zone related to heterogeneous development of F_4 folds.	Relative timing and orientation equivalent to regional D_3 event (cf. Valenta, 1994).

Table 2. Summary of major deformation events and mineralization styles at microscopic through to macroscopic scales at George Fisher and comparison with previous structural studies undertaken in the Mount Isa area.

MINERALIZATION STYLE	VARIETY OF MINERALIZATION STYLE	BASIS OF DEFINITION	SULPHIDE CONTENT AND RELATIVE ECONOMIC SIGNIFICANCE.	ASSOCIATED NON-SULPHIDE ASSEMBLAGE	DISTRIBUTION
STRATIFORM SPHALERITE-DOMINANT		Category characterized by very fine-grained occurrences of honey to light brown sphalerite in specific sedimentary layers. Individual styles differentiated on the basis of host rock.	MINOR		
	Rhythmically laminated siltstone-hosted	Hosted by light grey dolomitic laminations in rhythmically laminated carbonaceous and pyritic siltstones.	Sp only - minor	FeDol±Cal±Kfs	Mainly in the F and B stratigraphic intervals, deposit-wide.
	Nodular carbonate-hosted	Sphalerite hosted by nodular calcite bands.	Sp±Py - minor	Cal	Typical of F zone, deposit-wide
	Shale-hosted	Sphalerite hosted by the black shale component of shaly banded mudstones.	Sp±Py, rare Gn - minor	Cal-Bit±Kfs	Restricted to I and H stratigraphic zones.
	Mudstone-hosted	Sphalerite or galena hosted by mudstone bedding intervals.	Sp or Gn±Py - minor	±Cal ±FeDol±Kfs	Spatially associated with stratabound styles across deposit.
STRATABOUND SPHALERITE-DOMINANT		Category characterized by occurrence of vein and breccia-hosted light brown to red sphalerite mineralization. Styles differentiated on basis of sphalerite grain size and clast characteristics.	MAJOR		
	Banded, breccia-veins	Characterized by occurrence of semimassive, medium to coarse-grained sphalerite in layer-parallel bands.	Sp±Py±Po, rare Gn major	Cal±Kfs±Hyl±Qtz ±Hphl±FeDol	Occurs throughout all intervals, particularly to southern end of deposit.
	Fine-grained breccias	Sphalerite is fine-grained and occurs as breccia matrix. Breccia clasts are characteristically subrounded to rounded and preferentially oriented.	Sp±Py±Po, rare Gn major	Cal±Kfs±Hyl±Qtz ±Hphl±FeDol	Occurs throughout all intervals, particularly to northern end of deposit.

Table 3. Summary of mineralization styles classification scheme at George Fisher (continued over page).

MINERALIZATION STYLE	VARIETY OF MINERALIZATION STYLE	BASIS OF DEFINITION	SULPHIDE CONTENT AND RELATIVE ECONOMIC SIGNIFICANCE.	ASSOCIATED NON-SULPHIDE ASSEMBLAGE	DISTRIBUTION
STRATABOUND GALENA-DOMINANT		Category defined by the presence of galena as one of the dominant sulphide species. Specific styles differentiated on the basis of sulphide grainsize and dominant sulphide species.	MAJOR		
	Discordant veins	Medium- to coarse- grained galena occurs as the dominant constituent of discordant veins.	Gn±Sp±Py±Po minor	±Cal±FeDol	Spatially associated with coarser-grained galena breccias.
	Medium to coarse-grained breccias	Medium- to coarse-grained galena occurs as the dominant matrix constituent of stratabound breccias.	Gn±Py, rare Sp, Po major		Most common in the D and C intervals to the south of the deposit.
	Fine-grained breccias	Fine-grained galena occurs as the dominant matrix constituent. Clasts are typically rounded and display a preferential orientation.	Gn±Py±Sp±Po major		Most common in the D and C intervals, particularly to the north.
	Fine-grained mixed sulphide breccias	Breccia matrix consists of a variety very fine-grained sulphides. Sulphide varieties heterogeneously distributed through matrix.	Gn-Sp-Py-Po minor		Locally occurs in all stratigraphic intervals across deposit.
CHALCOPYRITE-BEARING		Category defined by the presence of chalcopyrite or abundant pyrrhotite.	MINOR		
	Chalcopyrite-bearing veins	Chalcopyrite occurs as infill in veins with a variety of sulphides, silicates and carbonates.	Cpy-Po± Py±Gn±Sp minor	±Chl±Bt±Ms±Ank± Sid	Typical of A and B intervals deposit-wide.
	Medium-grained pyrrhotite±chalcopyrite breccias	Medium-grained pyrrhotite ± chalcopyrite occurs the matrix component of stratabound breccias.	Po±Cpy±Gn±Sp minor		Typical of A and B intervals deposit-wide.
FAULT-HOSTED MINERALIZATION		Coarse-grained sulphides occur as infill in fault zones associated with displacement of stratigraphy including ore bodies.	MINOR		
	Coarse-grained carbonate-sphalerite, J75-type fault-fill	Coarse to very coarse-grained red-brown sphalerite occurs as infill with calcite and dolomite.	Sp, rare Py ± Gn ± Cpy ± Po minor	Cal±Dol	Occurs where late faults intersect ore zones.
	Calcite-sphalerite-galena L70-type fault-fill	Coarse to very coarse-grained sphalerite and galena occur as infill with white to pink calcite. Veined zones spatially associated with carbonaceous fault gouge.	Sp-Gn minor	Cal	Occurs where late faults intersect ore zones.

Table 3 continued.

DEPOSIT	TONNAGE (Mt)	Zn (%)	Pb (%)	Ag (g/t)	Cu (%)	Zn/Pb
Mount Isa	Pre-production ~ 150Mt [1]	7	6	150		~ 1.1
	1988 - 47Mt [1]	6.8	5.9	148		
	255Mt [2]				3.3	
Hilton	49Mt [1]	9.3	6.5	151		~ 1.4
	5 Mt [3]				0.5	
George Fisher	108Mt [4]	11.1	5.4	93	trace only	~ 2.0

Table 4. Metal budgets for the Mount Isa, Hilton and George Fisher deposits; [1.] Forrestal (1990), [2.] Perkins (1990), [3.] Mullens (1993), [4.] 1998 MIM report to shareholders.

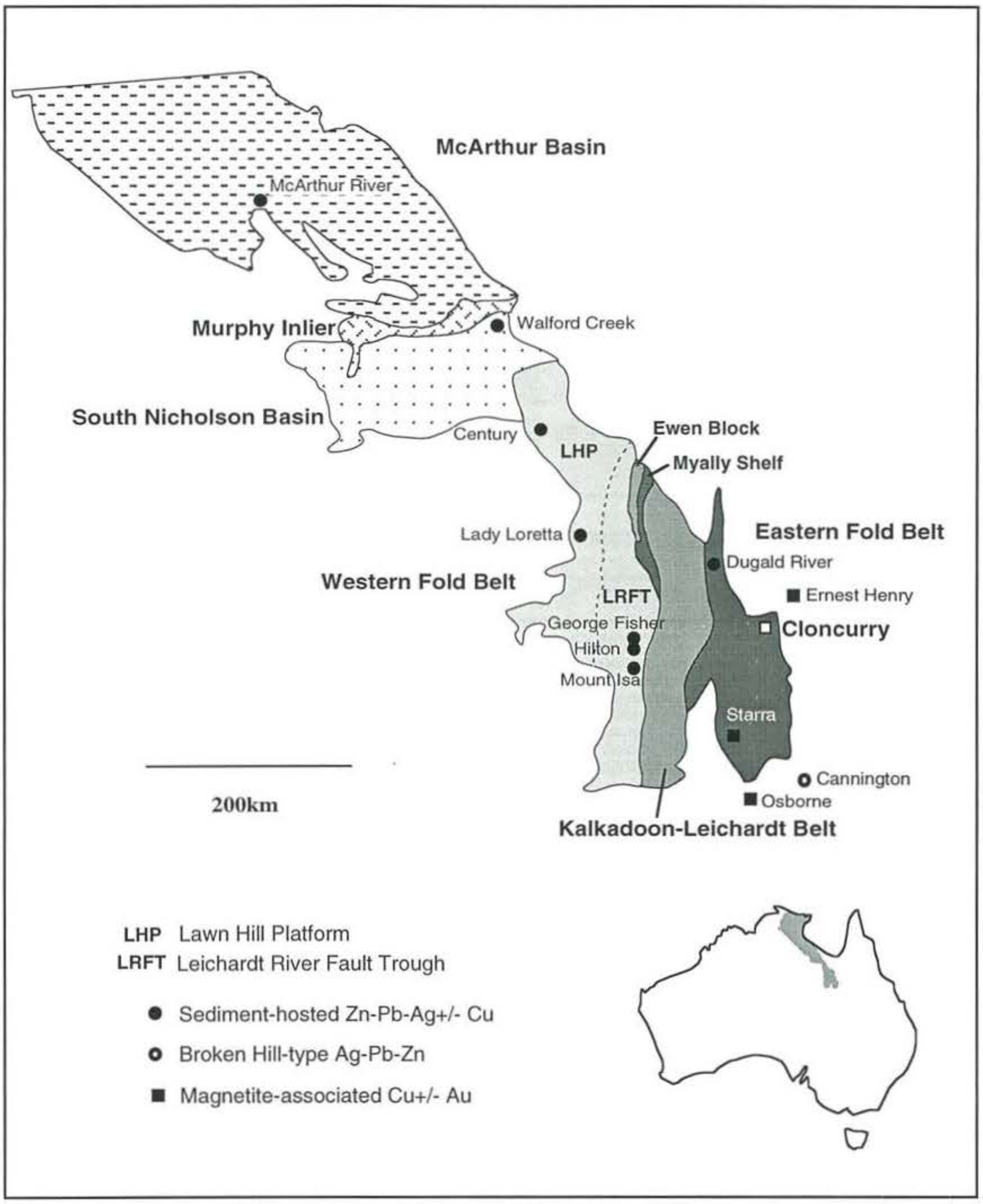

Figure 1. Map of the Mount Isa-McArthur minerals province illustrating major tectonostratigraphic subdivisions and the location of significant mineral occurrences (modified after Plumb et al. 1990, and Blake and Stewart, 1992).

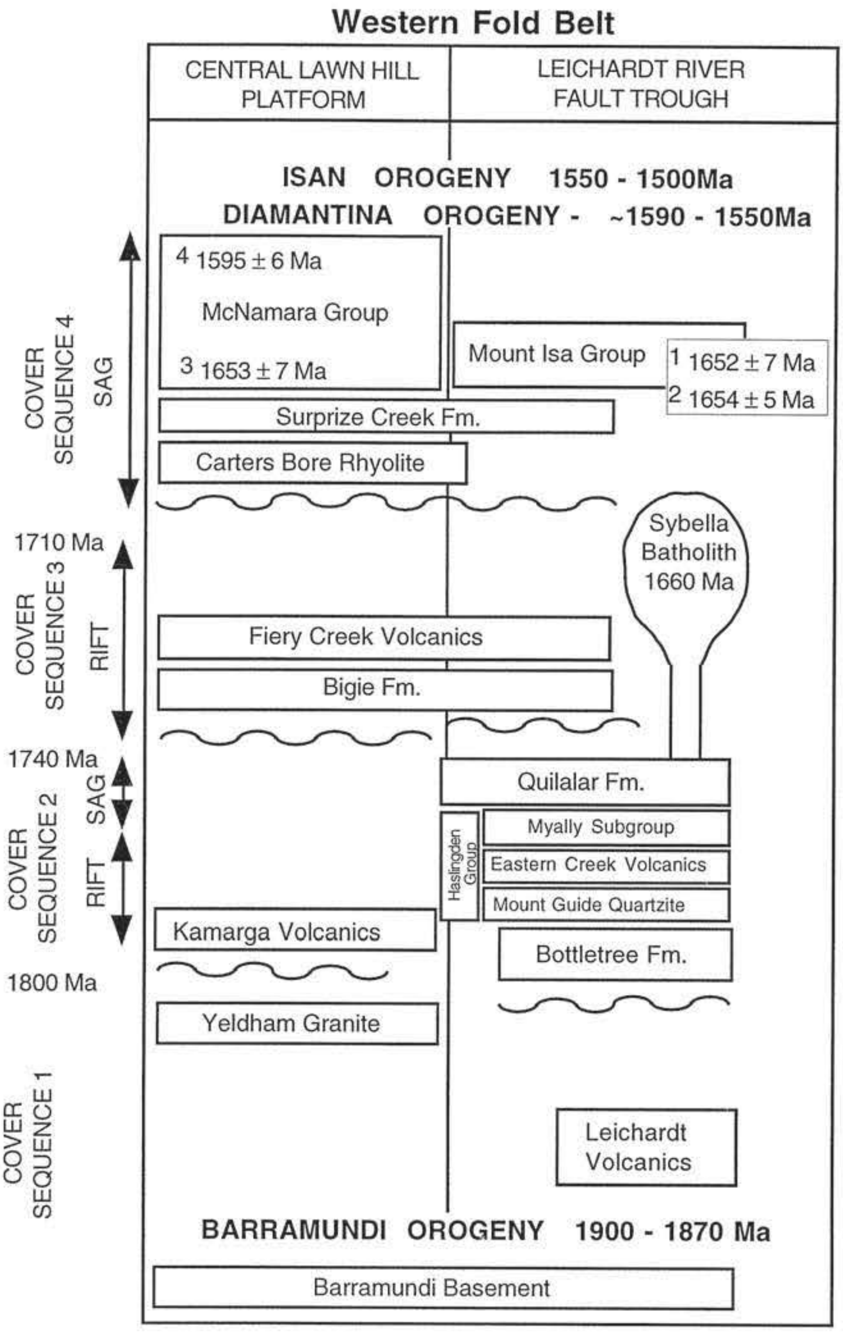

Figure 2. Stratigraphic framework of the Western Fold Belt, Mount Isa Inlier (compiled from Page and Sweet, 1998, O'Dea et al., 1997 and references therein). U-Pb SHRIMP results from Page and Sweet (1998) for [1]Urquhart Shale (Upper Mount Isa Group) at Mount Isa, [2]Urquhart Shale at Hilton, [3]Paradise Creek Formation (underlies host rocks to Lady Loretta deposit), [4]Upper McNamara Group of the Lawn Hill Formation which hosts the Century Deposit.

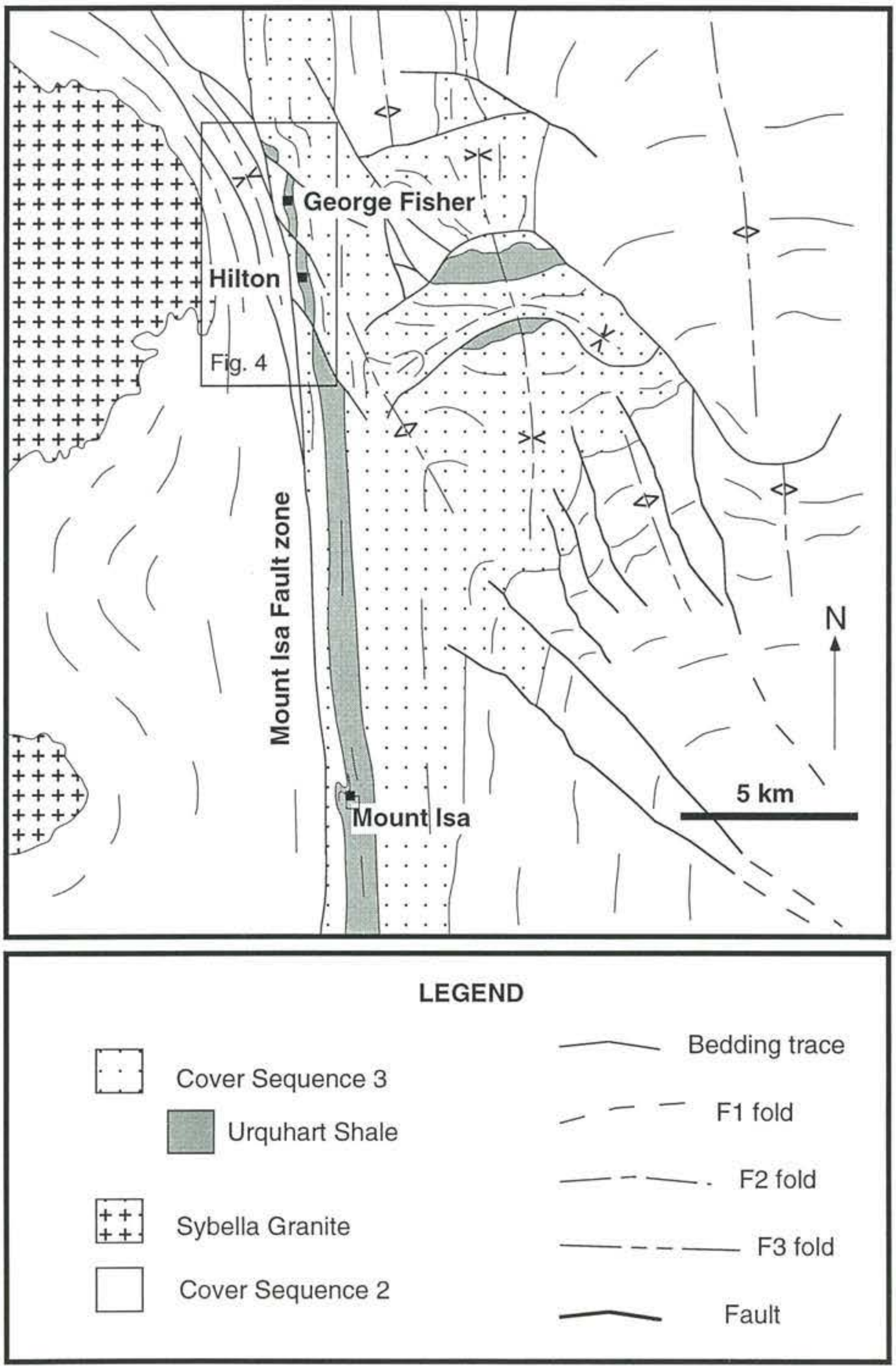

Figure 3. Geological map illustrating major structural and stratigraphic elements of the Mount Isa area (after Blake, 1987 and Valenta, 1994).

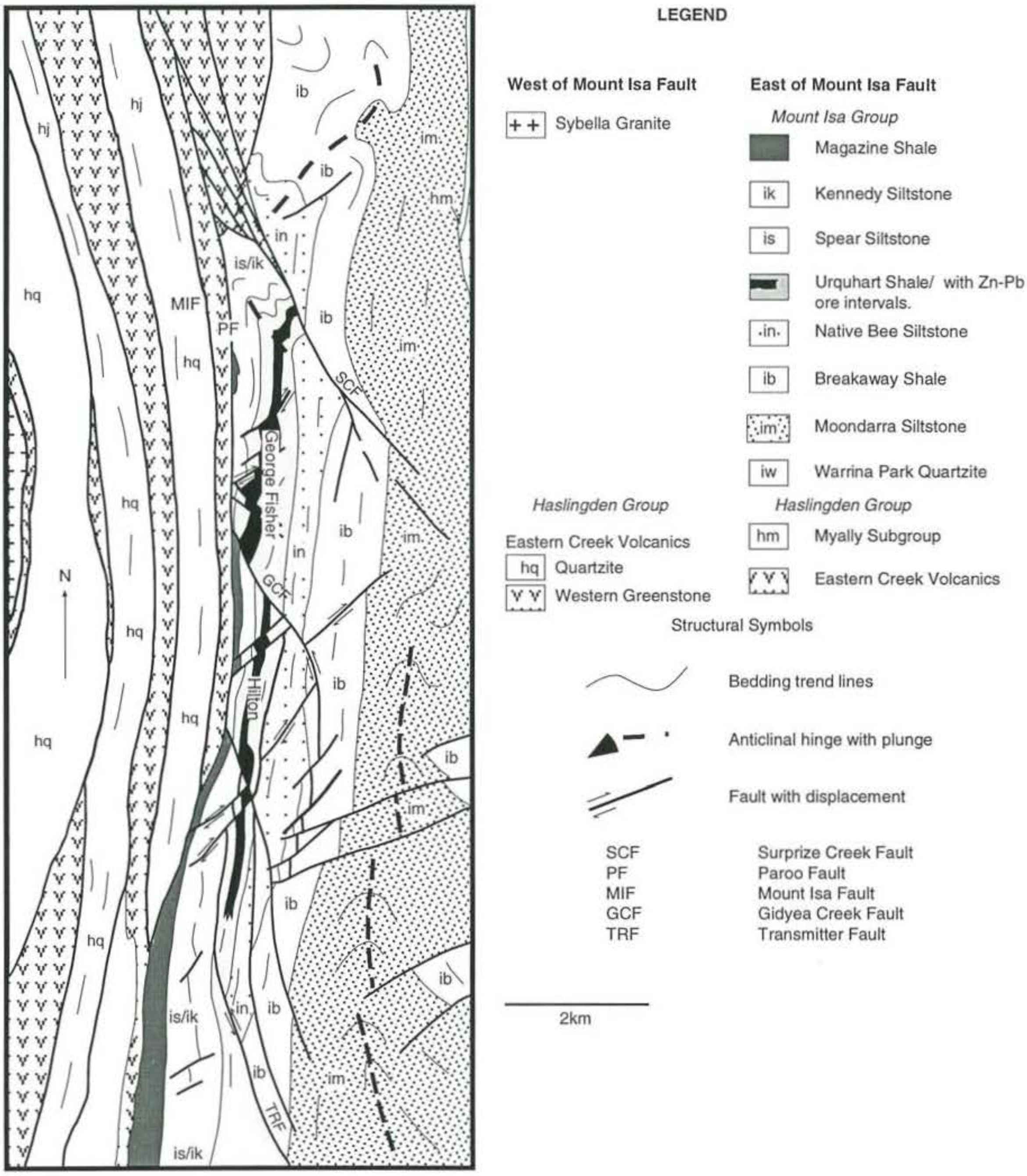

Figure 4. Geology map of George Fisher and surrounds (after Valenta, 1994).

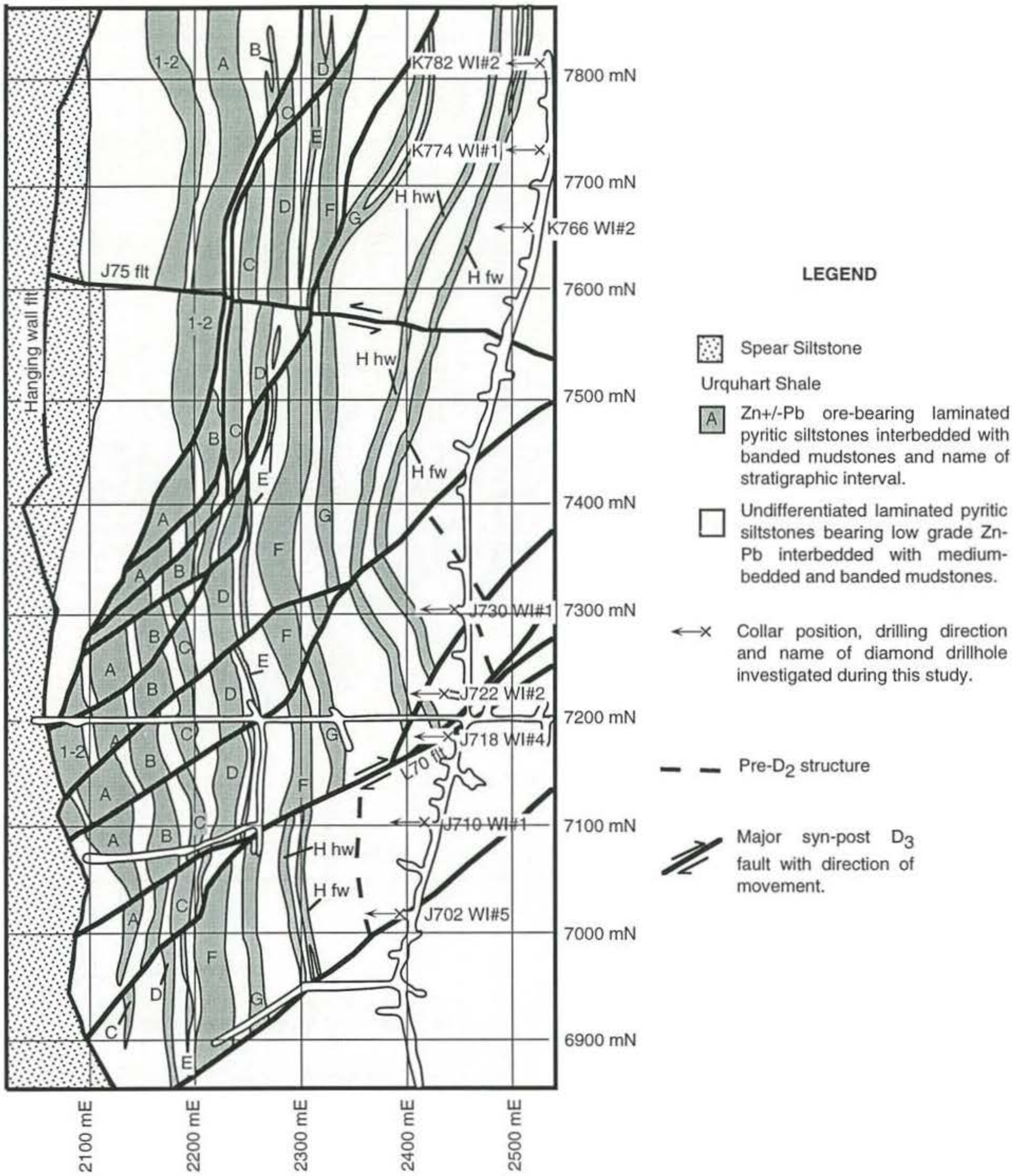

Figure 5. Interpreted plan geology map of the main economic zone at 12 level (approximately 700m below surface) illustrating the extent of underground development prior to the commencement of mining, major structural features and stylized outlines of Zn-Pb -rich zones. Collar positions of drill holes that were logged for this study are also illustrated (adapted from unpublished MIM Ltd data).

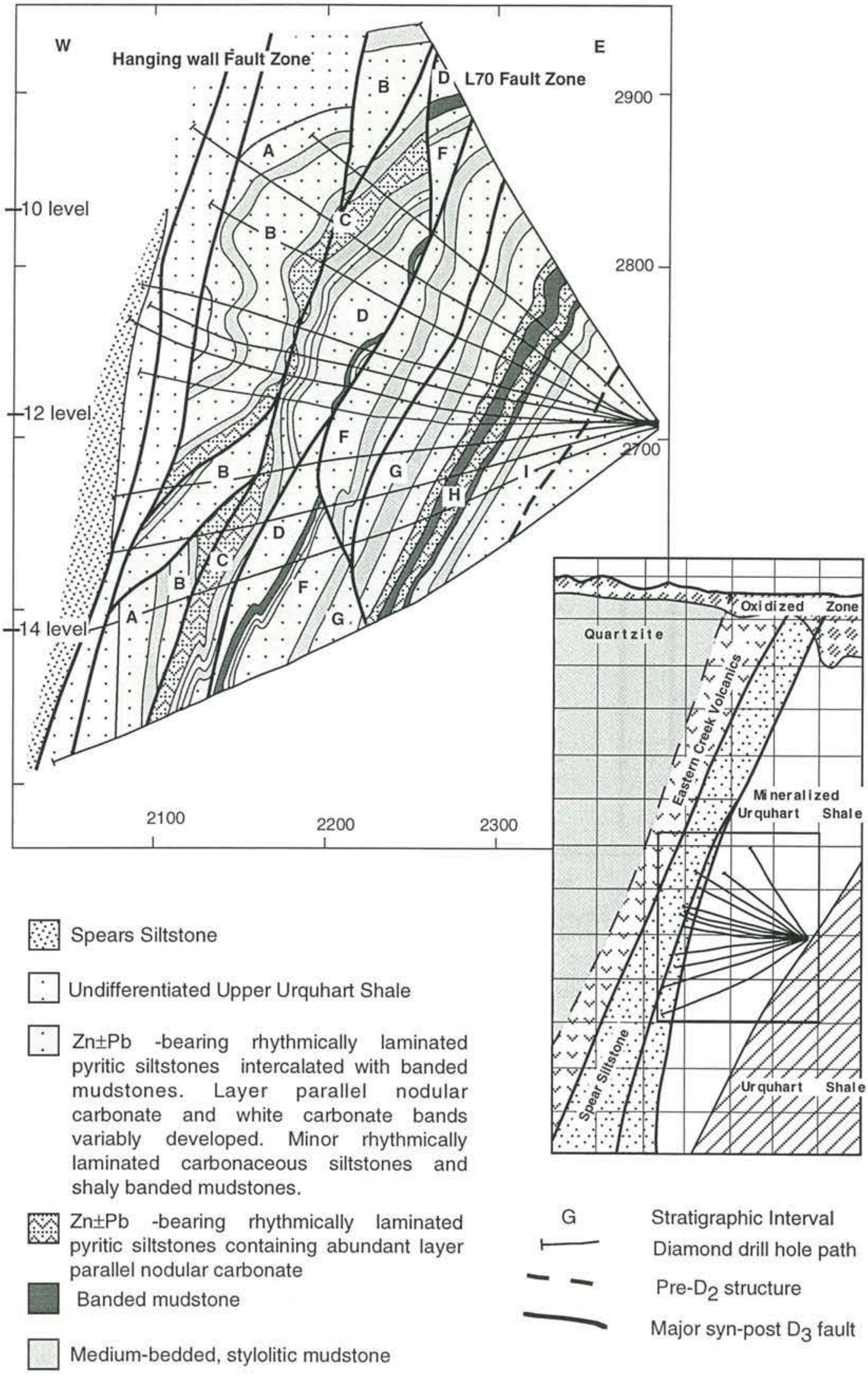

Figure 6. Interpreted geological cross-section at 7020mN illustrating major stratigraphic and structural elements at George Fisher. Fault interpretation has been adapted from MIM Ltd data and inset is adapted from Mullens (1990).

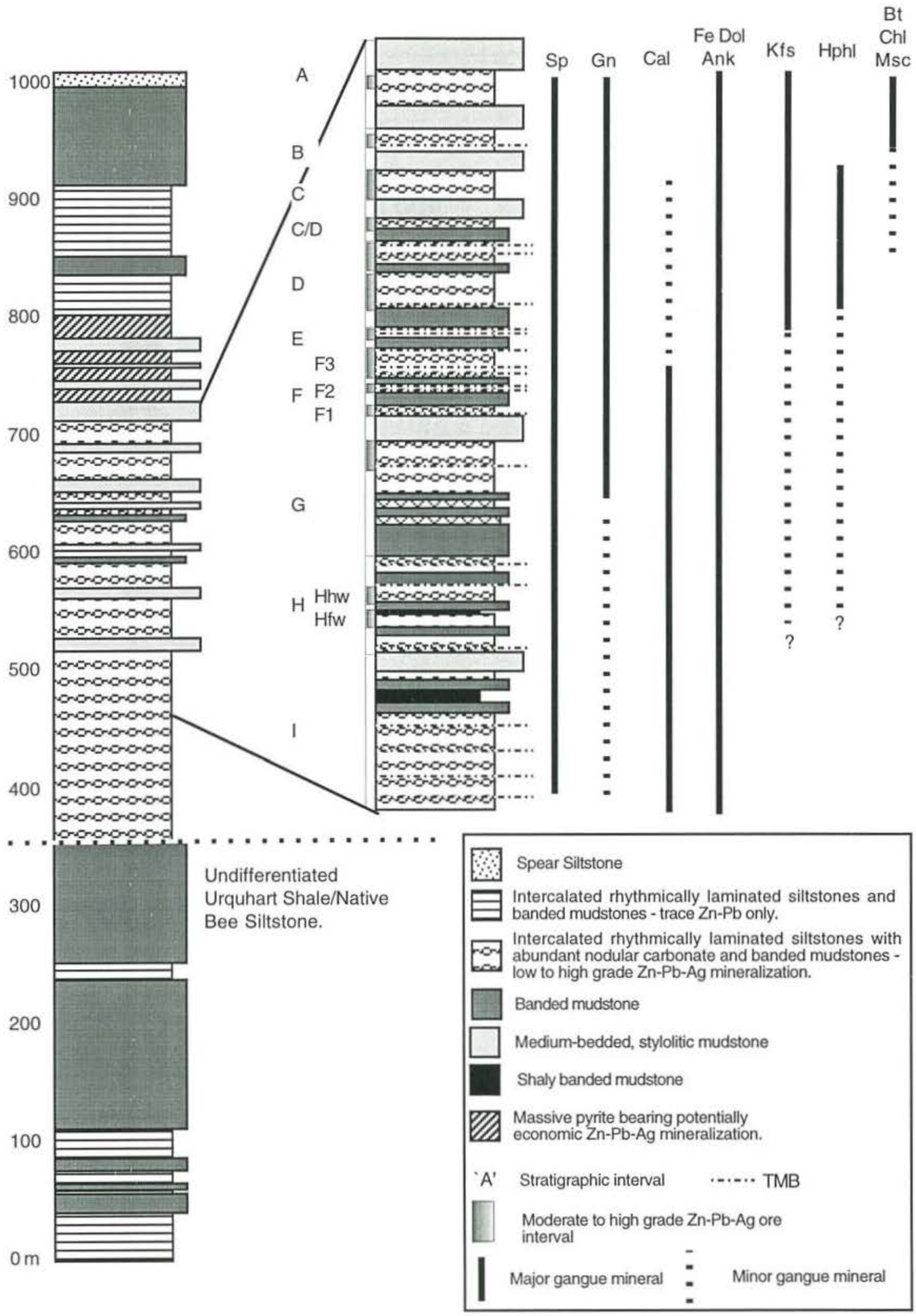

Figure 7. Simplified stratigraphic column with metal distribution patterns and dominant gangue at the George Fisher deposit. Relationships illustrated for Zn±Pb-bearing intervals based on relationships in the southern end of the deposit (this study). Tuff marker bed characterization was undertaken by MIM geologists and stratigraphy above the A interval, and below the I interval is adapted from Mullens (1990).

Key to Figure 8.

LEGEND FOR DRILL HOLE LOGS

Left hand side

Shaly banded mudstone

Banded mudstone

Stylolitic, medium-bedded mudstone

Flt Fault

Right hand side

Distribution and relative abundance of rhythmically laminated carbonaceous siltstone

Distribution and relative abundance of rhythmically laminated pyritic siltstone

Distribution and relative abundance of rhythmically laminated pyritic siltstone with interlayered nodular carbonate

0 100%

Massive sulphide

Denotes presence of layer-parallel white carbonate bands

Tuffaceous marker bed (TMB)

LEGEND FOR CORRELATED ZONES

Medium-bedded, stylolitic mudstone

Intercalated shaly banded mudstone and rhythmically laminated carbonaceous and pyritic siltstones

Banded mudstone

Intercalated banded mudstone and rhythmically laminated carbonaceous siltstone

Rhythmically laminated pyritic siltstone ± Zn-Pb bands

Rhythmically laminated pyritic siltstone with nodular carbonate ± Zn-Pb bands

Intercalated banded mudstone and rhythmically laminated carbonaceous and pyritic siltstones ± Zn-Pb bands

Intercalated banded mudstone and nodular carbonate-bearing rhythmically laminated pyritic siltstone ± Zn-Pb bands

Layer-parallel white carbonate bands

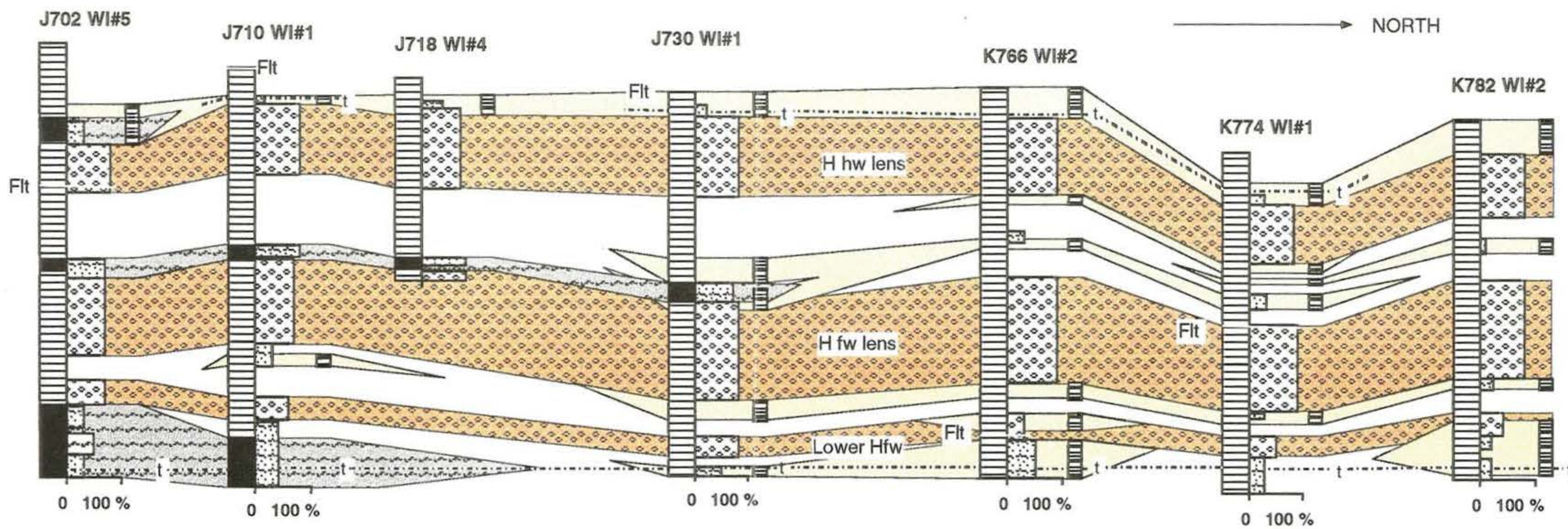

Figure 8a. Stratigraphic sections, drawn to true thickness, for the H stratigraphic interval from 7020 mN to 7820 mN. Intercalated shaly banded mudstones and rhythmically laminated carbonaceous and pyritic siltstones, nodular carbonate-rich rhythmically laminated pyritic siltstones and packages of layer-parallel white bands are correlated on this section.

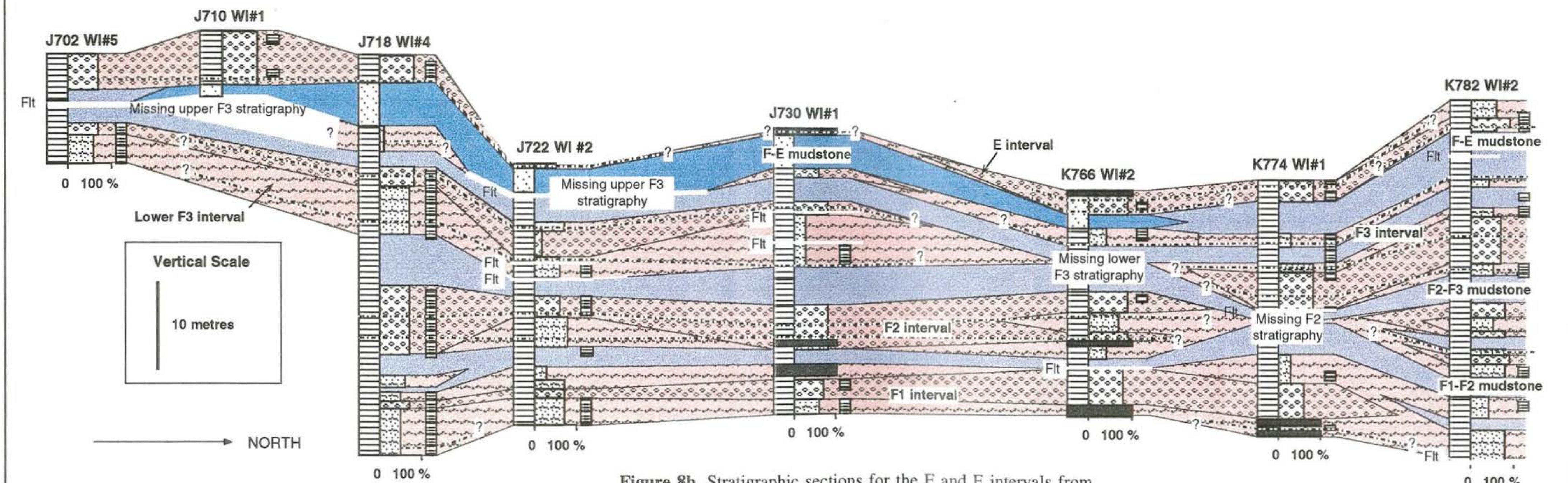

Figure 8b. Stratigraphic sections for the F and E intervals from 7020 mN to 7820 mN and drawn to true thickness. The distribution of major rock types and nodular carbonate-bearing intervals are highlighted.

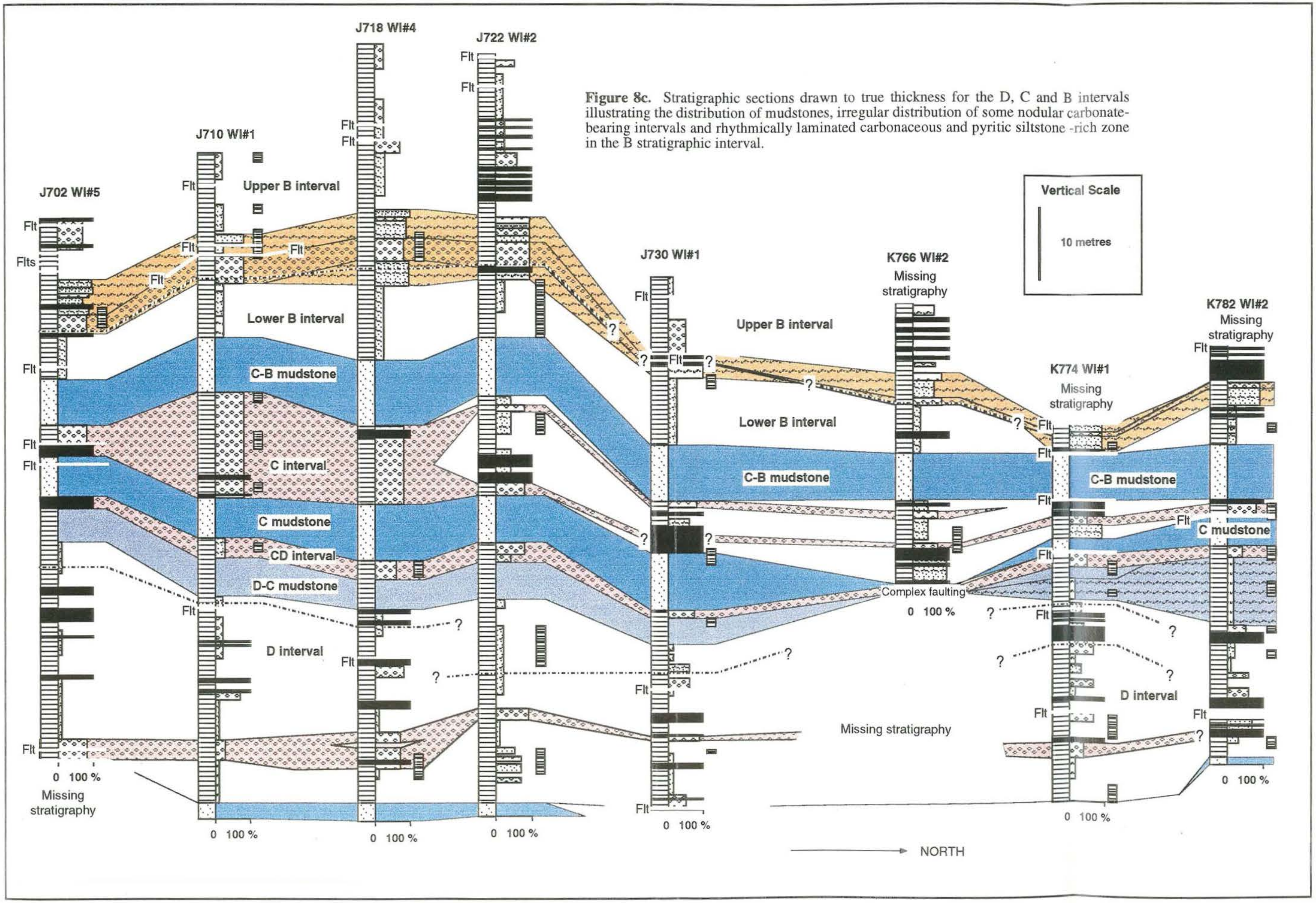

Figure 8c. Stratigraphic sections drawn to true thickness for the D, C and B intervals illustrating the distribution of mudstones, irregular distribution of some nodular carbonate-bearing intervals and rhythmically laminated carbonaceous and pyritic siltstone -rich zone in the B stratigraphic interval.

Figure 9.

(a) Planar laminated to massive and stylolitic, medium-bedded mudstone (MM) forms a sharp contact (arrow) with overlying intercalated banded mudstone and pyritic siltstone interval that contains abundant white calcite bands (WB) at its base. Way up is from top left to bottom right. (J702 WI#5, 56.5 - 64.7m).

(b) Planar laminated to massive, banded mudstones (BM) display distinctive light grey calcitic and dark grey dolomitic banding. The lower mudstone (top) forms a gradational contact over 10 cm characterized by abundant white calcite bands (WB) with the overlying rhythmically laminated pyritic siltstone (PS). This siltstone contains abundant layer-parallel nodular carbonate (Nod). The pyritic siltstone is juxtaposed against the upper mudstone (BM) by a L70-type late fault (arrow). The fault zone is approximately 20cm thick and is characterized by pink and white calcite-fill, and some carbonaceous gouge. Way up is from top left to bottom right. (J702 WI#5, 40.6-48.6m).

(c) Graded bedding intervals (way up to right) within a banded mudstone (BM) interval that contains abundant white calcite bands (WB). The white calcite bands have planar and stylolitic contacts along which pyrite and pyrrhotite (Po) are developed (HS# 24, J702WI#2, 38.6m).

(d) Thin shaly banded mudstone (SM) characterized by several cm-thick, pyritic black shale and cross-bedded shaly siltstone bedding intervals and bounded by intercalated rhythmically laminated pyritic siltstones (PS) and banded mudstones (BM). The start and end of the shaly banded mudstone interval is indicated with arrows. Fibrous calcite veins are developed near the base whereas white calcite bands (WB) are prevalent to the top. White bands occur in a triplet association. Way up is from top left to bottom right (HS# 29, J702WI#2, 48.5 - 50.2m).

(e) Rhythmically laminated carbonaceous siltstone characterized by sub-mm to mm -thick alternating wavy dark grey carbonaceous and light grey carbonate-rich laminations with intermittent mm-thick light grey planar laminations. Lens-like pyrrhotite aggregates with long axes oriented parallel to bedding are prominent central to the sample. Core is 4cm wide. (HS# 129, J702WI#6, 75.7m).

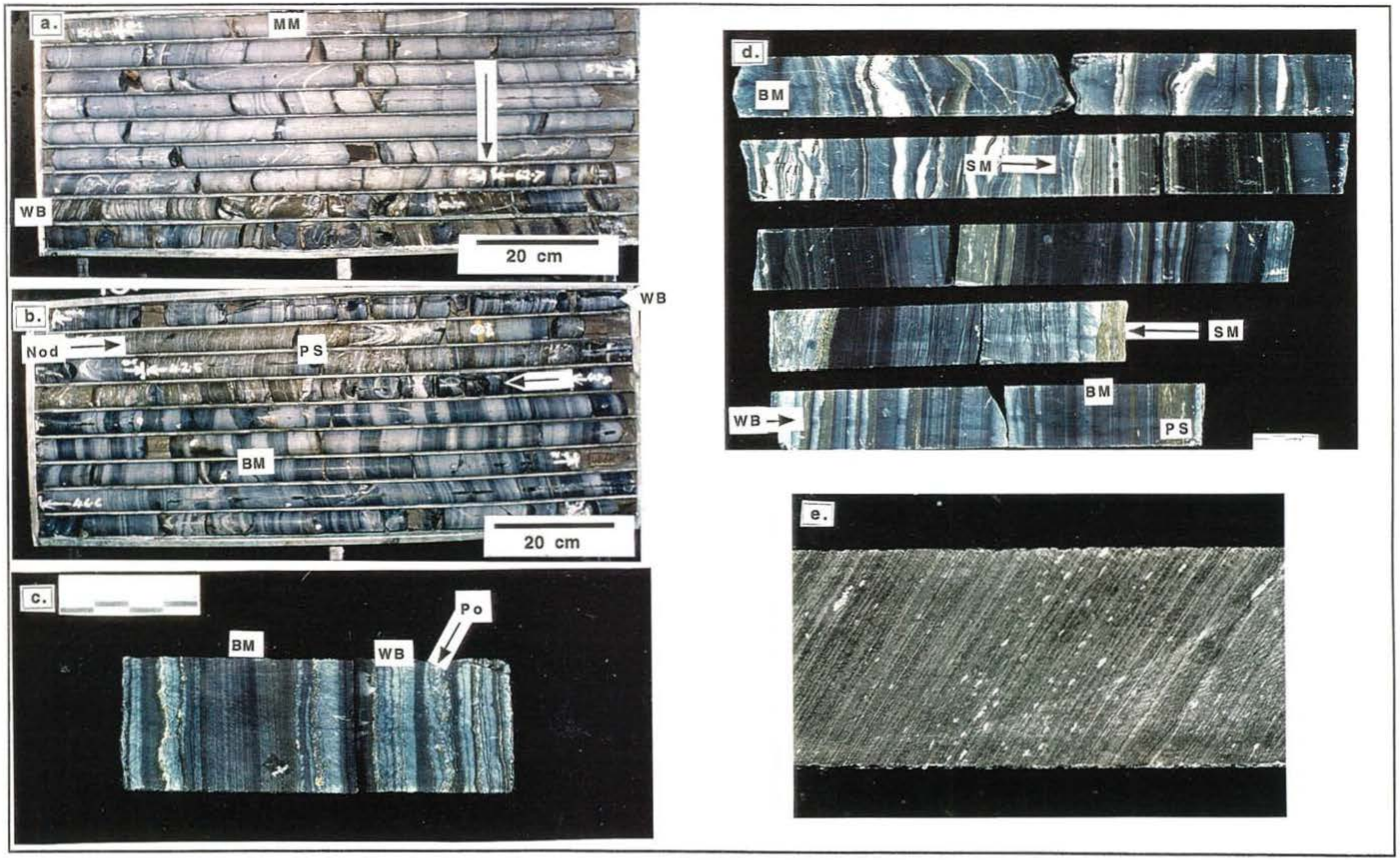
a.
MM
WB
20 cm
b.
WB
Nod
PS
BM
20 cm
c.
BM
WB
Po
d.
BM
SM
SM
WB
BM
PS
e.

Figure 9.

(f) Photomicrograph of a rhythmically laminated siltstone interval illustrating the discontinuous nature of wavy laminations compared with planar laminations (arrow) distinguished by an increase in proportion of relatively coarse-grained detrital quartz (Qtz) (HS# DC838, H766ED#1, 561m).

(g) Intercalated banded mudstone (BM) and rhythmically laminated pyritic siltstone with abundant white planar calcite bands (WB) and syndeformational, irregular calcite fibre veins (Cal). Way up is from top left to bottom right. (J702WI#5, 48.6-56.5m).

(h) Nodular carbonate (Nod) occurs as bedding parallel and displacive, wavy layers in thin pyritic siltstone beds (PS). The majority of bedding contacts in this section are stylolitic. White calcite bands occur as pyritic siltstone (PS) -banded mudstone (BM) -white band (WB) triplets in this specimen. Width of rock wafer is 2cm and way up is to the right (HS# DC845, H766ED#1, 554m).

(i) Photomicrograph illustrating the textural similarity between white band calcite (WB) and nodular calcite. The discontinuous nodular calcite layer is superimposed on a thin laminated pyritic siltstone bed (PS) and is discordant to and cross-cuts bedding at this scale. Note the relative abundance of detrital quartz within the pyritic bed and stylolitic nature of contacts (HS# DC845, H766ED#1, 554m).

(j) Banded, calcitic (Cal) and dolomitic (Dol) banded mudstone contains solitary and stacked white band couplets. White bands (WB) have sharp planar and stylolitic contacts and are spatially associated with elongate, smooth calcite nodules (N) (HS# 47, J702WI#5, 73.9m).

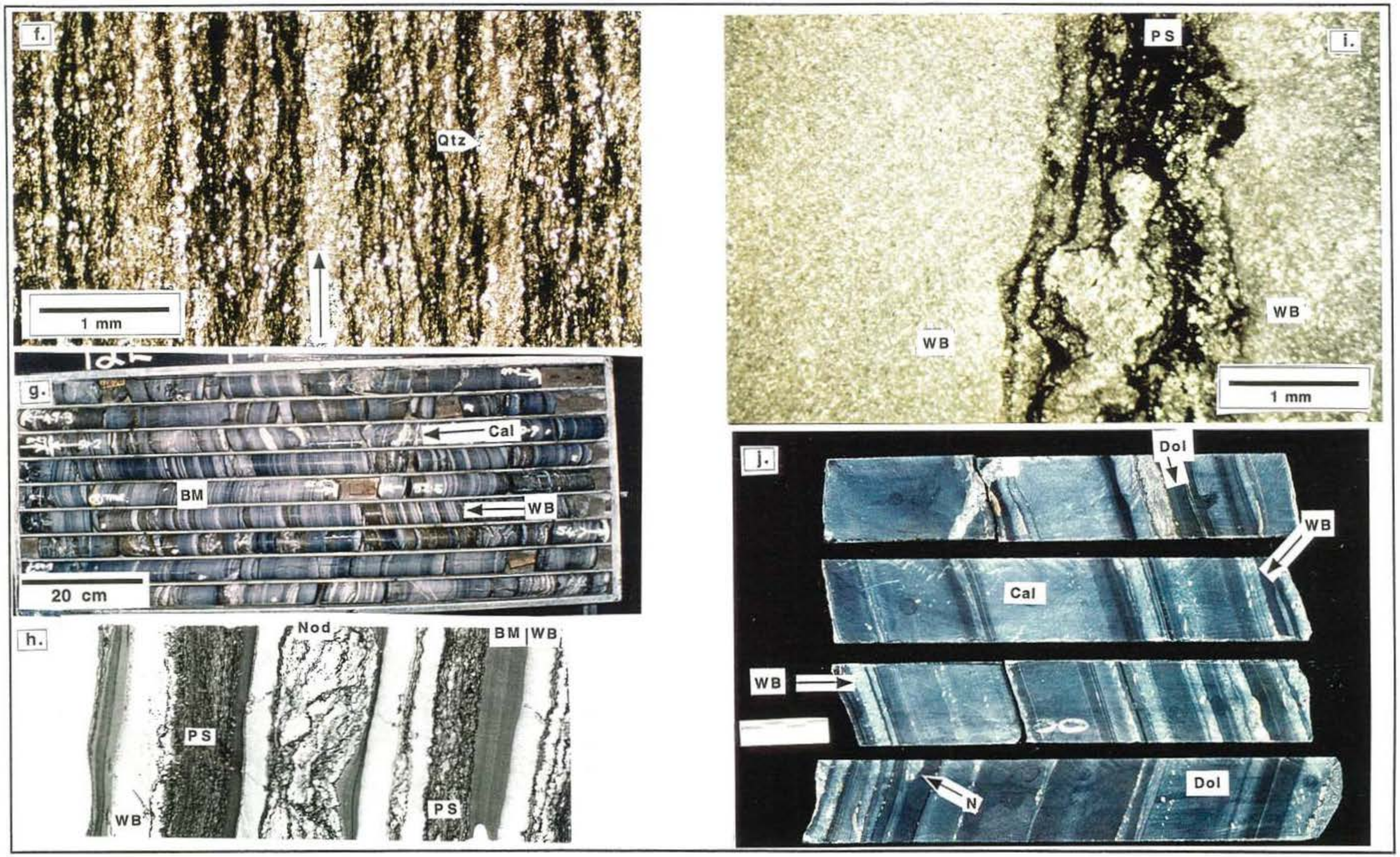

f.
Qtz
1 mm
g.
Cal
BM
WB
20 cm
h.
Nod
PS
WB
BM
WB
PS
i.
PS
WB
WB
1 mm
j.
Dol
WB
Cal
WB
Dol
N

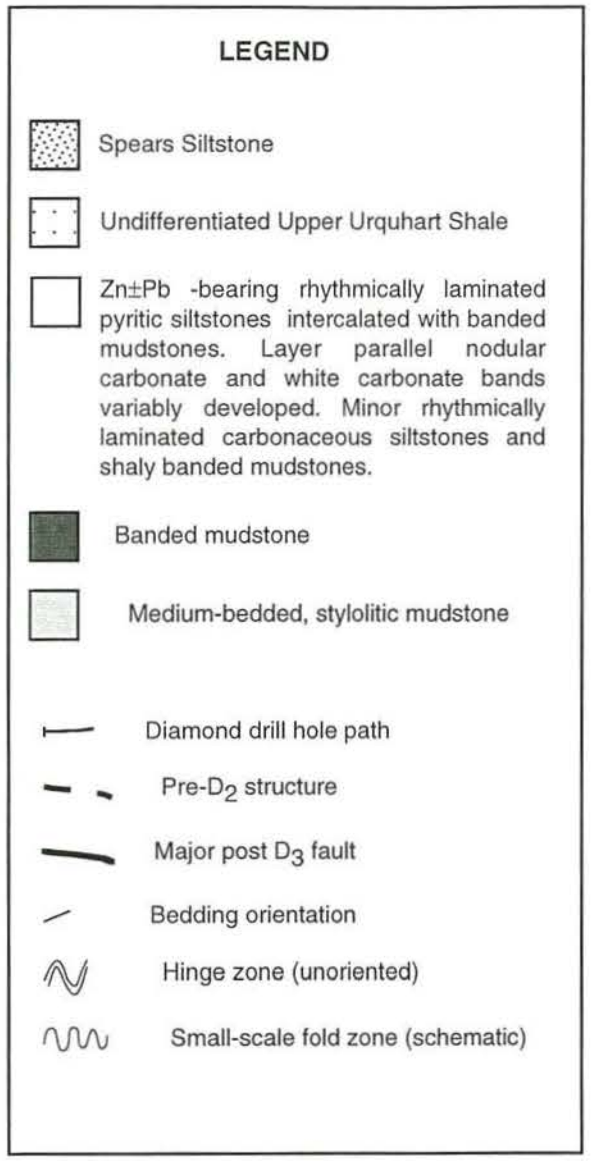

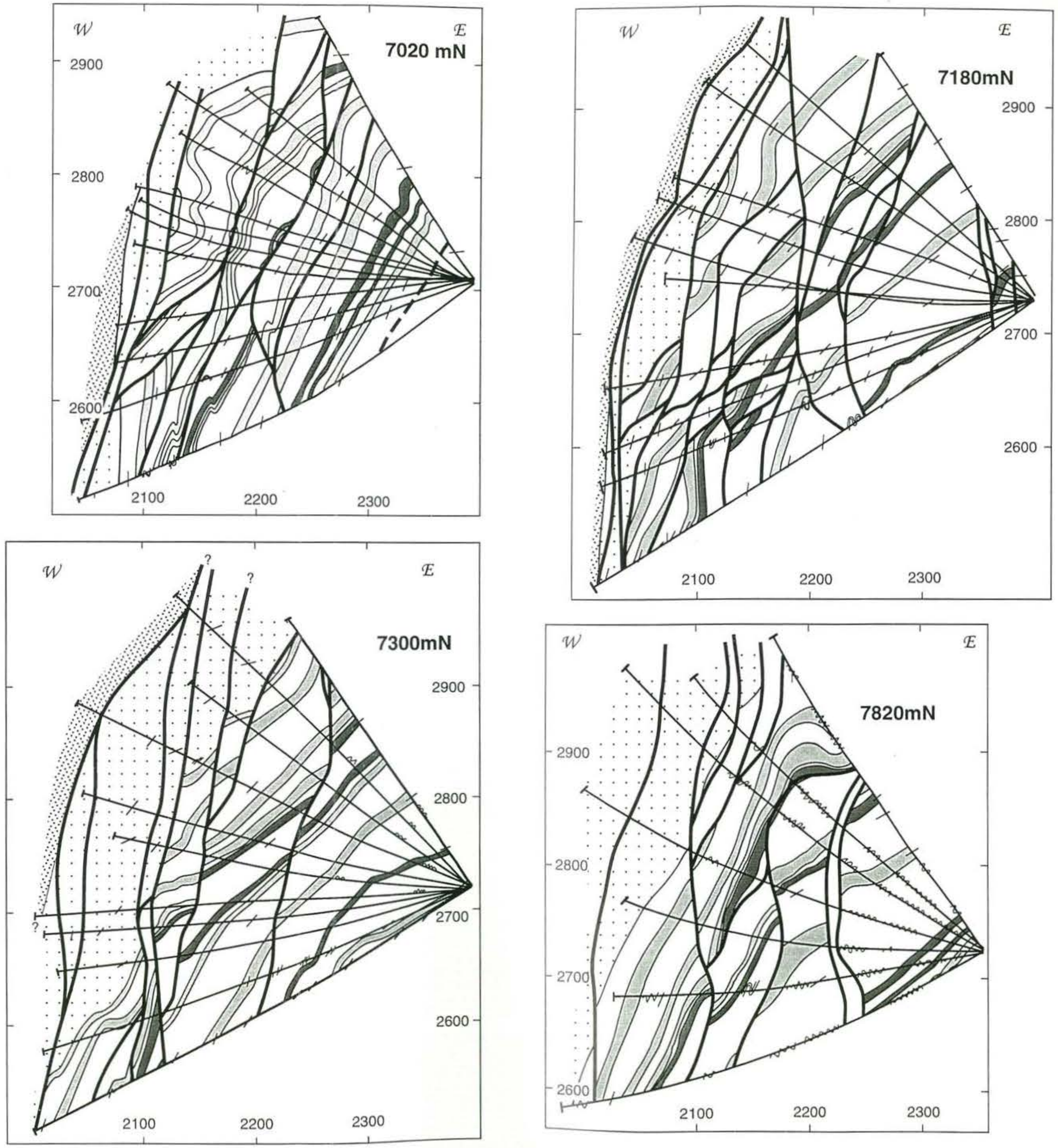

Figure 10. Interpretative cross-sections at 7020mN, 7180mN, 7300mN and 7820mN, illustrating major stratigraphic subdivisions and late-stage faults, core axis to bedding angles, and the distribution of small-scale fold zones (based on MIM Ltd data).

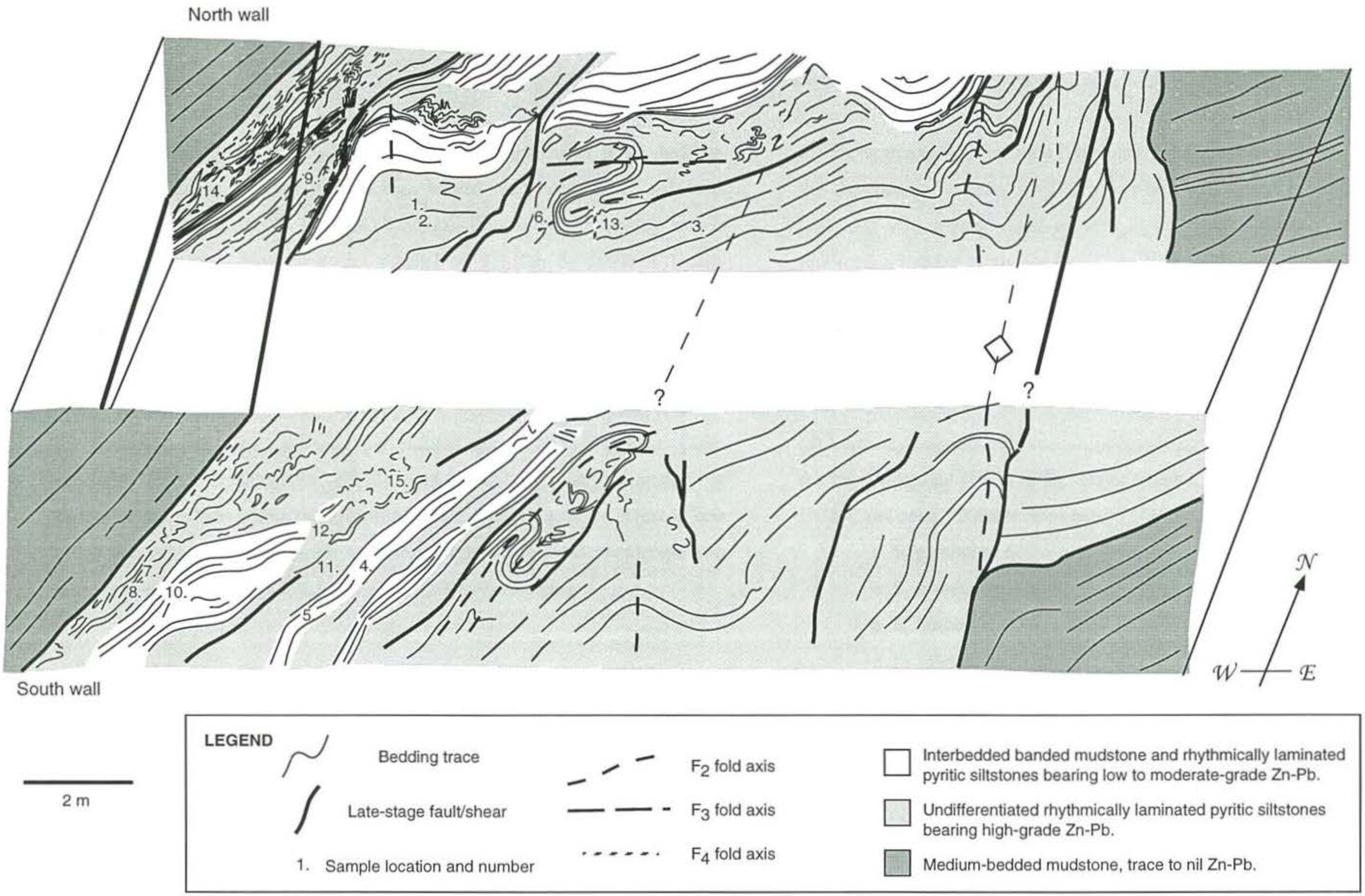

Figure 11. Mapped sections illustrating mesoscale structural features in the southern and northern walls of the C ore zone, 7200mN underground cross-cut.

Figure 12

(a) Photomicrograph illustrating the pervasive development of a D_1 bedding-parallel foliation in variably carbonaceous banded mudstones (BM) and local development of an upright D_2 foliation. A sub-mm thick sphalerite-bearing vein is boudinaged and pods have long-axes parallel to S_2. The S_2 fabric is locally intensified around these pods. Thin section is vertically oriented, west is to the left and photograph was taken looking north (HS# UG8, C ore zone, 7200mN cross-cut).

(b) Bedding-parallel and symmetrically infilled quartz (Qtz)-K-feldspar (Kfs)-sphalerite (Sp)-hydrophlogopite (Hphl) vein. Note that the orientation of hydrophlogopite laths within the vein mimics the orientation of S_1. West to east orientation runs from the top left to bottom right corners and photograph was taken looking north (HS# UG8, C ore zone, 7200mN cross-cut).

(c) Photomicrograph illustrating crenulate sphalerite-bearing vein margins. Note the abundance of euhedral pyrite (Py) crystals with quartz pressure shadows that have long axes oriented along probable S_2 reactivation planes. Vertically oriented thin section looking north (see Fig. 12d) (HS# UG8, C ore zone, 7200mN cross-cut).

(d) Vertically oriented thin section photomicrograph (looking north) illustrating the microstructural effects of D_2. Major features are illustrated by the inset (HS# UG8, C ore zone, 7200mN cross-cut):

a. S_0 parallel to S_1

b. S_1 is crenulated by S_2

c. S_1 hinges

d. S_2 differentiated cleavage

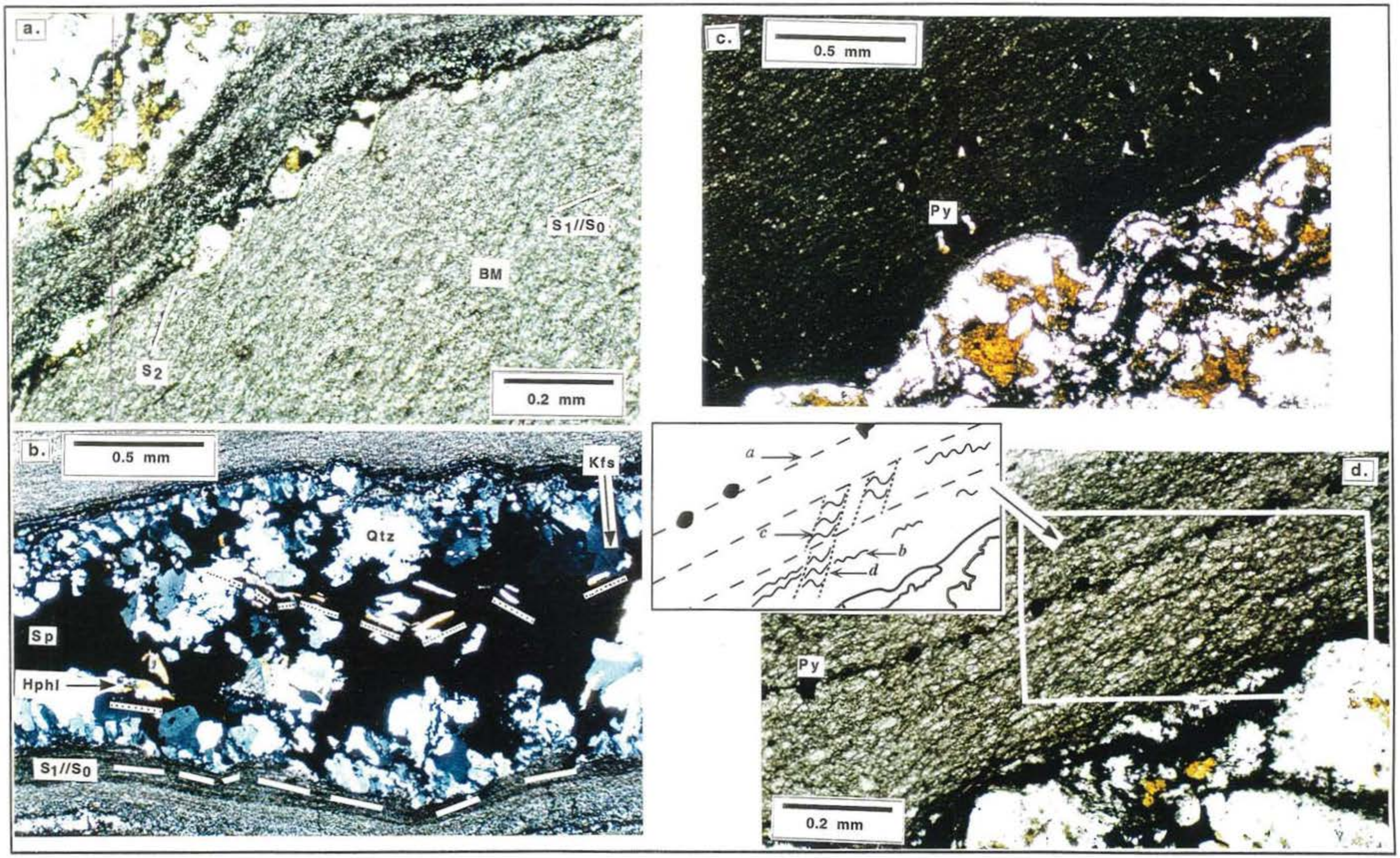
a.
$S_1//S_0$
BM
S_2
0.2 mm
c.
0.5 mm
Py
b.
0.5 mm
Kfs
Qtz
Sp
Hphl
$S_1//S_0$
a
c
b
d
d.
Py
0.2 mm

Figure 13. Photomicrograph mosaic and line diagram illustrating the microstructural effects of D_3 and D_4. Vertically oriented thin section looking south. The curved nature of fibres in carbonate-quartz veining to the top left indicate that these veins were emplaced synchronous with D_3 and/or D_4. Discordant veins with blocky carbonate infill (Carb, bottom centre) are interpreted to have been emplaced syn- to post-D_4 (HS# UG1, C ore zone, 7200mN cross-cut).

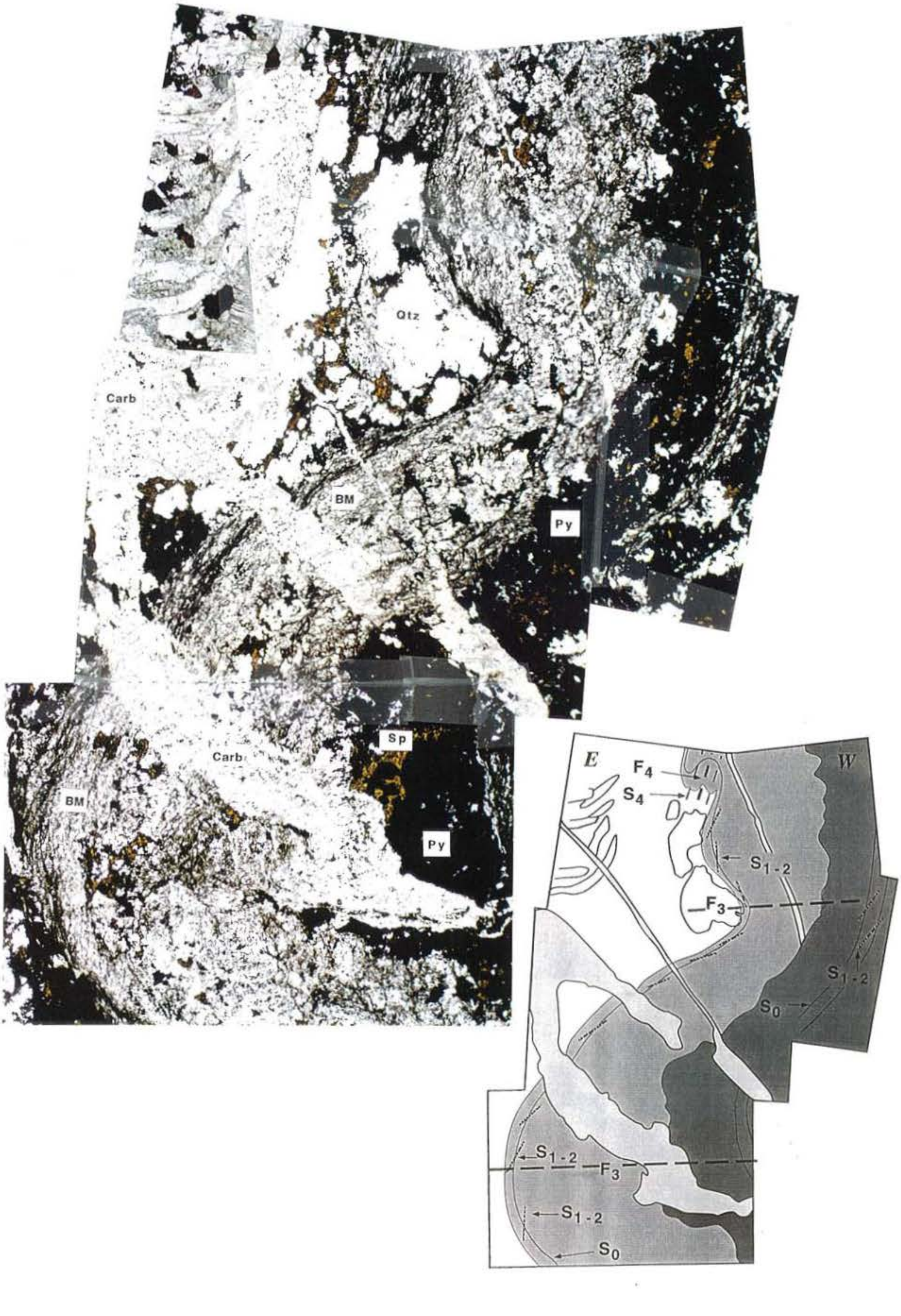
Qtz
Carb
BM
Py
Sp
Carb
BM
Py
E
W
F4
S4
S1-2
F3
S1-2
S0
S1-2
F3
S1-2
S0

Figure 14

(a) Rhythmically laminated pyritic siltstone folded around D_2 folds that have been variably rotated into inclined to subhorizontal orientations. A coarse-grained galena breccia is irregularly distributed in the lower part of the sample and spatially associated with the development a discordant coarse-grained galena vein set that cross-cuts the fold zone and is oriented NNE-SSW. Fine-grained sphalerite (Sp) breccias envelope the fold zone and contain sub-mm to mm-thick refolded mudstone layers (arrow). Sample is vertically oriented, west is to the right and south is into the page. (HS# UG2, C ore zone, 7200mN cross-cut).

(b) Flat-lying fold developed in intercalated rhythmically laminated pyritic siltstones and banded mudstones. Quartz fibre veins (Qtz) are developed in the hinge regions of these folds. Fibres have a subhorizontal elongation direction but are also bent into inclined orientations. This is probably associated with the development of the NNE-SSW oriented galena+sphalerite vein set (Gn) that cross-cuts the flat-lying fold. Vertically oriented sample looking south, with west to the right (HS# UG, C ore zone, 7200mN cross-cut).

(c) Complex refold patterns produced by the superposition of D_4 folds on D_2 folds rotated by D_3 are prevalent in the upper part of this sample (see inset). The central portion of the sample is carbonate-rich and irregularly brecciated by fine-grained sphalerite (Sp). Fine-grained sphalerite also occurs with galena in discordant NNW-SSE vein sets that cross-cut pyritic siltstones (PS) (HS# UG1, C ore zone, 7200mN cross-cut).

(d) An inclined D_2 fold in a pyritic siltstone (PS) is bounded to the west and east by fine-grained sphalerite (Sp) and galena (Gn) breccias, the former of which contains abundant mm-thick mudstone layers that have been refolded (arrow) (HS# UG5, C ore zone, 7200mN cross-cut).


a.
Sp
b.
Gn
Qtz
c.
Sp
PS
F3
F2
F4
d.
Gn
PS
Sp

Figure 15

(a) Rhythmically laminated carbonaceous siltstone (CS) -hosted sphalerite style characterized by alternating pale brown sphalerite-rich (Sp) and dark grey carbonaceous laminations (in this sample) and is spatially associated with mudstone-hosted orange sphalerite mineralization (arrow). Very fine galena veinlets (Gn) are developed perpendicular to bedding in this sample and occur as part of a vein array that includes layer-parallel pyrite-rich (Py) veins. Core is 4cm wide (HS# 131, J702 WI#6, 54.9m).

(b) Rhythmically laminated pyritic siltstone-hosted honey-coloured sphalerite is characterized by the preferential development of sphalerite in dolomite-rich rather than pyrite-rich (Py) laminations. Sphalerite (Sp) typically occurs in fleck-like patches in carbonate laminations oriented parallel to bedding, though sphalerite-rich zones also fringe pyrite laminations. Also note the irregular development of honey-coloured sphalerite in a mm-thick planar lamination near the centre of the sample. Cross-cutting carbonate veins contain variable proportions of honey-coloured sphalerite. Core is 4cm wide (HS# 137, J702WI#6, 200m).

(c) Nodular (Nod) calcite-hosted sphalerite. Sphalerite (Sp) is light honey-brown in colour whilst pyrite (Py) has a brassy appearance. Core is 4cm wide (HS#123, J702WD#4, 183.5m).

(d) Photomicrograph illustrating preferential development of sphalerite (Sp) in coarser-grained nodular calcite layers (Nod) rather than rhythmically laminated pyritic siltstone beds (PS) (HS#123, J702WD#4, 183.5m).

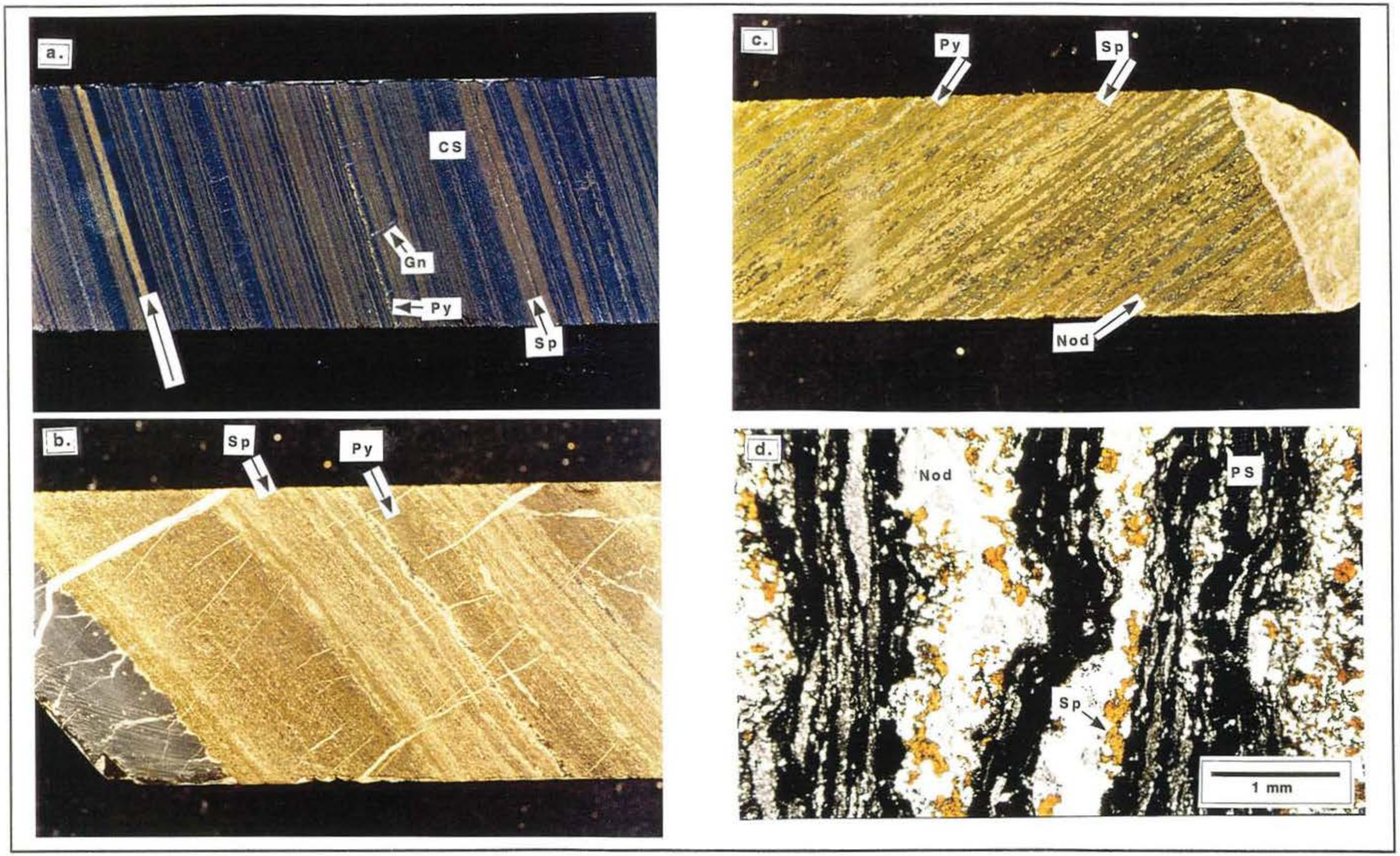
a.
CS
Gn
Py
Sp
c.
Py
Sp
Nod
b.
Sp
Py
d.
Nod
PS
Sp
1 mm

Figure 15

(e) Very fine-grained spheroidal pyrite (Py) and sphalerite (Sp) distributed along layers in a black shale. Pyrite-rich layers are brassy in appearance whilst sphalerite-rich layers are dull brown. A fibrous calcite vein is developed in the middle of the sample and localizes a vein network infilled by sphalerite-galena-pyrrhotite-pyrite-chalcopyrite. Core is 4cm wide (HS# 131, J702WI#6, 54.9m).

(f) Thin section photomicrograph of shale-hosted sphalerite which occurs with relatively coarse-grained calcite in pod-like zones. A significant proportion of the black material in this sample is cryptocrystalline bitumen (HS# 033d, J702WI#2, 55.4m).

(g) Fine-grained honey coloured sphalerite (Sp) is irregularly distributed along planar beds in a medium-bedded mudstone (MM). Its distribution also mimics bedforms in this sample. Mineralized layers are cross-cut and displaced by discordant dolomite veins. Core is 4cm wide (HS# 299, J718WI#4, 209.8m).

(h) Steel grey, fine-grained galena hosted by buff-coloured feldspathic mudstone layers from the D ore zone and spatially associated with galena-rich veins (Gn), orange mudstone-hosted sphalerite (Sp) and semi-massive orange and red-brown sphalerite bands. White calcite bands (Cal) and a large calcite nodule are also prominent features of this sample. Core is 4.5cm wide (HS# 254, J718 WI#5, 167.3m).

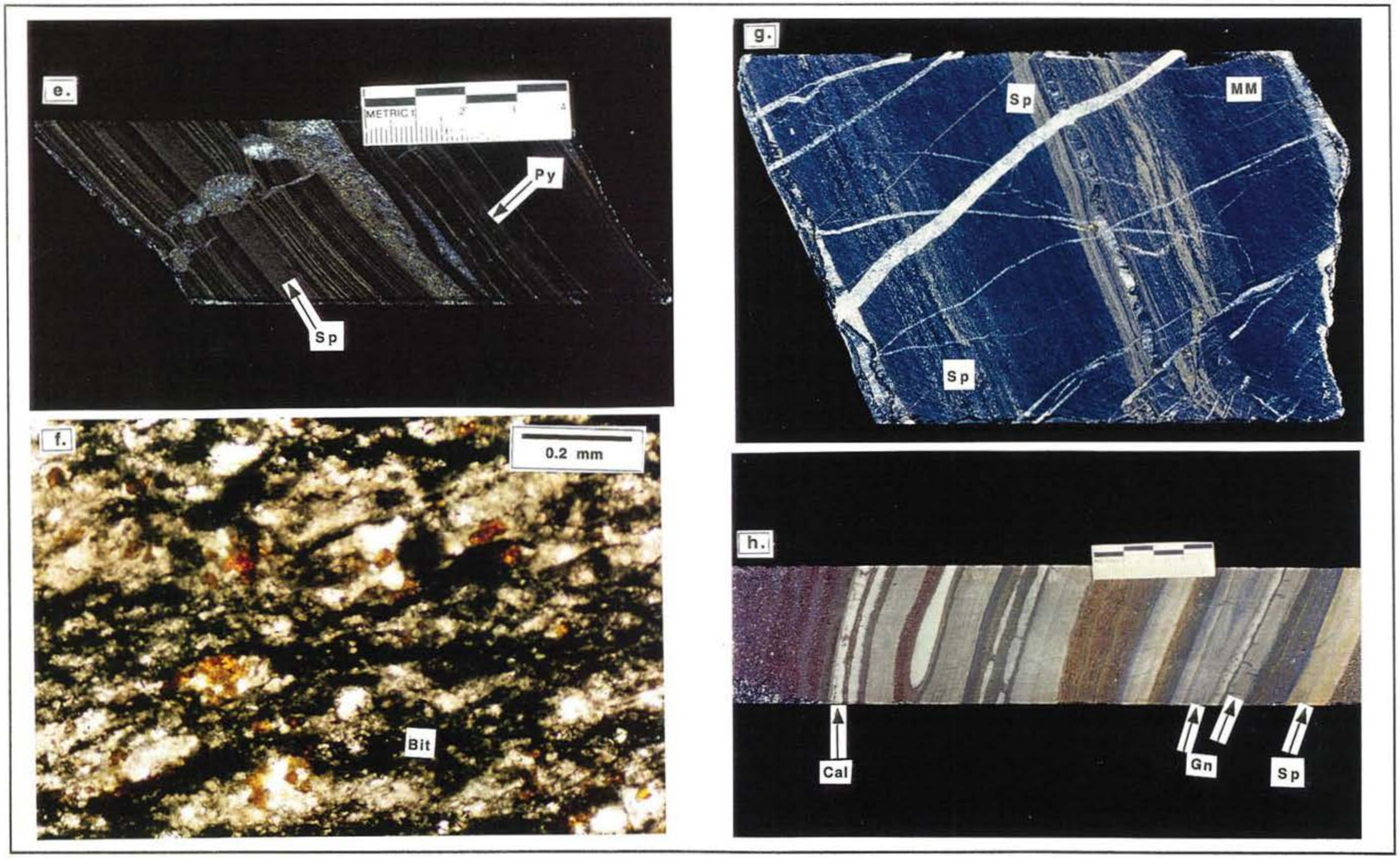
e.
METRIC
Py
Sp
f.
0.2 mm
Bit
g.
Sp
MM
Sp
h.
Cal
Gn
Sp

Figure 16

(a) A range of mineralization styles are represented in this sample. Sphalerite breccia-veins are prominent and typically a few mm thick. Veins to the far right contain semi-massive red-brown sphalerite bounded by folded sedimentary layers and are cross-cut by a cm-thick coarse-grained galena breccia and associated galena veins (Gn-arrow). A fine-grained galena breccia (Gn) is prominent to the left hand edge of the sample. Stratiform nodular carbonate (Nod) and rhythmically laminated pyritic siltstone-hosted honey-coloured sphalerite (PS) is also represented in this sample. Core is 4cm wide (HS# 63, J702WI#5, 199.8m) .

(b) Thin section photomicrograph of a sphalerite breccia-vein (Sp) developed at the contact between a banded mudstone (BM) and laminated pyritic siltstone (PS). Carbonate and quartz occur as infill and as clasts (along with pyritic siltstone fragments) enveloped by sphalerite. Layer-parallel and tapered discordant galena veinlets (Gn) are developed adjacent to the sphalerite breccia-vein (HS# 255, J718WI#5, 171.7m).

(c) Fine-grained sphalerite breccia (Sp) developed in the central portion of the sample which contains abundant nodular carbonate-hosted sphalerite. Attenuation of bedding, and brecciation of white carbonate veins is associated with the development of small-scale folds (arrow) and less regular distribution of sphalerite. (HS# 166, J718WD#5, 336.2m).

(d) Stratabound fine-grained sphalerite breccias (e.g. Sp) developed in a banded mudstone. Core is 4.5cm wide. (HS# 278, K782WI#1, 93.7m).

(e) Coarse-grained galena occurs as breccia matrix in this sample. Large clasts are composed of sphalerite and galena-bearing feldspathic mudstones, white calcite and semi-massive sphalerite mineralization. Note that abundant mm-sized sphalerite clasts (e.g. Sp) are dispersed throughout the galena matrix. (HS# 143, J702WI#6, 234.7m).

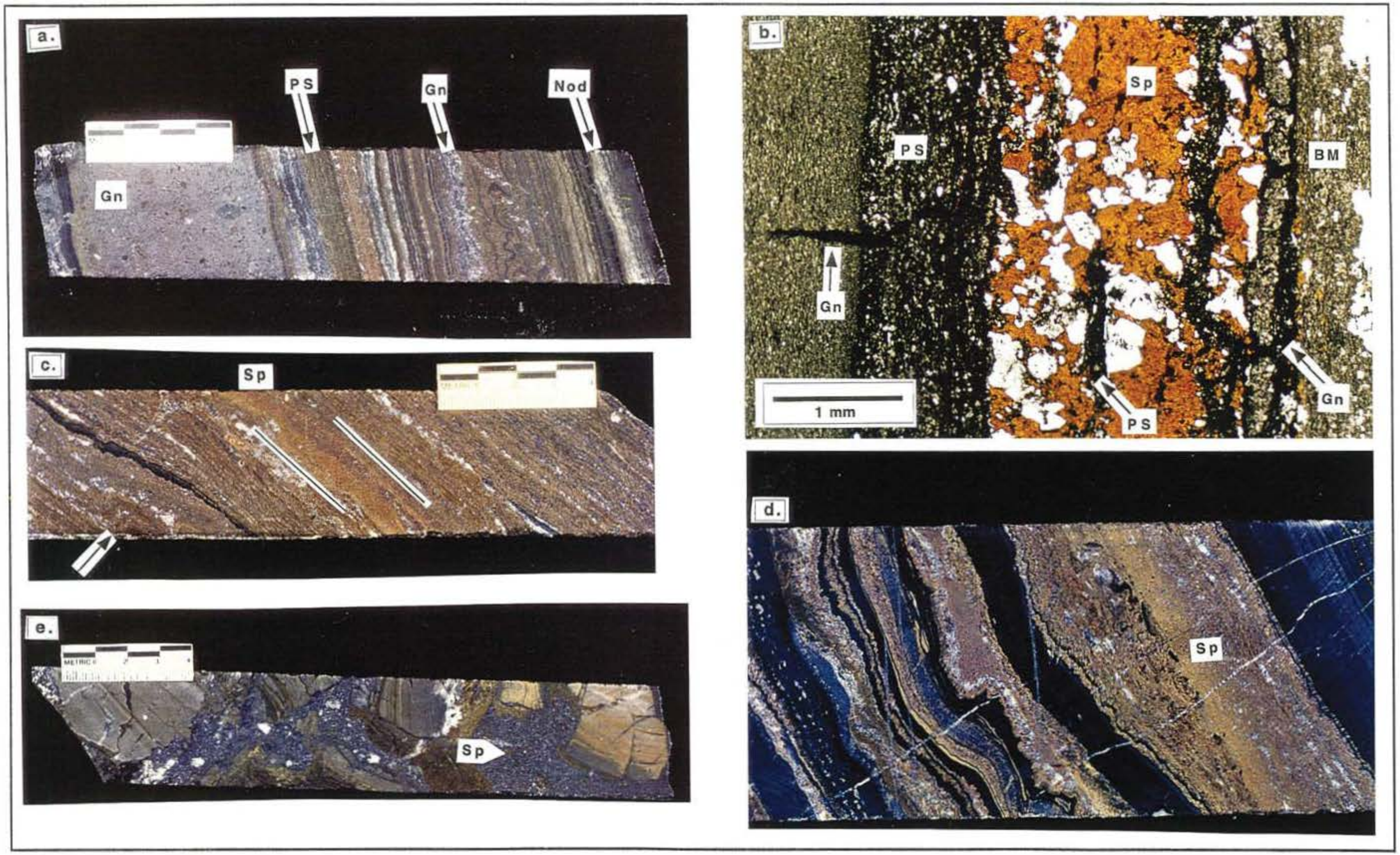
a.
PS
Gn
Nod
Gn
b.
PS
Sp
BM
Gn
1 mm
PS
Gn
c.
Sp
d.
Sp
e.
Sp

Figure 16

(f) Fine-grained galena breccia characterized by rounded clasts that exhibit a wide range of compositions including fine-grained sphalerite breccia (Sp), stratiform sphalerite (arrow) and carbonate (Carb). Note presence of coarse-grained sphalerite rims on some shale and carbonate fragments (e.g. Sp, left of centre) (HS# 181, J718WI#3, 175.4m).

(g) Mixed sulphide breccia containing flame-like pyrite (Py), galena (Gn) and sphalerite (Sp)-rich domains. Large, rounded clasts are composed predominantly of fine-grained red-brown sphalerite and pyrite whereas mudstone clasts in the galena-rich domain are sub-mm to a few mm in size and well rounded (HS# 169, J718 WD#5, 345.7m).

(h) Feldspathic rock with relict fine pyritic laminations reminiscent of rhythmically laminated siltstones cross-cut by discordant chalcopyrite-pyrrhotite±galena veins with irregular pyrrhotite-rich selvages. Several thin pyrrhotite breccias (Po) are developed parallel to bedding within the pyritic interval in the middle of the sample (HS# 268, J718 WI#5, 248.9m).

(i) Very coarse-grained sphalerite (Sp) - galena - pyrite (Py) - pyrrhotite (Po) - calcite (Cal) -dolomite (Dol) vein infill probably related to a J70-type fault (HS# 272, I698WI#3A, 78.9m).

(j) Coarse-grained honey-coloured sphalerite (Sp-arrow)-galena (Gn)-calcite occurs as infill in a tension gash vein array that displaces banded sphalerite (Sp) and is typical of L70-type fault-fill where these faults intersect orebody intervals (HS# 152, J702WI#6, 250.7m).

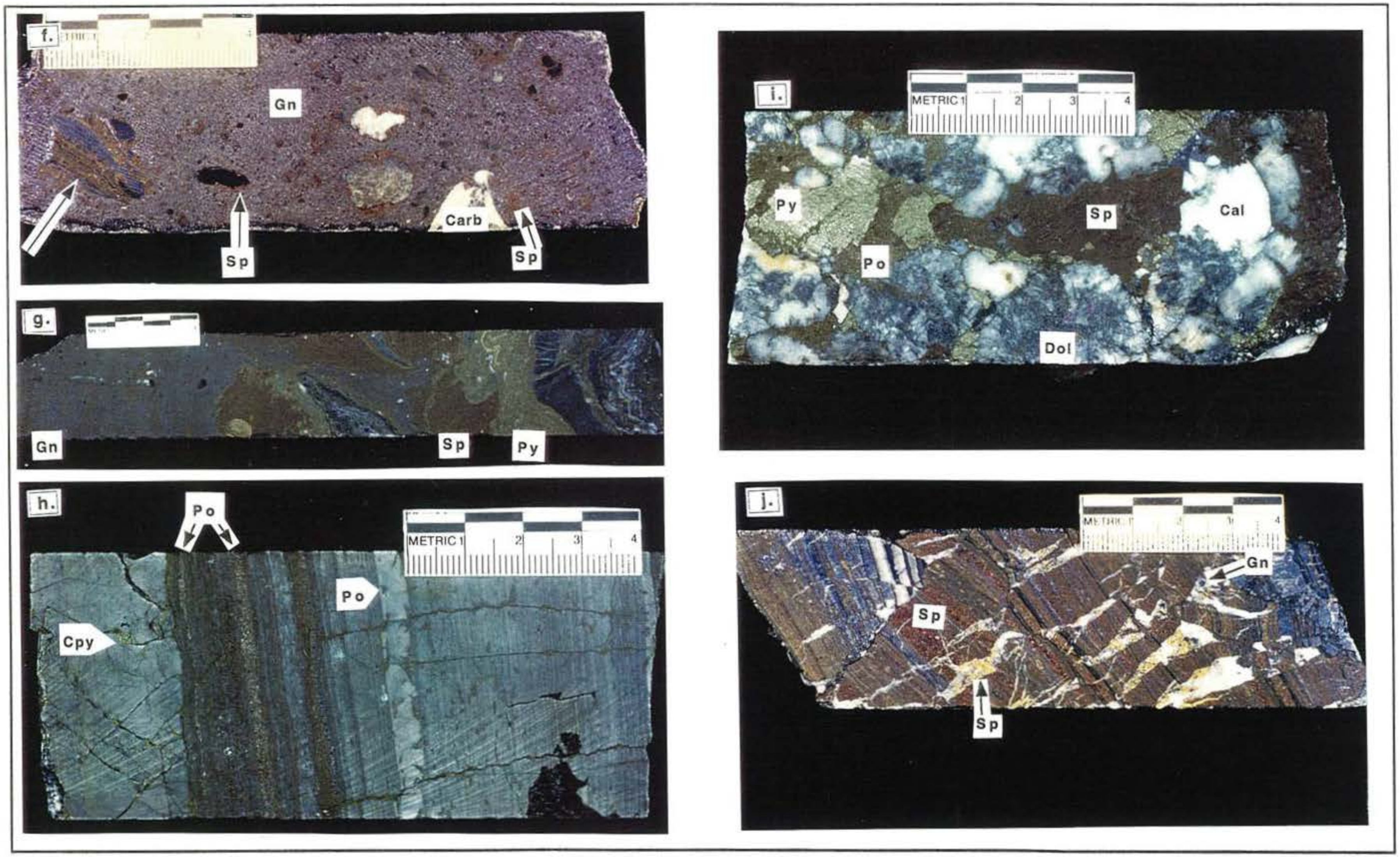
f.
Gn
Carb
Sp
Sp
g.
Gn
Sp
Py
h.
Po
Po
Cpy
METRIC 1 2 3 4
i.
METRIC 1 2 3 4
Py
Sp
Cal
Po
Dol
j.
Gn
Sp
Sp

KEY TO STRATIGRAPHIC COLUMN

Legend to accompany Figures 17a and b.

Left hand side

Stylolitic, medium-bedded mudstone

Bandedmudstone

Flt Fault

F1 TMB uncorrelated, with name

Right hand side

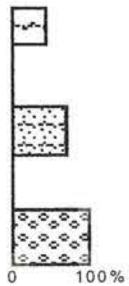

Relative abundance of rhythmically laminated carbonaceous siltstone

Relative abundance of rhythmically laminated pyritic siltstone

Relative abundance of nodular carbonate-bearing rhythmically laminated pyritic siltstone

Massive sulphide, mainly pyrite - host rock unidentifiable

Plot of Zn and Pb % with depth

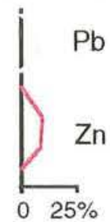

KEY TO CORRELATED INTERVALS

Intercalated banded mudstone and rhythmically laminated pyritic siltstones. Layer-parallel, planar and nodular carbonate layers generally abundant.

Rhythmically laminated carbonaceous and pyritic siltstones.

Medium-bedded or banded mudstone.

Tie line

F1 TMB correlation line and name

Distribution and relative abundance of mineralization styles

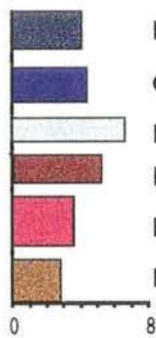

Fine-grained Gn breccia

Coarse-grained Gn breccia

Discordant vein-hosted Gn

Fine-grained Sp breccia

Breccia-vein -hosted Sp

NOD and PS -hosted Sp

Relative abundance of texture for designated depth interval.

1 - < 5%
2 - 5-15%
3 - 15-30%
4 - 30-45%
5 - 45-60%
6 - 60-75%
7 - 75-95%
8 - >95%

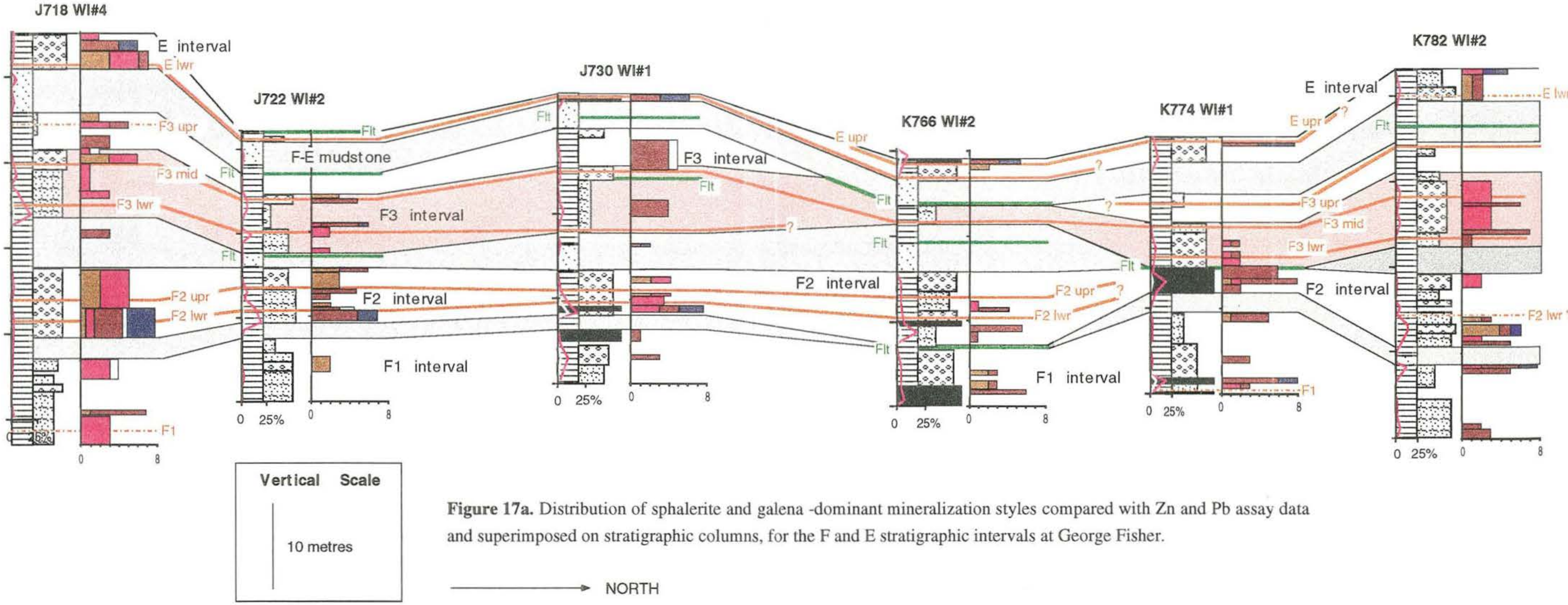

Figure 17a. Distribution of sphalerite and galena -dominant mineralization styles compared with Zn and Pb assay data and superimposed on stratigraphic columns, for the F and E stratigraphic intervals at George Fisher.

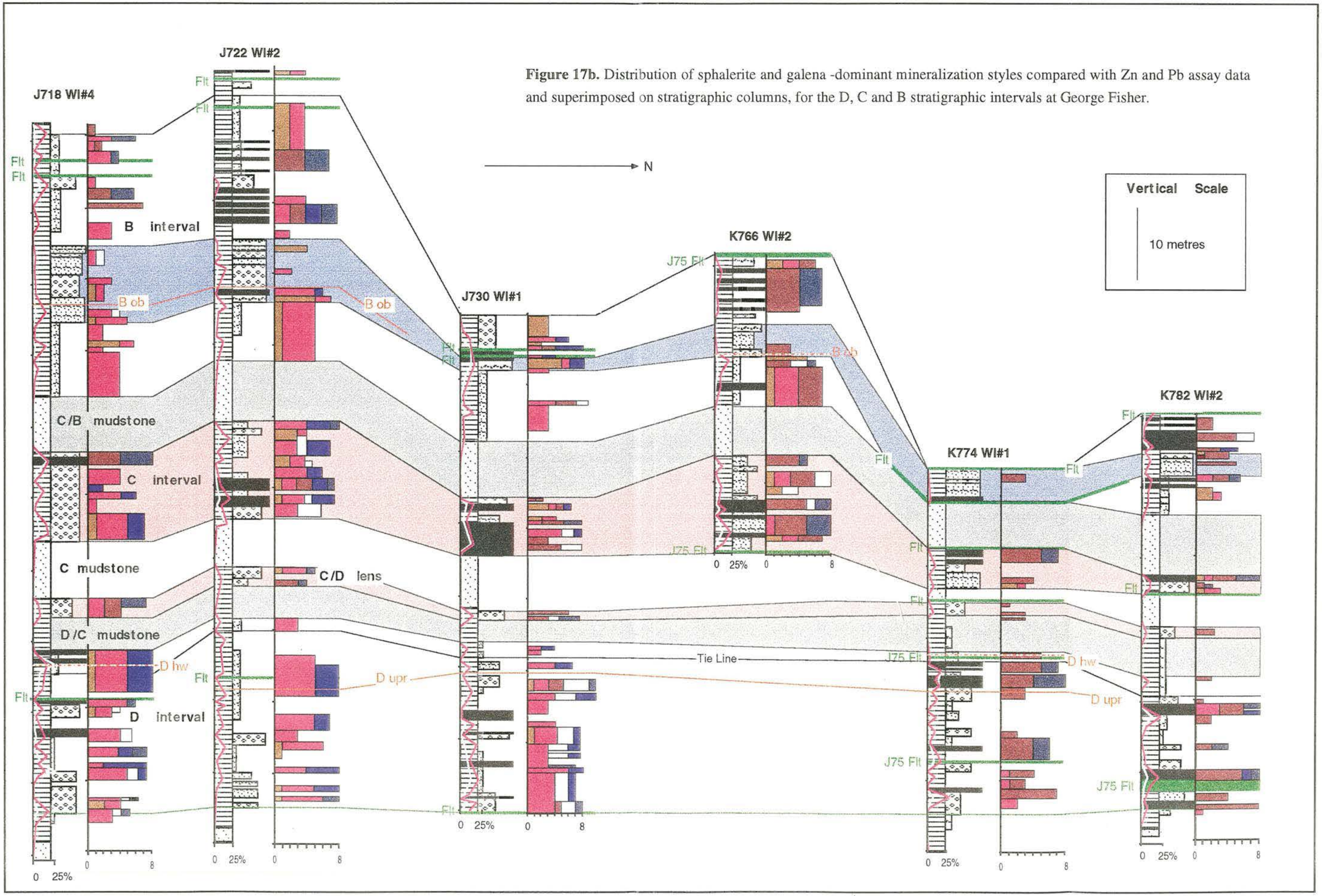

Figure 17b. Distribution of sphalerite and galena -dominant mineralization styles compared with Zn and Pb assay data and superimposed on stratigraphic columns, for the D, C and B stratigraphic intervals at George Fisher.

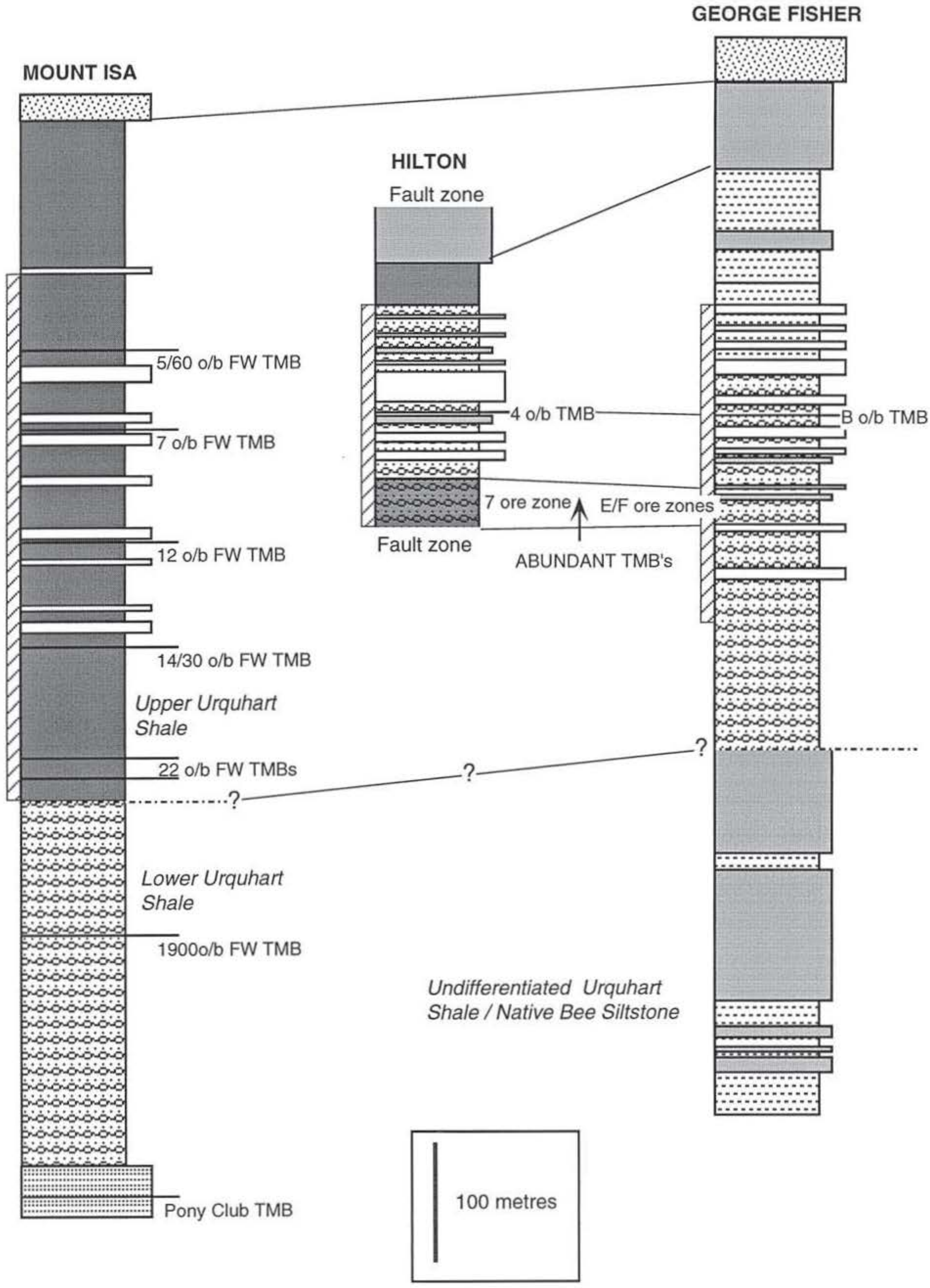
GEORGE FISHER
MOUNT ISA
HILTON
Fault zone
5/60 o/b FW TMB
4 o/b TMB
B o/b TMB
7 o/b FW TMB
7 ore zone
E/F ore zones
Fault zone
ABUNDANT TMB's
12 o/b FW TMB
14/30 o/b FW TMB
Upper Urquhart Shale
22 o/b FW TMBs
?
?
?
Lower Urquhart Shale
1900o/b FW TMB
Undifferentiated Urquhart Shale / Native Bee Siltstone
100 metres
Pony Club TMB

Figure 18. Simplified stratigraphic columns for Mount Isa, Hilton and George Fisher. Mount Isa stratigraphic column adapted from unpub. MIM Ltd. data, Perkins (1997) and Neudert (1983). Hilton and George Fisher columns adapted from unpub. MIM Ltd. data. Stratigraphic correlations between Hilton and George Fisher were established by A. Shaw (MIM geologist).

LEGEND

Spear Siltstone

Urquhart Shale

Interbedded rhythmically laminated pyritic siltstones and shales with minor banded mudstone.

Rhythmically laminated pyritic siltstones with moderate to abundant nodular carbonate and layer-parallel carbonate bands, interbedded with shales and minor banded mudstone.

Interbedded rhythmically laminated pyritic siltstones and banded mudstone with minor shale.

Interbedded banded mudstones and rhythmically laminated pyritic siltstones with moderate to abundant nodular carbonate and layer-parallel carbonate banding.

Massive and laminated, stylolitic mudstone.

Banded mudstone.

Native Bee Siltstone

Stratigraphic interval bearing economic Zn-Pb-Ag mineralization

Tuffaceous Marker Bed (TMB)

Line of stratigraphic correlation

PART B

STAGE	HR	I	II	III	IV a	IV b	IV c	IV d	V	VI	VII	VIII	IX a	IX b
DETRITAL QUARTZ	——													
DETRITAL MICA	- - -													
DETRITAL FELDSPAR	- - -													
FERROAN DOLOMITE	——			- - -					——		- - -	——	——	
CALCITE		——		——								——	——	——
PYRITE			—Py_s—		- - -	—Py_b—	-----	-----			—Py_y—	——	- - -	- - -
K-FELDSPAR		- - -		——										
HYALOPHANE				——										
CELSIAN				——										
QUARTZ				——								——	——	
MIGRABITUMEN					——	- - -	- ? -	- - ?						
HYDROPHLOGOPITE							——	-----						
SPHALERITE					-----	-----	-----	——	- - -		-----	——	- - -	- - -
GALENA					- - -				- - -		——	——	- - -	
PYRRHOTITE											-----	——	- - -	
CHALCOPYRITE												——	- - -	
MAGNETITE												——		
ANKERITE												——		
FERROAN ANKERITE												——		
SIDERITE												——		
BIOITE												——		
CHLORITE												——		
MUSCOVITE/PHENGITE												——		
GREENALITE												——		
NATIVE SILVER													- - -	
TETRAHEDRITE													- - -	
FLUORITE														——

HR = Host rock constituents

I - Calcitization and nodule development

STYLOLITIZATION

II - Spheroidal pyrite alteration

PRE- TO SYN- LOCAL D_1/ PRE- REGIONAL D_1

III - Celsian-hyalophane-K-feldspar/calcite-quartz vein development
IV - Sphalerite mineralization

REGIONAL DEFORMATION
(LOCAL D_2- D_3- D_4/ REGIONAL D_2 - $D_{2.5}$- D_3)

V - Sugary ferroan dolomite veining
VI - Fine-grained sphalerite breccia formation
VII - Galena mineralization
VIII - Copper mineralizatiion
IX - Late-stage faulting
    a - syn-post local D_4 (regional D_3)
    b - post local D_4 (regional D_3),
    possibly unrelated to Isan Orogeny?

- - - minor/ trace proportions
----- moderately abundant phase
—— major mineral phase

Py_s - spheroidal pyrite
Py_b - brassy pyrite
Py_y - yellow pyrite

Table 1. Alteration and mineralization paragenesis at the George Fisher deposit.

Stage	Infill Assemblages	Alteration Assemblages	Key Timing Criteria
I - Calcitization	Calcite	Calcite, minor K-feldspar	Replaces host rock ferroan dolomite. Cross-cut by bedding-parallel stylolites.
II - Pyritization		Spheroidal pyrite	Superimposed on carbonaceous stylolites.
III - Celsian-hyalophane-K-feldspar alteration	Cs-Hyl-Kfs-Cal±Qtz±FeDol Qtz-Cal±FeDol	Celsian-hyalophane-K-feldspar, minor calcite.	Veins cross-cut pyritized carbonaceous stylolites.
IV a - Migrabitumen b- Brassy pyrite alteration c - Hydrophlogopite d - Sphalerite mineralization	Bit$_1$±Py$_b$±Sp±Gn, Bit$_2$±Py$_b$±Sp±Po±Cal±Qtz±Gn Stage III Cal-Qtz±FeDol-Stage IV Sp±Py$_b$±Hphl Stage III Cs-Hyl-Kfs-Cal±Qtz±FeDol-Stage IV Hphl-Sp±Py$_b$	Sphalerite, brassy pyrite, minor hydrophlogopite, migrabitumen.	Migrabitumen occurs interstitial to calcite Brassy pyrite occurs as replacements and overgrowths on spheroidal pyrite & alteration of celsian-hyalophane-K-feldspar. Sphalerite replaces calcite, ferroan dolomite, spheroidal pyrite, celsian-hyalophane-K-feldspar. Hydrophlogopite infills after celsian-hyalophane-K-feldspar.
V - Sugary ferroan dolomite veining	FeDol±Sp±Gn	FeDol?	Cross-cuts banded and stratiform sphalerite mineralization.
VI - Fine-grained Sp breccia formation	Sp		Contains clasts of sugary ferroan dolomite veins.
VII - Galena mineralization	Gn± Py$_y$±Sp±Po±carb	Galena, yellow pyrite, pyrrhotite	Galena-pyrite-pyrrhotite brecciates all sphalerite-dominant mineralization styles and occurs as replacements of sphalerite.
VIII - Copper mineralization	Cal-Py-Po±Cpy±Sp±Gn Sid-FeAnk-Ank-FeDol±Cpy±Po±Py±Sp±Gn Bt-Po-Sp±Gn±Cpy±Py Chl±FeDol±Py±Po±Cpy Gre-Qtz±Chl	Po±Sp±Cal±Cpy Bt±Sp±Po±Py±Gn±Cpy Sid±FeDol±Ank±FeAnk±Mt±Po±Gn±Sp±Chl FeDol±Ank±Chl±Qtz±Msc±Phg±Gre	Po replaces fine and coarse-grained galena breccias and all textural varieties of sphalerite. Po-Cpy infill in discordant veins with late-stage sphalerite and galena. Phyllisilicates occur as replacements of carbonates and feldspar and infill in veins with Po-Cpy. Late-stage galena and sphalerite occur as replacements of these phyllosilicates.
IX - Late-stage fault-hosted mineralization a - J75-type fault matrix b - L70-type fault matrix	Dol±Gn±Tet±Ag Dol±Sp±Gn Cal±Qtz±FeDol±Sp±Gn±Py±Po±Cpy Cal±Fl Cal±Py±Sp		Late faults cross-cut and displace stratigraphy. Mineralization typically developed as fault matrix where faults intersect on ore lenses.

Table 2. Summary of major features of each paragenetic stage and key timing criteria (refer to List of Mineral Abbreviations).

MODEL	CONCEPT	PRECIPITATION MECHANISM	REFERENCE
MIXING MODEL	Metals transported as chloride complexes in slightly oxidized, weak acid to neutral, basin-derived brines and encounter reduced sulphur - bearing fluids at the site of ore deposition. Fluid-derived H_2S was either transported to the site or locally derived.	Mixing $M^{2+}Cl^{-}$ with H_2S derived from; 1. H_2S-rich pore fluids in carbonate host rocks. 2. Bacterial sulphate reduction of in situ or proximal sulphate evaporites. 3. Thermochemical sulphate reduction of in situ or proximal sulphate evaporites. 4. Degraded hydrocarbons (oil-field brines). 5. Preexisting sulphides.	e.g. Beales (1975) e.g. Beales and Jackson (1966) e.g. Anderson and Garven (1987) Kesler et al. (1994) e.g. Levanthal (1990) Kesler et al. (1994) e.g. Lovering (1961)
H_2S BASINAL DEGASSING MODEL	Metals transported to site of deposition as chloride complexes in basin-derived brines. H_2S gas generated as a result of hydrocarbon maturation during deep burial.	Precipitation occurs when either metal-bearing fluids encounter trapped gas pockets or when buoyant, ascending gas percolates through metal-bearing fluid.	Hill (1993)
METAL+SULPHATE-BEARING FLUID	Metals as chloride complexes and sulphate are transported to site of ore depostion in a fluid.	Precipitation occurs as a result of thermochemical sulphate reduction at site of metal deposition (increase reduced sulphur availability) by; 1. encounter with hydrocarbons or organic detritus. 2. addition of CH_4 gas generated from thermal maturation of organic material.	e.g. Hinman (1996) [1.] Broadbent et al. (1998)[2.] e.g. Anderson (1991)
METAL+HYDROCARBON-BEARING FLUID	Metal chloride complexes and hydrocarbons are transported to site of ore deposition in a strongly reduced basinal brine.	Precipitation occurs when fluid encounters evaporitic sulphate source.	Thompkins et al. (1994)
REDUCED ACID-BRINE MODEL	Metals transported as chloride complexes with reduced sulphur in acidic brines.	Precipitation occurs as a result of; 1. Neutralization 2. Decreasing temperature 3. Dilution	e.g. Anderson (1973) Sverjensky (1981)

Table 3. Common metal transport and precipitation models proposed for the formation of sediment-hosted Zn-Pb deposits.
[1.] Favoured model for the formation of the HYC deposit at McArthur River and [2.] the Century deposit, both of which are situated in the Northern Australian Proterozoic.

TEXTURAL AND MINERALOGICAL SETTING	REACTION	METAL PRECIPITATION MECHANISM AND SULPHUR SOURCE
Sphalerite precipitates in voids in veins and nodular calcite layers unaccompanied by carbonate dissolution (Figs. 4e and 5a).	(a) $Zn^{2+}(aq) + H_2S(aq/g) \rightarrow ZnS + 2H^+$ (b) $2CH_2O + SO_4^{=}(aq) \rightarrow 2HCO_3^- + H_2S(aq)$ (Machel, 1987) coupled with reaction (a) (c) $CH_4 + 2H^+(aq) + SO_4^{=}(aq) \rightarrow H_2S + 2HCO_3^-(aq)$ (Machel, 1987) coupled with reaction (a) Alternatively, decarboxylation of acetate produces CH_4 (d) $CH_3COOH + SO_4^{=} + 2H^+ \rightarrow H_2S + CH_4 + CO_2(aq) + 2O_2(g)$ (e) $CH_3COO^- + SO_4^{=} + 2H^+ + H_2O \rightarrow H_2S + CH_4 + HCO_3^-(aq) + 2O_2(g)$	Mixing Model; $H_2S(aq)$ or $H_2S(g)$ trapped in pore fluids or introduced via a separate fluid. Reaction (a). Metal+Sulphate Model; sulphate reduction by contact with organic material (sourced from adjacent pyritic siltstones?) Reaction (b) + (a). Metal+Sulphate Model; mixing with a reductant such as $CH_4(g)$ trapped in pores. Reaction (c), (d) or (e) +(a).
Sphalerite replaces carbonate (e.g. Fig. 12d).	(f) $Zn^{2+}(aq) + H_2S(aq) \rightarrow ZnS(s) + 2H^+$ drives the reaction (g) $2H^+(aq) + CaCO_3(s) \rightarrow Ca^{2+}(aq) + H_2CO_3(aq)$ which creates space for further metal precipitation (cf. Barnes, 1997) and additionally drives the reaction (h) $SO_4^{=}(aq) + 2H^+(aq) \rightarrow H_2S + 2O_2$	Mixing Model or Metal+Sulphate Model; Potential sulphur sources as above. Precipitation driven by availability of space. Metal+Sulphate Model; addition of reduced sulphur by sulphate reduction. Reaction (h).
Sphalerite replaces spheroidal pyrite (e.g. Fig. 12b).	(i) $2Zn^{2+}(aq) + FeS_2 + H_2O \rightarrow 2ZnS + Fe^{2+}(aq) + 2H^+ + \frac{1}{2}O_2$	Mixing Model; sulphur derived from preexisitng sulphide mineral. Reaction (i).
Sphalerite and galena occur as intergrowths with migrabitumen (e.g. Fig 10b).	(b) $2CH_2O + SO_4^{=}(aq) \rightarrow 2HCO_3^- + H_2S(aq)$ (Machel, 1987) induces metal precipitation (j) $Pb^{2+}(aq) + H_2S(aq) \rightarrow PbS(s) + 2H^+$ and is also coupled with reaction (a)	Metal+Sulphate Model; reduced sulphur derived by insitu thermochemical sulphate reduction by organic material. Reaction (b) + (a) and (j)

Table 4. Metal precipitation reactions derived to account for common textural associations at George Fisher. Precipitation mechanisms and sulphur source relate to fluid mixing and metal+sulphate models described in Table 3.

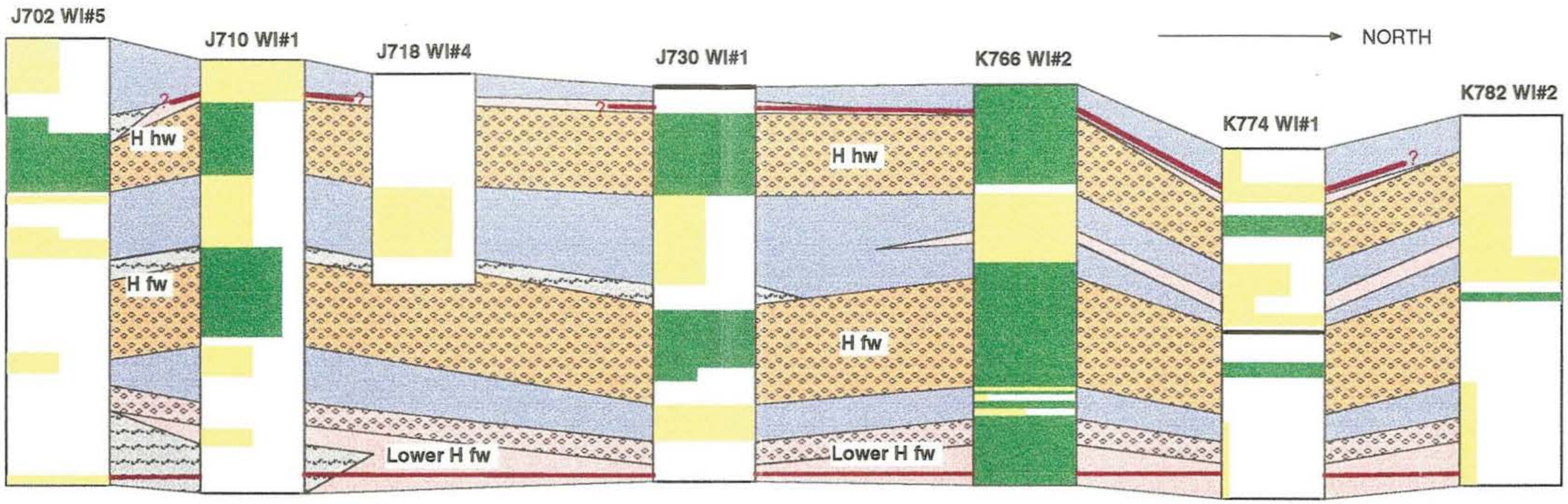

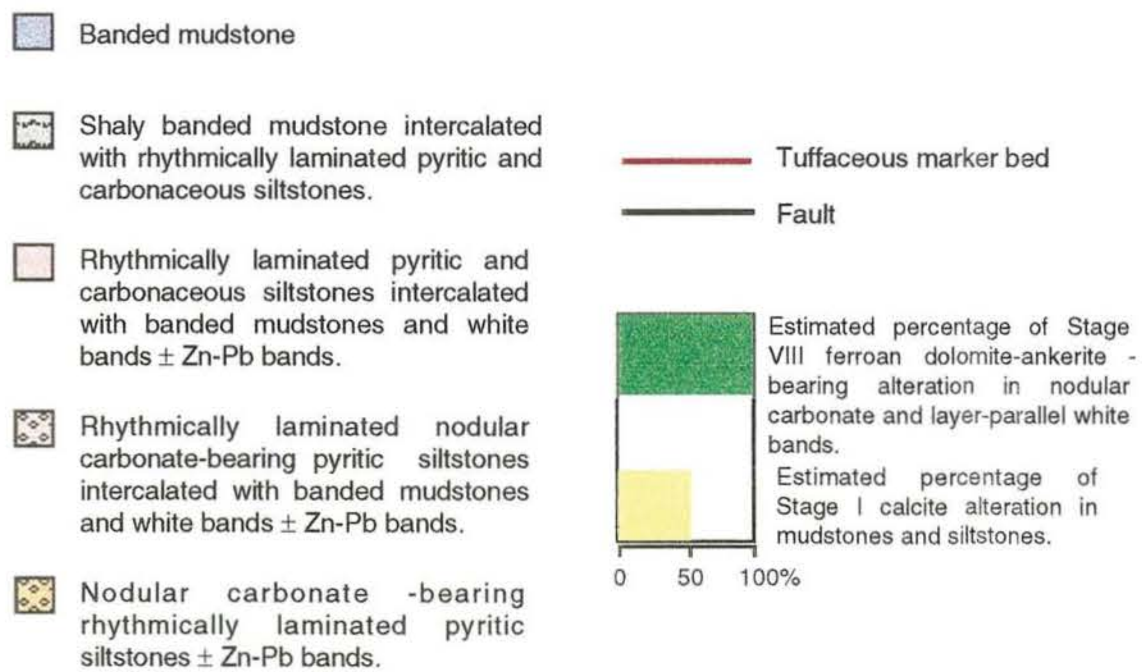

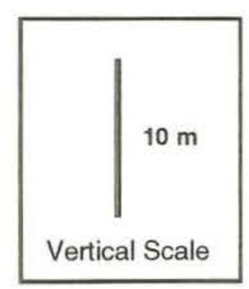

Figure 1. Carbonate distribution logs superimposed on a stratigraphic plan map of the H stratigraphic interval and illustrating the distribution of Stage I calcite developed in mudstones and siltstones and Stage VIII ferroan dolomite-ankerite-ferroan ankerite±siderite alteration in nodular carbonate layers and layer-parallel white bands. Refer to Part A, Fig. 5 for drill hole localities.

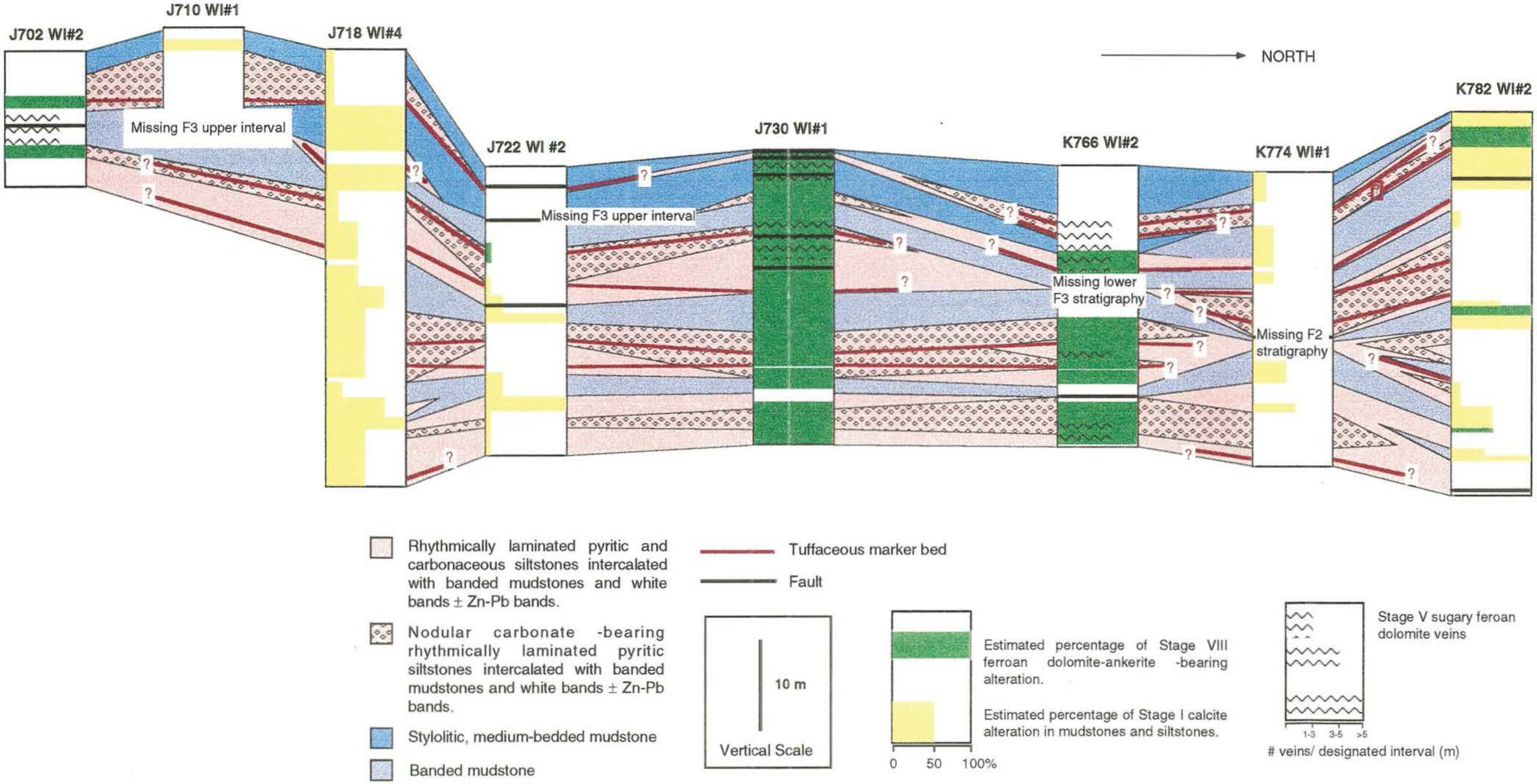

Figure 2. Carbonate distribution logs superimposed on simplified stratigraphic plan maps of the F and E stratigraphic intervals and illustrating the estimated percentage of Stage I calcite in mudstones and siltstones, Stage VIII feroan dolomite-ankerite-ferroan ankerite±siderite alteration in nodular layers and layer-parallel white carbonate bands and intensity of Stage V sugary ferroan dolomite veins. Refer to Part A, Fig. 5 for drill hole localities.

Legend to Figure 3.

D-C-B STRATIGRAPHIC INTERVAL

- Rhythmically laminated nodular carbonate-bearing or plain pyritic and carbonaceous siltstones intercalated with banded mudstones and white bands ± Zn-Pb bands.
- Rhythmically laminated nodular carbonate-bearing pyritic siltstones intercalated with banded mudstones and white bands ± Zn-Pb bands.
- Rhythmically laminated pyritic and carbonaceous siltstones ± Zn-Pb bands.
- Nodular carbonate -bearing rhythmically laminated pyritic siltstones ± Zn-Pb bands.
- Stylolitic, medium-bedded mudstone
- Banded mudstone

10 m

Vertical Scale

- Tuffaceous marker bed
- Fault
- Line defines point in stratigraphy above which no Stage I calcite has been observed and Stage VIII carbonates dominate.

Figure 3a

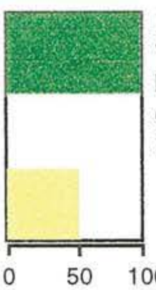

Estimated percentage of Stage VIII ferroan dolomite-ankerite -bearing alteration in nodular carbonate and layer-parallel white bands.

Estimated percentage of Stage I calcite alteration in mudstones and siltstones.

Figure 3b

Distribution of Stage VIII pyrrhotite breccias

Distribution of Stage VIII phyllosilicate alteration

Distribution of Stage III Hyalophane-K-feldspar alteration

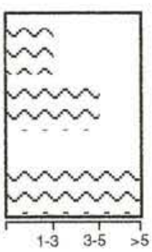

Stage V sugary ferroan dolomite veins

veins/ specified interval (m)

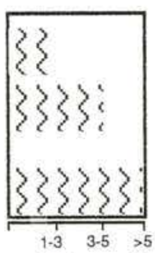

Stage VIII Chalcopyrite-bearing veins

veins/ specified interval (m)

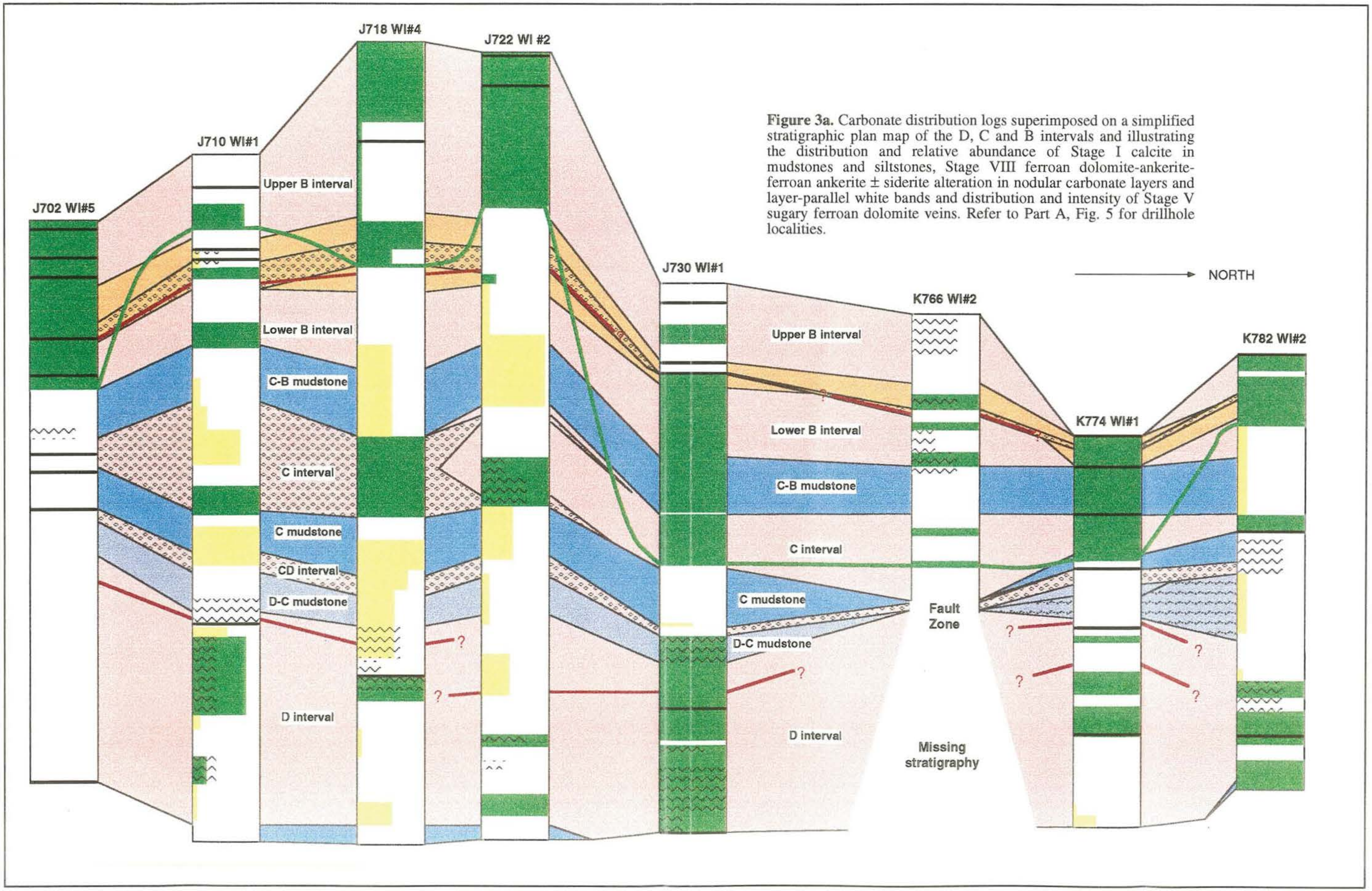

Figure 3a. Carbonate distribution logs superimposed on a simplified stratigraphic plan map of the D, C and B intervals and illustrating the distribution and relative abundance of Stage I calcite in mudstones and siltstones, Stage VIII ferroan dolomite-ankerite-ferroan ankerite ± siderite alteration in nodular carbonate layers and layer-parallel white bands and distribution and intensity of Stage V sugary ferroan dolomite veins. Refer to Part A, Fig. 5 for drillhole localities.

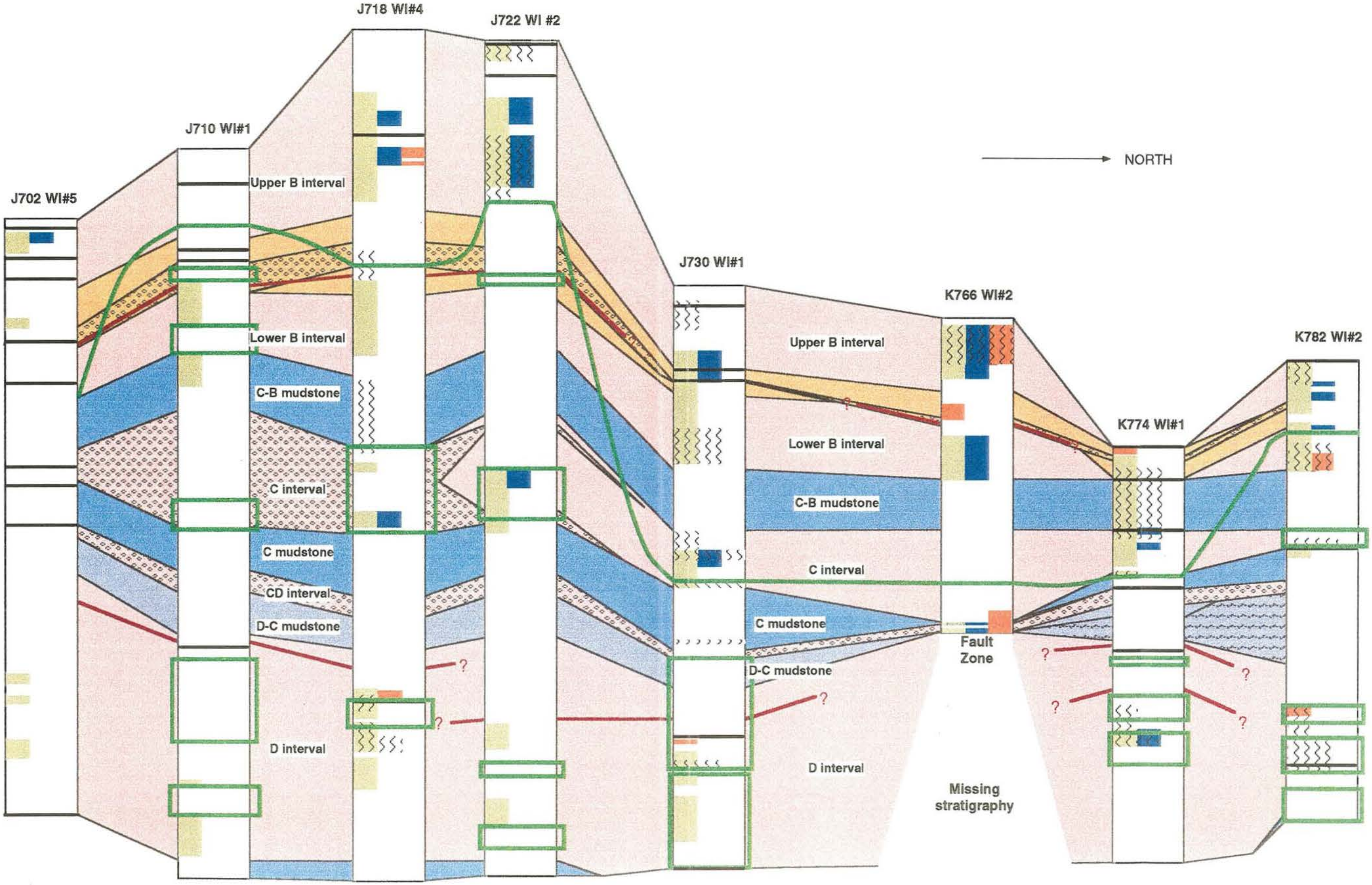

Figure 3b. Silicate-sulphide distribution logs superimposed on a simplified stratigraphic plan map of the D, C and B intervals and illustrating the distribution of Stage III hyalophane-K-feldspar alteration in mudstones and siltstones, Stage VIII phyllosilicate alteration, distribution of Stage VIII pyrrhotite breccias and distribution and intensity of Stage VIII chalcopyrite-bearing veins. The distribution of Stage VIII ferroan dolomite-ankerite-ferroan ankerite±siderite alteration is superimposed to illustrate the spatial association between this alteration style and phyllosilicate alteration. Refer to Part A, Fig. 5 for drillhole localities.

Figure 4

a. Light grey Stage I calcite alteration (Cal) irregularly developed in a dark grey planar to discontinuously laminated ferroan dolomite-bearing medium-bedded mudstone (Dol). Carbonaceous stylolites cross-cut and juxtapose calcite alteration zones (core width=4cm, HS# 078b, J710WI#1, 74m).

b. Stage I calcite alteration selectively developed in a ferroan dolomite-bearing banded mudstone (Dol). Calcite alteration has a bleached appearance, is spatially associated with white calcite nodules and include irregular bands of ferroan dolomite-bearing mudstones (dark grey) within otherwise pervasive alteration zones (core width=4cm, HS# 044i, J702WI#5, 45m).

c. Photomicrograph illustrating extensive Stage I calcite alteration in a medium-bedded mudstone interval. Calcite (Cal) is coarser grained than quartz and ferroan dolomite (Dol) that occur together in irregular clots. A stylolite is developed in the middle of the sample and bedding-parallel foliation is developed throughout. Note the sutured nature of calcite (Cal) grain boundaries (HS# 078b, J710WI#1, 71.1m, XPL).

d. Bedding-parallel to discordant nodular calcite developed in a rhythmically laminated pyritic siltstone (PS). Calcite (Cal) in nodular layers (Nod) is colourless and contains irregular ferroan dolomite±detrital quartz aggregates (e.g. Dol). Dark laminations consist predominantly of spheroidal pyrite and irregular stringers of spheroidal pyrite (Py_s) locally cross-cut a nodular calcite layer (HS# 050g, J702WI#5, 105.9m, PPL).

e. Microcrystalline subhedral to rhombohedral calcite crystals in a nodular calcite layer line microscopic vughs which are infilled by sphalerite (Sp) (HS# 050g, J702WI#5, 105.9m, PPL).

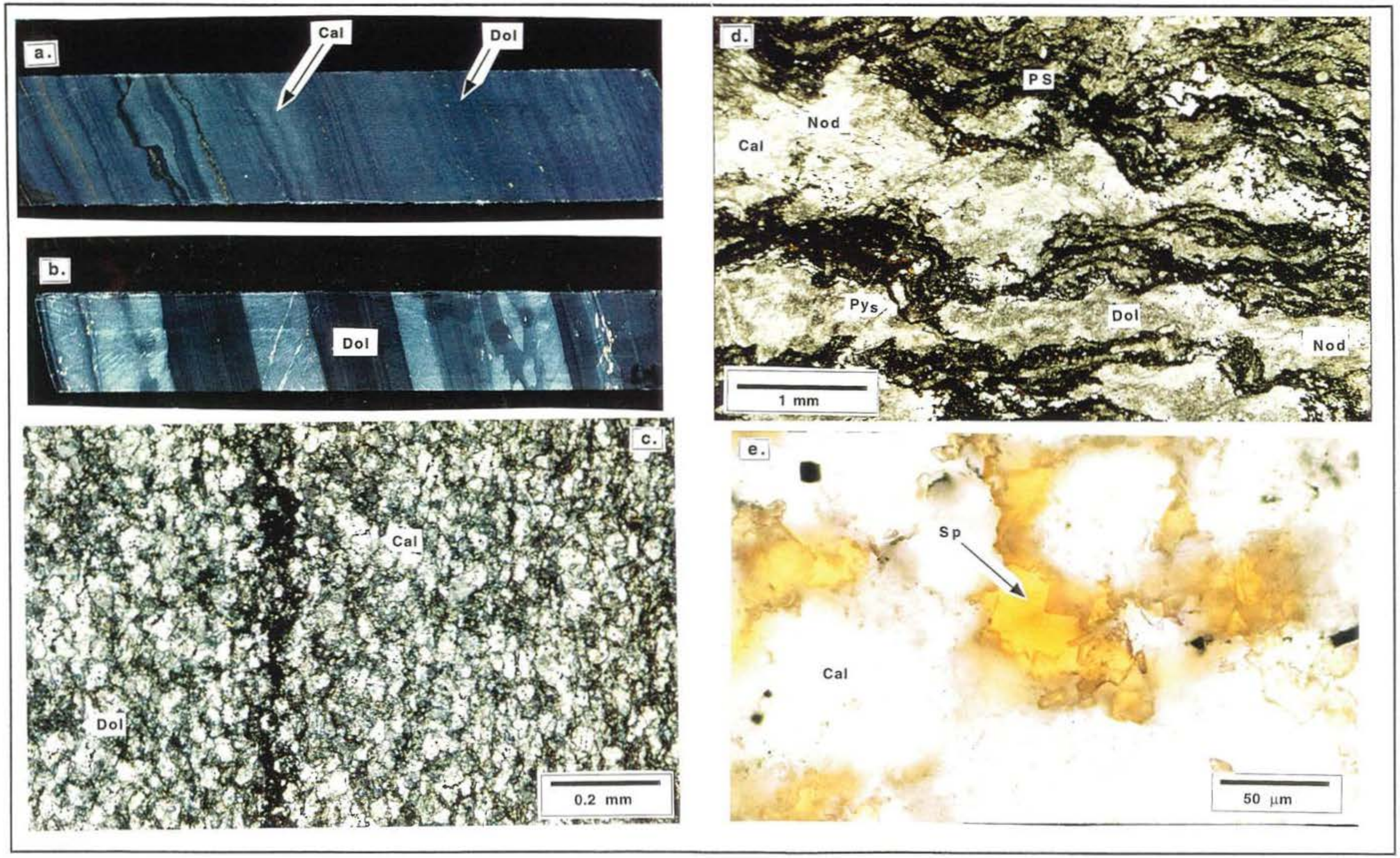

a.
Cal
Dol
b.
Dol
c.
Cal
Dol
0.2 mm
d.
PS
Nod
Cal
Pys
Dol
Nod
1 mm
e.
Sp
Cal
50 µm

Figure 5.

(a) Backscattered electron image illustrating abundant Stage I rhombohedral calcite (Cal) and Stage IV sphalerite (Sp) infill in a microscopic nodular layer. Rhombohedral calcite crystals abut Stage I calcite-altered quartz(Qtz)±ferroan dolomite(FeDol) bearing wall rock that contains irregularly distributed Stage II spheroidal pyrite (Py_s) and Stage IV brassy pyrite (Py_b) (HS# UG 9, C ore zone, 7200mN cross-cut).

(b) Backscattered electron image of two nodular calcite layers separated by a very fine ferroan dolomite-quartz lamination with spheroidal pyrite. Calcite is intergrown with K-feldspar in nodular layers and contains irregular clots of ferroan dolomite-quartz (HS# DC840b, H766ED#1, 558.6m)

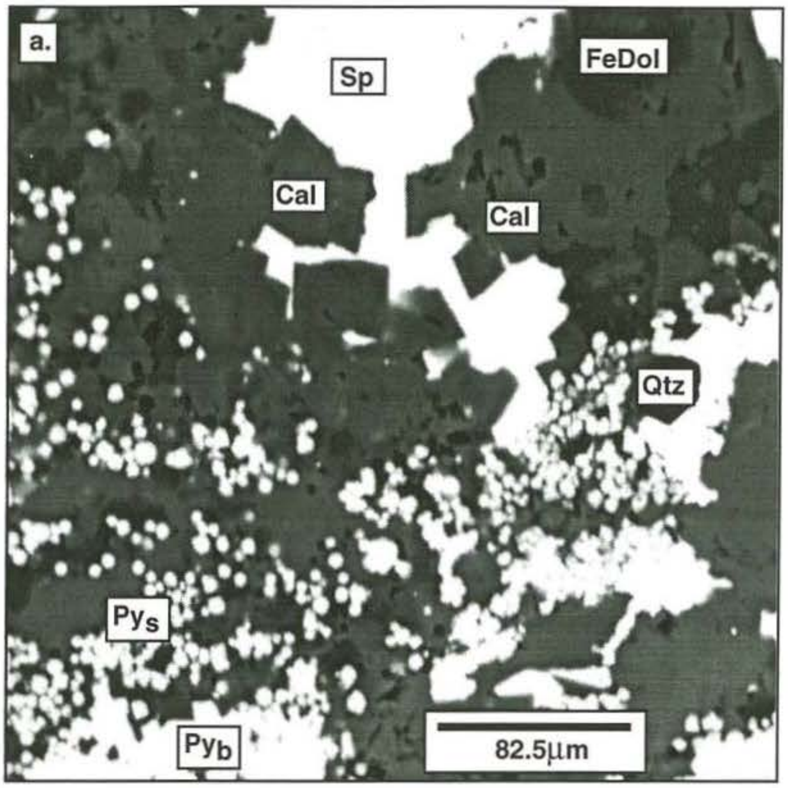
a.
Sp
FeDol
Cal
Cal
Qtz
Py_s
Py_b
82.5μm

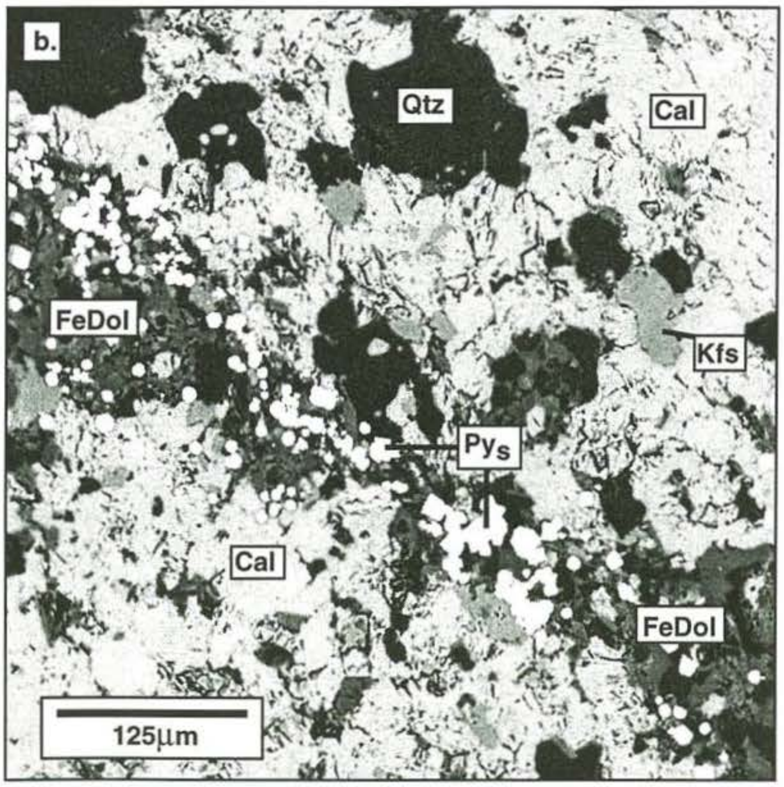
b.
Qtz
Cal
FeDol
Kfs
Py_s
Cal
FeDol
125μm

Figure 5.

c. BSE image illustrating diffuse nature of layer-parallel white band contacts with dolomitic banded mudstones (FeDol+Qtz), defined by the distribution of Stage I white calcite (Cal). A lens-shaped calcite nodule occurs adjacent to a white band central to the sample (HS# 051a, J702WI#5, 111.6m).

d. Quartz (Qtz) concentrated around a carbonaceous stylolite. The stylolite juxtaposes two Stage I calcite-altered mudstone beds. The upper layer is calcite-rich (Cal) whilst the lower bed contains less calcite and more ferroan dolomite and quartz (FeDol+Qtz). Stage II spheroidal pyrite (Py_s) preferentially replaces carbonaceous material along the stylolite (HS# 078b, J710WI#1, 71.1m).

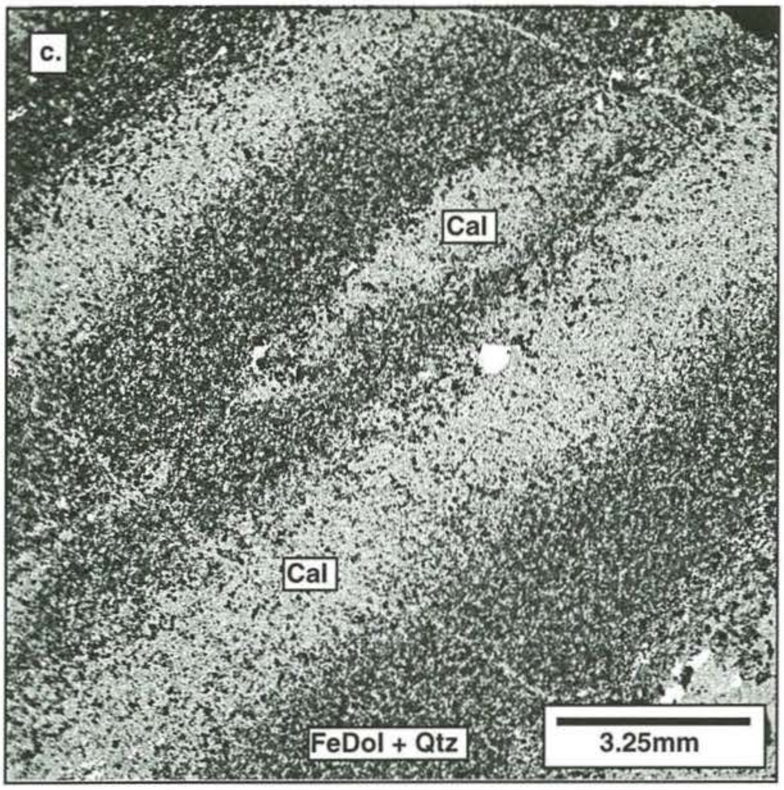
c.
Cal
Cal
FeDol + Qtz
3.25mm

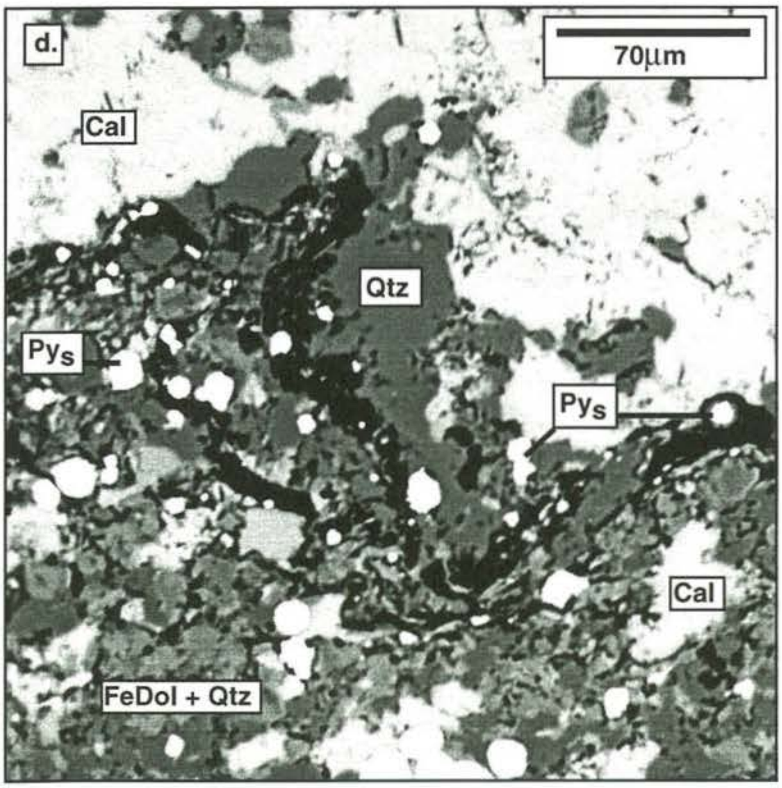
d.
70μm
Cal
Qtz
Pys
Pys
Cal
FeDol + Qtz

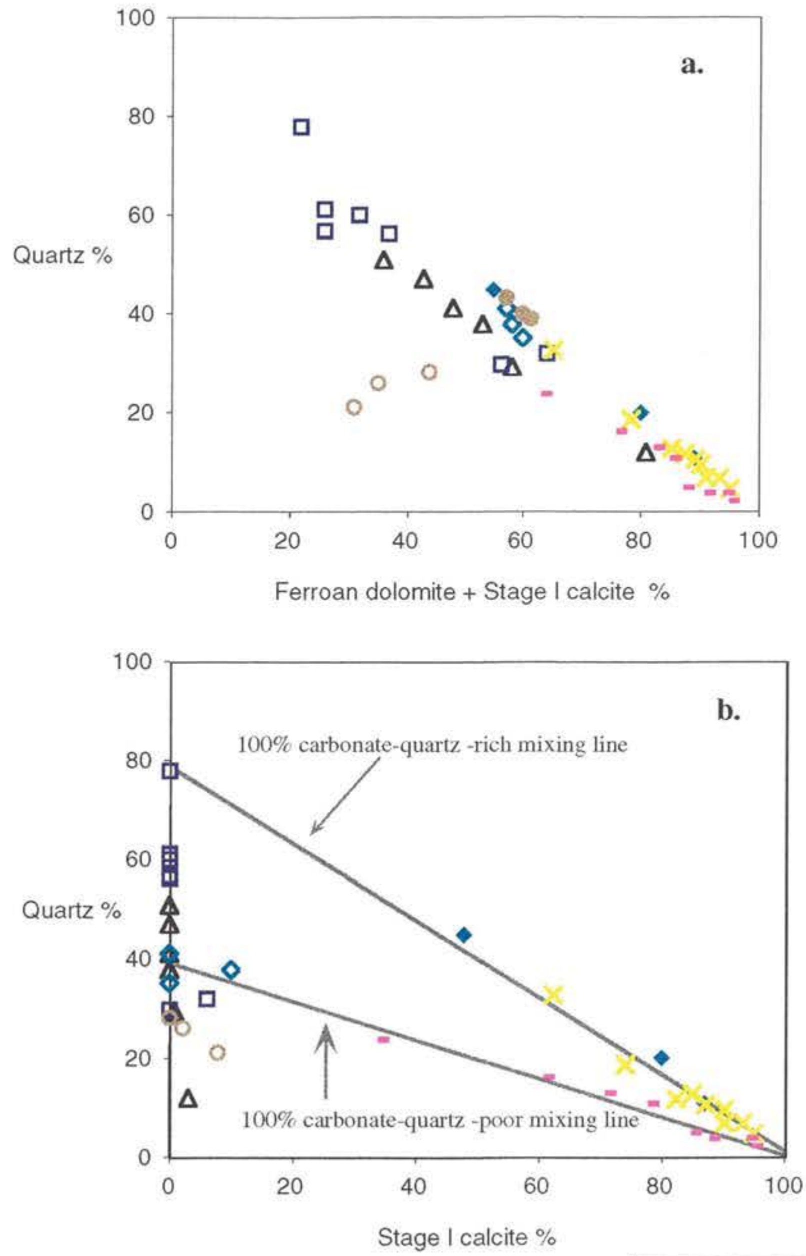

Figure 6. (a) Plot illustrating whole rock abundances of quartz versus ferroan dolomite+ Stage II calcite or representative samples of major rock types and carbonate banding. (b) Plot illustrating whole rock abundances of quartz versus Stage I calcite. The bulk of the quartz is assumed to be detrital based on thin section examination. Relative abundances were derived from XRD traces (see Appendix IX).

* Values for rhythmically laminated pyritic siltstones normalized to 100% quartz+whole rock carbonate.

Figure 7.

a. Celsian-hyalophane-K-feldspar alteration (Cs-Hyl-Kfs) is buff-white and preferentially developed along mudstone layers in this sample. Relict laminations and grey clots of ferroan dolomite-bearing host rock are preserved within altered beds. Banded sphalerite (Sp) in this sample is spatially associated with abundant orange sphalerite alteration in mudstones and semi-massive brassy pyrite (Py_b) that is commonly developed in rhythmically laminated pyritic siltstones but also occurs along a bedding contact in the middle of the sample (HS# 251, J718WI#5, 164.9m).

b. Intense buff-coloured hyalophane-K-feldspar Stage III alteration (Cs-Hyl-Kfs) developed in a medium-bedded mudstone. No internal bedding structures are preserved. However, Stage IX pyrrhotite alteration is preferentially developed along stylolitic planes and in discordant vein sets that are associated with lensoidal and spotted pyrrhotite-sphalerite alteration (HS# 213, J718WD#5, 380.6m).

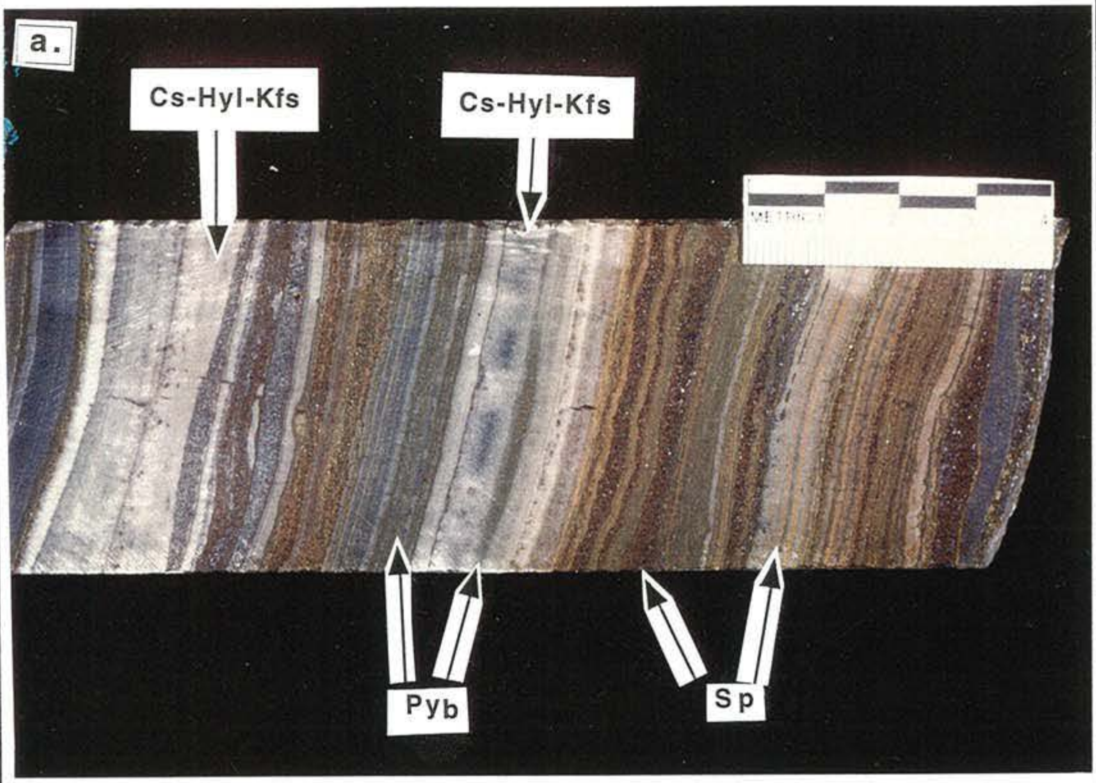
a.
Cs-Hyl-Kfs
Cs-Hyl-Kfs
Pyb
Sp

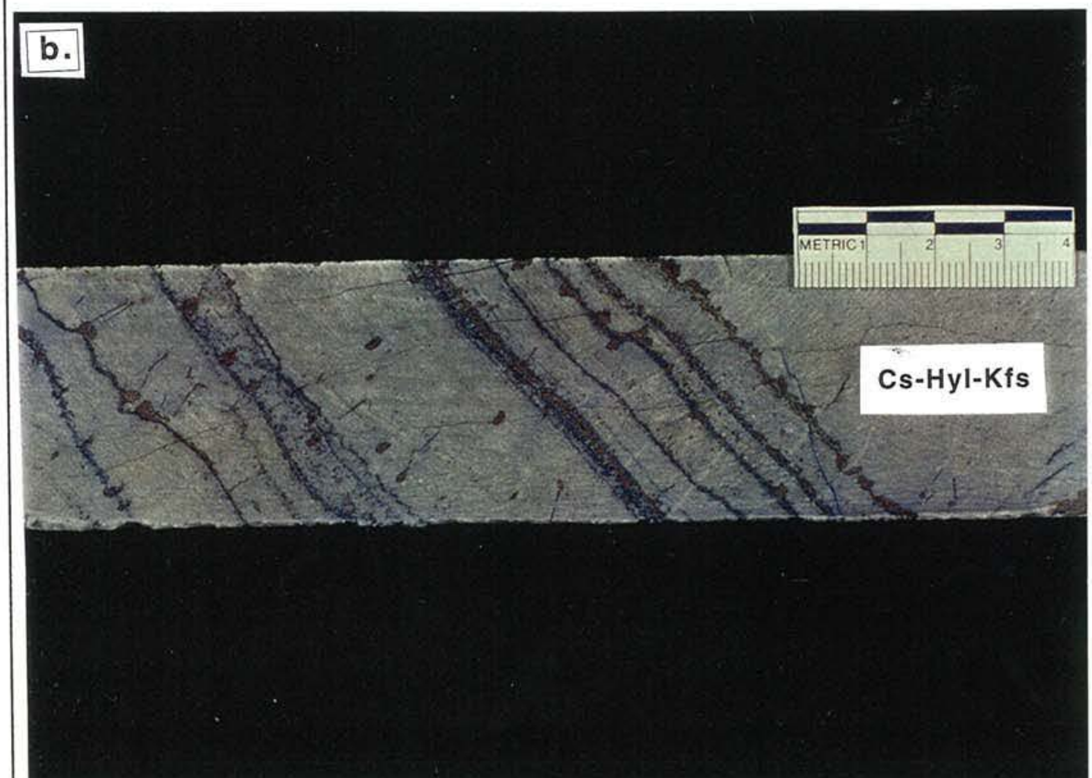
b.
METRIC 1 2 3 4
Cs-Hyl-Kfs

Figure 8.

a. Discordant vein sequentially infilled by Stage III celsian (Cs), hyalophane (Hyl), K-feldspar (Kfs) and calcite (Cal). Feldspars in this vein exhibit at least three growth zones distinguished by progressively decreasing Ba. The vein is developed in a ferroan dolomite-quartz-bearing banded mudstone (FeDol+Qtz) and is associated with diffuse hyalophane-K-feldspar alteration (Cs-Hyl-Kfs) within the wall rock (BSE image, HS# 253, J718WI#5, 166.9m).

b. BSE image illustrating paragenetic associations within a sphalerite breccia-vein. Earliest infill in the vein is Stage III hyalophane-K-feldspar zoned from a blocky K-feldspar core (black-Kfs) that is consecutively rimmed by relatively Ba-rich (light grey), Ba-poor (medium grey) hyalophane (Hyl). Feldspars are irregularly intergrown with calcite (Cal) and both are microbrecciated and/or replaced by Stage IV sphalerite (Sp). Stage IV hydrophlogopite laths infill within the sphalerite microbreccia zone (HS#251, J718 WI#5, 164.9m).

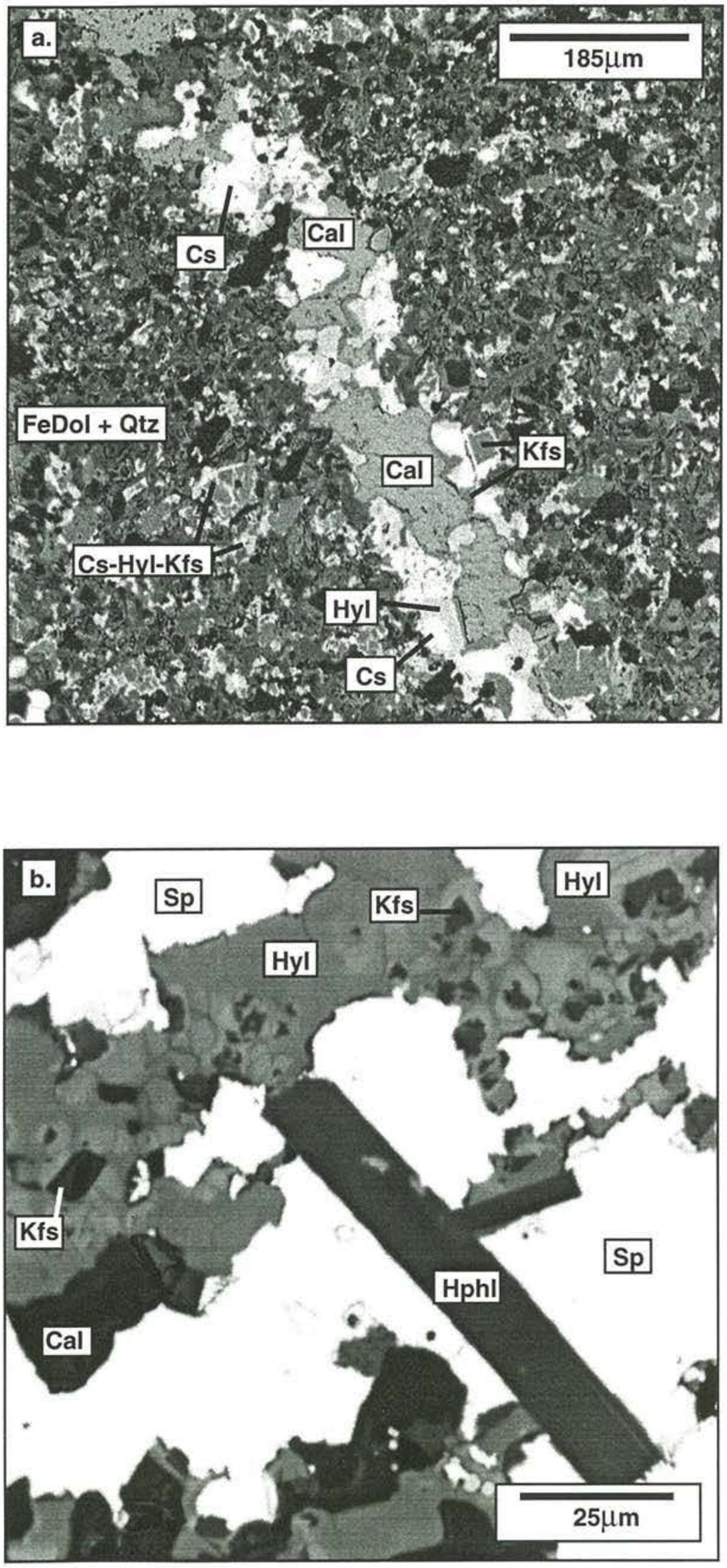
a.
185μm
Cs
Cal
FeDol + Qtz
Kfs
Cal
Cs-Hyl-Kfs
Hyl
Cs
b.
Sp
Kfs
Hyl
Hyl
Kfs
Sp
Hphl
Cal
25μm

Figure 8.

c. Hyalophane-K-feldspar alteration concentrated in a dolomitic banded mudstone (BM) rather than a rhythmically laminated pyritic siltstone (PS). Stage IV sphalerite (Sp) is superimposed on Stage III Ba-K-feldspar alteration at the base of the BSE image (Cs-Hyl-Kfs) (HS# 254b, J718 WI#5, 167.3m).

d. Ultrafine-grained celsian-hyalophane-K-feldspar (Cs-Hyl-Kfs) developed along spheroidal pyrite (Py_s), quartz (Qtz) and ferroan dolomite (FeDol) grain contacts (BSE image, HS# 251, J718 WI#5, 164.9m).

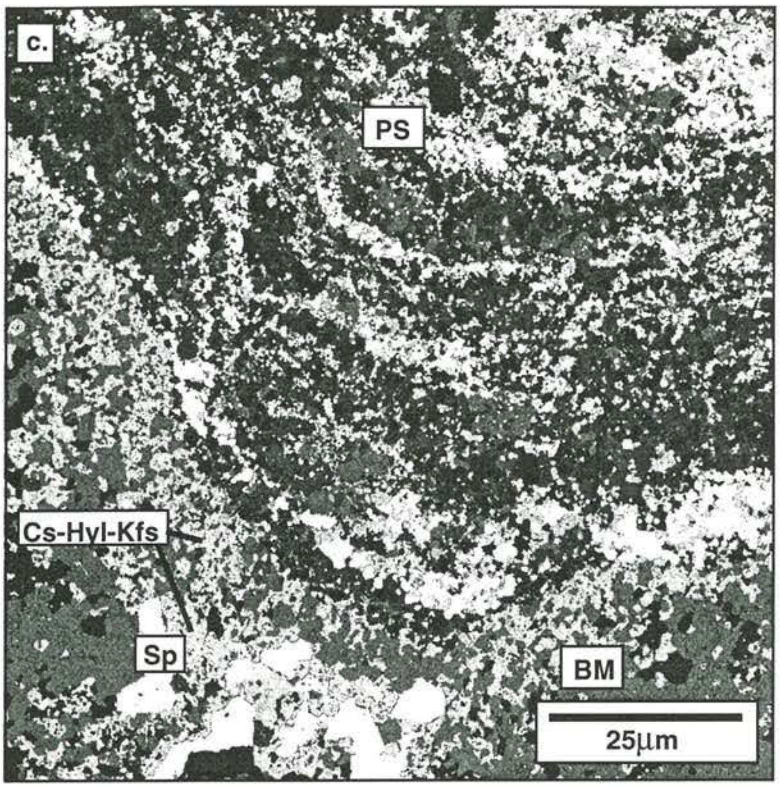
c.
PS
Cs-Hyl-Kfs
Sp
BM
25μm

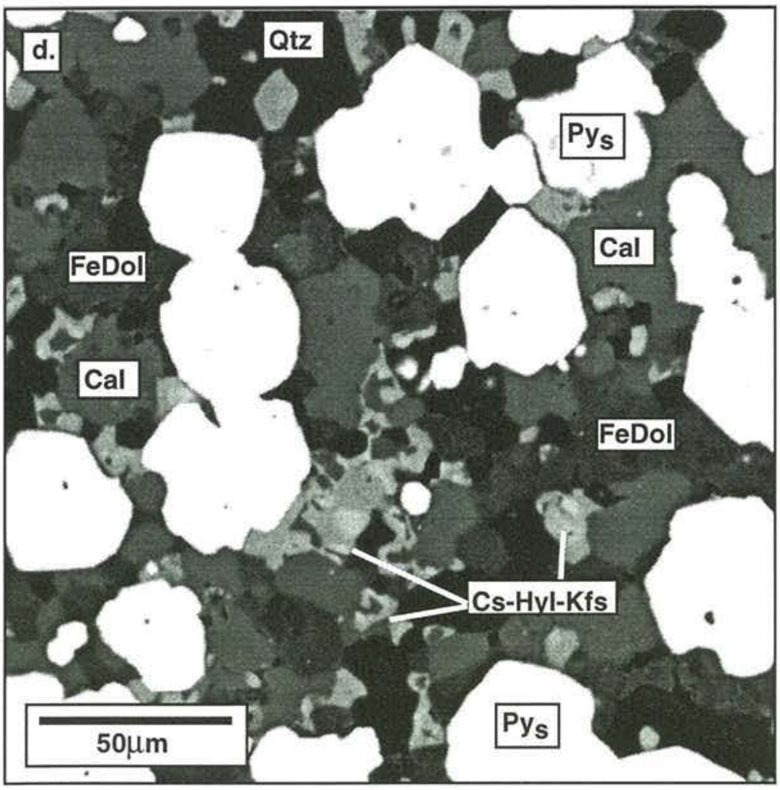
d.
Qtz
Pys
Cal
FeDol
Cal
FeDol
Cs-Hyl-Kfs
50μm
Pys

Figure 9.

a. Ultrafine-grained celsian-hyalophane-K-feldspar (Stage III, Cs-Hyl-Kfs) is developed in a calcite-altered (Stage I, Cal)) banded mudstone as preferential alteration of a coarse, elongate precursor. Brassy pyrite (Stage IVc) and sphalerite (Stage IVd) occur as preferential replacements of feldspars whilst minor spheroidal pyrite (Py_s) is disseminated throughout calcite (HS# 251, J718WI#5, 164.9m, XPL).

b. Calcite-celsian-hyalophane-K-feldspar-calcite vein (Cs-Hyl-Kfs, Cal) cross-cuts a stylolite bearing abundant spheroidal pyrite (Py_s). Brassy pyrite (Py_b) and sphalerite alteration is superimposed on the vein in the vicinity of the stylolite. The vein is developed in a ferroan dolomite-bearing banded mudstone (FeDol) (HS# 254b, J718WI#5, 167.3m, XPL).

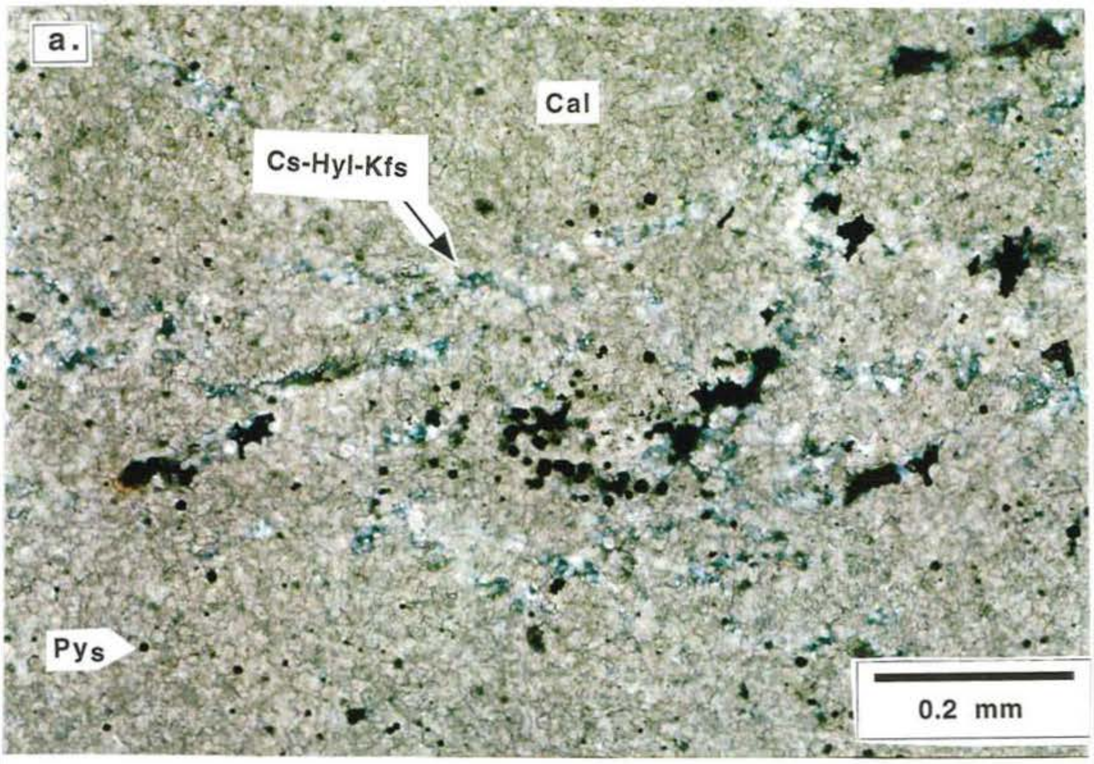
a.
Cal
Cs-Hyl-Kfs
Pys
0.2 mm

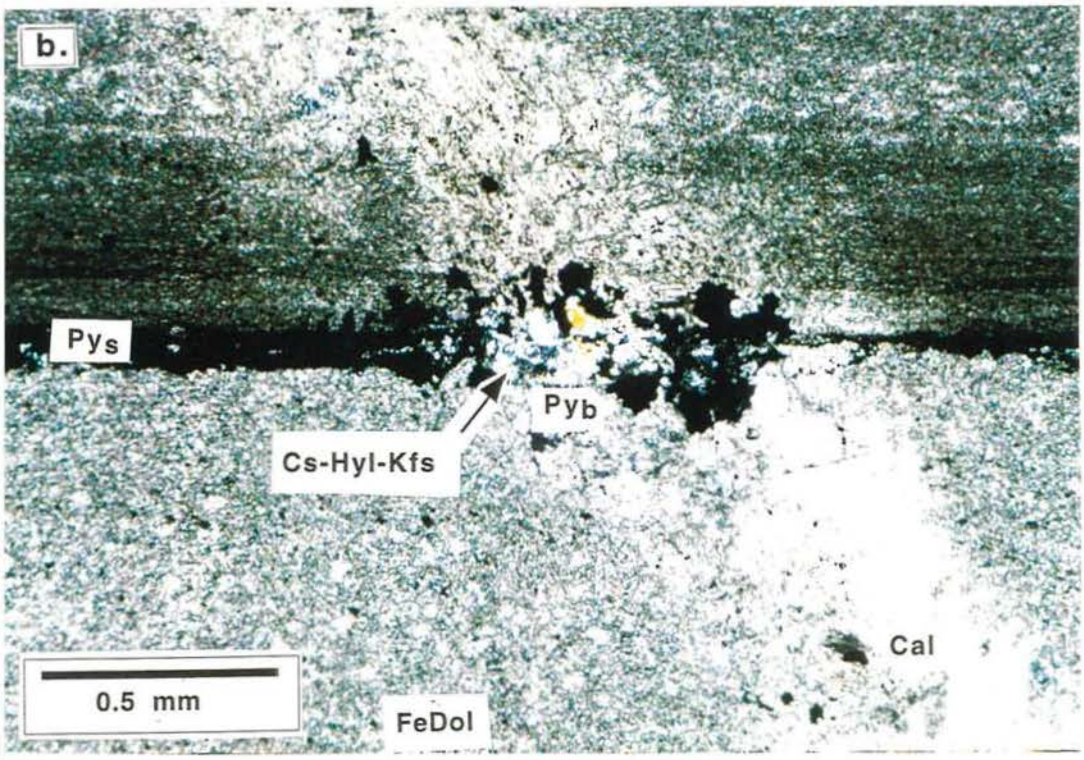
b.
Pys
Pyb
Cs-Hyl-Kfs
Cal
0.5 mm
FeDol

Figure 10.

a. Bitumen (Bit) and sphalerite (Sp) are intergrown and occur interstitial to carbonate and quartz in a banded mudstone bed (HS# 305, J730WI#1, 189.8m, refl.).

b. Stringers of brown migrabitumen (epi-impsonite, Bit) contain sphalerite, pyrite and galena inclusions in a shaly banded mudstone layer at the base of the photo. Sphalerite (Sp), galena (Gn), migrabitumen (Bit) and calcite appear to infill a vugh in the upper part of the photo (HS# 033d, J702WI#2, 55.4m, refl.).

c. Edge of a migrabitumen (epi-impsonite, Bit) -sphalerite (Sp)-brassy pyrite (Py) alteration zone (Stage IV) in a Stage I calcite-altered (Cal) mudstone bed (HS# 033d, J702WI#2, 55.4m, PPL).

d. Calcite - quartz - sphalerite (Sp) - brassy pyrite (Py_b) infill after fragmented solid migrabitumen (cata-impsonite, Bit). The latter is distinguished by the presence of devolatization pores. Stage II spheroidal pyrite (Py_s) is present in mudstone wall rock (HS# 117, J702WD#4, 141.1m, refl.).

e. Photomicrograph of textural zonation exhibited by meso-impsonite (second migrabitumen population, Bit). Cores (C) of fragmented grains are isotropic. Grain rims can be subdivided into three texturally distinct zones. The inner zone is defined by a fine pin-point anisotropy (1), that grades outwards into a coarse pin-point anisotropy (2). The outer rim forms sharp contacts with the latter and displays a coarse anisotropy and fibrous texture. The photograph was taken by P. Crosdale (HS# 086l, J710WI#1, 42.6m , refl-in oil).

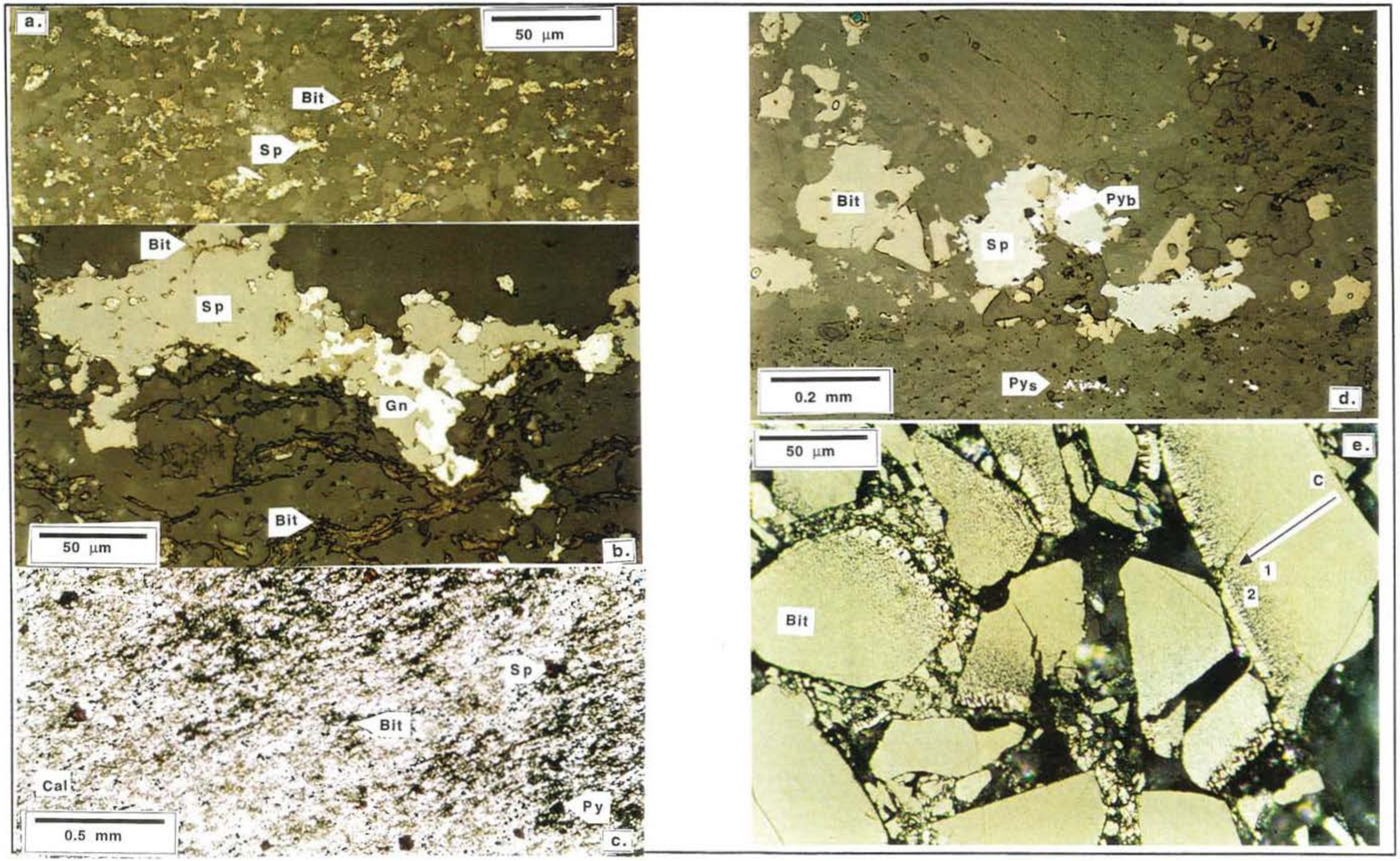
a.
50 µm
Bit
Sp
Bit
Sp
Gn
Bit
50 µm
b.
Sp
Bit
Cal
Py
0.5 mm
c.
Bit
Pyb
Sp
0.2 mm
Pys
d.
50 µm
e.
C
1
2
Bit

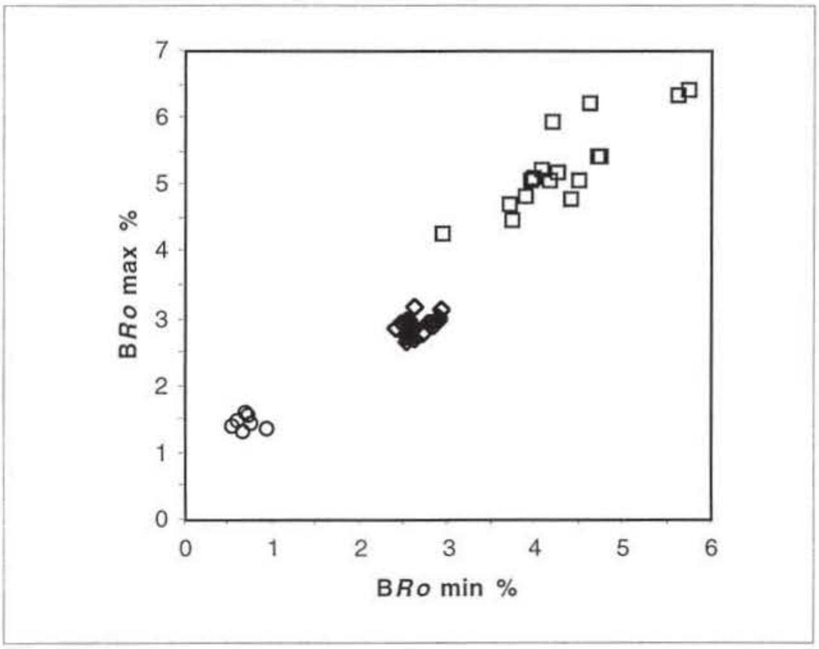

Migrabitumen - population 1

○ Epi-impsonite from shaly banded mudstone. n = 7.

Migrabitumen - population 2

□ Meso-impsonite from calcite-dolomite-quartz filled structure in I stratigraphic interval. n= 22

◇ Vein-hosted cata-impsonite. n= 18

Figure 11. Plot of Maximum versus minimum bitumen reflectance (in oil) for migrabitumen populations 1 and 2.

Figure 12.

a. A brassy pyrite alteration band (Py_b) is irregularly bounded by hydrophlogopite (Hphl) and contained within a sphalerite-rich band (Sp). The band is complexly folded. Note that spheroidal pyrite grains can not be distinguished in the band (HS# 260b, J718WI#5, 202.9m, PPL).

b. Semi-massive sphalerite (light grey) breccia contains coarse grained celsian-hyalophane-K-feldspar-calcite clasts (b) and microbrecciates adjacent pyritic wall rock (a). Euhedral brassy pyrite (Py_b) occurs as infill along clast margins and spheroidal pyrite is disseminated within wall rock (a). However, the bulk of the spheroidal and brassy pyrite in this field of view has been replaced by sphalerite to form atoll textures (HS# 063a, J702WI#5, 199.8m, refl.).

c. Photomicrograph illustrating paragenetic associations from an economic intersection containing breccia-vein hosted sphalerite. Semi-massive sphalerite (Sp) microbrecciates coarse-grained Stage III celsian-hyalophane-K-feldspar and calcite (Cal) and envelopes euhedral hydrophlogopite laths (Hphl). The majority of opaque inclusions within the main sphalerite band are pyrrhotite. Sphalerite-hydrophlogopite alteration is preferentially developed within a celsian-hyalophane-K-feldspar-celsian altered mudstone layer (BM) central to the sample (HS# 251, J718WI#5, 164.9m, PPL).

d. Sphalerite (Sp) occurs as extensive alteration of fine- to coarse-grained carbonate and celsian-hyalophane-K-feldspar in breccia-veins, and adjacent wall rock. The only indication of a precursor host rock in this sample is spheroidal pyrite (Py_s). Brassy pyrite (Py_b) is abundant to the left of the sample, hydrophlogopite (Hphl) occurs with sphalerite in breccia-veins and pyrrhotite inclusions are abundant in sphalerite (HS# 251, J718WI#5, 164.9m, refl.).

e. Photomicrograph of a sphalerite breccia-vein. Sphalerite microbrecciates and replaces Stage III celsian-hyalophane-K-feldspar (Kfs) and calcite (Cal). The majority of inclusions in sphalerite are pyrrhotite (Po) (HS# 251, J718 WI#5, 164.9m, refl.).

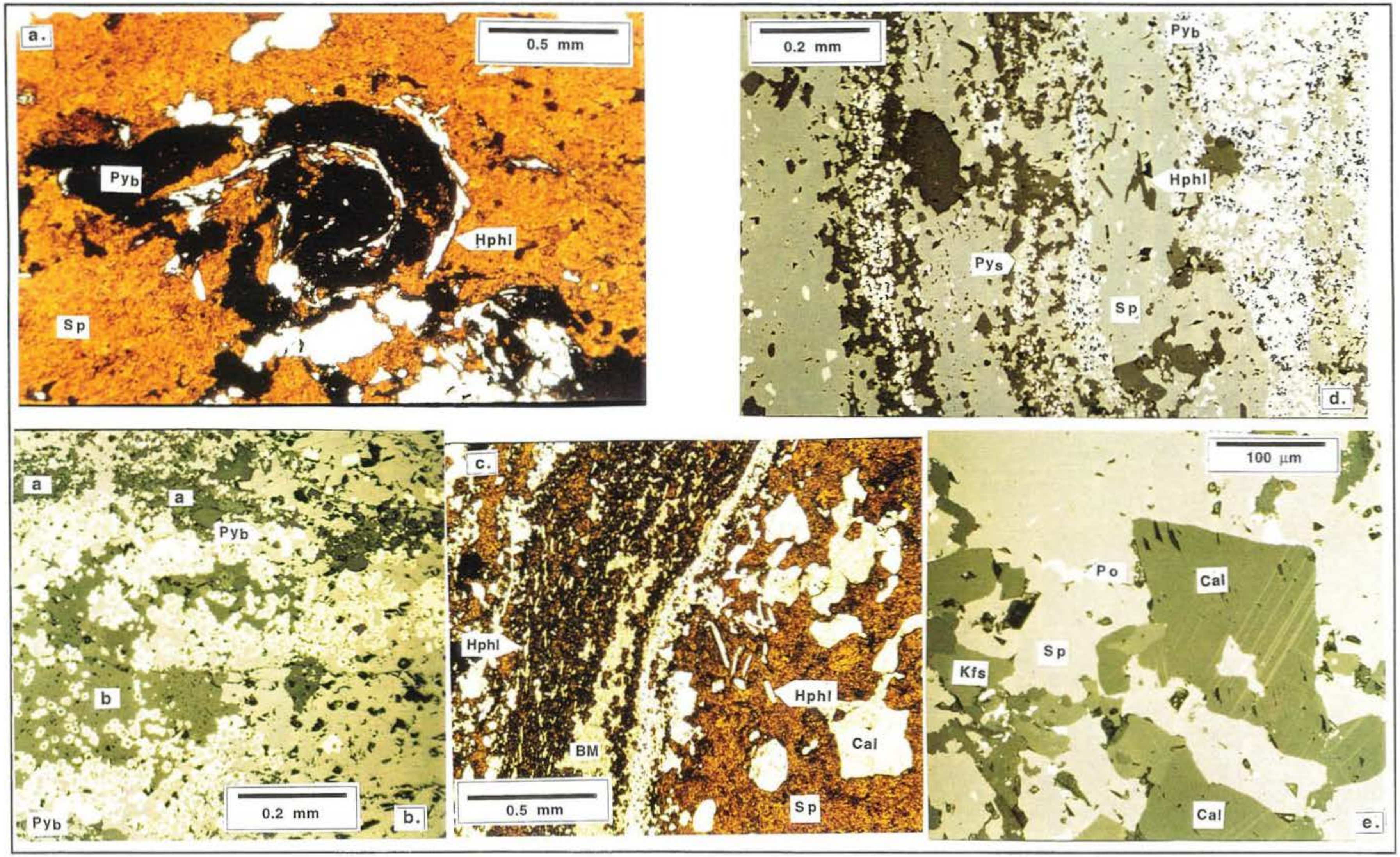

a.
0.5 mm
Pyb
Hphl
Sp
0.2 mm
Pyb
Hphl
Pys
Sp
d.
a
a
Pyb
b
0.2 mm
Pyb
b.
c.
Hphl
BM
Hphl
Cal
0.5 mm
Sp
100 µm
Po
Cal
Sp
Kfs
Cal
e.

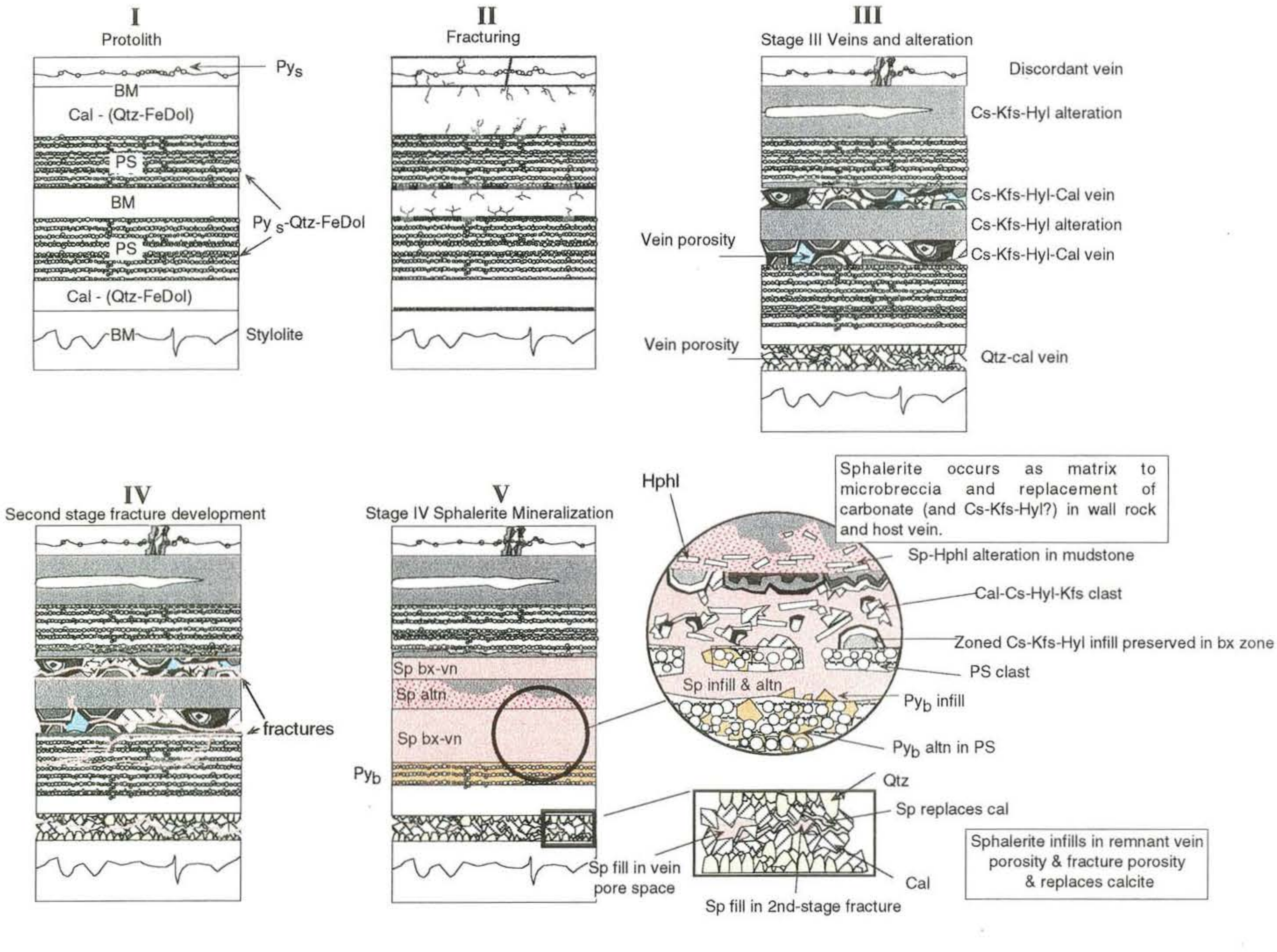

Figure 13. Proposed model for the paragenetic and structural evolution of Stage IV breccia-vein -hosted sphalerite (banded sphalerite) at George Fisher. The model depicts the formation of Stage III Cal-Qtz±Kfs±Hyl veins and the fundamental association between the two paragenetic stages. The 'protolith' to stage III and IV alteration has been subjected to stage I calcitization which has preferentially developed in mudstone bands, stylolitzation and Stage II spheroidal pyritization which is preferentially developed along carbonaceous horizons including styloiitic surfaces and laminations in rhythmically laminated siltstones.

Figure 14.

a. Warped Stage VI sugary ferroan dolomite vein set cross-cuts Stage IV stratiform sphalerite whilst clasts of the same material are included in a Stage V fine-grained sphalerite breccia (right). Coarse-grained sphalerite irregularly rims these clasts (HS# 248, J718WI#5, 158.4m, core width = 4.5cm).

b. Preferential development of folds, and irregular brecciation of a sugary ferroan dolomite vein in sphalerite bands. Sugary dolomite veins (FeDol) also cross-cut fine-grained sphalerite breccias in this sample (HS# 282, K782WI#1, 127.3m, core width = 4.5cm).

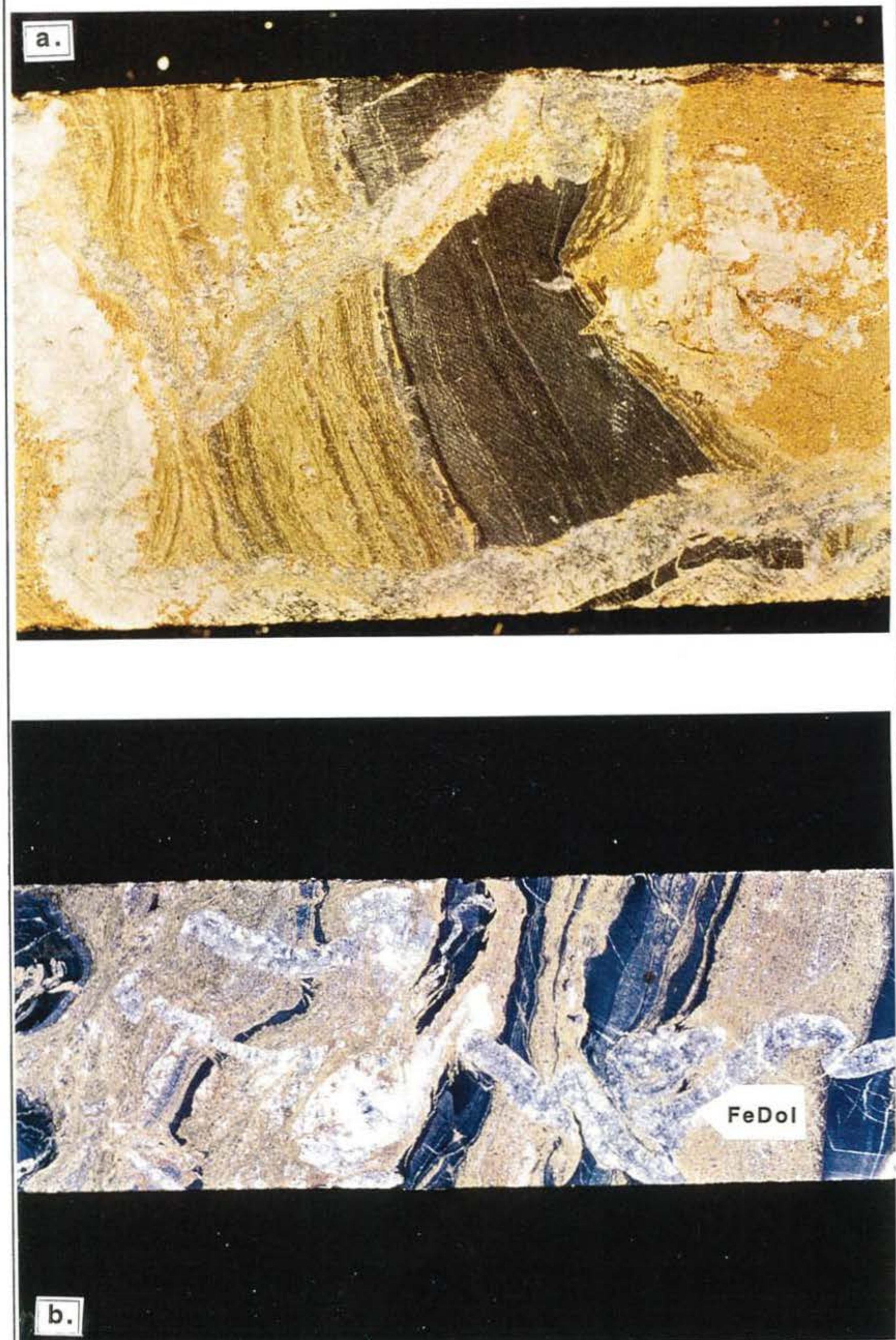
a.
b.
FeDol

Figure 15.

a. Coarse-grained galena breccia containing large clasts of banded and stratiform sphalerite (e.g. arrow). Discordant galena veins (Gn) brecciate celsian-hyalophane-K-feldspar altered mudstone clasts and wall rock (BM) and are structurally continuous with the main galena breccia (HS# 060g, J702WI#5, 183.4m).

b. Medium-grained galena breccia (Gn) is selectively developed in banded sphalerite and structurally continuous with discordant galena-sphalerite veins (Gn,Sp) in celsian-hyalophane-K-feldspar altered mudstone layers (e.g. BM). Galena breccia margins are irregular in this sample. Note the disharmonic folding exhibited by mudstone layers of different thicknesses (HS# 254a, J718WI#5, 167.1m).

c. Photomicrograph illustrating abundance of sphalerite clasts (Sp) in a medium-grained galena breccia. (HS# 143, J702 WI#6, 234.7m, refl.).

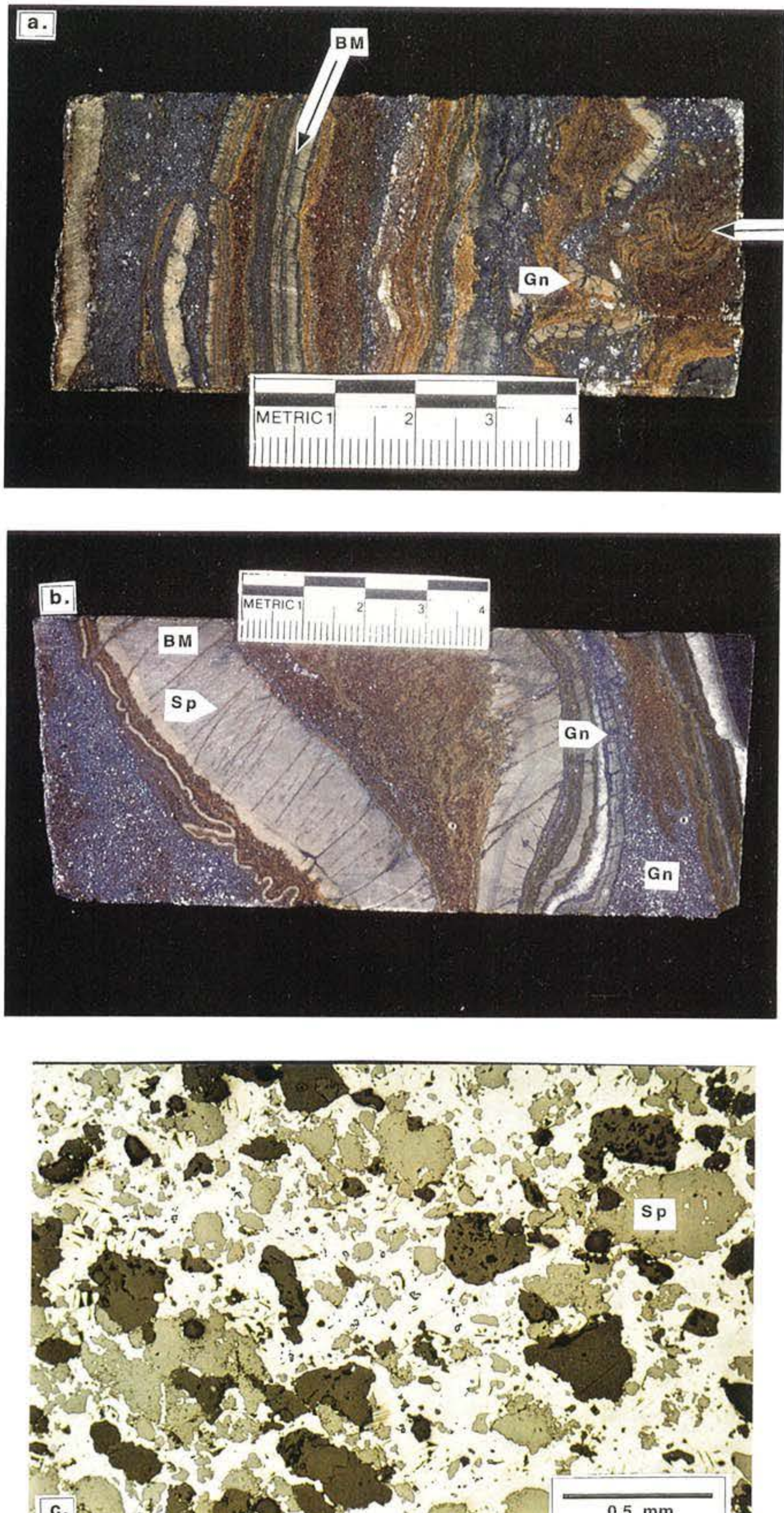
a.
BM
Gn
METRIC 1 2 3 4
b.
METRIC 1 2 3 4
BM
Sp
Gn
Gn
c.
Sp
0.5 mm

Figure 15.

d. Galena microbreccia contains fragments of sphalerite with ragged contacts. The large sphalerite fragment (Sp) appears to have been once continuous with adjacent clasts illustrating that at least a component of the galena occurs as infill. However, the imperfect fit of clasts and ragged nature of sphalerite fragments illustrates that galena also occurs as a replacement of sphalerite (HS# 143, J702WI#6, 234.7m, PPL).

e. Medium- to coarse-grained galena microbrecciates banded sphalerite (Sp). This microbreccia zone constitutes diffuse breccia margins seen in hand specimen (cf. Fig. 15b, HS# 143, J702 WI#6, 234.7m, refl.).

f. Photomicrograph illustrating interconnectivity of galena textural varieties. A medium-grained galena breccia (a) is preferentially developed in a sphalerite band. Mudstone-hosted galena (b) occurs as an alteration selvage to the breccia and discordant galena veins (c) developed in the mudstone layer are structurally continuous with the breccia (HS# 143, J702 WI#6, 234.7m, refl.).

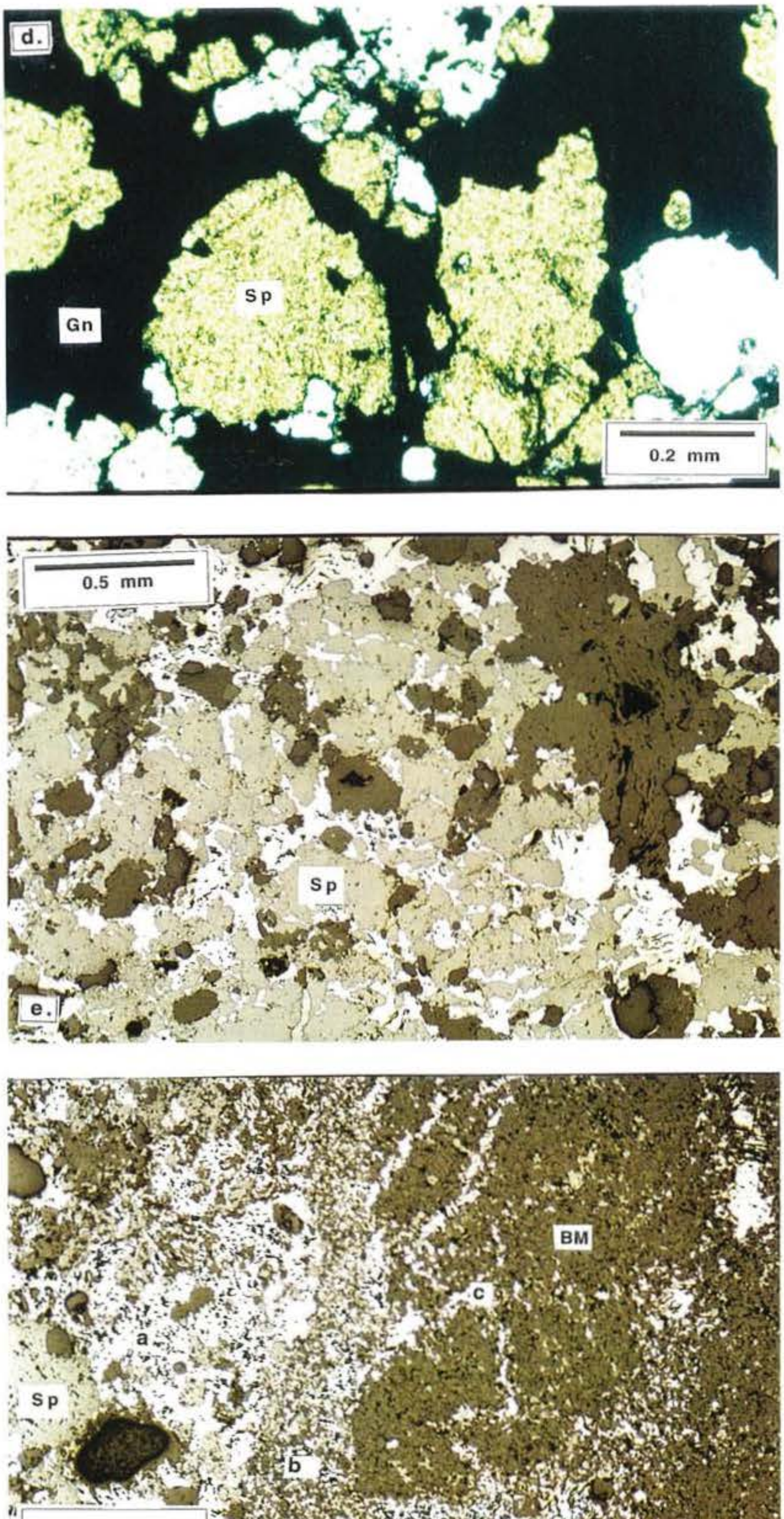
d.
Gn
Sp
0.2 mm
0.5 mm
Sp
e.
BM
c
a
Sp
b
0.5 mm
f.

Figure 15.

g. Fine-grained galena breccia contains elongate clasts of fine-grained sphalerite breccia (Sp, pale brown), angular carbonaceous mudstone fragments (black) and minor coarse-grained sphalerite clasts (Sp, red-brown). Thin discordant galena veins locally cross-cut clasts (e.g. Gn). Note that fine-grained sphalerite breccia and thin carbonaceous mudstones are major constituents of adjacent wall rock visible to the top right (HS# 150, J702WI#6, 244.5m).

h. Photomicrograph of a fine-grained galena breccia with abundant ultrafine sphalerite clasts (medium grey). Larger clasts are composed predominantly of carbonate (dark grey). However, the large rounded clast (left of centre) consists of sphalerite (Sp), celsian-hyalophane-K-feldspar, calcite and brassy pyrite. The composition of these clasts is equivalent to breccia-vein -hosted sphalerite illustrating that this galena breccia preferentially developed in a sphalerite-rich band (HS# 063a, J702 WI#5, 199.8m, refl.).

i. Galena (Gn)-yellow pyrite (Py_y)-pyrrhotite (Po) vein preferentially developed in a sphalerite band. The vein microbrecciates sphalerite and preexisting carbonate fragments. Galena, pyrite and pyrrhotite also occur as replacements of sphalerite (HS# 267a, J718WI#5, 248.2m, refl.).

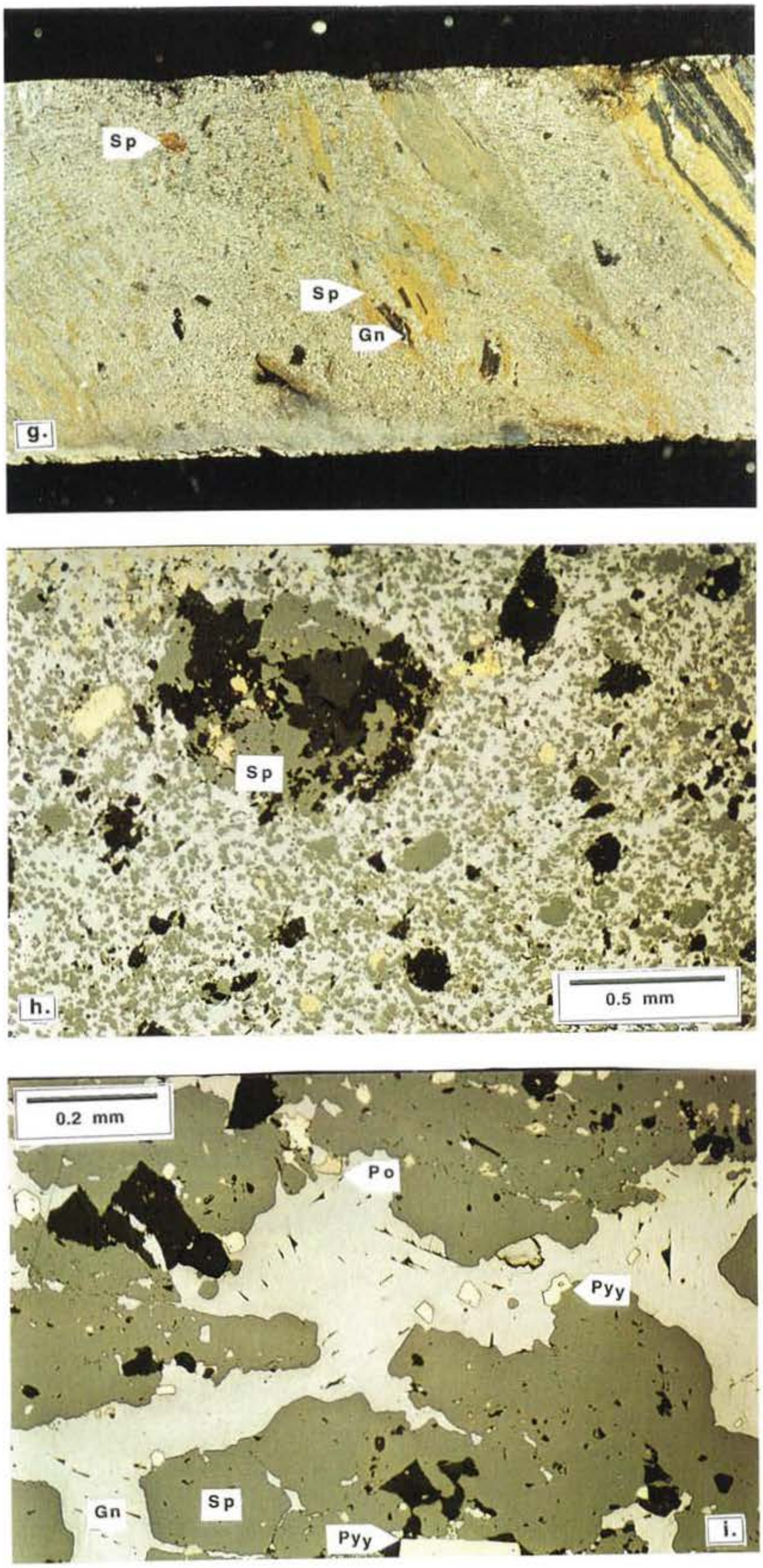
Sp
Sp
Gn
g.
Sp
0.5 mm
h.
0.2 mm
Po
Pyy
Gn
Sp
Pyy
i.

Figure 16.

a. Chalcopyrite veinlets (Cpy) superimposed on a deformed sugary ferroan dolomite vein and host rock. The sugary ferroan dolomite vein cross-cuts rhythmically laminated siltstone-hosted sphalerite. Pyrrhotite occurs predominantly as alteration preferentially developed along layering (e.g. Po) and is abundant throughout (HS# 276a, K766 WI#2, 241.2m).

b. Stage VIII Magnetite (Mt), chlorite, biotite and ankerite-siderite (Ank-Sid) alteration cross-cuts stratiform sphalerite. Stage VIII Fe-rich carbonate alteration zones are typically yellow/rust -coloured compared with buff-white celsian-hyalophane-K-feldspar alteration zones (HS# 310, J722 WI#2, 199.8m).

c. Pyrrhotite microbreccias (Po) developed along clast margins and bedding planes and cross-cut fine-grained sphalerite and coarse-grained galena breccias. Pale green chlorite-rich alteration (Chl) is pervasive in a mudstone interval left of the breccia zone (HS# 173b, J718 WD#5, 351.9m).

d. Biotite (Bt) and zoned celsian-hyalophane-K-feldspar (Cs-Hyl-Kfs) infill developed along alternate vein walls with pyrrhotite infill (Po) in the core of the vein. Pyrrhotite also microbrecciates zoned celsian-hyalophane-K-feldspar infill and wall rock. The wall rock to the left consists of ultrafine-grained celsian-hyalophane-K-feldspar and carbonate. Chlorite microbrecciates (Chl) celsian-hyalophane-K-feldspar-carbonate wall rock to the right of the vein (HS# 173a, J718 WD#5, 351.9m, XPL).

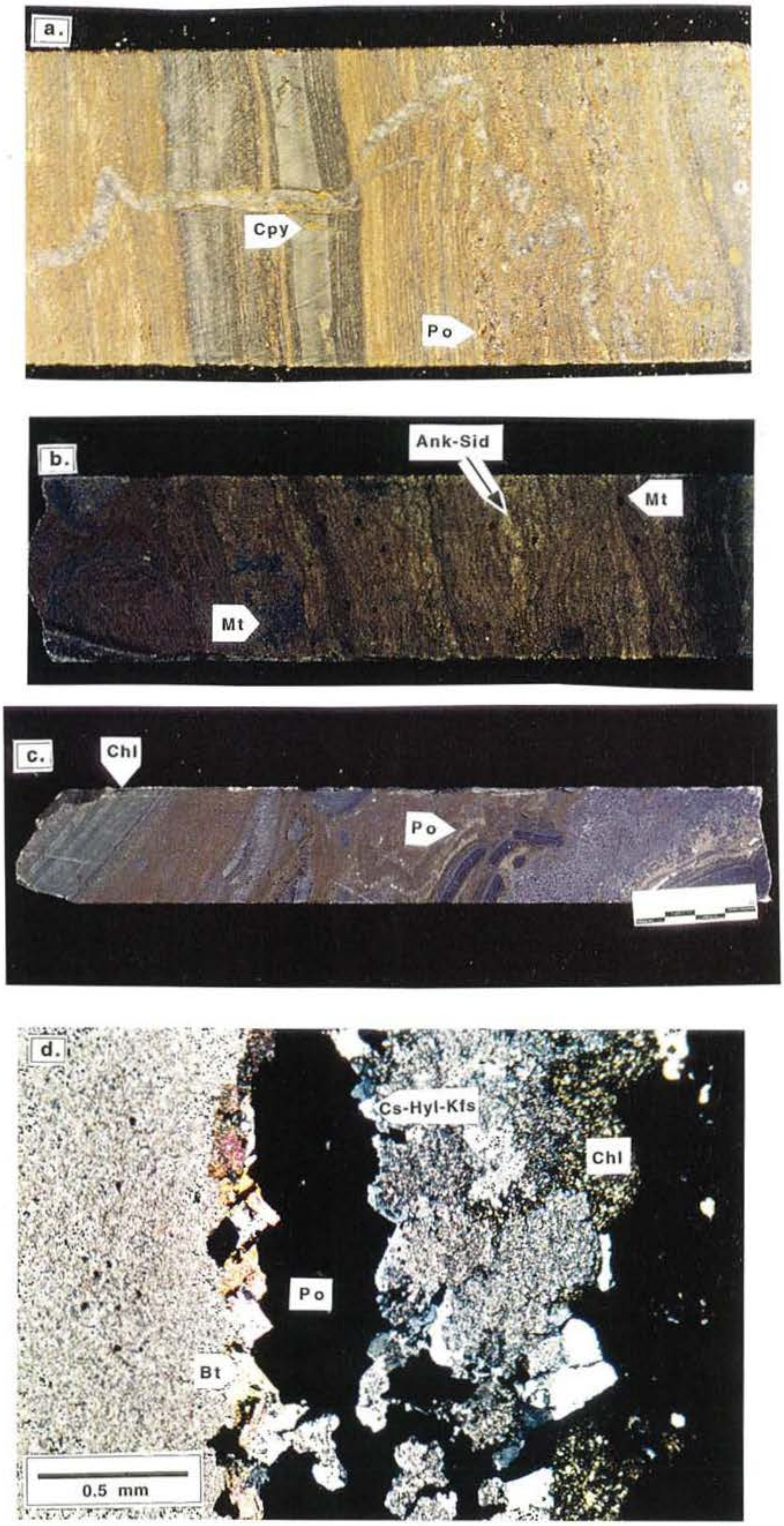
a.
Cpy
Po
b.
Ank-Sid
Mt
Mt
c.
Chl
Po
d.
Cs-Hyl-Kfs
Chl
Po
Bt
0.5 mm

Figure 16.

e. Photomicrograph of a lenticular pyrrhotite alteration pod as commonly observed at a hand specimen scale in mudstones. Pyrrhotite (Po) replaced biotite (pale brown) and coarse-grained carbonate in this case. Relatively coarse-grained Stage VIII red-brown sphalerite (Sp) and biotite (pale brown) alteration is dispersed through celsian-hyalophane-K-feldspar-carbonate wall rock (HS# 208, J718WI#3, 257.5m, PPL).

f. Stage VIII galena as selective replacement of Stage VIII biotite, both of which occur as an alteration selvage to a pyrrhotite vein (HS#173a, J718WD#5, 351.9m, refl.).

g. Ultrafine-grained carbonate-dominant (carb) and phengite+muscovite -dominant (Phg-Ms) alteration zones developed in a banded mudstone are spatially associated with a coarse grained pyrite-sphalerite-carbonate-chlorite vein set (e.g. Chl). The vein set has either displaced altered beds, or phyllosilicate alteration has preferentially developed in brecciated layers due to a preexisiting chemical heterogeneity (HS# 256, J718WI#5, 174m, XPL).

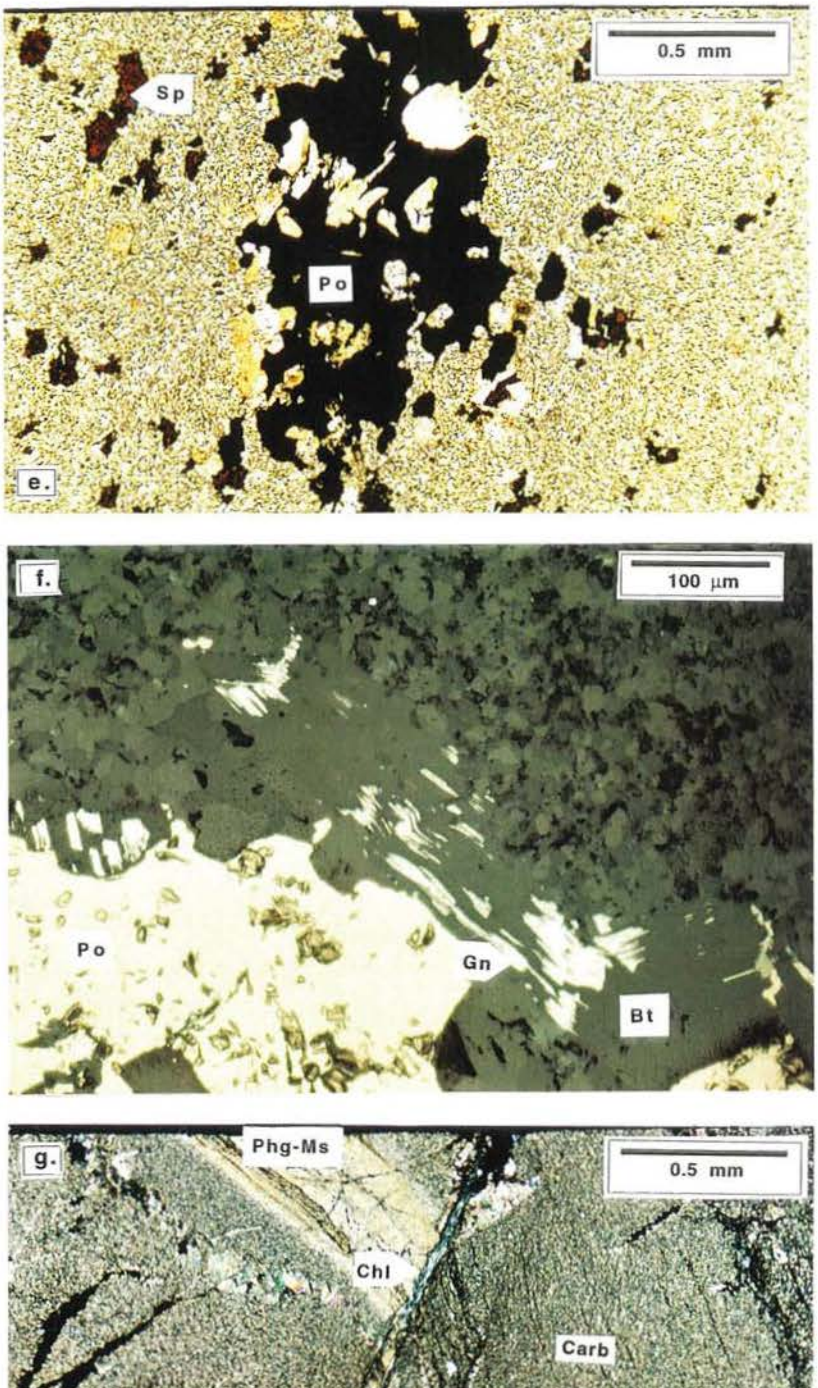
0.5 mm
Sp
Po
e.
f.
100 μm
Po
Gn
Bt
g.
Phg-Ms
0.5 mm
Chl
Carb

Figure 16.

h. Pyrrhotite (Po) and rare chalcopyrite lenses are preferentially developed in Stage I calcite-rich mudstones and layer-parallel white bands or as an alteration of brassy pyrite (Py_b) (HS# 88, J710WI#1, 89.6m).

i. Dark-coloured sphalerite enveloped and microbrecciated by irregular orange-brown sphalerite. Coarse-grained Stage VIII calcite (VIII-Cal) rims sphalerite alteration zones in a layer-parallel white band that otherwise consists of finer-grained Stage I calcite (I-Cal) (HS# 107, J702WD#4, 90.4m, PPL).

j. Inclusion-free, relatively coarse-grained Stage VIII sphalerite is rimmed by inclusion-free calcite (VIII-Cal) and occurs as an overgrowth on Stage IV sphalerite riddled with galena inclusions. Calcite rims abut a sphalerite-rich calcite layer (Cal) (HS# 090a, J710WI#1, 197.8m, PPL).

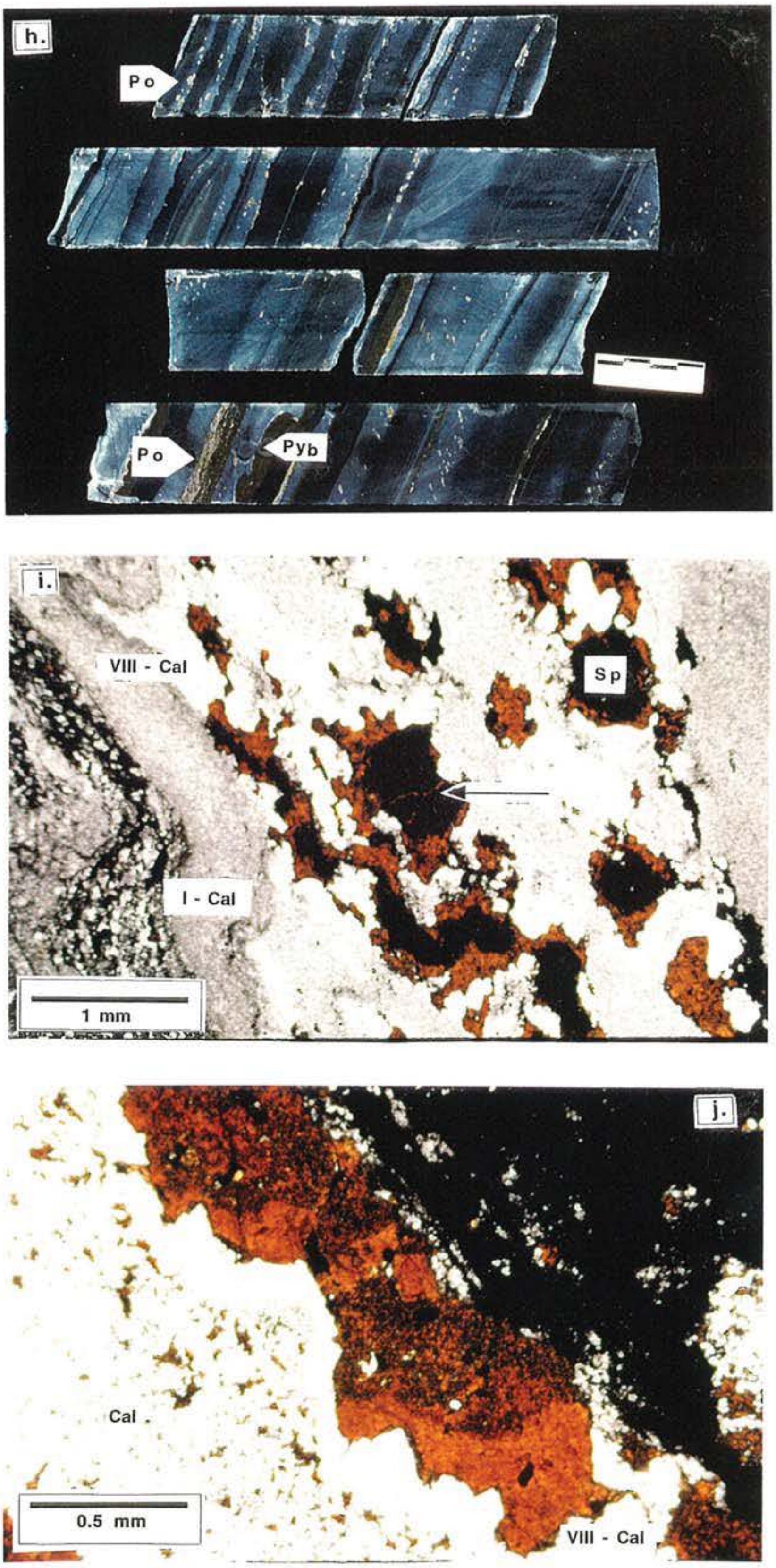
h.
Po
Po
Pyb
i.
VIII - Cal
Sp
I - Cal
1 mm
j.
Cal
0.5 mm
VIII - Cal

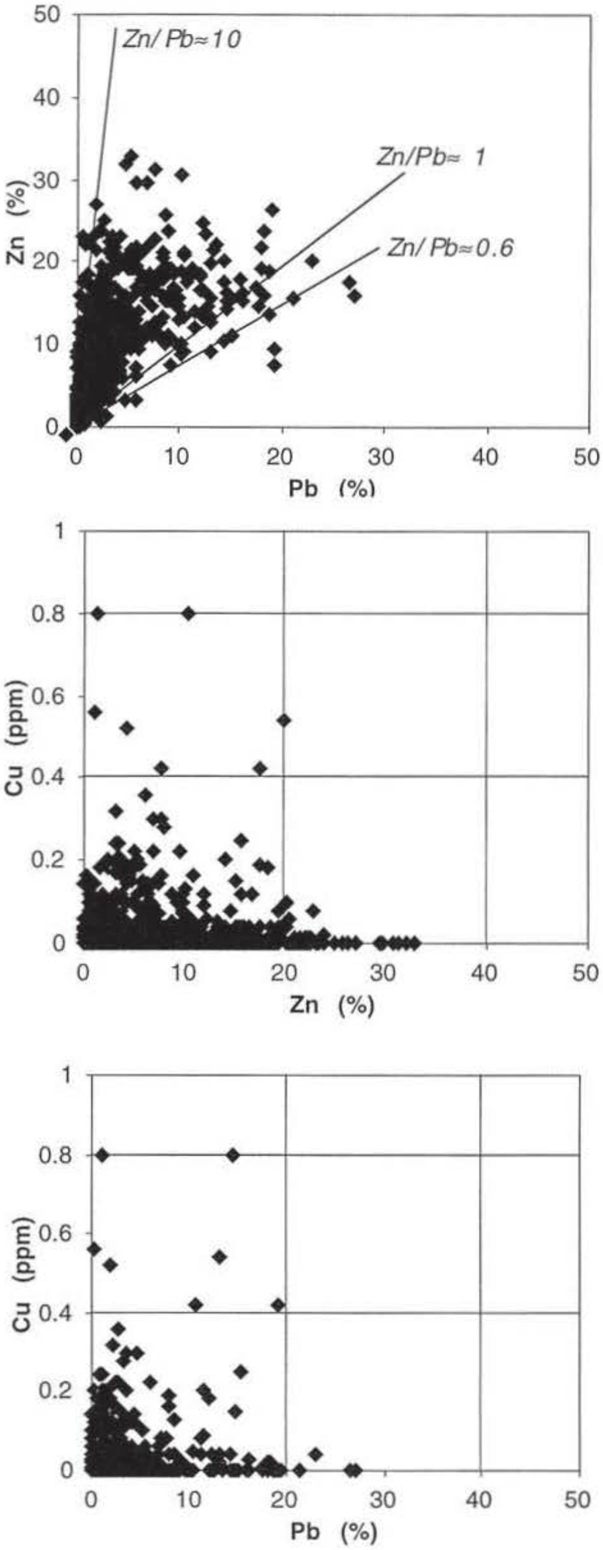

Figure 17a. Plots illustrating metal grade associations for Zn vs Pb, Cu vs Zn and Cu vs Pb derived from unpublished MIM Ltd assay data for diamond drill holes that were graphically logged as part of this study. Total number of samples points for each plot is 1766.

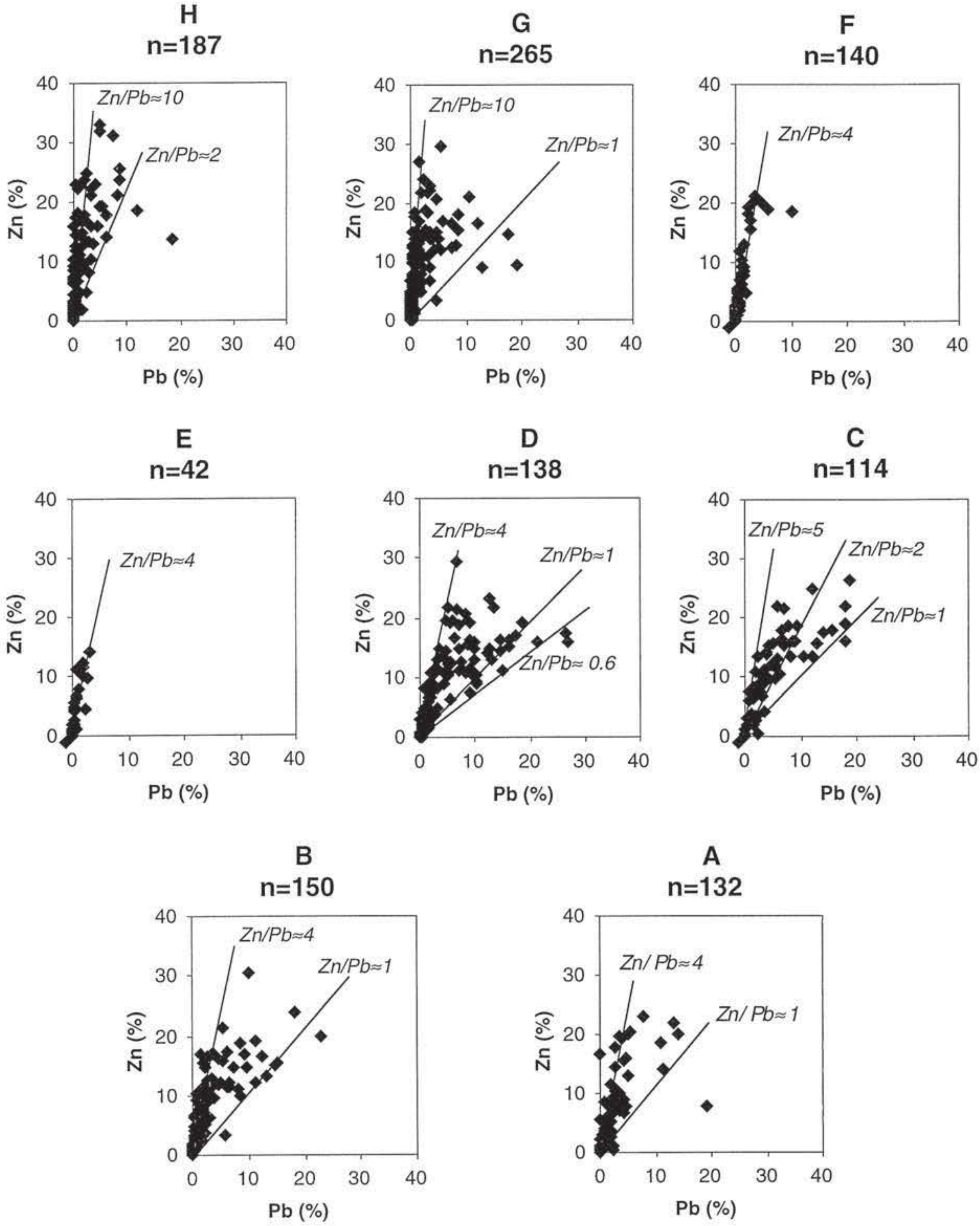

Figure 17b. Metal grade plots illustrating Zn vs Pb for the H through to A stratigraphic intervals and derived from the same diamond drillholes as represented in figure 17a (Unpub. MIM Ltd data).

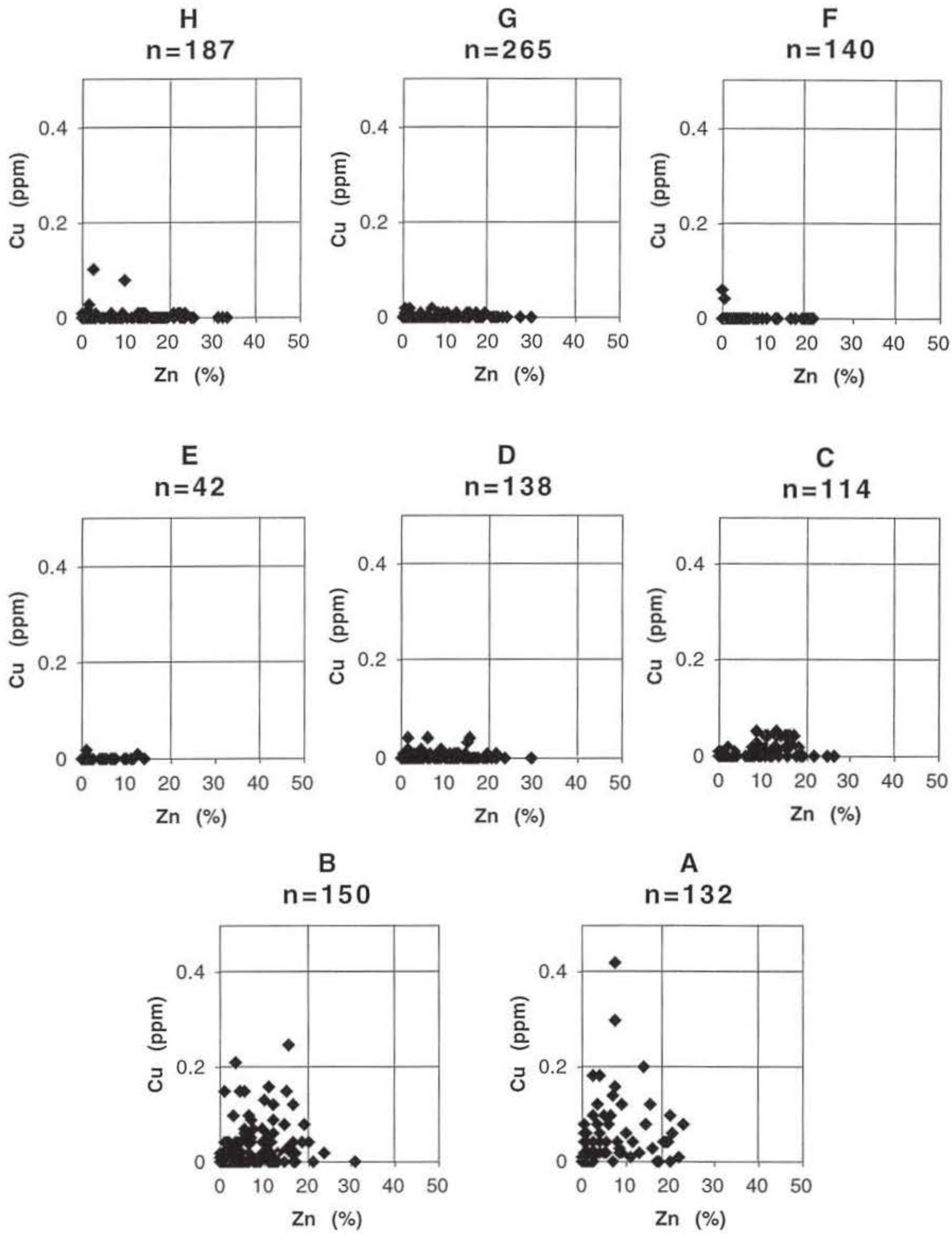

Figure 17c. Metal grade plots illustrating Cu vs Zn for the H through to A stratigraphic intervals and derived from the same diamond drillholes as represented in figure 17a (Unpub. MIM Ltd data).

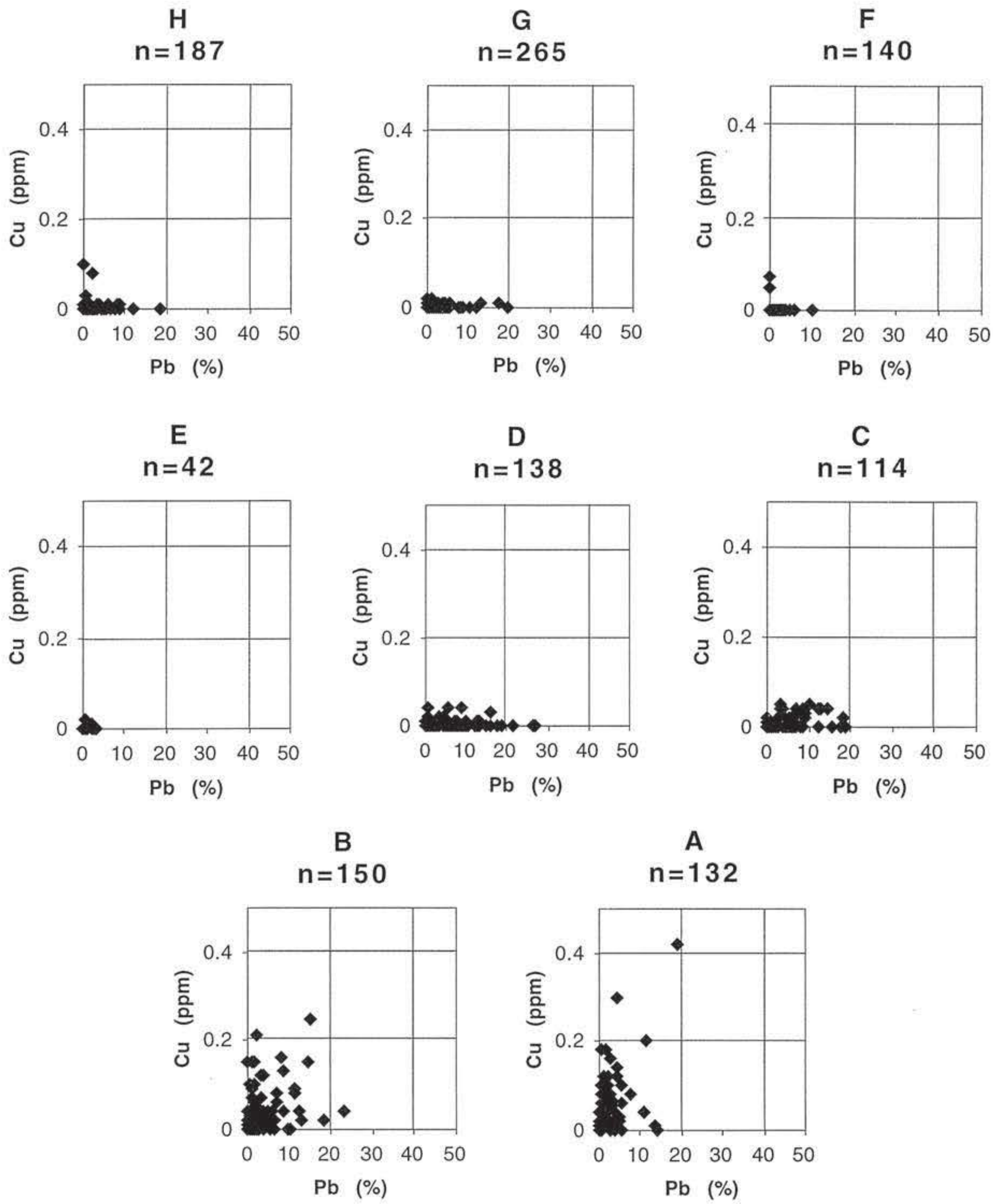

Figure 17d. Metal grade plots illustrating Cu vs Pb for the H through to A stratigraphic intervals and derived from the same diamond drillholes as represented in figure 17a (Unpub. MIM Ltd data).

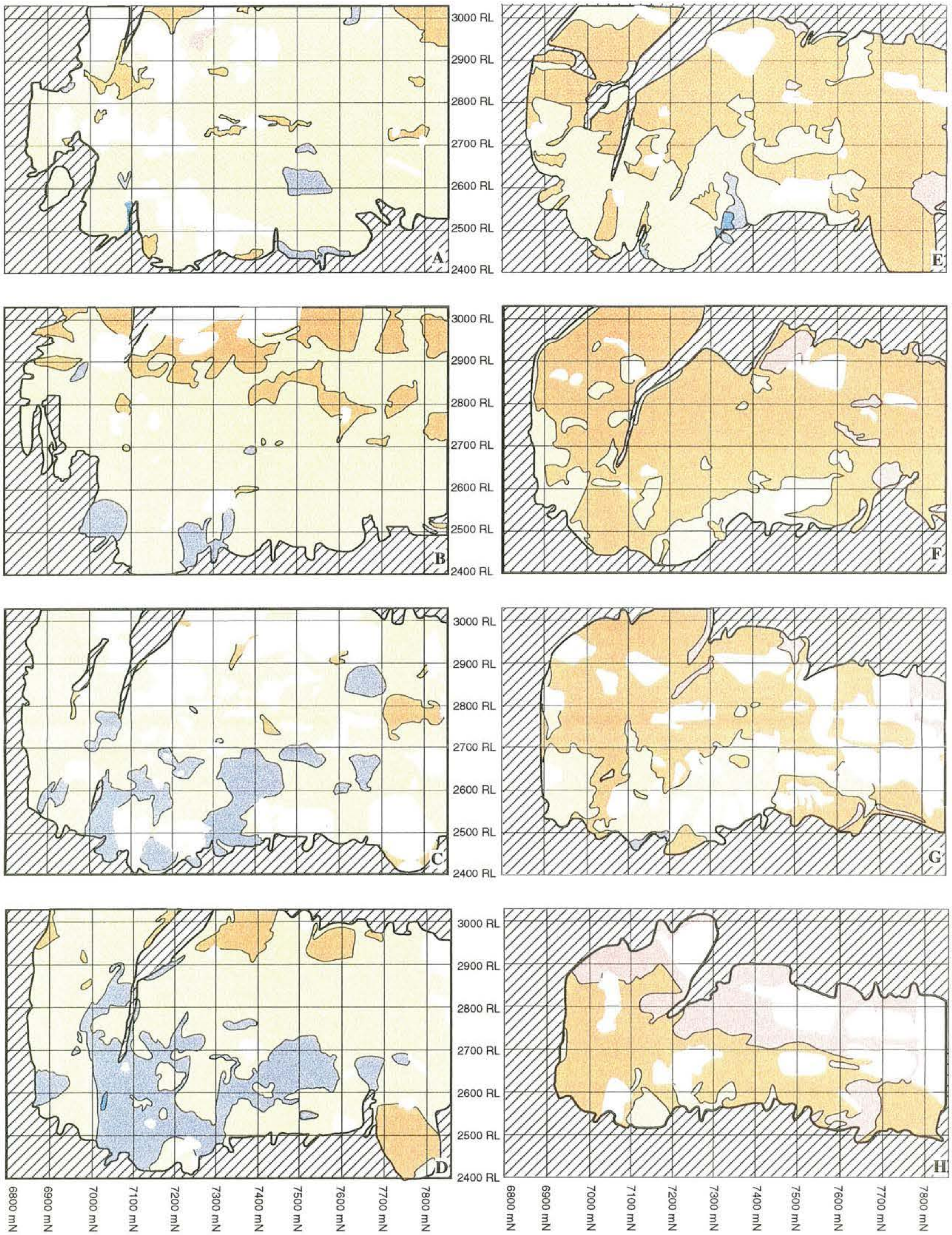

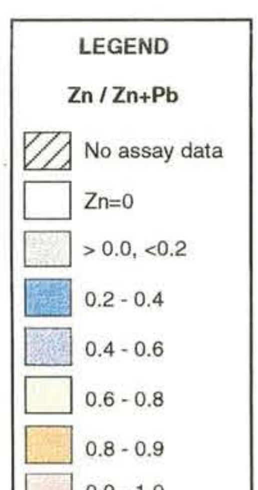

Figure 18a. Simplified longsections for A through to H stratigraphic ore-bearing intervals illustrating Zn/Zn+Pb. Zones with steep contour gradients are to fine to represent at this scale. Such zones are not outlined in black. Plots were derived by projecting ratio data for each respective interval from 6800mN to 7820mN (main economic zone) on to a vertical plane. Orebody outlines represent limit of assay data and are a true reflection of ore body shape. Areas with Zn=O represent undifferentiated fault windows and zones in which Zn and Pb levels were lower than the limit of analytical detection. Original plots were produced by S. Versace from unpublished MIM Ltd data.

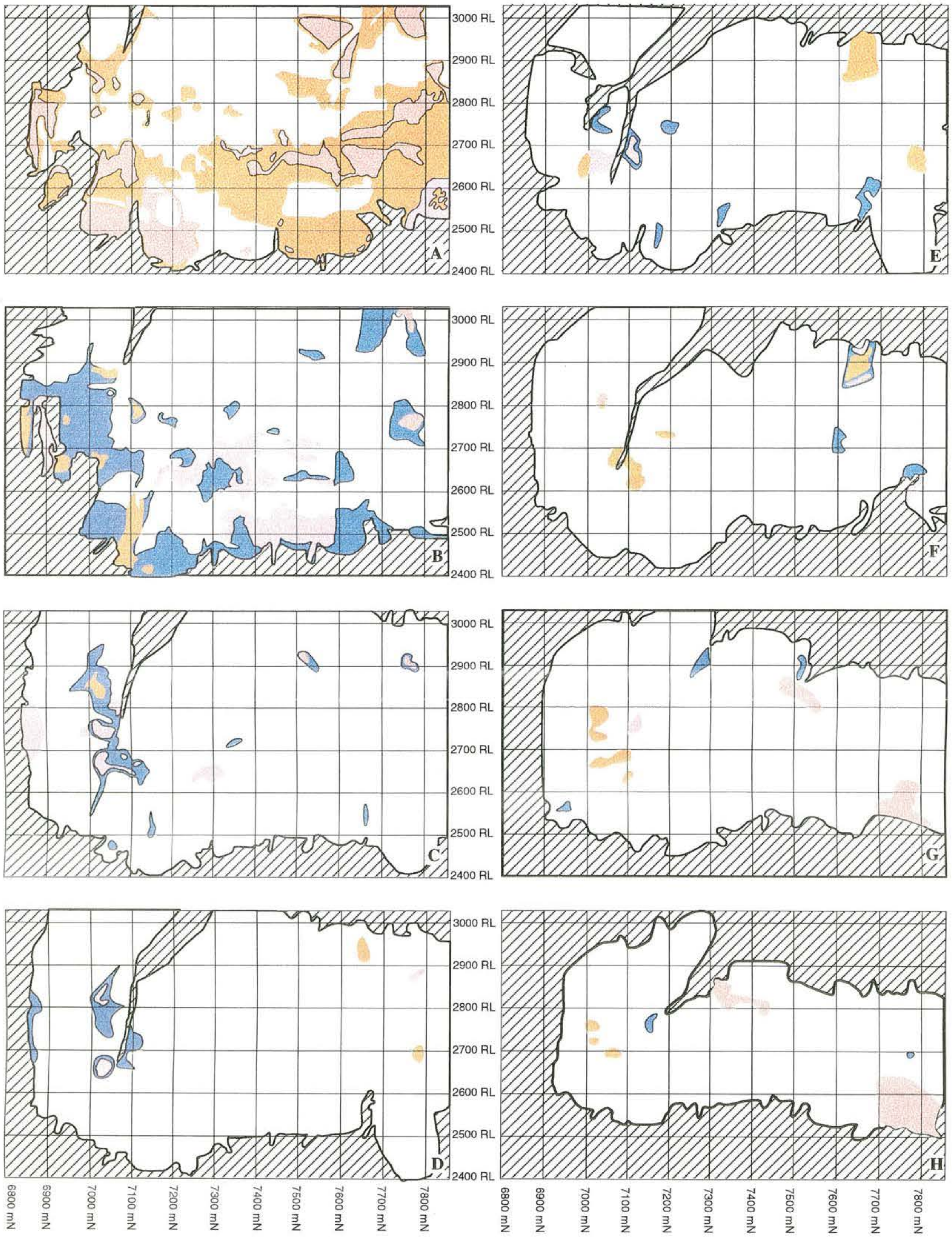

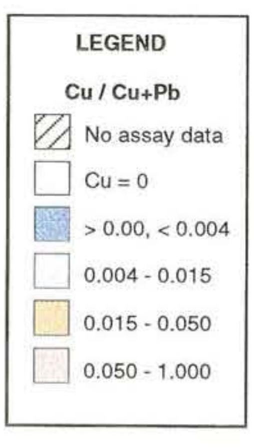

Figure 18b. Simplified longsections for A through to H stratigraphic ore-bearing intervals illustrating Cu/Cu+Pb. Zones with steep contour gradients are too fine to represent at this scale and are not outlined in black. Plots were derived by projecting ratio data for each respective interval from 6800mN to 7820mN (main economic zone) on to a vertical plane. Orebody outlines represent limit of assay data and are a true reflection of ore body shape. Areas with Cu=O represent undifferentiated fault windows and zones in which Cu levels were lower than the limit of analytical detection. Original plots were produced by S. Versace from unpublished MIM Ltd data.

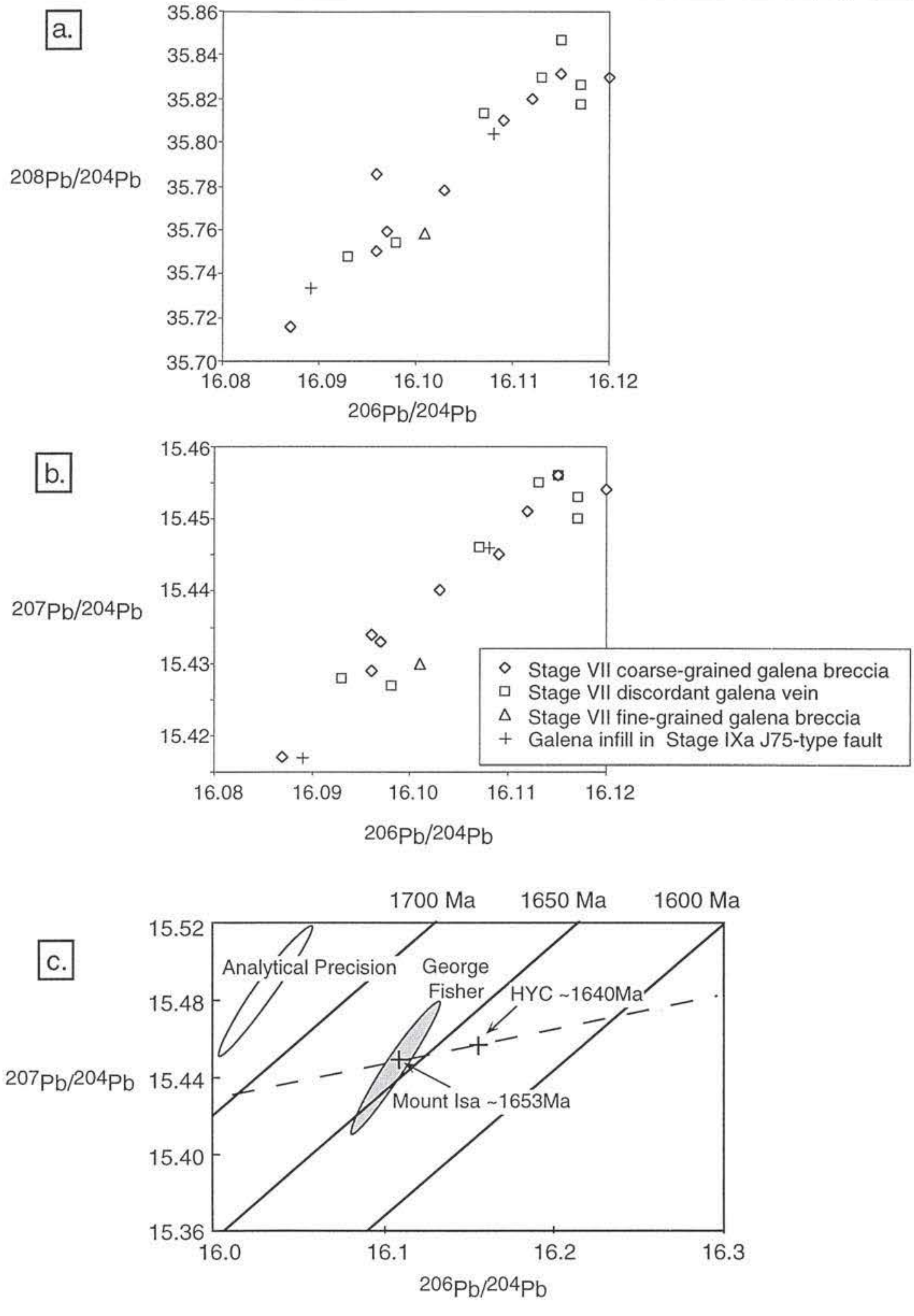

Figure 19. (a) Plot of $^{208}Pb/^{204}Pb$ versus $^{206}Pb/^{204}Pb$ for Stage VII and Stage IXa galena from a range of textural settings. (b) Plot of $^{207}Pb/^{204}Pb$ versus $^{206}Pb/^{204}Pb$ for the same samples. (c) Plot illustrated in (b.) superimposed on Pb-age model curve, and illustrating data for Mount Isa and HYC at McArthur River derived by Sun et al., (1994) for the Mount Isa Inlier and McArthur River area.

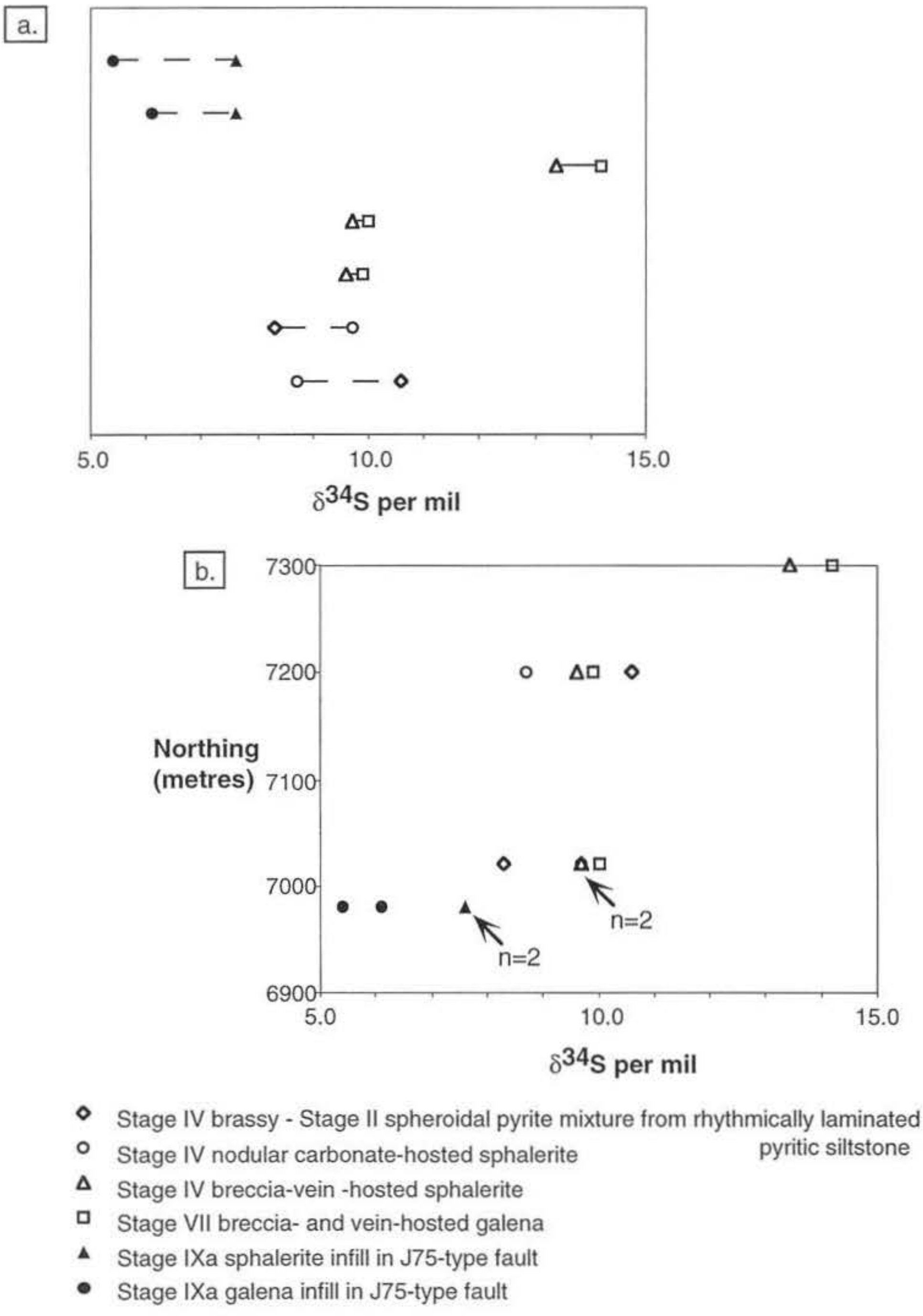

Figure 20 . (a) Plot of $\delta^{34}S$ for adjacent samples.
(b) Plot of $\delta^{34}S$ and sample location with respect to northing.

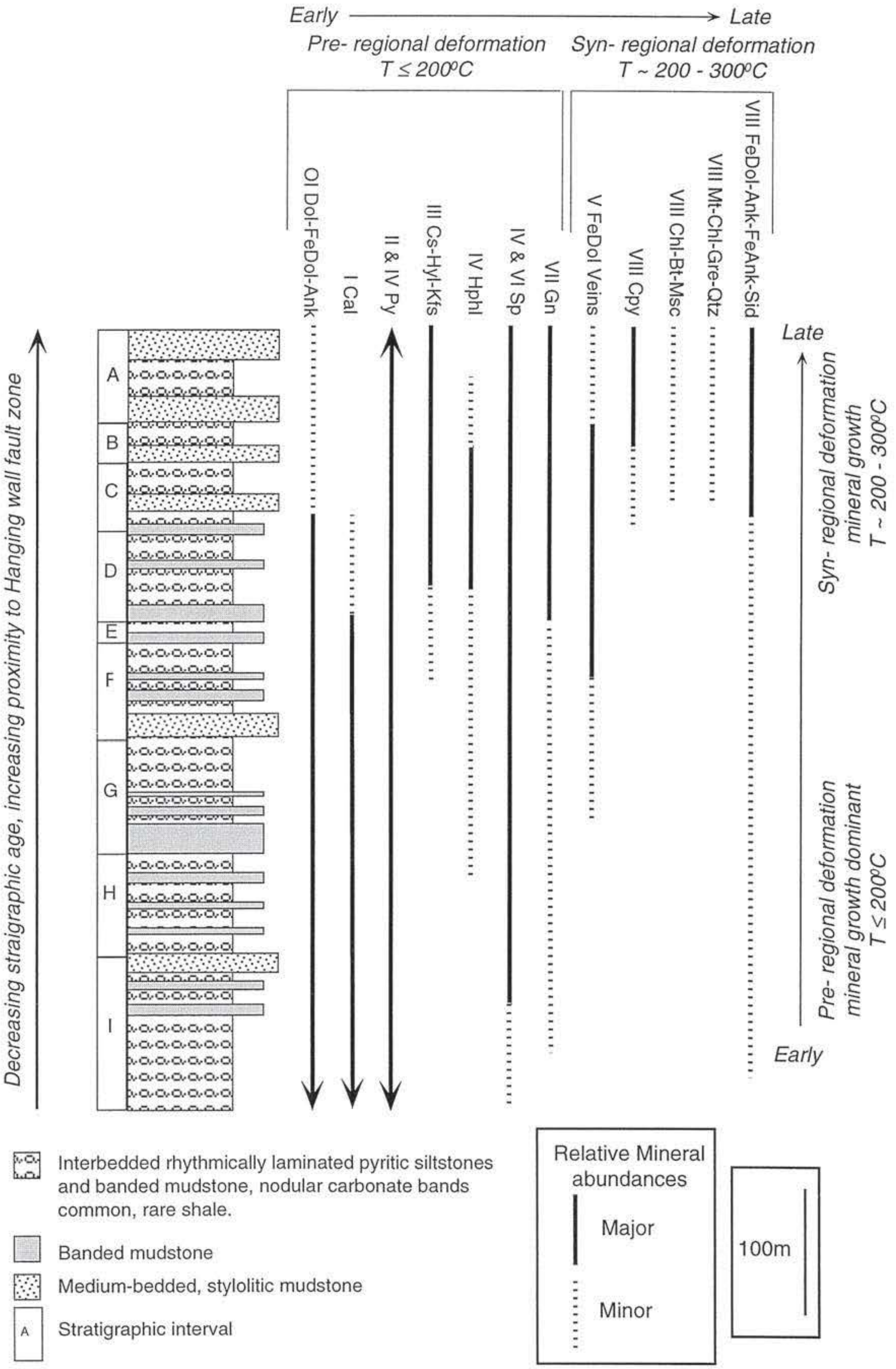

Figure 21. Schematic stratigraphic column and mineral distribution logs illustrating spatial-temporal-temperature zonation patterns at George Fisher.

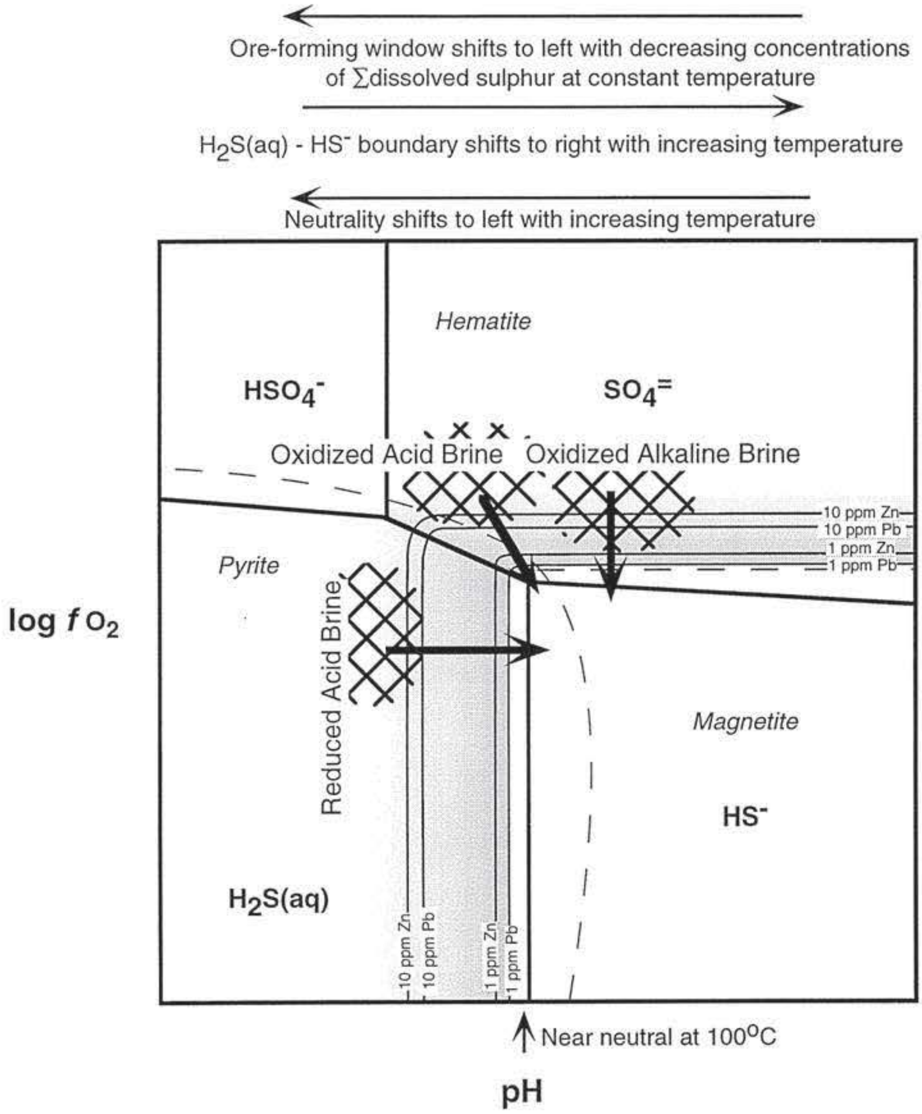

Figure 22. Cartoon Log$f$O$_2$-pH diagram illustrating approximate stability fields for aqueous sulphur species and iron mineral stability fields relative to metal solubility contours. The shaded area defines the window of fluid compositions that are considered capable of transporting ore-forming quantities of metals. Hatched zones approximate fluid compositions estimated for reduced acid brines carrying metal as chloride complexes (Sverjensky, 1984), slightly oxidized brines carrying metals as chloride or organic complexes (e.g. Anderson, 1975, Giordano, 1992, Cooke and Large, 1998) and oxidized alkaline brines (Cooke and Large, 1998). Arrows illustrate pathways of metal precipitation (cf. Table 3). Adapted from Anderson (1973), Anderson (1975), Giordano and Barnes (1981), Sverjensky (1984), Giordano (1992), Cooke and Large (1998).

PART C

Carbonate type	Location	Interpretation	Reference
Dolomite and ferroan dolomite micrite as a major constituent of Urquhart Shale mudstones and siltstones.	Mount Isa area, distal to Pb-Zn	Endogenic intrabasinal carbonate mud.	Neudert (1983)
Dolomite-ankerite microspar in association with Zn-Pb mineralization.	Mount Isa Zn-Pb ore bodies	Carbonate recrystallization during metamorphism. Metasomatic	Van den Heuval (1969) Blanchard and Hall (1942)
Siderite as constituent of mudstones in association with Zn-Pb mineralization.	Mount Isa Zn-Pb ore bodies	Sedimentary-diagenetic	Swager et al. (1987)
Calcite as a constituent of Urquhart Shale mudstones and siltstones	Lower Urquhart Shale - peripheral to Mount Isa Mine Upper Urquhart Shale - peripheral to Mount Isa Mine	Meteoric diagenetic cement Metasomatic	Neudert (1983) Neudert (1983)
Calcite as a constituent of Urquhart Shale mudstones and siltstones	Mount Isa Mine and Urquhart Shale distal to Mount Isa.	Metamorphic calcite as product of Kfs + Dol ↔ Phl + Cal decarbonation reaction.	Waring (1990a), Waring et al. (1998).
Nodular carbonate	Mount Isa and Hilton Mines - Nodular dolomite	Syntectonic hydrothermal carbonate alteration related to Cu mineralization.	Perkins (1997) - Mount Isa, Perkins and Bell (1998) - Hilton
Nodular carbonate	Mount Isa Mine and Urquhart Shale distal to Mount Isa - Nodular dolomite and calcite	Hypersaline, shallow water to emergent depositional environment. Sabkha-type sulphate evaporite pseudomorphs.	Neudert (1983)
Nodular carbonate	Hilton and George Fisher - Nodular dolomite and calcite	Deep water, depositional environment. Subaqueous and displacive -type sulphate evaporite pseudomorphs.	Clark (1993)
Layer-parallel, white carbonate bands	Mount Isa Mine and Urquhart Shale distal to Mount Isa.	Metamorphic calcite as product of Kfs + Dol ↔ Phl + Cal decarbonation reaction.	Waring (1990a), Waring et al. (1998).
Layer-parallel, white carbonate bands	Mount Isa Mine and Urquhart Shale distal to Mount Isa	Supratidal Carbonate crusts.	Neudert (1983)
Layer-parallel, white carbonate bands	Hilton and George Fisher	Sulphate evaporite layers pseudomorphed by carbonate.	Clark (1993)

Table 1. Summary of previous interpretations on the origin of Urquhart Shale host rock carbonate constituents.

Table 2. Modified paragenesis of the George Fisher deposit with emphasis on carbonate evolution. 1. Peak temperature estimates for metamorphism based on migrabitumen reflectance data (Part B). 2. Hydrothermal temperature of copper event based on phyllosilicate associations (Part B). Refer to Part A for explanation of age constraints. ↗ = carbonate phase dissolution or replacement, x = carbonate recrystallization, ← - - = deformation of Stage IV sphalerite and galena. Dolomite textural classification after Sibley and Gregg (1987). PL-S = subhedral grains with planar grain boundary contacts, PL-E=euhedral crystals, Npl=non-planar grain boundary contacts, Matrix-R=matrix is replacive in origin.

Stage	HR	OI	I	STY	II	III	IV	V	VI	VII	VIII
Detrital quartz	—										
Organic detritus	—										
Detrital mica	- - -										
Detrital feldspar	- - -										
Detrital dolomite	- -?- -	↗	↗	↗							↗ x
Dolomite - PL-S, matrix-R, cement?		—a—↗	↗	↗				x			↗ x
Ankerite - PL-E & NPL, matrix-R		-b—↗ —d—	↗	↗				x			↗ x
Ferroan dolomite - PL-E & NPL, matrix-R		- - -b_2— c —d—	↗	↗		- - -		x			↗ x
Calcite -NPL, matrix-R: PL-E void fill			—	↗		—					↗ x
Calcite nodules in mudstones			—	↗							
Pyrite alteration					—Py_s—		—Py_b—			—Py_y—	
Ba K-feldspar S_0//vein infill & alt.						—					
Ferroan dolomite - S_0//vein infill,						—					↗
Calcite - S_0//vein infill						—					↗
Migrabitumen emplacement							—				
Hydrophlogopite							—				
Sphalerite							—	←- -	←- -	←- -	—
Galena							—	←- - -	←- - -	←- - -	—
Sugary ferroan dolomite - vein infill								—			
Pyrrhotite											—
Chalcopyrite											—
Magnetite											—
Fe dol - NPL to PL-E matrix-R: vein infill											—
Ankerite - NPL to PL-E matrix-R: vein infill											—
Fe Ankerite - NPL to PL-E matrix-R: vein infill											—
Siderite - vein infill											—
Bioite -chlorite -muscovite -phengite - greenalite											—

Geodynamic regime	Sedimentation ca. 1654Ma	Diagenesis	Regional Deformation & metamorphism
		1654Ma - - - - - - - - - - - - - - - - - - - → ? early - - - - - - - - - - - - - - - - - - - → late prechemical compaction→ advanced lthification →hydrocarbon maturation increasing burial depth - - - - - - - →	1580 → 1530Ma D_2 → D_3 200°C[1.] → 300°C[2.]

Table 3. Summary table listing carbonate chemistry. Carbonate populations are subdivided according to paragenesis, textural characteristics, and setting. A selection of chemical analyses of Hilton Mine and Mount Cu Mine carbonates are taken from Valenta (1988), Tuesley (1993) and Waring (1990a). [1.] Colour refers to the variation in electron density of the particular carbonate group as seen in BSE and referred to here relative to an arbitrary grey. [2.] Setting of the carbonates for each population on the basis of sample location with in the Mount Isa system (Isa=Mount Isa area, Hil=Hilton Mine, GF=George Fisher deposit), and the relative proximity of the sample to Zn-Pb-Ag or Cu ore bodies (economic=sample located in an ore body, proximal=mine environment near ore body, distal=peripheral to ore system), and development of other paragenetic stages with in the same sample (e.g. Stage I calcite alteration, Stage III celsian-hyalophane-K-feldspar alteration, Stage VIII phyllosilicate alteration). [3.] Paragenetic stage for George Fisher samples as for Table V including differentiation of early carbonates as Stage OI from clastic grains. Paragenetic associations for samples from Hilton and Mount Isa are correlated with George Fisher events (denoted equ. = equivalent) on the basis of comparisons of textural and/or mineralogical and/or structural timing comparisons.

Paragenetic Stage[3]	Texture and Colour[1]	Setting[2]	Carbonate Type	Host Rock[4]	$CaCO_3$ (mol. %)	$MgCO_3$ (mol. %)	$MnCO_3$ (mol. %)	$FeCO_3$ (mol. %)	$(Fe,Mn)CO_3$ (mol. %)	Fe+Mn: Mg	n
Early dolomite Stage OI a	dark grey cores	GF proximal Zn-Pb-Ag proximal subeconomic Cu	dolomite >> ferroan dolomite	PS, CS, MM, BM, SM	49.34 - 56.22	41.78 - 49.54	0.02 - 0.43	0.31 - 3.48	0.55 - 3.88	11.74 - 86.84	11
Early dolomite Stage OI b	light grey inner rims	GF proximal Zn-Pb-Ag proximal subeconomic Cu	ankerite >> ferroan dolomite	CS, MM, SM	49.60 - 52.57	31.27 - 41.90	0.27 - 3.45	7.85 - 14.09	8.26 - 17.23	1.85 - 5.08	12
Early dolomite Stage OI c	medium grey outer rims and matrix	GF proximal Zn-Pb-Ag proximal subeconomic Cu	ferroan dolomite >> ankerite	PS, CS, MM, BM, SM	48.43 - 52.81	36.84 - 45.21	0.25 - 2.60	4.14 - 9.32	4.61 - 10.62	3.22 - 9.76	33
Early dolomite Stage OI d	light grey outer rims and matrix	GF proximal Zn-Pb-Ag proximal subeconomic Cu	ankerite >> ferroan dolomite	CS, MM, SM	48.40 - 52.10	32.40 - 42.64	0.40 - 2.83	6.76 - 13.40	7.24 - 16.00	2.03 - 4.82	26
Early dolomite Stage OI a - d	relict core/rim/matrix	GF proximal Zn-Pb-Ag proximal subeconomic Cu Stage I calcite zone	dolomite, ferroan dolomite, ankerite	MM, BM	49.22 - 51.51	36.51 - 48.99	0 - 3.19	0 - 10.74	0 - 13.93	0 - 9.75	11
Early dolomite Stage OI a	dark grey cores	GF economic Zn-Pb-Ag proximal subeconomic Cu Stage III feldspar alteration	dolomite	BM	47.84 - 55.94	42.8 - 49.22	0.05 - 1.05	0.05 - 1.89	0.1 - 2.94	16.74 - 460.1	6

PARAGENETIC STAGE[3]	TEXTURE AND COLOUR[1]	SETTING[2]	CARBONATE TYPE	HOST ROCK[4]	$CaCO_3$ (mol. %)	$MgCO_3$ (mol. %)	$MnCO_3$ (mol. %)	$FeCO_3$ (mol. %)	$(Fe,Mn)CO_3$ (mol. %)	Fe+Mn: Mg	n
Early dolomite Stage OI c	Medium grey matrix	GF economic Zn-Pb-Ag proximal subeconomic Cu Stage III feldspar zone	ferroan dolomite > ankerite	BM	48.66 - 50.35	39.91 - 43.15	1.68 - 3.20	5.14 - 8.00	8.12 - 11.20	3.56 - 5.26	4
Early dolomite Stage OI d	Light grey matrix	GF economic Zn-Pb-Ag proximal subeconomic Cu Stage III feldspar zone	ankerite	BM	38.53 - 50.35	34.13 - 41.51	0 - 2.98	10.06 - 18.76	12.86 - 19.95	1.97 - 3.13	4
Early dolomite Stage OI a equ.	dark grey cores	Isa distal Zn-Pb-Ag/Cu	dolomite	BM	49.80 - 50.40	48.07 - 48.48	0.36 -0.89	0.76 - 1.10	1.23 - 1.72	28.19 - 39.35	5
Early dolomite Stage OI b equ.	Light grey rim	Isa distal Zn-Pb-Ag/Cu	ferroan dolomite	BM	48.52 - 49.62	43.69 - 45.48	0.34 - 1.39	4.73 - 6.40	6.0 - 6.89	6.34 - 7.58	3
Early dolomite Stage OI c/d equ.	Medium grey matrix	Isa distal Zn-Pb-Ag/Cu	ferroan dolomite	BM	48.96 - 50.21	41.88 - 47.46	0.24 - 0.73	3.30 - 7.59	3.59 - 8.24	5.08 - 13.22	9
Stage I calcite	matrix	GF proximal Zn-Pb-Ag proximal subeconomic Cu	calcite	BM, MM	94.30 - 96.85	1.4 - 2.27	0.79 - 2.24	0.69 - 2.14	1.69 - 3.45	-	12
Stage I calcite	matrix	GF proximal Zn-Pb-Ag proximal subeconomic Cu	calcite	WB	95.91 - 98.40	0.18 - 1.93	0.62 - 1.58	0.21 - 1.17	0.96 - 2.43	-	9
Stage I calcite	matrix and infill	GF proximal Zn-Pb-Ag proximal subeconomic Cu	calcite	Nod	95.84 - 98.32	0.44 - 1.76	0.45 - 1.52	0.49 - 1.29	1.24 - 2.37	-	10
Stage I calcite equ.	matrix	Isa distal Zn-Pb-Ag/Cu	calcite	BM	96.36 - 98.29	0.98 - 2.96	0.02 - 0.71	0.12 - 1.15	0.34 - 0.73	-	6
Syntectonic ferroan carbonates Stage VIII	grey matrix and rhomb rim	GF proximal Zn-Pb-Ag proximal subeconomic Cu	ankerite > ferroan dolomite	MM, BM	48.32 - 51.31	44.21 - 36.65	0.80 - 3.77	3.69 - 11.82	4.49 - 14.36	2.58 - 9.85	25
Syntectonic ferroan carbonates Stage VIII	light grey matrix and rhomb core	GF proximal Zn-Pb-Ag proximal subeconomic Cu	ankerite >> ferroan ankerite	MM, BM, PS	47.98 - 52.01	36.29 - 25.44	1.18 - 4.50	11.42 - 22.79	14.97 - 26.05	0.98 - 2.38	24
Syntectonic ferroan carbonates Stage VIII	grey matrix	GF proximal Zn-Pb-Ag subeconomic Cu Stage VIII phyllosilicate with Stage III feldspar zone	ferroan ankerite >> ankerite	MM	47.35 - 49.05	27.66 - 30.76	2.69 - 3.87	17.23 - 21.1	19.97 - 24.71	1.12 - 1.64	9
Syntectonic ferroan carbonates Stage VIII	Vein Infill	GF proximal Zn-Pb-Ag subeconomic Cu Stage VIII phyllosilicate with Stage III feldspar zone	ferroan ankerite >> ankerite	-	48.79 - 52.21	18.94 - 31.27	1.52 - 3.5	17.17 - 29.53	19.52 - 32.38	0.56 - 1.60	10

Paragenetic Stage[3]	Texture and colour [1]	Setting [2]	Carbonate Type	Host Rock[4]	$CaCO_3$ (mol. %)	$MgCO_3$ (mol. %)	$MnCO_3$ (mol. %)	$FeCO_3$ (mol. %)	$(Fe,Mn)CO_3$ (mol. %)	Fe+Mn: Mg	n
Syntectonic ferroan carbonates Stage VIII	Vein Infill	GF proximal Zn-Pb-Ag subeconomic Cu Stage VIII phyllosilicate with Stage III feldspar zone	siderite	-	0.62 - 0.77	14.53 - 15.15	3.05 - 3.57	80.63 - 81.80	84.07 - 84.85	0.17 - 0.18	3
Syntectonic ferroan carbonates Stage VIII	Vein Infill	GF proximal Zn-Pb-Ag subeconomic Cu	ferroan ankerite	-	47.82 - 51.35	23.50 - 29.84	2.46 - 3.37	18.26 - 24.29	20.72 - 27.60	0.85 - 1.44	6
Syntectonic ferroan carbonates Stage VIII	Grey matrix	GF proximal Zn-Pb-Ag proximal subeconomic Cu	ferroan dolomite >> ankerite	Nod	49.70 - 50.75	39.55 - 42.13	2.60 - 3.50	4.50 - 7.52	7.96 - 10.75	3.68 - 5.29	8
Syntectonic ferroan carbonates Stage VIII	Light grey matrix	GF proximal Zn-Pb-Ag proximal subeconomic Cu	ferroan ankerite >> ankerite	Nod	51.77 - 54.99	24.23 - 27.33	1.81 - 2.87	17.20 - 21.11	19.09 - 23.78	1.05 - 1.39	15
Stage V sugary ferroan dolomite	Vein Infill	GF proximal Zn-Pb-Ag proximal subeconomic Cu	ferroan dolomite ankerite	-	48.77 - 50.45	37.77 - 43.23	0.84 - 2.24	5.41 - 10.47	7.21 - 12.40	3.05 - 6.00	20
Wall rock to Stage V veins	Grey matrix	GF proximal Zn-Pb-Ag proximal subeconomic Cu	ferroan dolomite	-	48.31 - 50	35.8 - 45.26	0.96 - 1.82	4.89 - 13.39	5.85 - 15.01	2.39 - 7.74	9
Stage III carbonate infill	Vein Infill	GF economic Zn-Pb-Ag proximal subeconomic Cu	calcite	-	94.88 - 98.01	0.95 - 2.72	0 - 1.95	0 - 1.42	0.53 - 2.79	-	24
Stage III carbonate infill	Vein Infill	GF economic Zn-Pb-Ag proximal subeconomic Cu	ferroan dolomite	-	47.28 - 48.24	44.84 - 47.55	1.09 - 3.52	3.41 - 5.19	4.75 - 6.93	6.47 - 10.01	7
Stage VIII equ.	Matrix and vein infill	Hil economic Zn-Pb-Ag subeconomic Cu Valenta (1988)	ferroan dolomite, ankerite, ferroan ankerite, siderite	NA	0.40 - 57.54	9.60 - 37.56	1.20 - 15.32	3.70 - 85.90	0.14 - 7.67	4.90 - 90.00	14
Stage VIII equ.	Matrix	Hil economic Zn-Pb-Ag subeconomic Cu Stage III equ. feldspar Stage VIII equ. phyllosilicate alteration. Tuesley (1993)	ferroan ankerite, siderite	NA	0.41 - 49.81	16.52 - 34.59	1.54 - 12.98	14.06 - 63.22	15.60 - 74.77	0.34 - 2.22	8
Stage VIII equ.	undifferentiated	Isa silica-dolomite, economic Cu, adjacent Zn-Pb-Ag zones. Waring, 1990	dolomite, ferroan dolomite, ankerite	NA	49.07 - 54.18	26.39 - 48.60	0 - 2.98	1.45 - 19.27	1.36 - 32.65	1.45 - 19.85	50
Stage VIII equ.	undifferentiated	Isa silica-dolomite, economic Cu, adjacent Zn-Pb-Ag zones. Waring, 1990	siderite-magnesite		0.10 - 0.22	78.86 - 80.27	0.89 - 1.38	18.72 - 19.95	19.61 - 21.00		5
Stage VIII equ.	undifferentiated	Isa silica-dolomite, economic Cu, adjacent Zn-Pb-Ag zones. Waring, 1990	Calcite		95.68 - 99.25	0.52 - 3.11	0 - 0.64	0 - 1.07	0.18 - 1.53		23

CARBONATE TYPE	LOCATION	ASSOCIATIONS	INTERPRETATION
Stage OI cryptocrystalline zoned dolomite-ferroan dolomite-ankerite grains and matrix.	Mount Isa area distal to Zn-Pb. George Fisher proximal and economic Zn-Pb-Ag zones.	Stage I calcite alteration. Stage III So-parallel carb-Kfs veins. Stage VIII Cu and phyllosilicate alteration absent.	Syndiagenetic hydrothermal dolomitization. Earliest alteration to accompany Zn-Pb-Ag hydrothermal event.
Stage II fine-grained calcite: calcitic mudstones, layer-parallel planar white bands, nodular calcite layers in pyritic siltstones.	Mount Isa area distal to Zn-Pb. George Fisher proximal and economic Zn-Pb-Ag zones.	Stage III So-parallel carb-Kfs veins. Stage VIII Cu and related phyllosilicate alteration absent. Replaces Stage OI early dolomites.	Syndiagenetic hydrothermal calcitization. Precursor to main stage Zn-Pb-Ag hydrothermal event.
Stage VIII Dolomite-ankerite-ferroan ankerite-siderite microspar.	Mount Isa, Hilton and George Fisher Zn-Pb ore bodies in subeconomic zones of Cu mineralization	Stage VIII phyllosilicate, magnetite and minor chalcopyrite-pyrrhotite alteration and ferroan ankerite-siderite veining. Absence of Stage I calcite (i.e. nodular dolomite). Accompanied by abundant sugary ferroan dolomite veining.	Syntectonic hydrothermal alteration developed peripheral to economic zones of Cu mineralization i.e. outer alteration zone cf. silica-dolomite.

Table 4. Summary of carbonate constituents of the Urquhart Shale in the Mount Isa area including mineralogical and vein-associations and genetic interpretation based on this study.

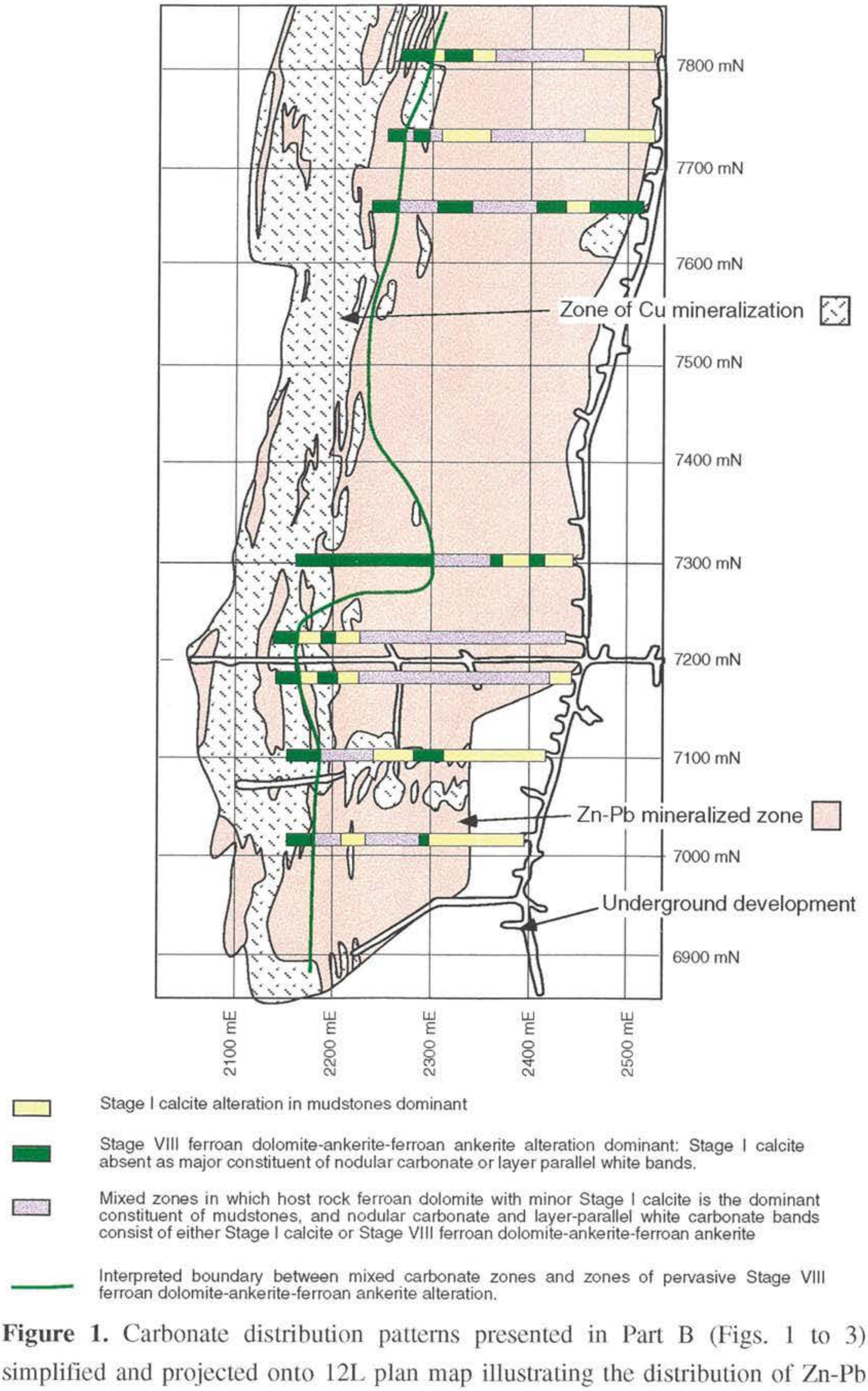

Figure 1. Carbonate distribution patterns presented in Part B (Figs. 1 to 3) simplified and projected onto 12L plan map illustrating the distribution of Zn-Pb and Cu mineralization (unpub. MIM data).

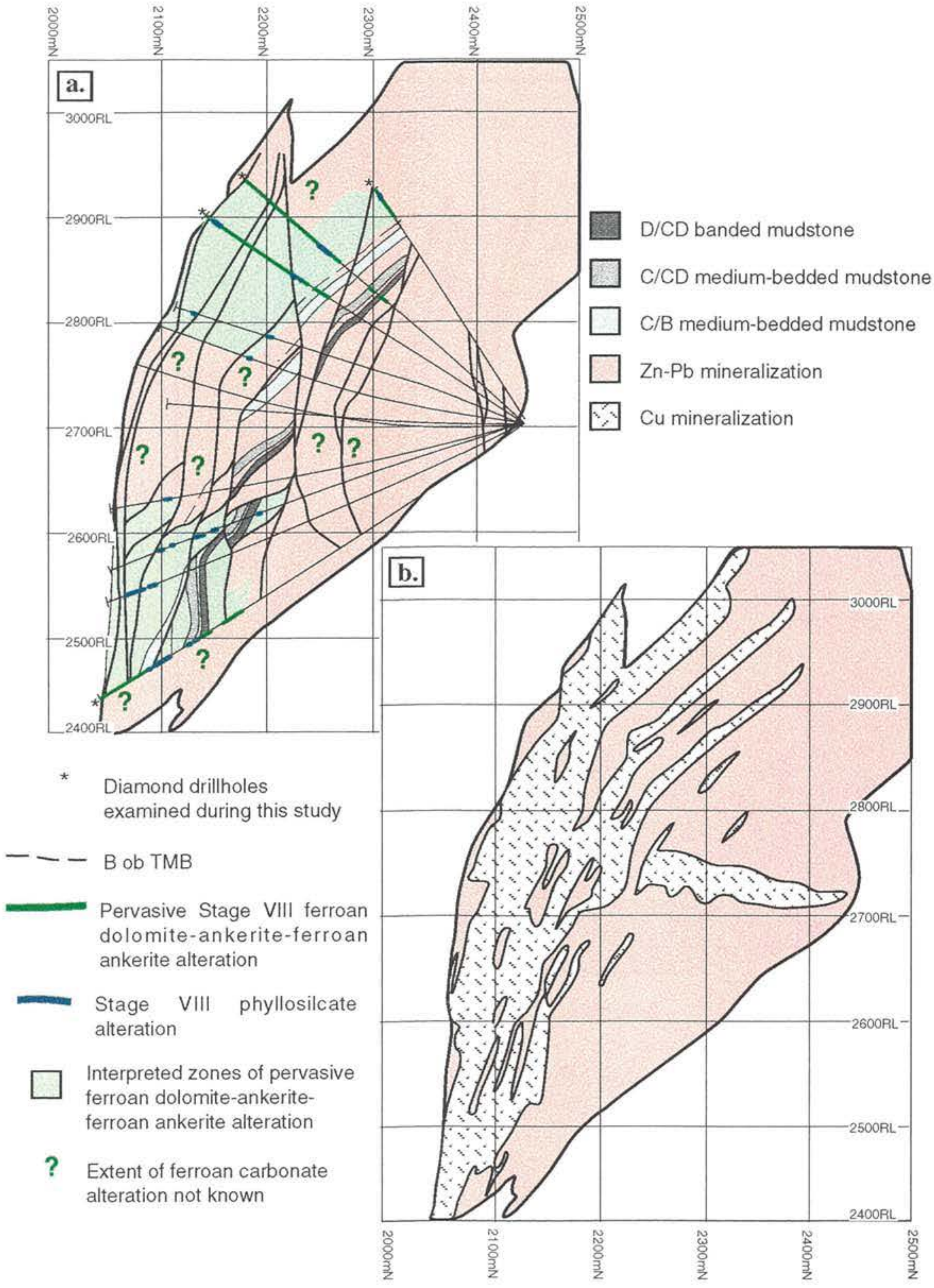

Figure 2. Schematic cross sections at 7180mN illustrating (a) distribution of large-scale pervasive Stage VIII alteration zones and Stage VIII phyllosilicate alteration determined during this study or interpreted from MIM drill logs and compared with the distribution of Zn-Pb mineralization. Interpretation of alteration zone is in part inferred from the distribution of Stage VIII phyllosilicate alteration (cf. Part B). (b) Distribution of Cu mineralization compared with Zn-Pb mineralization (unpub. MIM data). Footwall stratigraphic intervals are characterized by small-scale Stage VIII ferroan carbonate alteration zones and abundant Stage I calcite (cf. fig. 1 and Part B).

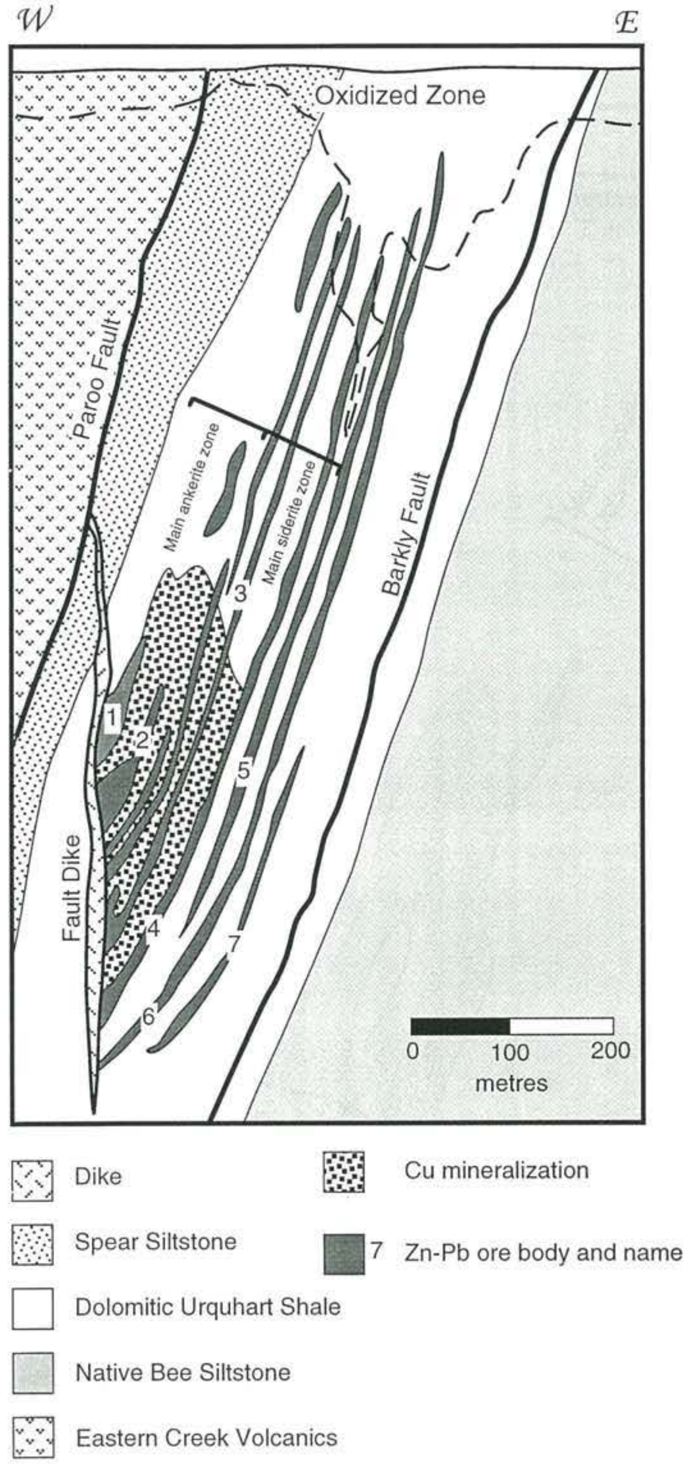

Figure 3. Stylized cross-section of Hilton Mine illustrating large-scale distribution of Cu and Zn-Pb mineralization, and ankerite and siderite - rich portions of stratigraphy in otherwise ferroan dolomite-bearing Urquhart Shale. Modified after Suttill, 1990, Tuesley, 1993 and Valenta, 1988.

Figure 4. Simplified northern cross-section of Mount Isa Mine illustrating large-scale distribution of Cu and Zn-Pb mineralization, and nodular dolomite - rich portions of stratigraphy in otherwise ferroan dolomite-bearing Urquhart Shale (after Perkins, 1997).

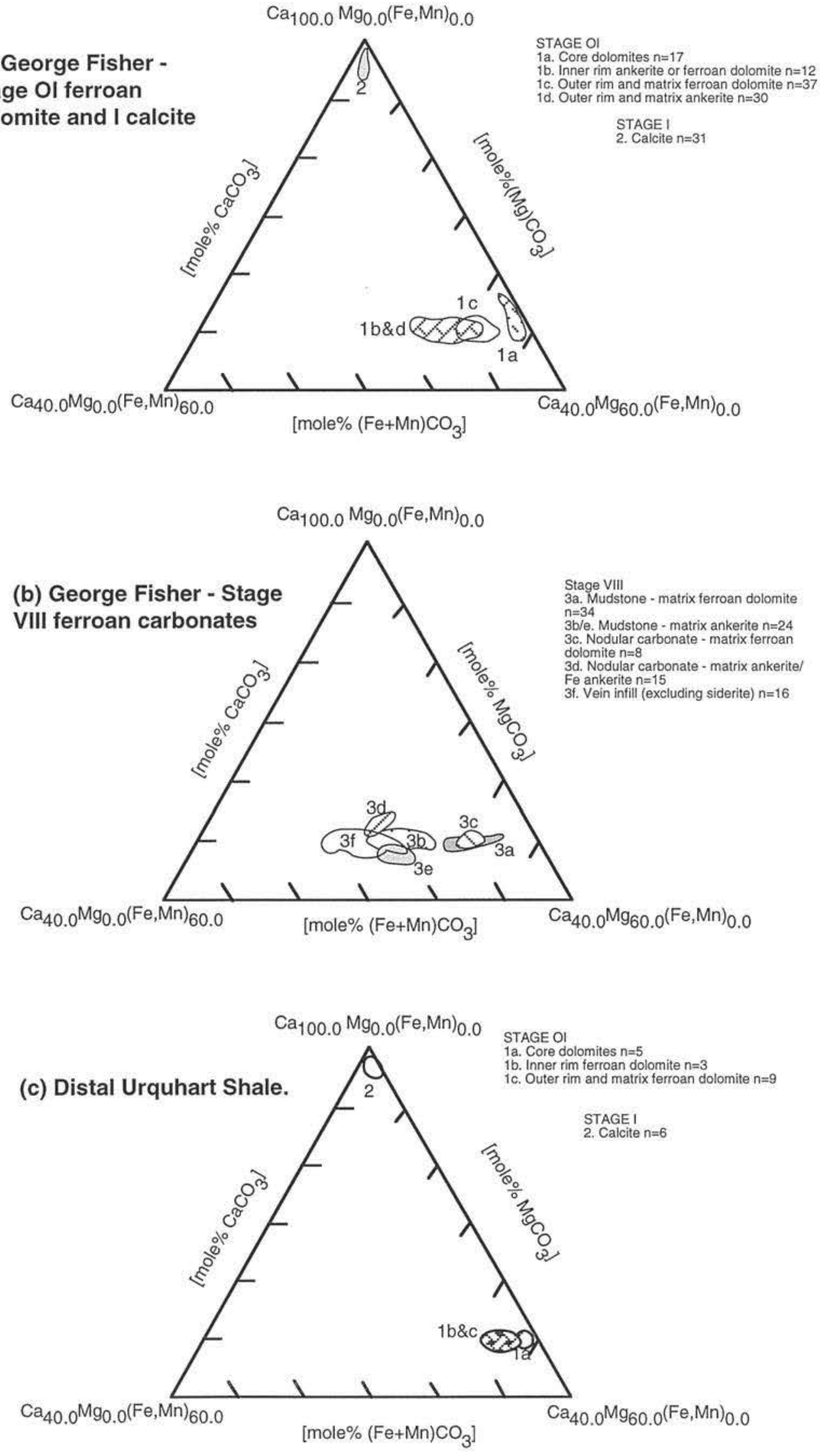

Figure 5. Ternary diagrams illustrating carbonate compositions from George Fisher and distal Urquhart Shale (refer Table 3).

Figure 6.

a. Abundant Stage OI early dolomite alteration developed in a mudstone includes an array of grains which are zoned from dolomite cores to inner ankerite rims and outer ferroan dolomite rims. The unusually coarse dolomite core to the right itself has an inclusion-rich core which has a rounded shadow grain outline. Ferroan dolomite forms the dominant matrix component in this field of view (BSE image, PTS# 131, HS# DC838, H766ED#1, 564m).

b. Abundant zoned stage OI early dolomite grains exhibit irregular to rhombohedral outlines defined by the zonation of ferrroan dolomite to ankerite in outer rims. One grain is characterized by an ankerite core (BSE image, PTS# 131, HS# DC838, H766ED#1, 564m).

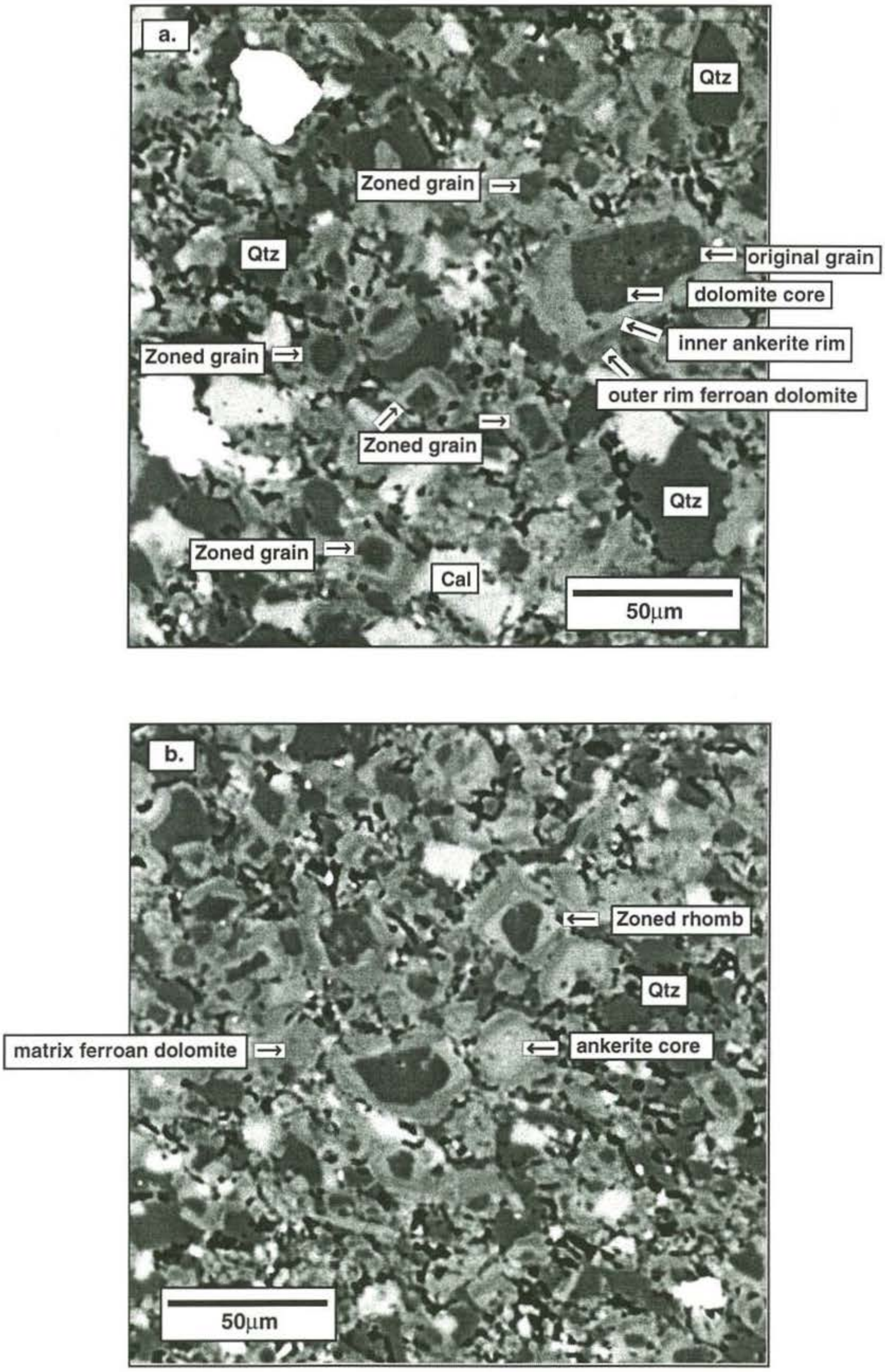

a.
Qtz
Zoned grain
Qtz
original grain
dolomite core
inner ankerite rim
Zoned grain
outer rim ferroan dolomite
Zoned grain
Qtz
Zoned grain
Cal
50µm
b.
Zoned rhomb
Qtz
matrix ferroan dolomite
ankerite core
50µm

Figure 6.

c. High magnification BSE image illustrating systematic zonation of ankerite and ferroan dolomite around an inclusion-rich dolomite core in a shaly banded mudstone. Ankerite and ferroan dolomite are matrix components (PTS# 8, HS#052g, J702WI#5, 113.8m).

d. BSE image illustrating abundance of Stage OI early dolomites in a rhythmically laminated pyritic siltstone. Stage I calcite and K-feldspar alteration and Stage II spheroidal pyrite are also present. Note grain truncation along microstylolitic seams at the base of the image (PTS# 130, HS# DC840a, H766ED#1, 558.0m).

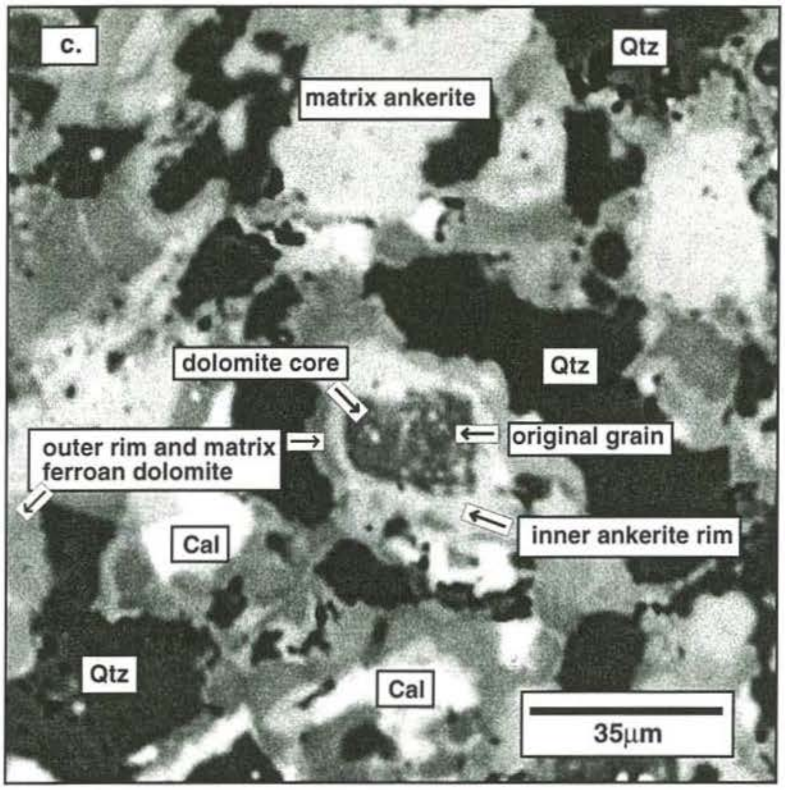
c.
Qtz
matrix ankerite
dolomite core
Qtz
outer rim and matrix
ferroan dolomite
original grain
inner ankerite rim
Cal
Qtz
Cal
35μm

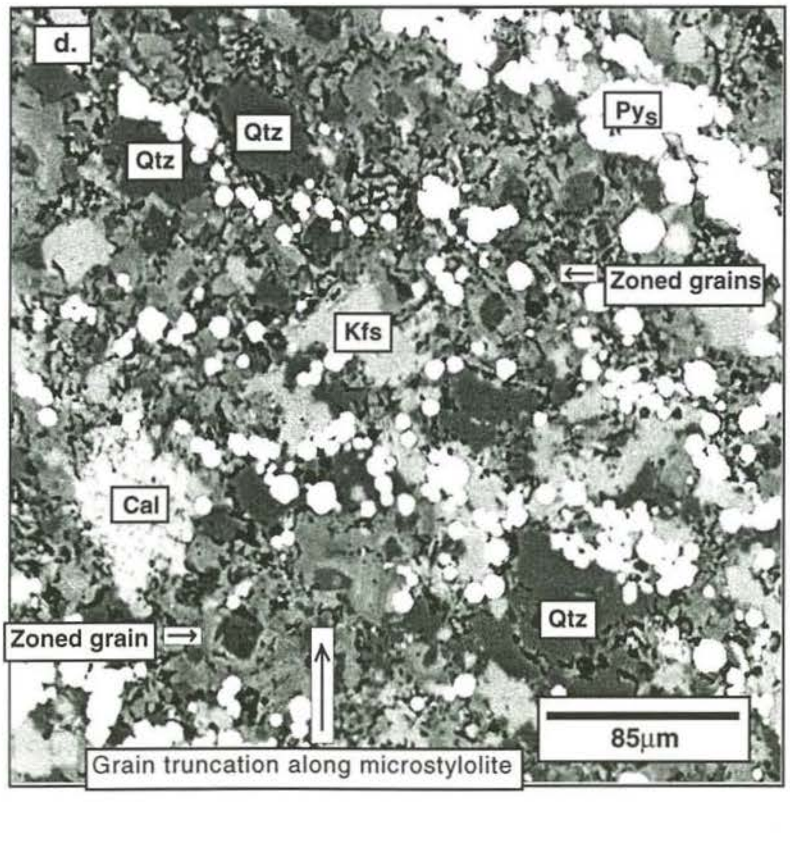
d.
Py
Qtz
Qtz
Zoned grains
Kfs
Cal
Qtz
Zoned grain
85μm
Grain truncation along microstylolite

Figure 7.

a. BSE image illustrating abundant Stage I calcite alteration (Cal) in a layer-parallel white band and preservation of irregular clots of Stage OI dolomite-ferroan dolomite-ankerite and detrital quartz (Zoned Dol, Qtz) (PTS# 18, HS# 051a, J702WI#5, 111.65m).

b. BSE image illustrating abundant Stage I calcite alteration in a medium-bedded mudstone and preservation of irregular clots of Stage OI dolomite-ferroan dolomite-ankerite and detrital quartz. A bedding-parallel foliation is developed with a preferred orientation defined by elongation of grain aggregates (PTS# 103, HS# 044b, J702WI#5, 45m).

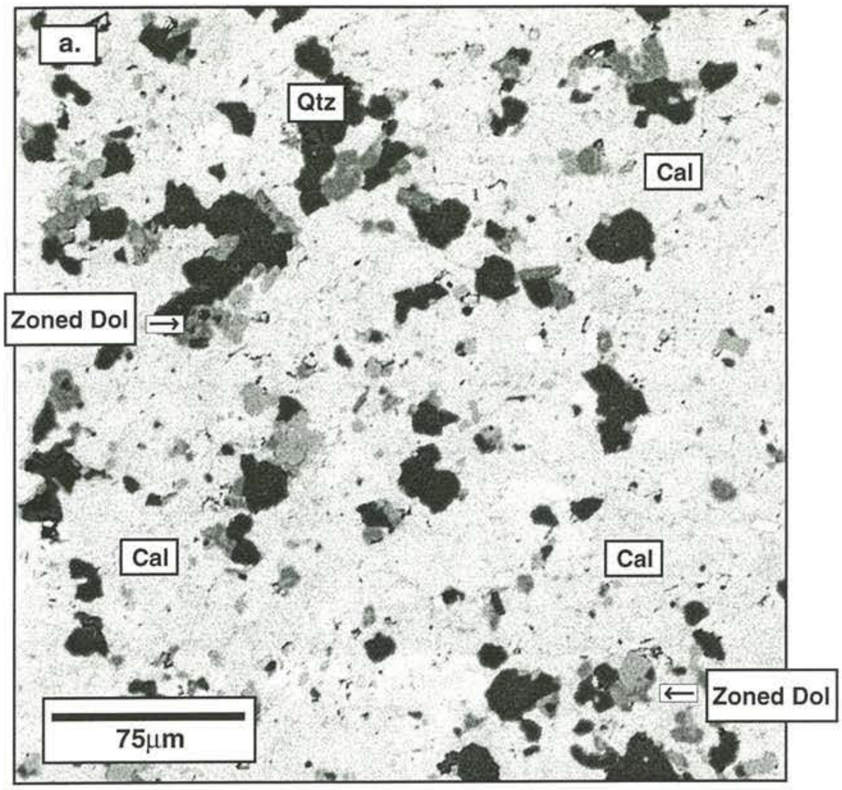
a.
Qtz
Cal
Zoned Dol
Cal
Cal
Zoned Dol
75μm

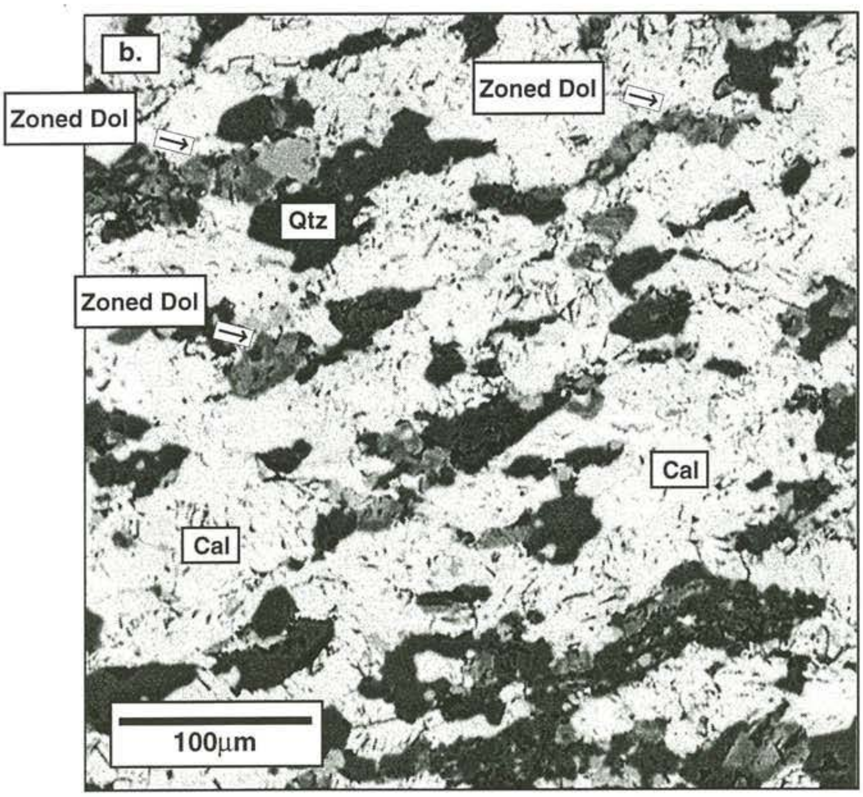
b.
Zoned Dol
Zoned Dol
Qtz
Zoned Dol
Cal
Cal
100μm

Figure 7.

c. BSE image illustrating contact relationships between a nodular calcite layer and rhymically laminated pyritic siltstone. Calcite laths in the nodular band form radiating arrays around spheroidal pyrite grains but the majority of calcite in the band is blocky. The former textural association suggests that a component of nodular calcite formed after the spheroidal pyrite or that the nucleus of calcite growth was susceptible to later spheroidal pyrite alteration. Calcite microbreccias are continuous with nodular bands and microbrecciate core-rim-matrix zonation patterns defined by Stage OI early dolomites (PTS# 14, HS# 050g, J702WI#5, 105.9m).

d. BSE image from the same sample above illustrating ultrafine network of Stage I calcite developed along quartz-Stage OI dolomite grain contacts in a rhythmically laminated pyritic siltstone.

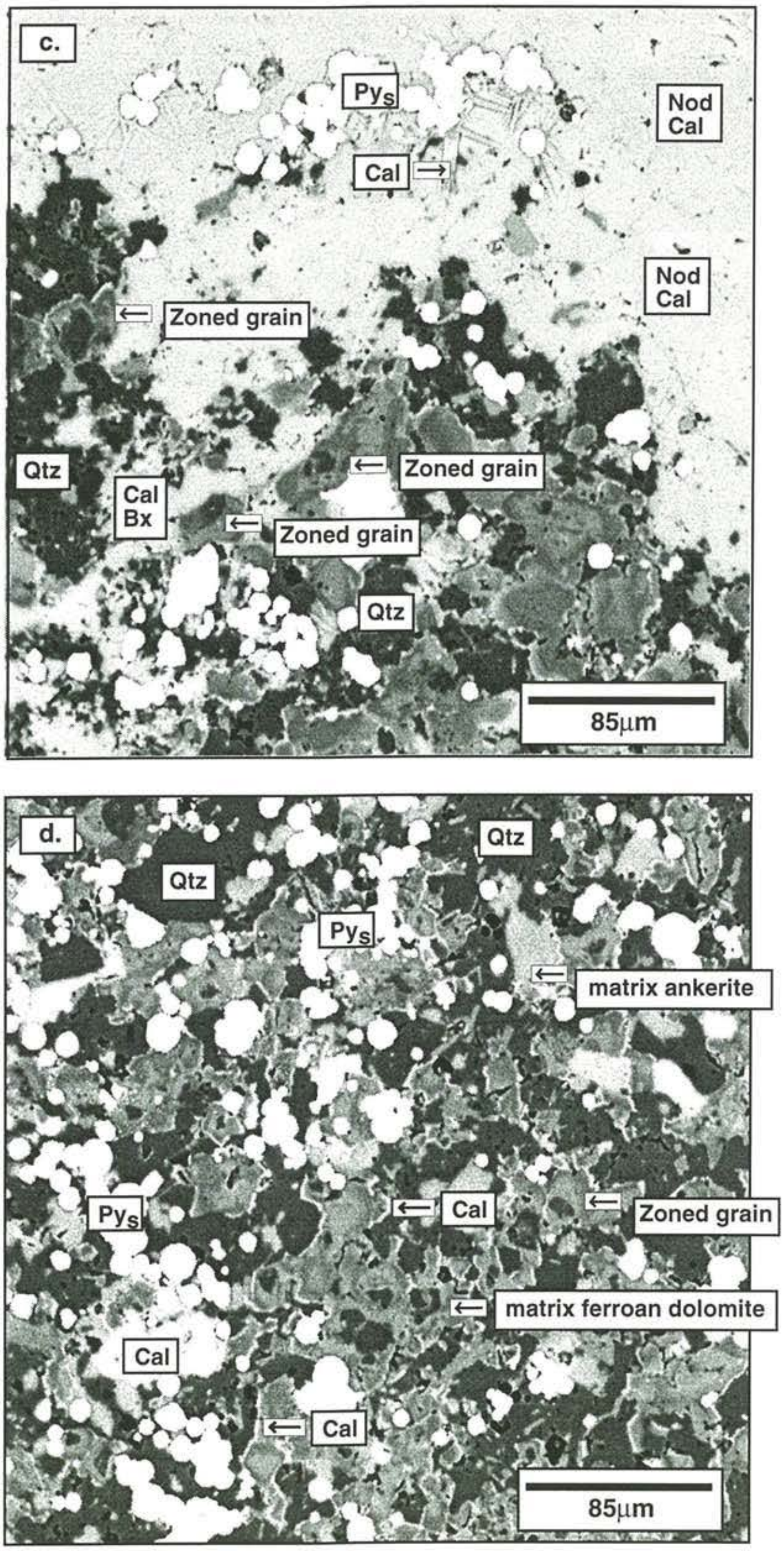

c.
Pys
Nod Cal
Cal
Nod Cal
Zoned grain
Qtz
Cal Bx
Zoned grain
Zoned grain
Qtz
85μm
d.
Qtz
Qtz
Pys
matrix ankerite
Pys
Cal
Zoned grain
matrix ferroan dolomite
Cal
Cal
85μm

Figure 8.

a. Dominant carbonate constituents in a mudstone sampled from the B stratigraphic interval include irregular, subhedral Stage VIII ferroan carbonate matrix which display a systematic zoning from ankerite to ferroan dolomite and rare Stage OI early dolomite grains (BSE image, PTS# 43, HS# 202b, J718WI#3, 237.8m).

b. High magnification BSE image from same samplke above illustrating that Stage VIII zoned, ferroan ankerite-ankerite-ferroan dolomite rhombs are relatively coarse grained relative to Stage OI dolomite grains and are accompanied by Stage VIII quartz (Qtz) development.

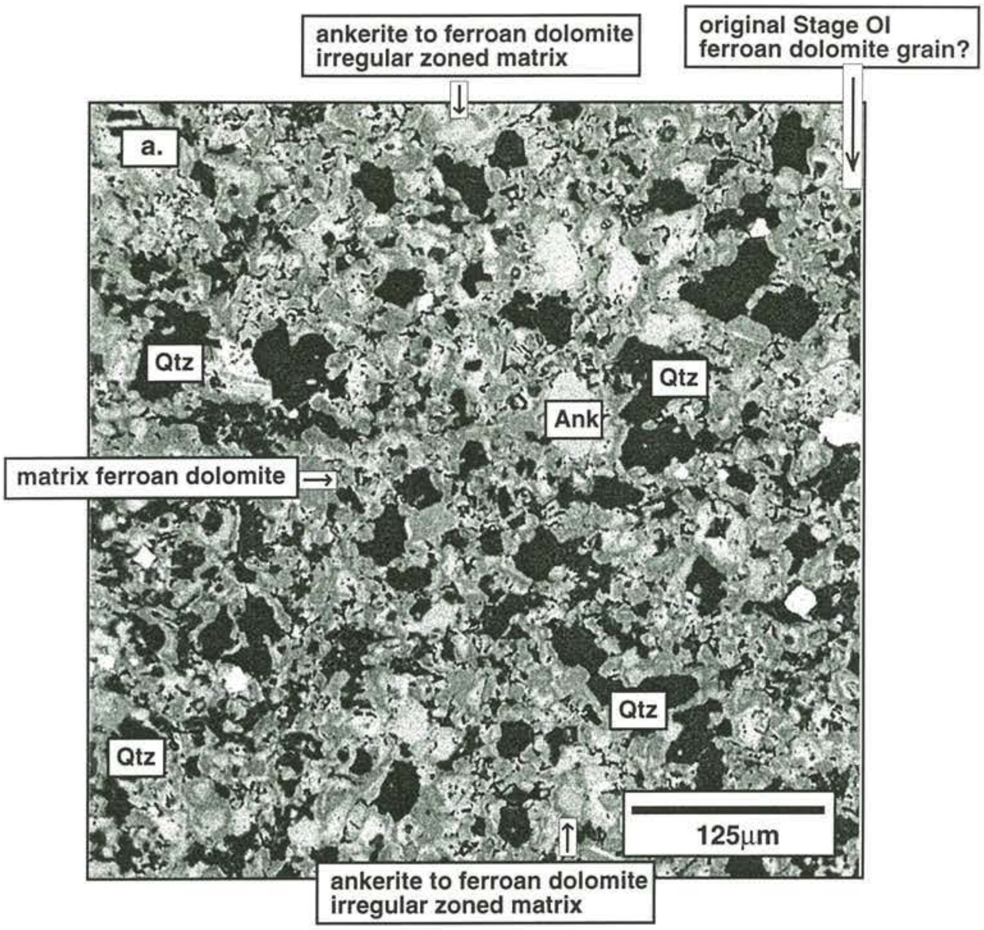
ankerite to ferroan dolomite
irregular zoned matrix
original Stage OI
ferroan dolomite grain?
a.
Qtz
Qtz
Ank
matrix ferroan dolomite
Qtz
Qtz
125μm
ankerite to ferroan dolomite
irregular zoned matrix

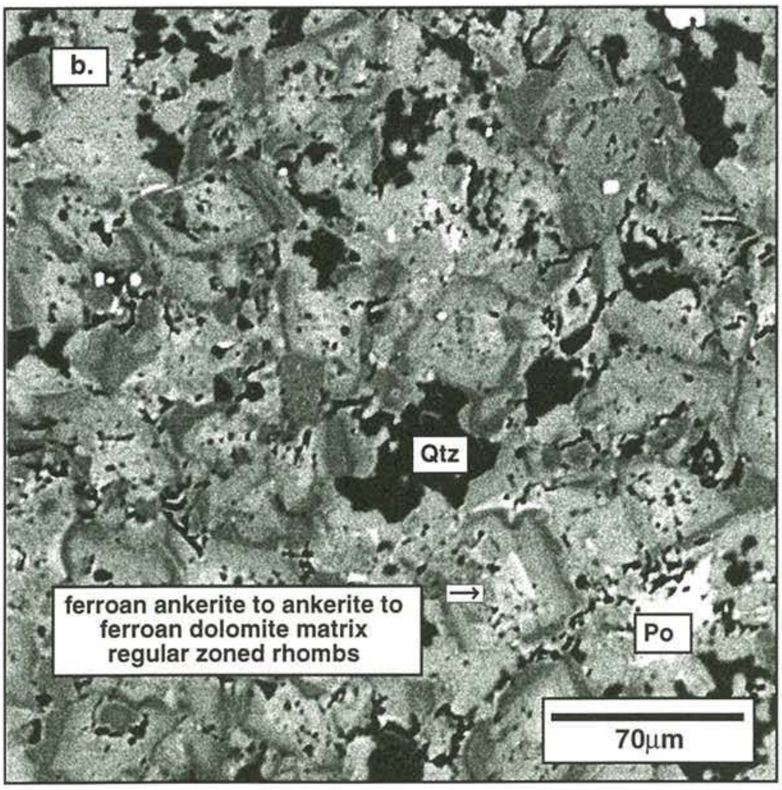
b.
Qtz
ferroan ankerite to ankerite to
ferroan dolomite matrix
regular zoned rhombs
Po
70μm

Figure 8.

c. BSE image of a nodular carbonate band which consists of an irregular array of Stage VIII ferroan dolomite and ferraon ankerite. The domain characterized by abundant quartz is interpreted to be relict of a Stage OI early dolomite clast that commonly are preserved in Stage I nodular calcite bands. However, no Stage OI early dolomite or Stage I calcite is preserved in this sample (PTS# 49, HS# 118, J702WD#4, 168.4m).

d. Stage VIII zoned ferroan dolomite-ankerite rhombs are the matrix component in this mudstone. Abundant quartz alteration post-dates the ferroan carbonates (BSE Image, PTS# 121, HS# 256, J718WI#5, 174m).

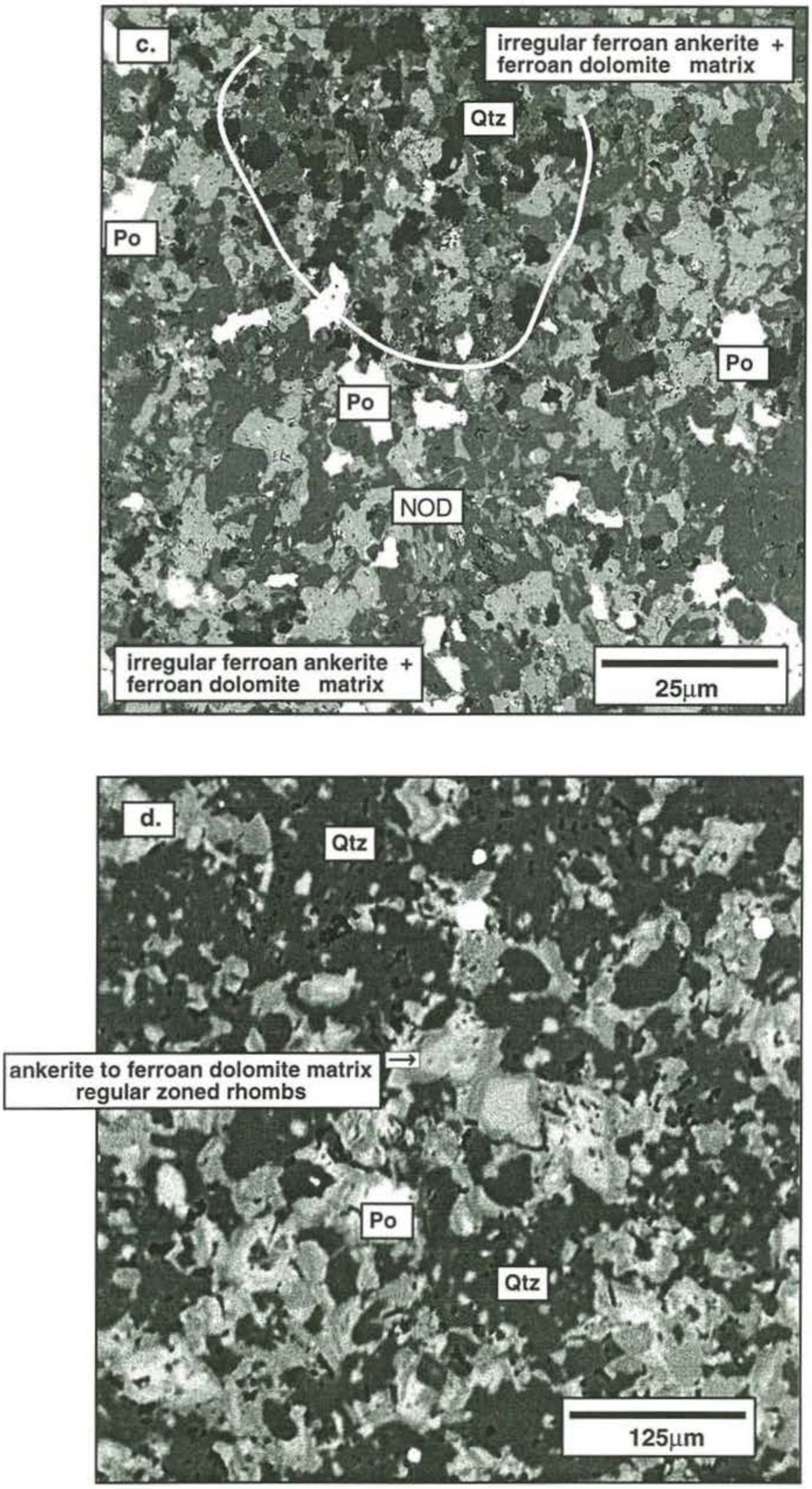
c.
irregular ferroan ankerite + ferroan dolomite matrix
Qtz
Po
Po
Po
NOD
irregular ferroan ankerite + ferroan dolomite matrix
25μm
d.
Qtz
ankerite to ferroan dolomite matrix regular zoned rhombs
Po
Qtz
125μm

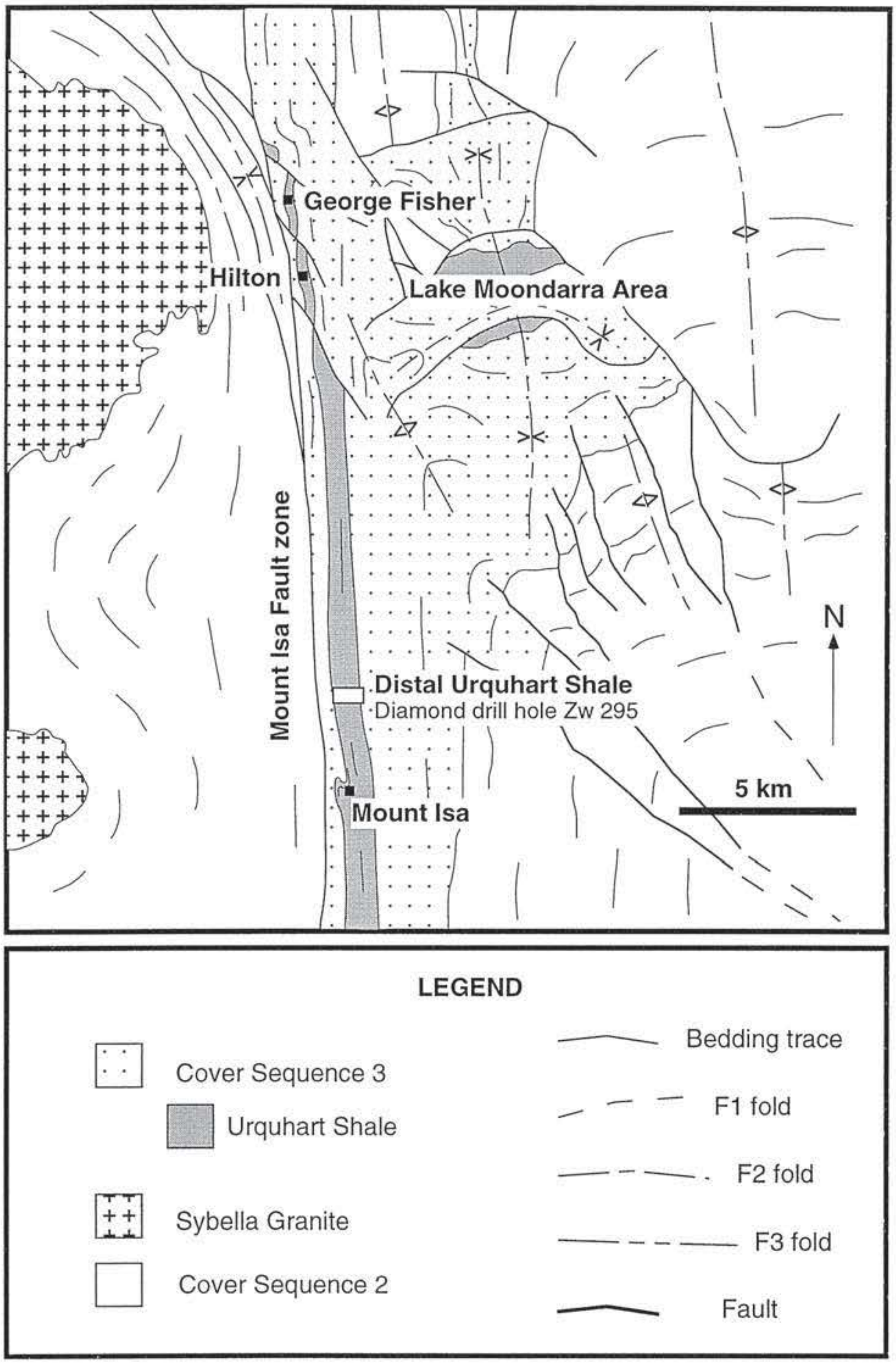

Figure 9. Geological map of the Mount Isa area illustrating major structural and stratigraphic elements and the general area from which samples of distal Urquhart Shale examined during this study were collected (after Blake, 1987, Valenta, 1988, Painter and Neudert, 1994).

Figure 10.

a. Dominant carbonate constitutents in a mudstone (distal to mineralization) include ferroan dolomite matrix which envelopes very fine-grained carbonate grains which have subrhombic dolomite cores and poorly defined ferroan dolomite rims. Abundant coarse calcite occurs as an alteration of ferroan dolomite matrix (BSE Image, PTS# MPC2a, HS# MPC, Zw295, 822.2m).

b. Zoned, subhedral and euhedral, dolomite-ferroan dolomite grains enveloped by ferroan dolomite matrix and replaced by calcite (BSE Image, PTS# MPC1a, HS# MPC, Zw295, 822.2m).

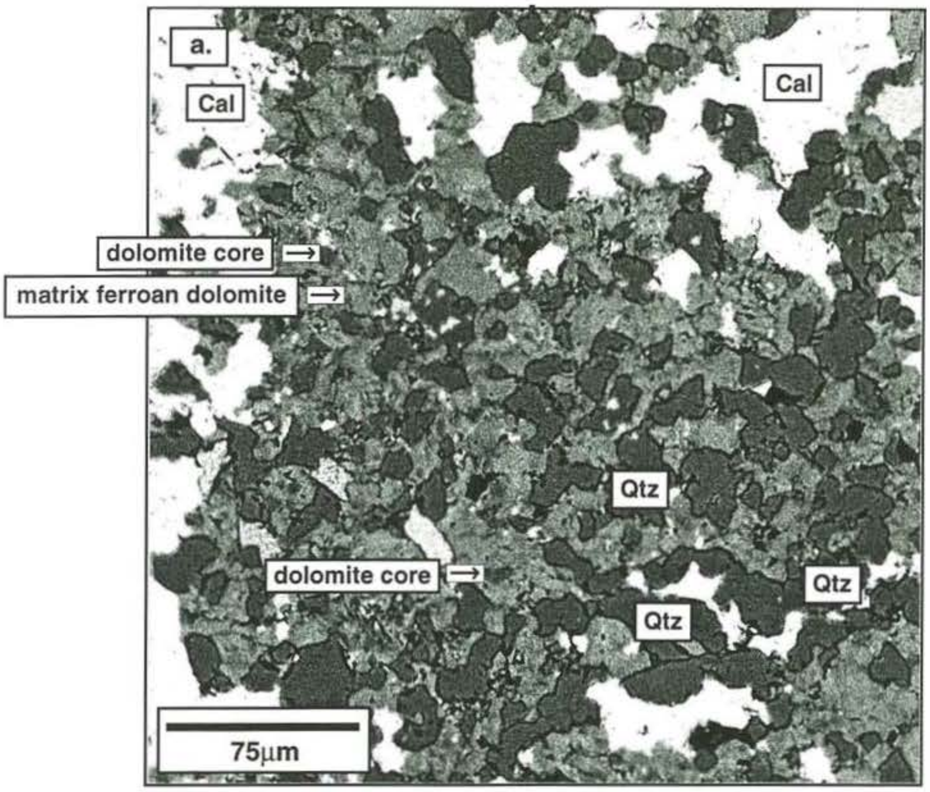
a.
Cal
Cal
dolomite core
matrix ferroan dolomite
Qtz
dolomite core
Qtz
Qtz
75µm

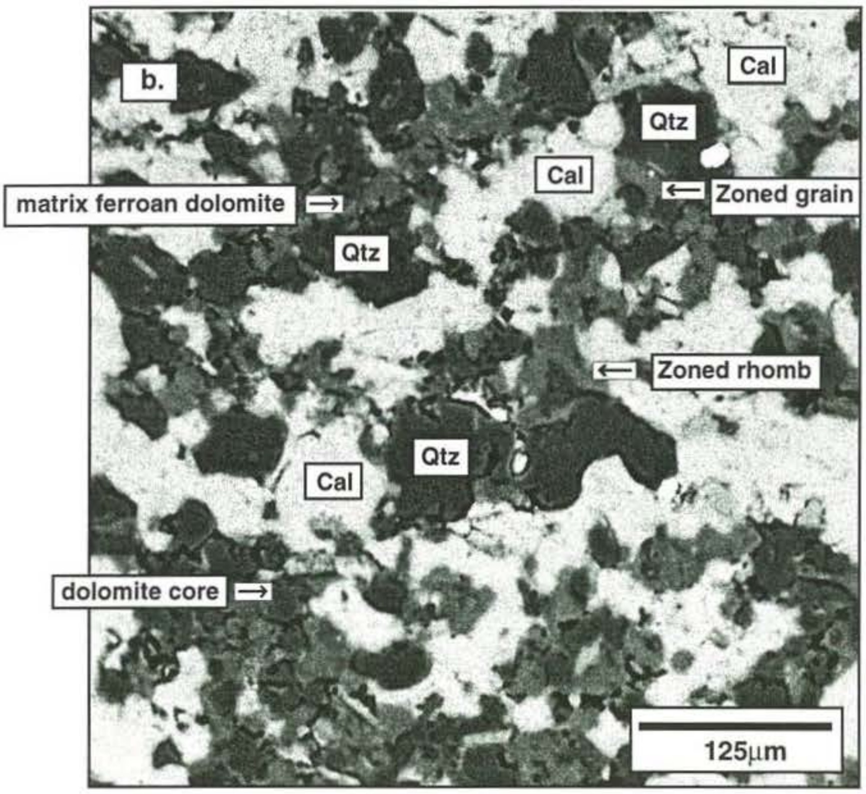
b.
Cal
Qtz
Cal
Zoned grain
matrix ferroan dolomite
Qtz
Zoned rhomb
Qtz
Cal
dolomite core
125µm

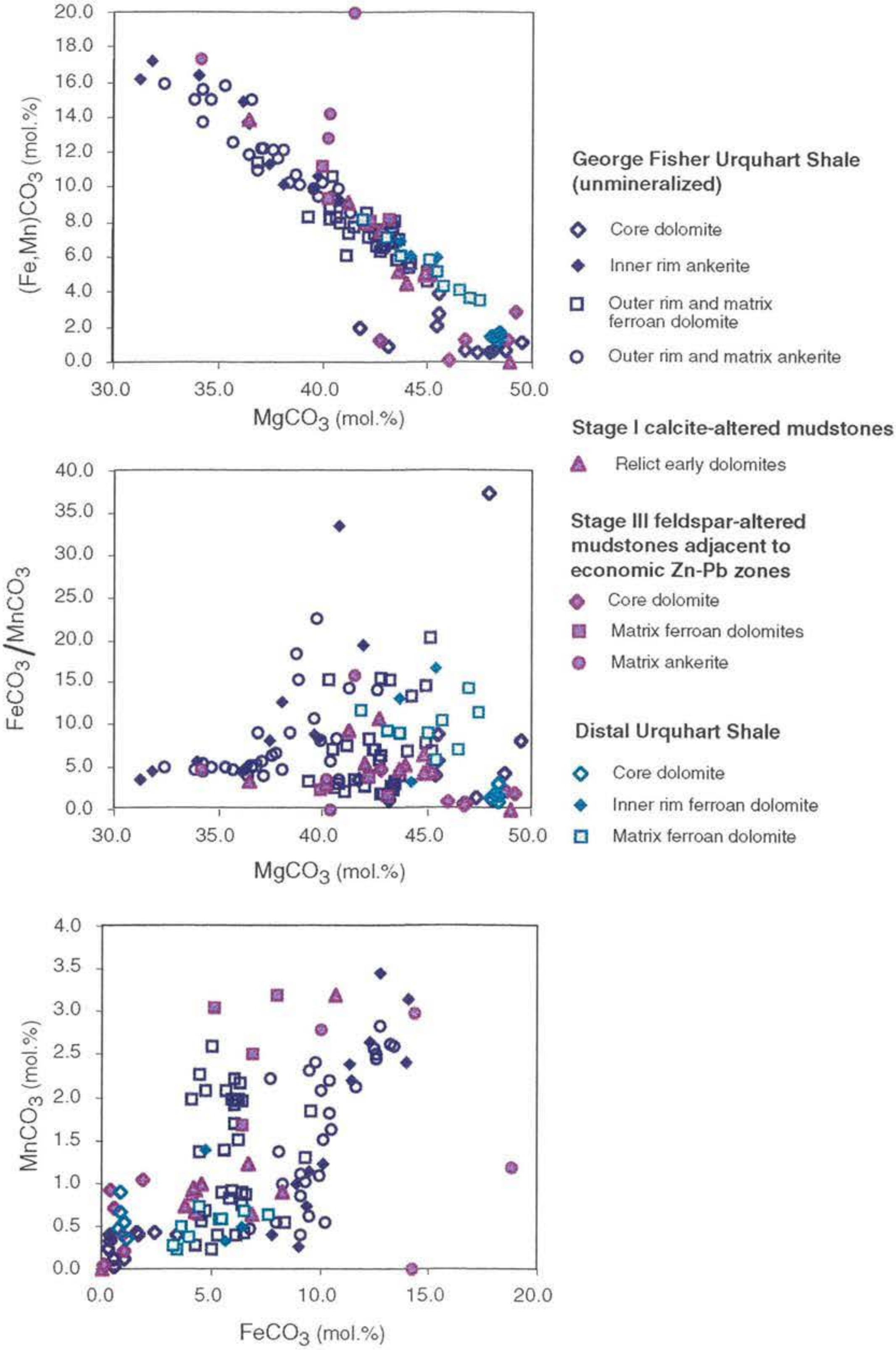

Figure 11. Plots illustrating variation in carbonate compositions of Stage OI early dolomites from a number settings at George Fisher and examples of carbonate constituents of Urquhart Shale distal to Mount Isa Mine.

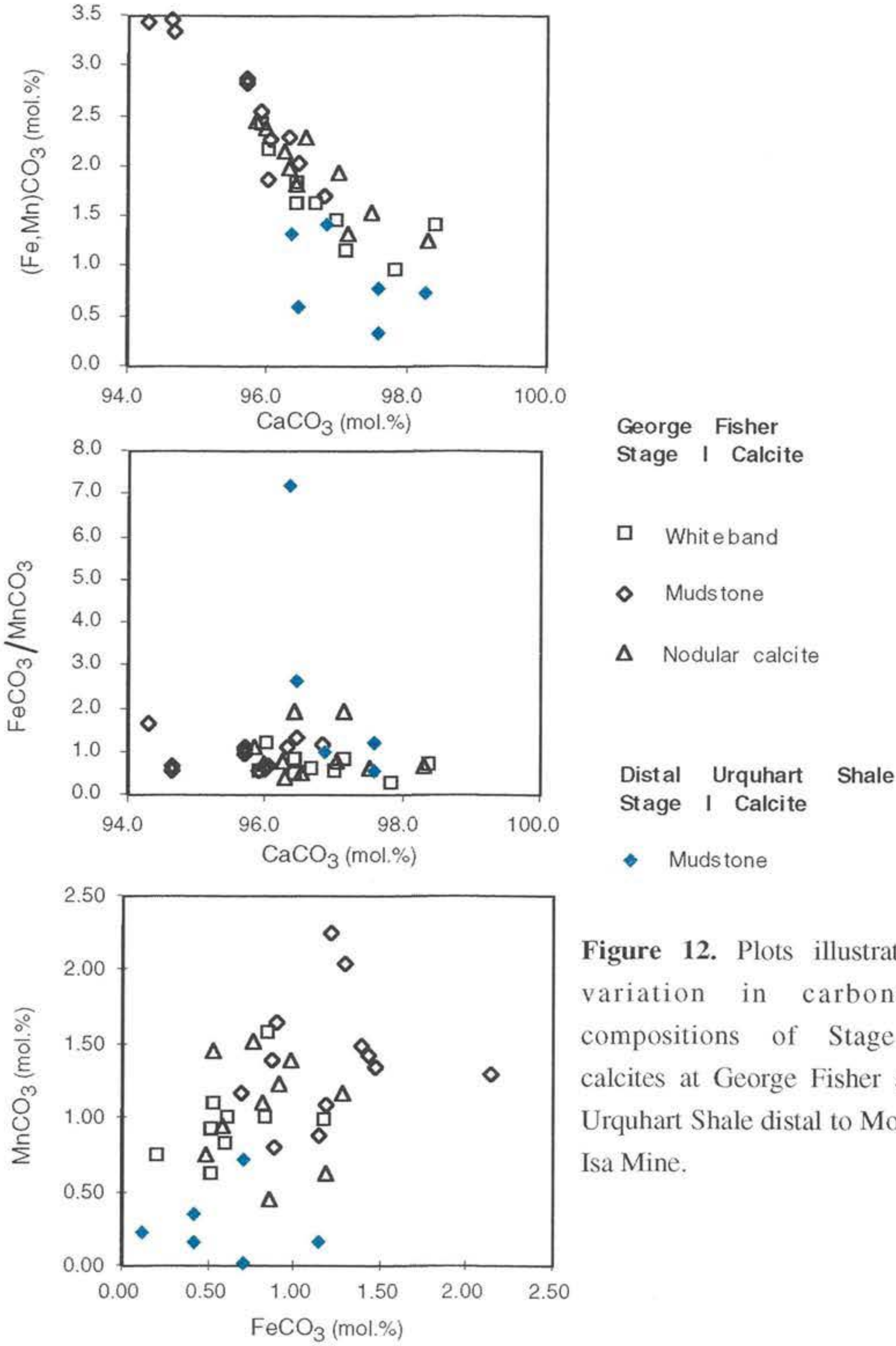

Figure 12. Plots illustrating variation in carbonate compositions of Stage I calcites at George Fisher and Urquhart Shale distal to Mount Isa Mine.

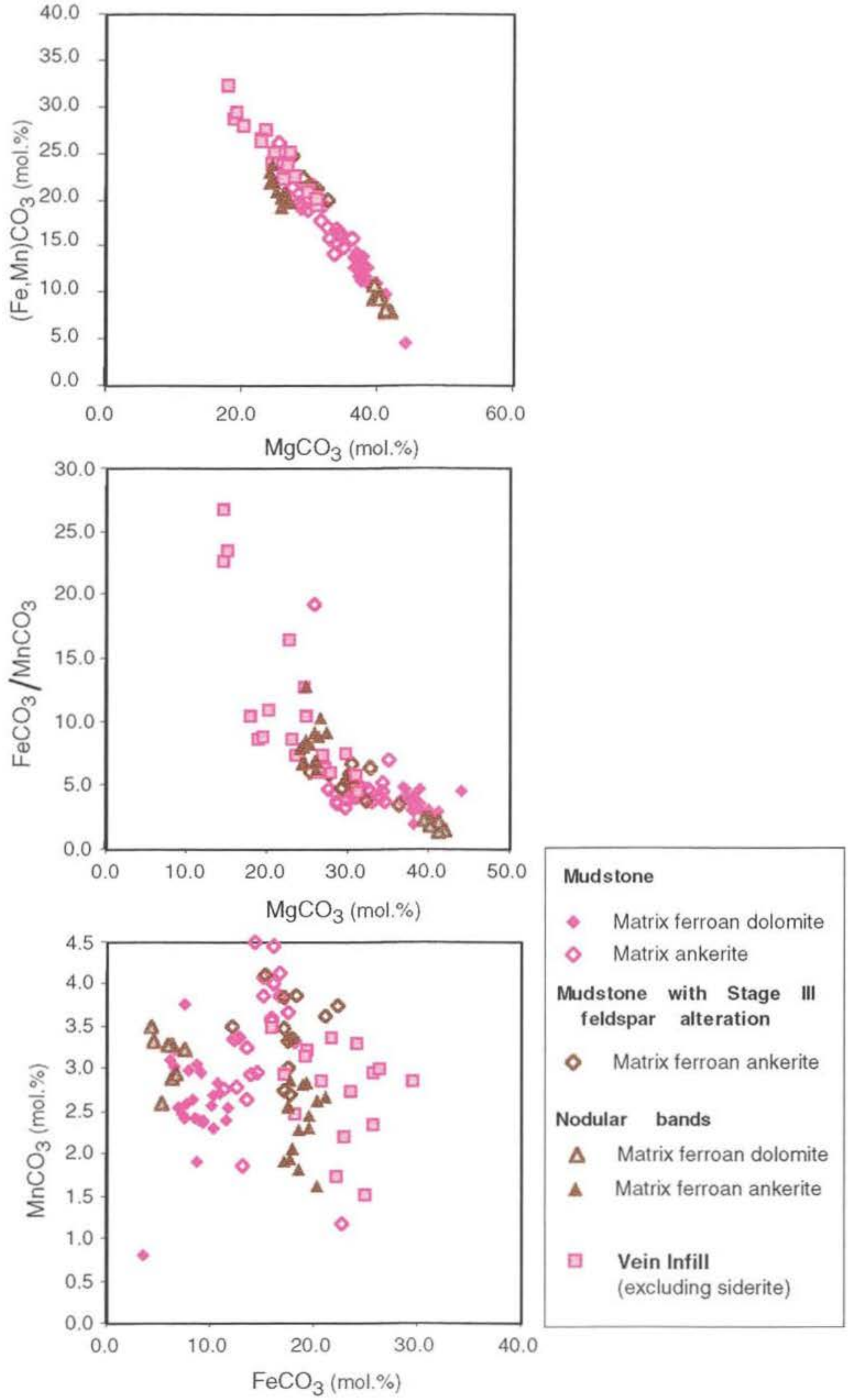

Figure 13. Plots illustrating variation in composition of Stage VIII ferroan carbonates at George Fisher.

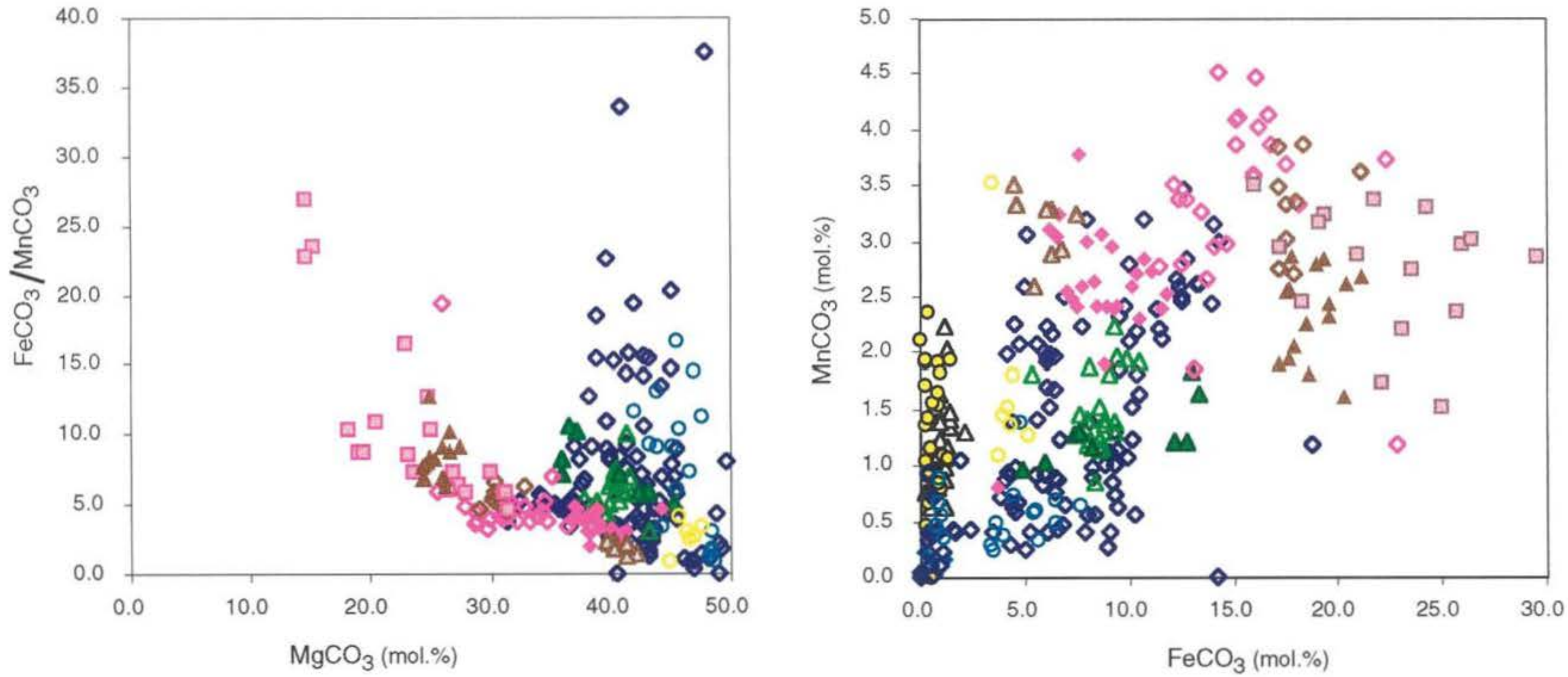

Figure 14. Plots illustrating variation in carbonate compositions of Stage OI early dolomites, Stage I calcites (b. only), Stage VIII ferroan carbonates and Stage III and V carbonate vein infill. Refer to the legend on Figure 13 for the key to Stage VIII ferroan carbonate symbols.

SYNDIAGENTIC CARBONATES

◇ Stage OI dolomite - GF

△ Stage I calcite - GF

○ Stage OI dolomite - distal

◆ Stage I calcite - distal

VEIN INFILL

○ Stage III dolomite vein infill

● Stage III calcite vein infill

▲ Stage V Sugary dolomite vein infill

△ Dolomite in wall rock to Stage V veins

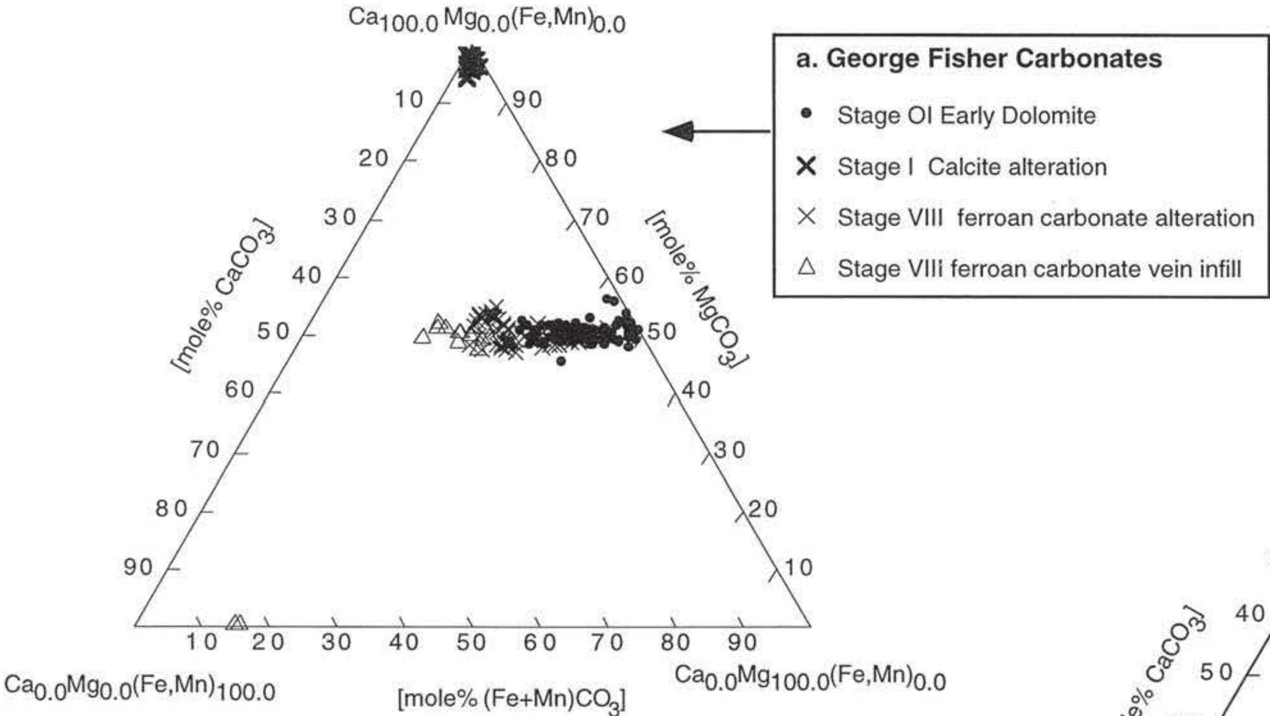

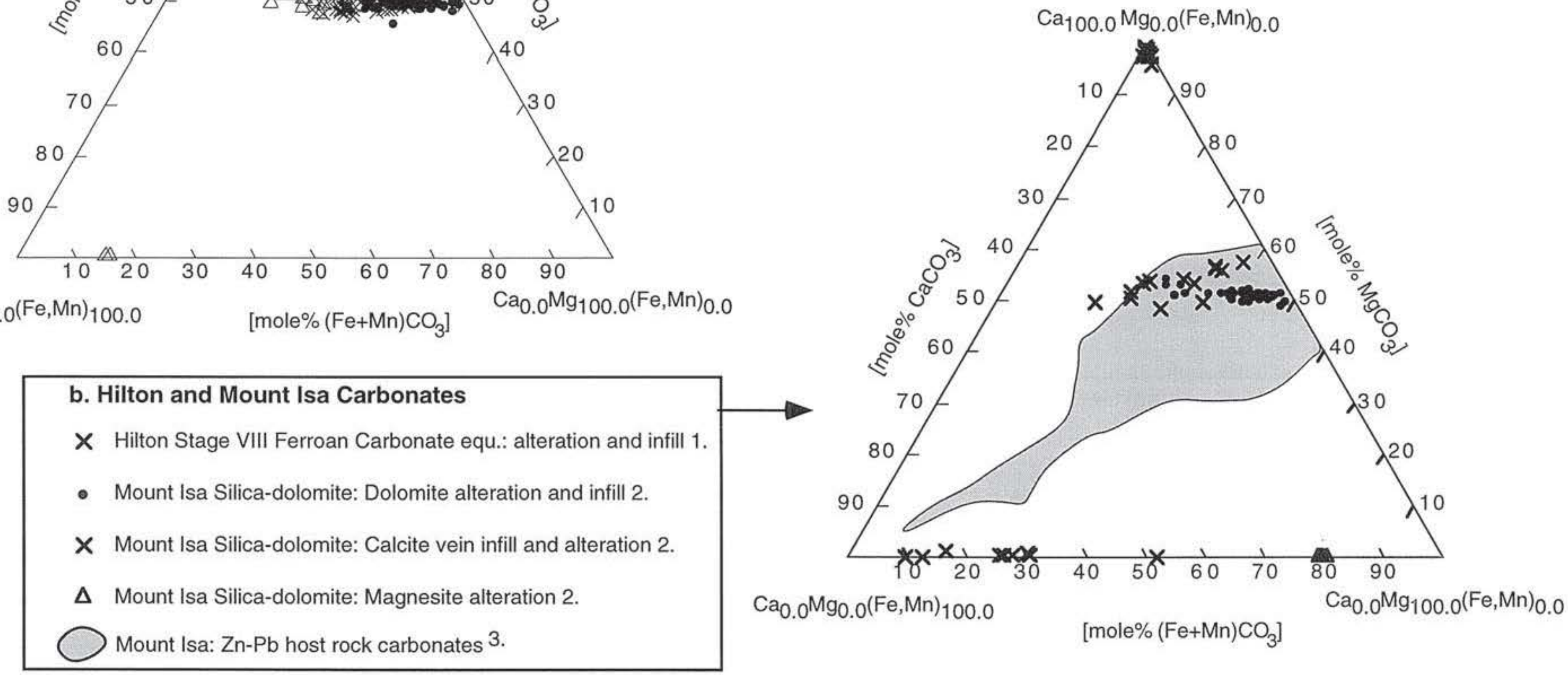

Figure 15. Ternary diagrams illustrating carbonate compositions at (a.) George Fisher compared with (b.) Mount Isa and Hilton. [1] Valenta (1988) and Tuesley (1993), [2] Waring (1990), [3] Stanton (1963).

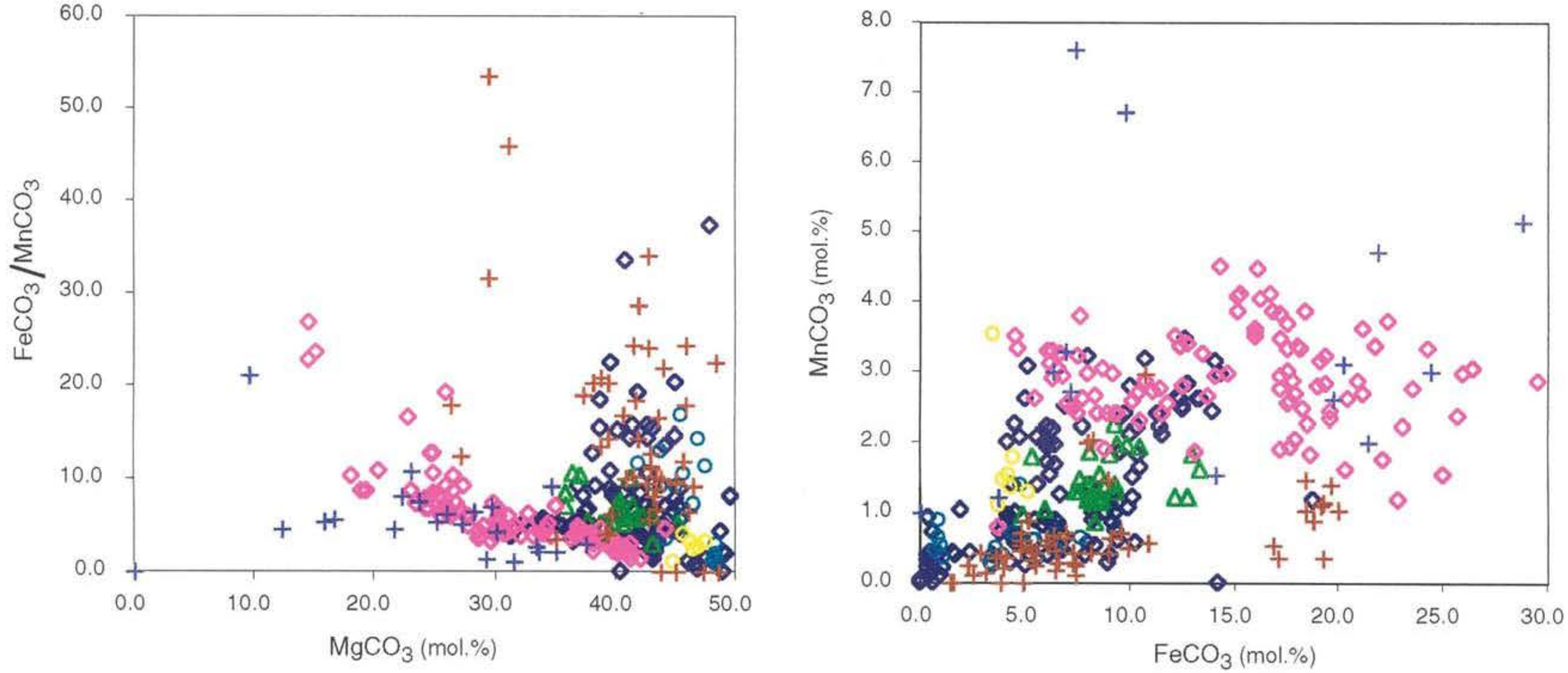

Figure 16. Plots illustrating variation in carbonate compositions of Stage OI early dolomites, Stage III and V dolomite vein infill and Stage VIII ferroan carbonates from George Fisher with Stage VIIIequ. Hilton carbonates, and distal and Cu-related carbonates at Mount Isa.

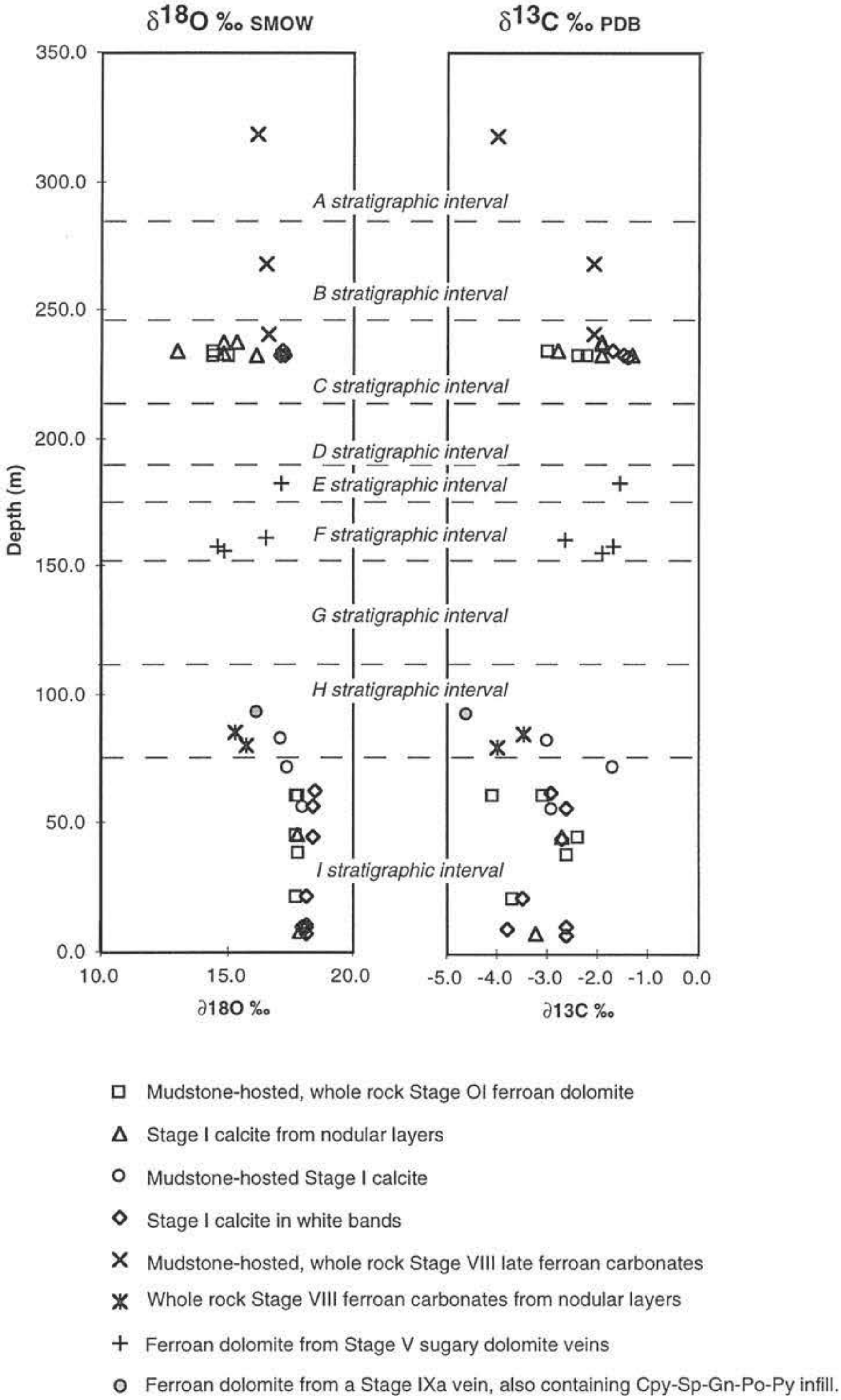

Figure 17. $\delta^{18}O$ and $\delta^{13}C$ variation relative to stratigraphic position.

Figure 18. Plots of depth versus $\delta^{13}C$ ‰PDB and $\delta^{18}O$ ‰SMOW superimposed against a simplified stratigraphic column, for carbonates sampled from the I stratigraphic interval.

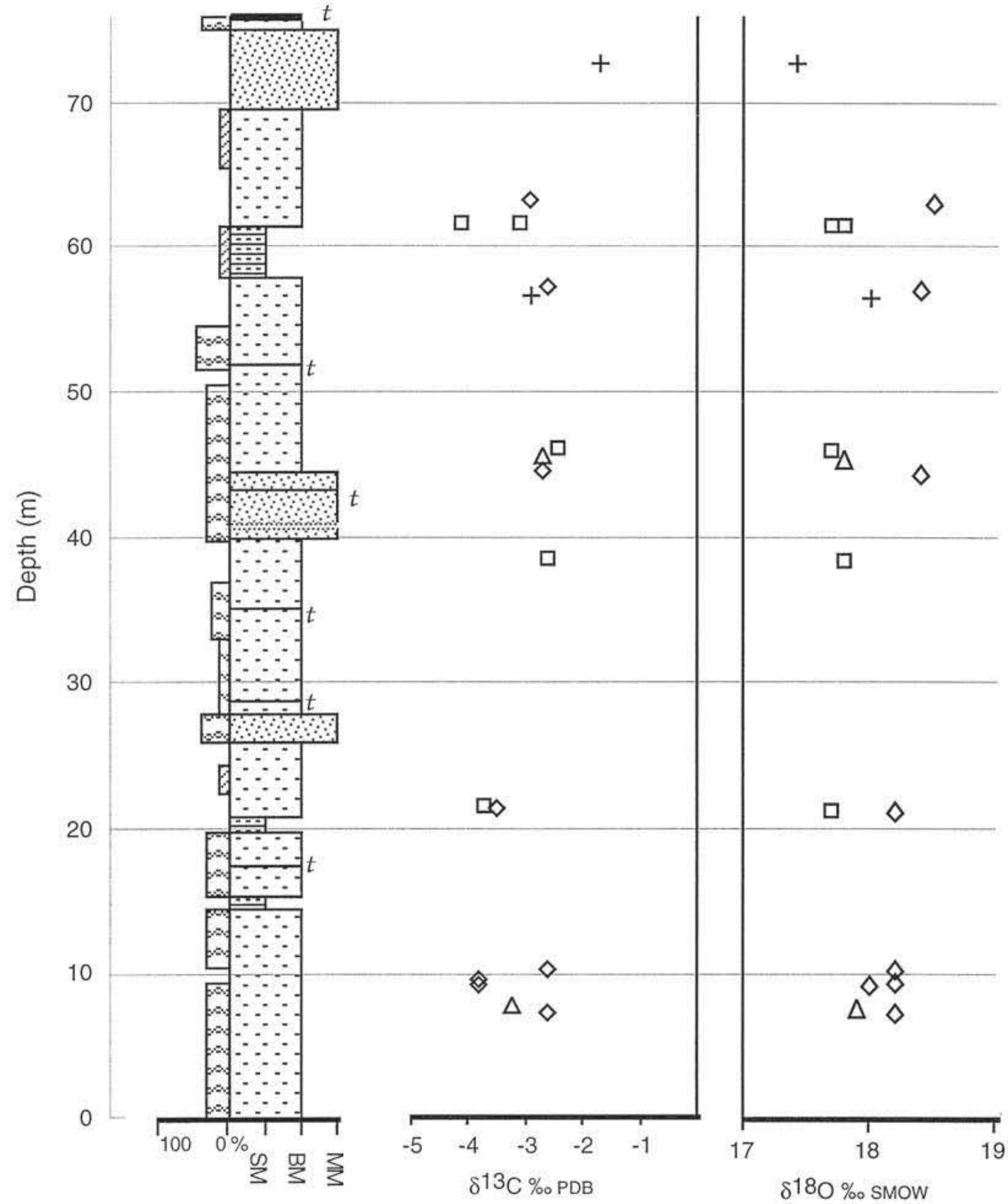

Rhythmically laminated pyritic siltstone

Rhythmically laminated pyritic siltstone with abundant nodular carbonate layers.

MM Medium-bedded, stylolitic mudstone

BM Banded mudstone

SM Shaly banded mudstone

— *t* Tuffaceous marker bed

◇ Mudstone-hosted, whole rock Stage OI ferroan dolomite

□ Stage I calcite white bands

△ Stage I calcite from nodular layers

+ Mudstone-hosted Stage I calcite

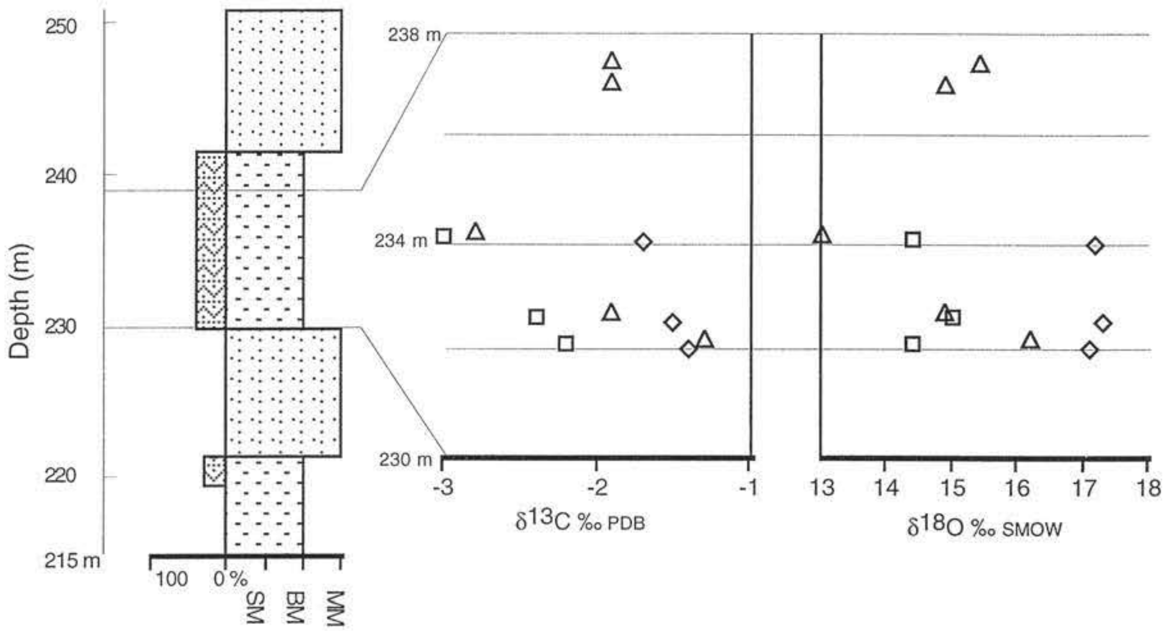

Rhythmically laminated pyritic siltstone

Rhythmically laminated pyritic siltstone with abundant nodular carbonate layers.

MM Medium-bedded, stylolitic mudstone

BM Banded mudstone

SM Shaly banded mudstone

— *t* Tuffaceous marker bed

◇ Mudstone-hosted, whole rock Stage OI ferroan dolomite

□ Stage I calcite white bands

△ Stage I calcite from nodular layers

+ Mudstone-hosted Stage I calcite

Figure 19. Plots of depth versus $\delta^{13}C$ ‰PDB and $\delta^{18}O$‰SMOW superimposed against a simplified stratigraphic column, for carbonates sampled from the C stratigraphic interval.

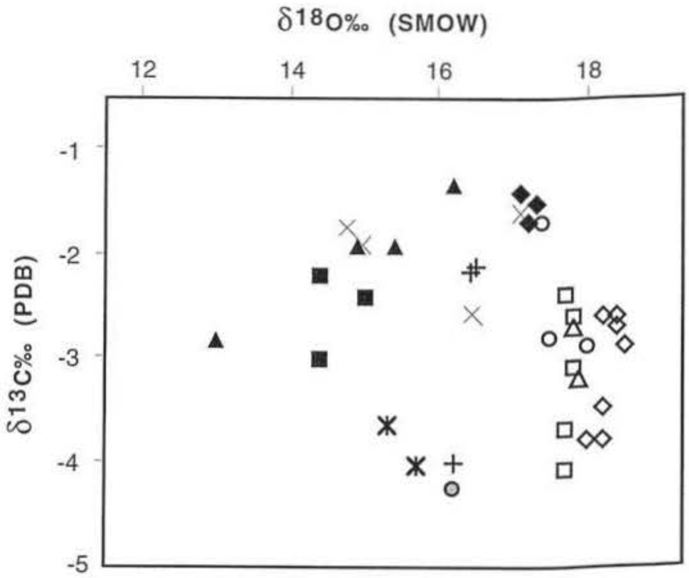

GF South - I stratigraphic sequence

◇ Mudstone-hosted, whole rock Stage OI ferroan dolomite

□ Stage I calcite white bands

△ Stage I calcite from nodular layers

○ Mudstone-hosted Stage I calcite

GF North - C stratigraphic sequence

◆ Mudstone-hosted, whole rock Stage OI ferroan dolomite

■ Stage I calcite white bands

▲ Stage I calcite from nodular layers

GF South - Ankerite alteration

\+ Mudstone-hosted whole rock Stage VIII Ferroan carbonate .

✱ Whole rock Stage VIII ferroan carbonate from nodular layers .

GF South - carbonate veins

× Stage V sugary dolomite veins

● Ferroan dolomite from Stage IXa vein, also containing Cpy-Sp-Gn-Po-Py infill.

Figure 20. Plot illustrating $\delta^{13}C$ versus $\delta^{18}O$ for carbonates from George Fisher.

Legend for Figure 21.

GF South - I stratigraphic sequence

◇ Mudstone-hosted Stage OI whole rock ferroan dolomite

○ Mudstone-hosted Stage I calcite

△ Stage I calcite from nodular layers

□ Stage I calcite from white bands

GF North - C stratigraphic sequence

◇ Mudstone-hosted Stage OI whole rock ferroan dolomite

□ Stage I calcite from nodular layers

△ Stage I calcite from white bands

GF South - Stage VIII Ankerite alteration

× Mudstone-hosted Stage VIII whole rock ferroan carbonate

+ Whole rock Stage VIII ferroan carbonate from nodular layers

GF South - carbonate vein infill

+ Stage V sugary ferroan dolomite vein infill

○ Ferroan dolomite from Stage IXa vein, also containing Sp-Gn-Po-Py-Cpy infill.

Hilton Mine and Lake Moondarra carbonates

○ Whole rock shale-hosted dolomite from the Lake Moondarra area (Waring, 1990)

◆ Carbonate infill sampled from an early bedding parallel vein (Valenta, 1988)

◆ Hilton Mine Cu-related vein-filling and whole rock carbonates (Valenta, 1988)

Carbonate Populations

Field 1. Mount Isa; late-stage dolomite alteration associated with subeconomic Cu drillhole intersections 2km south of the mine (Waring, 1990).

Field 2. Mount Isa; late-stage dolomite alteration from the 1100 Cu orebody at 4200mN (Waring, 1990).

Field 3. Mount Isa; late-stage dolomite alteration from the 1100 Cu orebody at 5030mN (Heinrich et al., 1989).

Field 4. Mount Isa; late-stage dolomite alteration from the 650 Cu orebody (Heinrich et al., 1989).

Field 5. Mount Isa; Urquhart Shale distal to 1100 Cu orebody at 4200mN (Waring, 1990).

Field 6. Mount Isa; Urqhuart Shale proximal to 1100 Cu orebody at 5030mN (Heinrich et al., 1989).

Field 7. Mount Isa; Urquhart Shale proximal to 1100 Cu orebody at 4200mN (Waring, 1990).

Field 8. Mount Isa; Urquhart Shale adjacent to subeconomic Cu drillhole intersections 2km south of Mount Isa Mine (Waring, 1990).

Field 9. Mount Isa; Urqhart Shale samples located furthest away from Cu intersections south of Mine (Waring, 1990).

Field 10. Hilton Mine; Cu-related vein-filling and whole rock carbonates (Valenta, 1988).

Field 11. George Fisher deposit; Stage V vein-filling ferroan dolomite, Stage VIII whole rock ferroan carbonate alteration and Stage IXa vein-filling ferroan dolomite.

Field 12. George Fisher deposit - north; Stage OI whole rock ferroan dolomite and Stage I calcite.

Field 13. George Fisher deposit - south; Stage OI whole rock ferroan dolomite and Stage I calcite.

Field 14. Lake Moondarra; Whole rock shale-hosted dolomite (Waring, 1990).

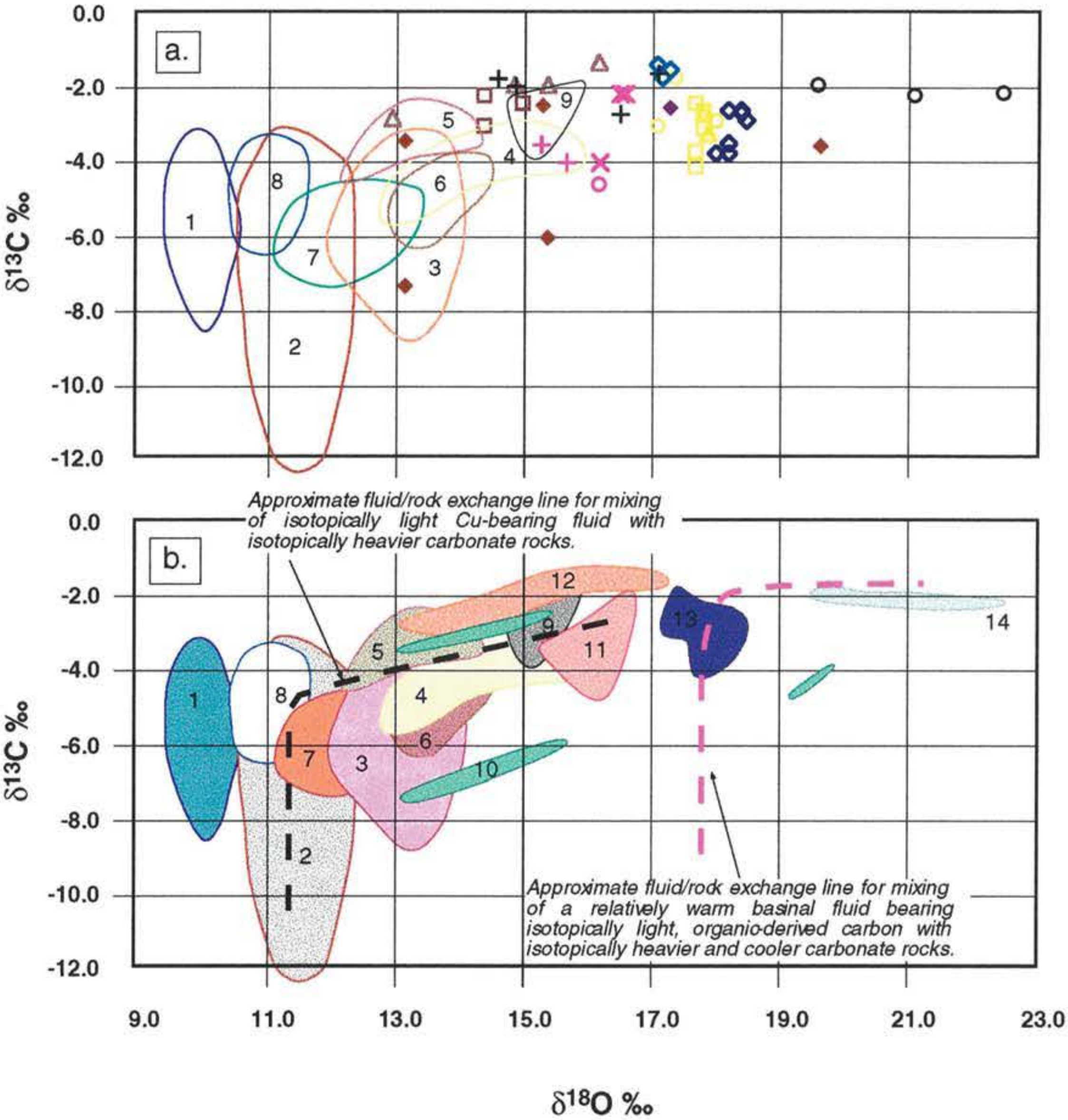

Figure 21. Plots illustrating carbon (PDB) versus oxygen (SMOW) isotope compositions for carbonates from the George Fisher deposit compared with data previously collected at Mount Isa Mine (Heinrich et al., 1989, Waring, 1990a), Hilton Mine (Valenta, 1988) and Lake Moondarra (Waring, 1990a). Data points for George Fisher, Hilton and Lake Moondarra samples are illustrated in (a), whilst fields defined by proposed carbonate populations for the Mount Isa mineralization system as a whole are presented in (b). Carbon and oxygen isotope compositions for carbonates at George Fisher overlap with Cu-related carbonate populations at Mount Isa Mine and Hilton Mine and define a new niche of values not previously identified in the Mount Isa mineralization system. Approximate fluid/rock isotope exchange lines for Cu-bearing fluids (after Waring, 1990a) and early carbonates associated with Zn-Pb-Ag mineralization at George Fisher are also illustrated.

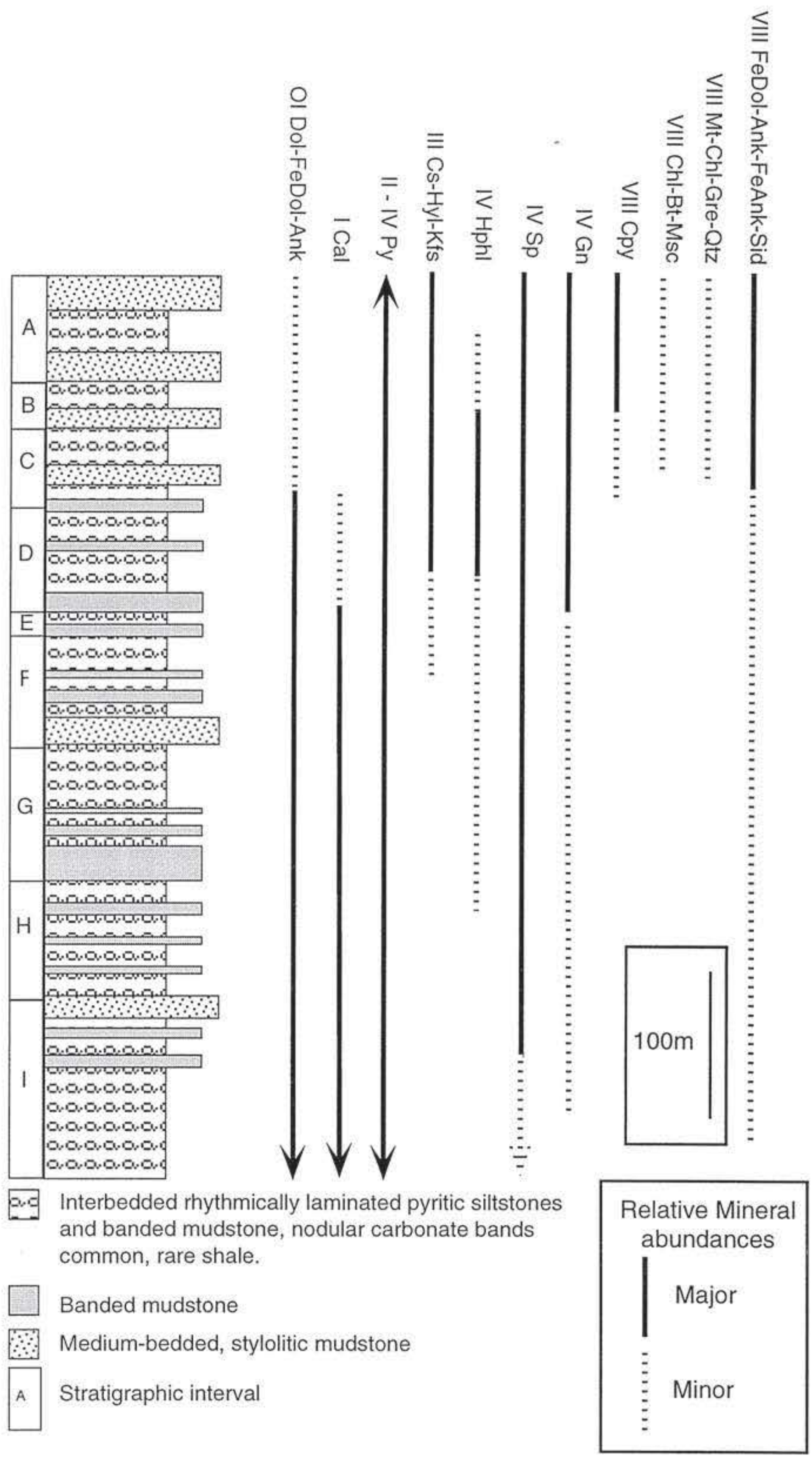

Figure 22a. Simplified stratigraphic column illustrating the distribution of major rock types, nodular carbonate banding, economic sulphides and alteration assemblages at George Fisher.

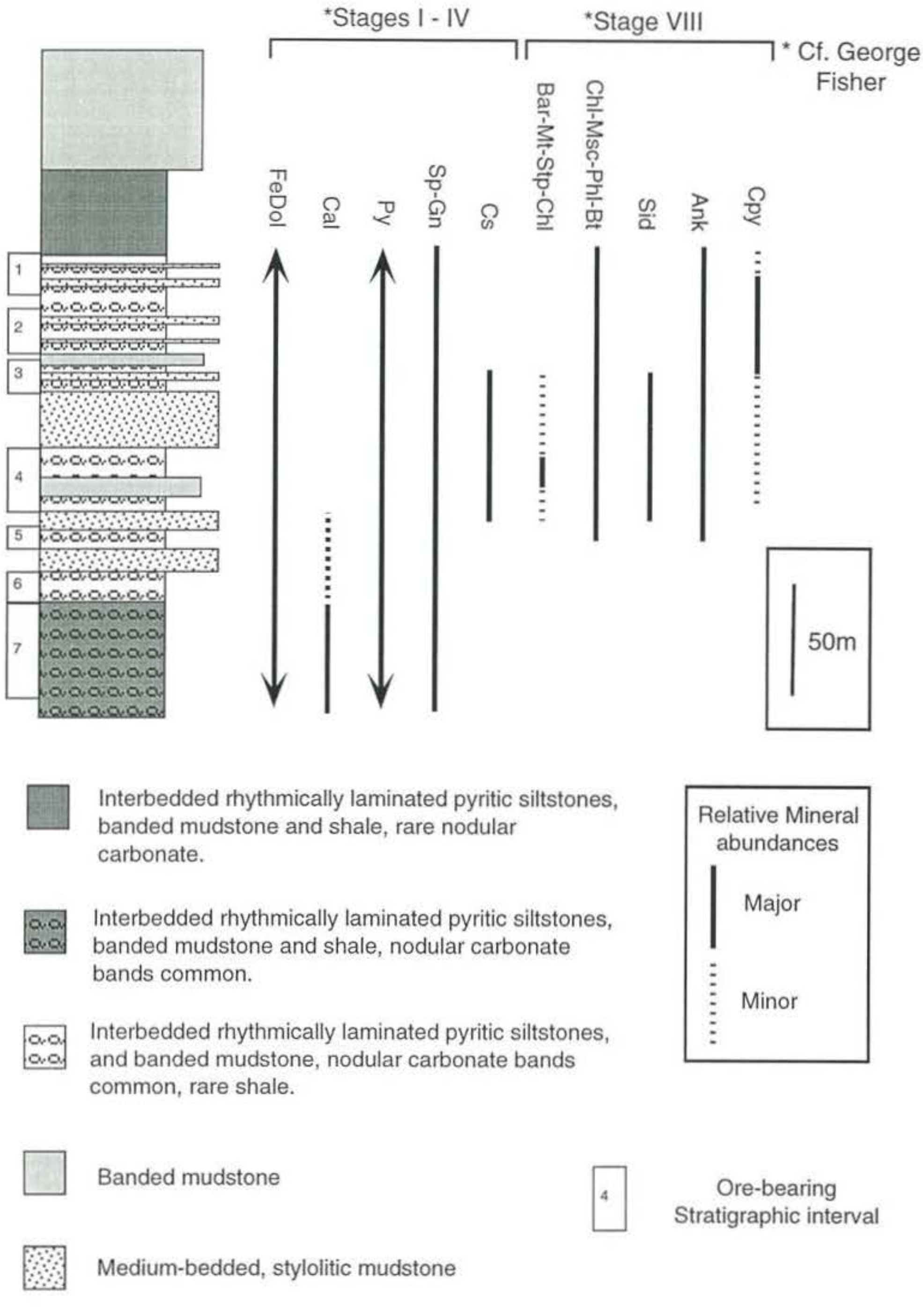

Figure 22b. Simplified stratigraphic column illustrating the distribution of major rock types and nodular carbonate banding, and distribution of economic sulphides and alteration assemblages at Hilton Mine. A generalized comparison with George Fisher is also included (adapted from unpub. MIM Ltd data, Tuesley (1993), Valenta (1988) and Perkins and Bell (1998)).

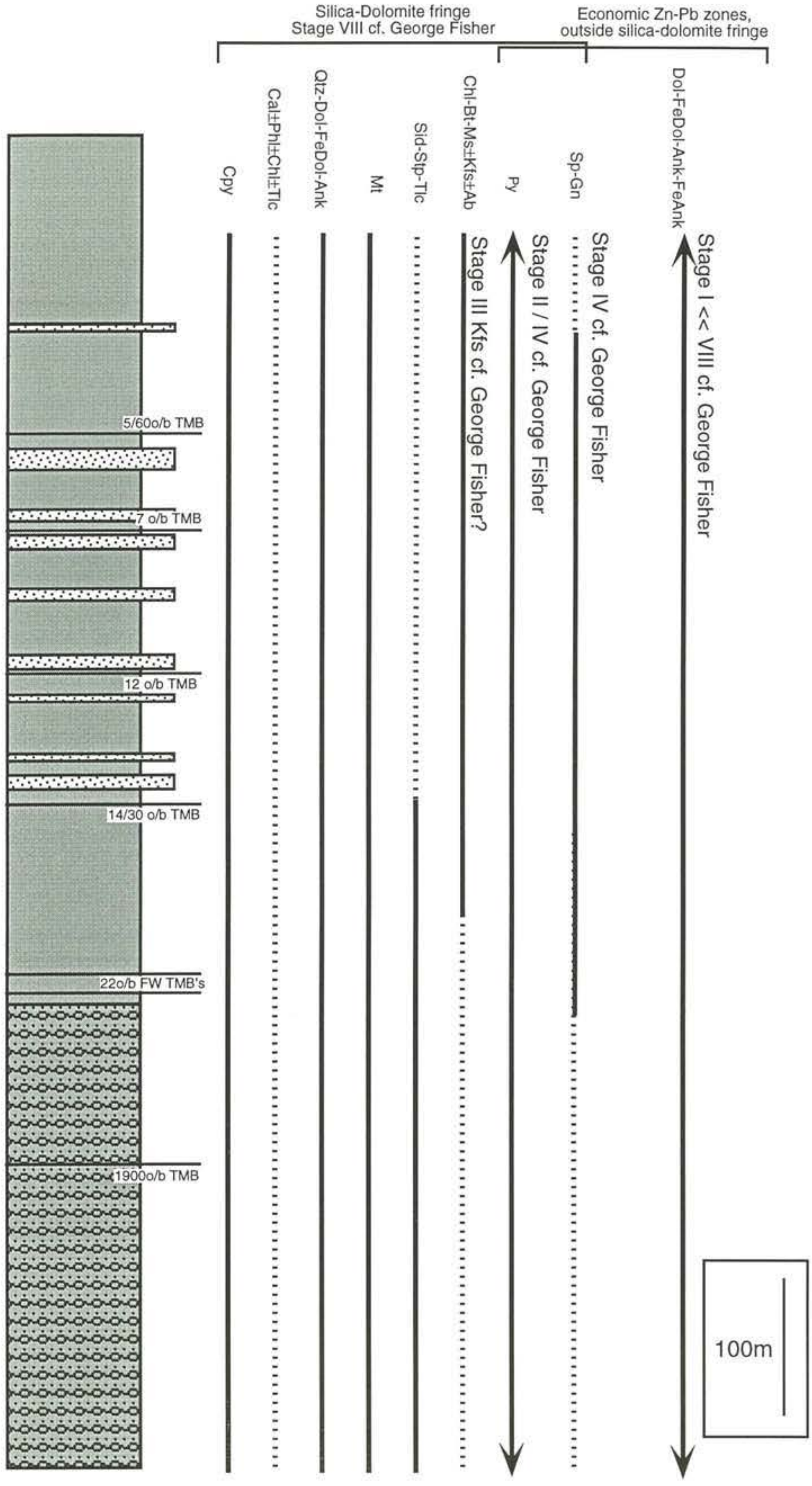

Figure 22c. Simplified metal and alteration distribution patterns at Mount Isa (adapted from Stanton, 1963, Waring, 1990, Swager, et al., 1987, and Perkins, 1997). Refer to Fig. 23b for legend.